

Technical Workshop

Innovative methods for solute flux measurement in the subsurface environment, with technology demonstration and practical field training

7-9 March 2018

Mol, Belgium

Conventionally, the distribution and transport of solutes in groundwater is determined by taking groundwater samples at specific times and locations. These measurements, however, provide only snapshots of solute concentration in the subsurface environment but contain no information on solute fluxes. Measurement of solute fluxes is now widely acknowledged to be the preferred and technically superior approach to the assessment of solute transport in both surface water (e.g. rivers) and groundwater bodies. Solute fluxes can only be determined indirectly using related information on groundwater velocity and direction, as well as solute concentration. However, this concept offers considerable improvements in the resolution of processes controlling solute behaviour and can address inherent uncertainties in "snapshot"-style monitoring. It has specific importance to studies of contaminant fate and performance assessment of restoration or management measures in many contexts (e.g. investigation and management of environmental impacts from agricultural, industrial and natural sources). In recent years several methods have been developed to directly measure solute fluxes in the subsurface.

The aim of this workshop is to explore the principles and applications of innovative approaches available for sampling groundwater using solute flux-based concepts. Participants will gain an understanding of the theory which underpins this approach, the different methods available and receive hands-on field training with different technologies.

The sessions will be presented by experienced training facilitators and experts from the INSPIRATION Innovative Training Network (www.inspirationitn.eu) and iFLUX. The programme includes technical sessions and hosted field trip, with the objective of consolidating participant understanding and skills development.

The workshop is open to external participants including, but not limited to, stakeholders, practitioners, managers, researchers and students with interests in the monitoring, assessment and management of groundwater resources in different contexts. Participants with backgrounds in agricultural/environmental engineering, hydrogeology, hydrology, environmental sciences and applied geosciences are encouraged to attend. The course will be attended by scientists and researchers from the INSPIRATION Innovative Training Network, providing a unique opportunity for networking with leading experts in the field.

Further information on the technical programme, joining instructions and venue for the workshop is provided overleaf.

Programme

Wednesday 7 March : Principles and theoretical background (VITO, Mol)

12.50-13.00: Introduction and welcome (*Ingeborg Joris, VITO, Belgium*)

13.00-14.00: Good practices and pitfalls in conventional groundwater sampling (*Instructor: Johan Vos, VITO, Belgium*)

14.15-15.45: Passive sampling techniques to measure solute fluxes in the subsurface (*Instructor: Goedele Verreydt, iFLUX, Belgium*)

16.00-17.30: Using tracers to assess the movement of solutes in the subsurface environment (*Instructor: Serge Brouyère, University of Liege, Belgium*)

Thursday 8 March : Practical training in different methods and technologies (University of Liege, Liege)

09.00-17.00: Demonstration and hands-on training of different field-based methods for groundwater sampling, including conventional techniques, tracer tests and passive sampling techniques. This is provided at the University of Liege field site in Hermalle-sous-Argenteau. (*Instructors: Johan Vos, VITO, Belgium; Goedele Verreydt, iFLUX, Belgium; Ilse Van Keer, VITO, Belgium; Pierre Jamin, University of Liege, Belgium*).

Friday 9 March : Interpretation and use of flux measurements (VITO, Mol)

09.00-12.30: Hands-on training in the interpretation and use of flux measurements. Participants will get a case study with data on concentrations and flux measurements collected with the different methods discussed. Using the appropriate calculation tools they will interpret the transport and dispersion of solutes in a groundwater body based on different types of measurements and the concentration and mass that will reach the receptors present. Participants will have the opportunity to present the case to each other. (*Instructors: Goedele Verreydt, iFLUX, Belgium; Ilse Van Keer, VITO, Belgium; Pierre Jamin, University of Liege, Belgium; Laurent Piron, Geolys, Belgium*).

Registration

Registration for this workshop is essential as places are limited. **Deadline for registration is 28th February 2018.**

You can register for the workshop using this [link](#). If you have further questions please contact Katrien.Bultynck@vito.be.

Cost

The fee for the workshop is €180, payable electronically when registering. This covers course notes, lunch, coffee/tea breaks, field site visit, transport from and to Mol train station (on Wednesday 7 March and Friday 9 March) and Certificate of Attendance.

Accommodation is available in the Lakehouse hotel, close to the workshop venue (address overleaf). If you wish to stay in the Lakehouse, please indicate this on the application form. Participants must cover their accommodation costs directly with the hotel. Room rates per night, including breakfast, are: single room with parkview: € 78,00; single room with lakeview: € 88,00; double room with lakeview: € 96,00. All rooms have a bathroom with shower, colour TV, minibar and free wireless Internet.

Venue & Location

Venue

The workshop will be hosted in the Jupiter Meeting Room at VITO (see picture below). VITO is a short distance from the Lakehouse hotel and Mol town centre. Taxis are available.

VITO TAP – Meeting Room Jupiter

Boeretang 282

2400 Mol

Belgium

[Route description](#)

[Route description with Googlemaps](#)



Location map

The map below shows the location of the workshop venue and Lakehouse hotel. There is a frequent rail service to Mol from Brussels, with a journey time of 1.5 to 2 hours. Mol train station is located in the centre of the town. Taxis are available outside Mol train station. Details of the Lakehouse hotel are provided below.

Lakehouse hotel

Boeretang 201

B-2400 Mol, Belgium

+32 14 33 20 60 of +32 14 33 20 57

+32 14 31 27 71

info@lakehouse.be

<http://lakehouse.sckcen.be/en>



Workshop manual

Inspiration Workshop - Innovative methods for solute flux measurement in the subsurface environment, with technology demonstration and practical field training (07-09/03/2018)

Ilse Van Keer, Serge Brouyère, Pierre Jamin, Ingeborg Joris, Laurent Piront, Goedele Verreydt, Johan Vos

7-9 March 2018



VITO NV

Boeretang 200 - 2400 MOL - BELGIE
Tel. + 32 14 33 55 11 - Fax + 32 14 33 55 99
vito@vito.be - www.vito.be

BTW BE-0244.195.916 RPR (Turnhout)
Bank 375-1117354-90 ING
BE34 3751 1173 5490 - BBRUBEBB

TABLE OF CONTENTS

Table of Contents	I
Evaluation form	II
Welcome	III
Speakers / Organizers	IV
Participants	VII
Programme	VIII
1. Presentations (07/03/2018)	1
2. Field training (08/03/2018)	3
2.1 Schedule	3
2.2 Teams	3
2.3 Exercises	3
2.4 Experimental field site	4
2.5 Finite Volume Point Dilution Method to measure groundwater flux on Hermalle-sous-Argenteau experimental test site (Pierre Jamin)	7
2.6 Application of iFLUX sampler – Prospector	13
2.7 Volume based & low flow groundwater sampling (Johan Vos / Ilse Van Keer)	15
2.7.1 Goal	15
2.7.2 Material	15
2.7.3 Well characteristics	15
3. Evaluation & discussion of field measurements	17
3.1 Groundwater sampling	17
3.1.1 Correction measured ORP to H ₂ -electrode	17
3.1.2 Divers, programming – read out	18
3.2 Evaluation FVPDM results – calculation of groundwater flux	18
3.3 Evaluation results iFLUX – calculation of mass fluxes	19
Contaminant mass flux	19
Contaminant mass discharge	19
Groundwater flow field distortion	20
4. Additional information FVPDM & heat tracer test	23
5. Info	25
Wednesday 7/3	25
Thursday 8/3	26
Friday 9/3	26

EVALUATION FORM

WELCOME

Dear participant,

The quality of soil and water resources is a major concern for the coming decades. According to the EU Thematic Strategy on Soil Protection and the EU Water framework Directive, the soil, and surface and groundwater quality needs to be improved.




To this purpose, reliable measurement of soil, surface water and groundwater characteristics, and pollutant fluxes are of major importance. Conventionally, the dispersion of solutes in groundwater is determined by taking groundwater samples at specific times and locations. These measurements provide snapshots of solute concentration in the subsurface environment but contain no information on the fluxes of the solute. These can only be determined indirectly using other information on groundwater velocity and direction. Over the last years, several methods have been developed to overcome these drawbacks and directly measures fluxes in the subsoil. During this workshop, the principles of the different methods are explained and hands-on training with different technologies is offered. Furthermore, the oral presentations together with the field training provide a forum for discussion, the exchange of information and experiences





We wish a warm welcome to all of you, participants and lecturers, and enjoy the workshop!

The VITO-Inspiration team

Ingeborg, Ilse, Johan, Katrien, Steven, Piet, Priyanka and Gisela

SPEAKERS / ORGANIZERS

	<p>Serge Brouyère (Prof. Dr. Ir) is senior researcher and associate professor at the University of Liège in Belgium, with 25 years of experience in applied research projects and consultancy in groundwater quality and contaminant hydrogeology, in Belgium and abroad, including developing countries. His experience goes from the application of artificial tracers in different contexts such as the delineation of protection zones for groundwater catchments, the evaluation of contaminant transport processes in the soil – unsaturated zone – groundwater – river continuum or the use of applied tracer techniques in contaminated sites. One of the main contribution of S.Brouyère to the field of applied tracer techniques consists in the development of a fully innovative tracer technique, the Finite Volume Point Dilution Method (FVPDM), which allows quantifying and monitoring with time groundwater fluxes in the subsurface. Ongoing developments consist in combining this innovative tracer technique with low-flow sampling technologies and with contaminant passive sampling and monitoring. More recently, S.Brouyère has also gained experience in the use of natural and environmental tracers for characterizing groundwater systems contamination sources and contaminant fate in the subsurface, mostly based on isotopic fractionation of stable isotopes of different groundwater pollutants and compounds (organic contaminants, nitrate, sulfate...). S.Brouyère has also developed researches and projects in the development and application of groundwater flow and reactive transport models in different contexts such as dispersion and attenuation of contaminants in brownfield or regional transport of nitrate in aquifers or climate change impacts on groundwater resources.</p>
	<p>Katrien Bultynck is an administrative assistant at VITO since 2006. She graduated in 2004 as Bachelor in Marketing. The main activities she has been involved in are general administration for the Unit Environmental Modelling, preparation of national and international proposals and the organization of conferences, events and workshops. Over the last ten years he has organized over twenty events. She was involved in the many aspects of event management from location hunting to designing badges, from communication with catering to program planning.</p>
	<p>Pierre Jamin is teaching assistant and PhD student at the University of Liège. After 4 years of research on different research projects, he invested himself in a PhD on the methodological, numerical and technical development of a single well tracer technique (FVPDM) able to measure and monitor groundwater and contaminant fluxes in polluted aquifers. He is in charge of the exercise sessions for 4 courses about groundwater quality and hydrogeological characterisation. Pierre is also responsible for lab and field equipments management and maintenance within his research group.</p>

	<p>Ingeborg Joris (Prof. Dr. Ir.) is a project manager at VITO specialised in soil and water modelling and guest professor at the UAntwerp (since 2018). She joined VITO in 2003 and is part of the Water Management and Technology team. Her expertise lies in modelling of water flow and solute transport in soils and she has been involved in several projects concerning risk of contaminant leaching to groundwater and mitigation strategies for reducing pesticide loads in agricultural catchments. These included developing decision-support systems for risk assessment and groundwater vulnerability maps for the Flemish authorities, stewardship projects for industry, a Europe Aid project on heavy metals in the environment in China and the H2020 WaterProtect project on protecting drinking water resources. She was also the VITO contact for the Marie Curie ITN networks ADVOCATE and INSPIRATION.</p> <p>ingeborg.joris@vito.be</p>
	<p>Laurent Piront (Ir.) is a Director at Geolys Sprl, a private consulting company specialized in soil investigation and groundwater management. He graduated in 2005 as an engineer in hydrogeology at the University of Liège. From 2005 to 2007, he worked as a research engineer at the university of Liège. His experience lies in groundwater management studies such as the delineation of protection zones for groundwater catchments, groundwater risk assessment, the design of drawdown system in urban area, the evaluation of transport processes in the groundwater, the design of rainwater management system.</p> <p>laurent.piront@geolys.be</p>
	<p>Ilse Van Keer (PhD) graduated as a geologist in 1991 at the KU Leuven. After being a research assistant in the field of sandstone diagenesis, she obtained her PhD in 1999. Subsequently, she was employed for two years by the centre of nuclear energy (SCK) in Belgium. She joined VITO in November 2000 and has 18 years of experience contributing to and coordinating research projects with respect to the characterisation of soil and groundwater quality and the associated risks for human and ecosystem. She advises the government on soil investigations, risk evaluation, soil remediation and the development of decision support systems. Ilse is expert in the application of alternative soil and groundwater investigation techniques. Since 2014 she also gives additional training to consultants with respect to the Flemish guidelines concerning soil and groundwater sampling techniques.</p> <p>ilse.vankeer@vito.be</p>
	<p>Goedele Verreydt (PhD) is inventor and source of inspiration of the iFLUX technology. She is expert in terms of flux sampling of soil and groundwater contamination. She obtained her Master degree in Environmental Sciences at the Hogeschool West-Vlaanderen in 2004. After a couple of years of experience as a soil expert, Goedele conducted research during her PhD at VITO into the applicability of techniques to directly determine mass fluxes. After obtaining her PhD degree in 2012 Goedele lead a team of researchers and product developers in the field of groundwater contamination and soil remediation. As a result of the development and valorization of the iFLUX technology she started in November 2017 as Technical manager of iFLUX.</p> <p>goedele@ifluxsampling.com</p>



Ing. Johan Vos (Ing.) graduated in 1997 as an engineer in the direction of environmental technology. From 1997 to 1999 he worked as a project engineer at the environmental consultancy Ecozem. Since 1999 he has been working at VITO where he was active until 2008 within the group Separation and Conversion Techniques. Within this group he was responsible for drawing up and supervising lab and pilot tests on soil remediation and for monitoring and controlling soil remediation on behalf of the government (OVAM). Since 2009 he has been part of the Water Management and Technology team where he is responsible for the coordination of inspections of ongoing remediation and pilot tests. He advises the Flemish government (OVAM) on soil investigations and soil remediation, is one of the authors of the Compendium for Sampling and Analysis of OVAM (CMA) and is responsible for the training courses for soil remediation experts on soil and groundwater sampling techniques.

johan.vos@vito.be

PARTICIPANTS

Last Name	First name	Company
Amoah-Antwi	Collins	Warsaw University of Technology
Ariza Carricondo	Cristina	University of Antwerpen
Banerjee	Priyanka	VITO
Bujak	Izabela	Helmholtz Zentrum für Umweltforschung - UFZ
Damala	Polyxeni	Geolys sprl
Dhaese	Kristiaan	pcfruit vzw
Ezzati	Golnaz	ESR INSPIRATION Phd Candidate
Geukens	Lana	KUL Soil and Water Management
Giber	Alexandra	IWW Water Centre
Gill	Richard	Shell Global Solutions
Gillett	Andrew	Land Quality Management Ltd
Naert	Martijn	Mava/Witteveen + Bos
Neyens	Cas	VUB
Nikolenko	Olha	University of Liege
Quaglia	Gisela	VITO
Saputra	Bastian	University of Sheffield
Soria Penafiel	Rosa Isabel	University of Sheffield
Tegenbos	Julie	ERM
Van Humbeeck	Thomas	Arcadis Belgium
von Chamier	Julia	Helmholtz-Zentrum für Umweltforschung - UFZ
Weatherl	Robin	Eawag and University of Neuchâtel
Yendell	Alan	Scottish Environment Protection Agency

PROGRAMME

Wednesday, 7 March 2018

12.15 - 12.50	Registration
12.50 - 13.00	Introduction & welcome <i>I. Joris, VITO</i>
13.00 - 14.00	Good practices and pitfalls in conventional groundwater sampling <i>J. Vos, VITO</i>
14.00 - 14.15	Coffee break
14.15 – 15.45	Passive sampling techniques to measure solute fluxes in the subsurface <i>G. Verreydt, iFLUX</i>
15.45 – 16.00	Coffee break
16.00 – 17.30	Using tracers to assess the movement of solutes in the subsurface environment <i>S. Brouyère, ULg</i>
17.30 – 17.40	Introduction to the field training <i>I. Van Keer, VITO</i>

Thursday, 8 March 2018

8.15	Assembly at VITO, TAP building
8.30	Departure to the field site
10.00	Coffee break
10.15	Introduction to the field site & field training

Team 1*

10.30	Groundwater flux measurement
11.30	Application of iFLUX sampler - prospector
12.30	Lunch
13.15	Volume based groundwater sampling
14.15	Low flow sampling
15.15	Coffee break
15.30	Departure
17.00	Arrival @ VITO – TAP

* 1 Team consists of 5-6 people

Team 2

10.30	Volume based groundwater sampling
11.30	Low flow sampling
12.30	Lunch
13.15	Groundwater flux measurement
14.15	Application of iFLUX sampler - prospector
15.15	Coffee break
15.30	Departure
17.00	Arrival @ VITO - TAP

Team 3

10.30	Application of iFLUX sampler - prospector
11.30	Groundwater flux measurement
12.30	Lunch
13.15	Low flow sampling
14.15	Volume based groundwater sampling
15.15	Coffee break
15.30	Departure
17.00	Arrival @ VITO - TAP

Team 4

10.30	Low flow sampling
11.30	Volume based groundwater sampling
12.30	Lunch
13.15	Application of iFLUX sampler - prospector
14.15	Groundwater flux measurement
15.15	Coffee break
15.30	Departure
17.00	Arrival @ VITO - TAP

Friday, 9th March 2018

9.00-9.30	Redox calculations + diver readings & baro correction (Johan Vos)
9.30-9.50	Calculation and interpretation of FVPDM data (Pierre Jamin)
9.50-10.10	Calculation and interpretation of mass fluxes (Goedele Verreydt)
10.15-10.30	Coffeebreak
10.30-11.15	Participants @work, including preparation of presentation
11.15-12.30	Presentations & discussion
	Team 1
	Team 2
	Team 3
	Team 4

1. PRESENTATIONS (07/03/2018)

GOOD PRACTICES AND PITTFALLS IN CONVENTIONAL GROUNDWATER SAMPLING

Johan Vos

4/03/2018

©VITO – Not for distribution

1

GROUNDWATER SAMPLING

- Goal:
 - Is the groundwater contaminated?
 - What is the overall condition of the groundwater?
- Good groundwater sampling:
 - Location of the monitoring well and filter
 - Apply the correct/most appropriate sampling equipment
 - Correct use of pumps, field equipment, ...
 - Work according to the current national or state guidelines

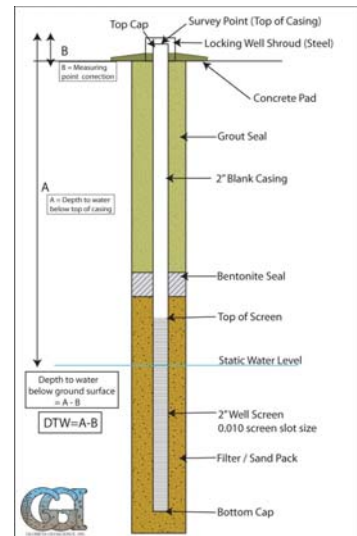
4/03/2018

©VITO – Not for distribution

2

MONITORING WELLS

- Permanent wells
 - Monitoring groundwater over a longer time period
 - Several sampling rounds over time possible
 - Installation of monitoring devices possible (diver, iFLUX, ...)
- Temporary well
 - Only 1 sampling round possible
 - No monitoring over time
- Installment
 - Filter needs to be installed in the aquifer and on the depth that needs to be sampled
 - Correct layout needs to be known to be able to interpret the results correctly



4/03/2018

©VITO – Not for distribution

3

MONITORING WELLS

- Minimal diameter
 - Measuring devices
 - Monitoring equipment
 - Pump
- Monitoring well needs to be closed off from outside influences on the surface
- Label:
 - Unique name
 - Installment date
 - Depth filter
 - Qualitative indications of groundwater flow (good, moderate, bad)

4/03/2018

©VITO – Not for distribution

4

SAMPLING EQUIPEMENT

- Pumps have to be chosen based on:
 - Depth monitoring well
 - Diameter monitoring well
 - Groundwater level
 - Presence of VOC
 - Risk of cross contamination



Parts of the pump that come in contact with the groundwater need to be

- Made of inert materials (stainless steel, teflon, ...)
- Cleanable or replaceable

PUMP SELECTION

Pump	Well refreshment		Sampling						Installation		
	low permeable layer	good permeable layer	low permeable layer (excl.peat)	good permeable layer	low permeable layer	possibility of in-line filtration	risk of cross contamination	maximal groundwater depth (m-bgs)		suitability for analysis on VOCs LNAPL / DNAPL	required minimal well diameter (mm)
Gas pressure system (e.g. bellows pump)	+	+	+	+	+	+	-	40	-	-	25
Bailer sampling device	-	+	+	+	-	+/-	+/-	90	-	-	25
Centrifugal pump	+	+	-	-	-	-	-	6	-	-	45
Centrifugal submersible Pump	+	+	-	+	+	+	-	80	+	-	50
Footvalve/ball valve	+	+	-	+	+	+/-	-	40	+	-	25
Peristaltic pump	+	+	+	+	+	+	+	7	+	-	25
Vacuum pump	+	+	-	-	-	-	-	8	-	-	25
Liquid layer sampler	na	na	+	+	-	-	-	25	-	+	35

* function of groundwater depth & well diameter

"-": not allowed in the framework of the Flemish soil decree

na: not applicable

"+": suitable

"+/-": less suitable

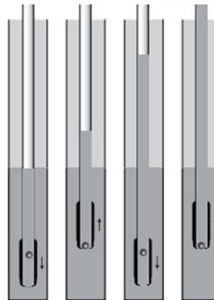
PERISTALTIC PUMP

- Manually or electrically driven (internal battery)
- Silicon tubing in pump, PE or teflon sampling tubing
- Tubing easily replacable
- Several diameters tubing available
- Short contact with air during the filling of the tubing
- Maximum head 7 to 8 meter below groundsurface



BALL VALVE PUMP

- Manually or mechanically driven
- Only contact between groundwater and ball valve and tubing
- Ball valve is easily cleanable and replacable
- Mechanically driven pumping very well suited for deep groundwater levels



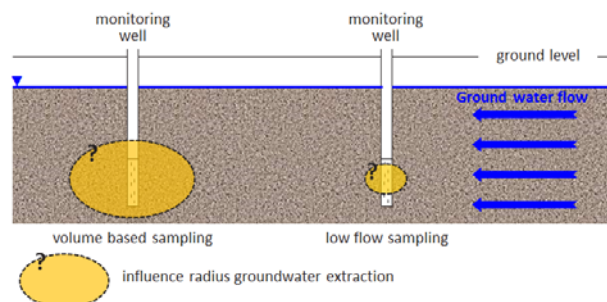
SUBMERSIBLE PUMP

- Large flow variance possible
- Flow finely adjustable
- Suitable for deep groundwater levels
- Low turbulence
- No air in pump and tubing during correct use
- Possible threat of cross contamination
- External electricity source needed



GROUNDWATER SAMPLING

- Aim of the sampling:
 - Overall status of the groundwater
 - Sampling over a larger volume
 - **Volume based sampling**
- Research into the potential contaminations in the groundwater and the demarcation
 - Point samples
 - **Low flow sampling/micropurging**



GROUNDWATER SAMPLING

- Check condition of monitoring well
- Measure groundwater level
- Measure free product (if present)
- Measure monitoring well characteristics
- Pre-pump / refresh the groundwater
- On-site measurements groundwater (pH, O₂, conductivity, temperature, other site specific parameters, ...)
- Sampling (filtration when necessary)

GROUNDWATER LEVEL

- Measure relative to a fixed point
- More than 1 well: calculate groundwater levels to 1 fixed point for all
 - Chosen point on site
 - Belgium: mTAW
- Correctly note in field report
 - Relative to top monitoring well: m-tw (meters below top well)
 - Relative to surface level: m-sl (meters below surface level)
 - Relative to fixed point (can be calculated later)
- Devices:
 - Measuring tape (audio and/or visible signal)
 - Diver (water level logger)
 - Monitoring over longer periods: temperature, water level, conductivity
 - Barometric compensation necessary



VOLUME BASED SAMPLING

- Pre-pumping:
 - Minimal volume: 5 times the volume of the monitoring well
 - Example:
 - Monitoring well 50mm, depth 10m: pre-pumping at least 40 liters
 - Monitoring well 100mm, depth 10m: pre-pumping at least 157 liters
 - Stable field parameters (pH, conductivity, O₂, ...)
- High flow possible for pre-pumping
- Low flow for sampling (laminar flow for sampling)
- Large volumes of waste water

diam well (mm)	volume/m (l)	5*vol/m (l)
100	3,14	15,71
50	0,79	3,93
30	0,28	1,41

LOW FLOW SAMPLING - MICROPURGING

- Pre-pumping
 - Low flow rate: 0,1 to 0,5 l/min
 - Natural recharge rate of the aquifer may not be exceeded (stable drop of groundwater level during pumping)
 - Maximum drop of groundwater level during pre-pumping:
 - Shallow wells (< 15 m depth): 10 cm
 - Deep wells (> 15m depth): 50 cm
 - Keep groundwater level above filter during pre-pumping
 - End pre-pumping:
 - Conductivity stable and 5 times the volume of the filter removed
 - Conductivity and dissolved oxygen stable
 - Value turbidity < 10 NTU
 - None of the above possible: remove 3 times the volume of the well
- Low volumes of waste water

FIELD MEASUREMENTS

- Measured in a flow through cell
 - pH
 - Conductivity
 - Temperature
 - ORP
 - Dissolved oxygen
 - Turbidity
 - Research dependant parameters



FIELD MEASUREMENTS

- pH
 - Calibrated measurement
 - Store in 3M KCl
 - Stable: max. fluctuation of 0,1 per minute
- Conductivity
 - Stable: max. fluctuation of 5% per minute
- Temperature
 - Stable: max. fluctuation of 5% per minute
- Dissolved oxygen
 - Calibrated measurement
 - Stable: max. fluctuation of 5% per minute

FIELD MEASUREMENTS

- **ORP (oxido-reduction potential)**
 - No calibration possible, check the electrode on a regular basis
 - Stable: max. fluctuation of 10 mV per minute
 - Measurements need to be recalculated to a H₂-electrode:
 - $E_H = E_m + E_{ref}$
 - E_H = ORP relative to a H₂-electrode
 - E_m = ORP measured with an Ag/AgCl(3M)-electrode
 - E_{ref} = electrode and temperature depending reference-value

T (°C)	E _{ref}	T (°C)	E _{ref}	T (°C)	E _{ref}	T (°C)	E _{ref}
0	224,2	25	207	50	188,4	75	167,7
5	220,9	30	203,4	55	184,4	80	163,1
10	217,4	35	199,8	60	180,3	85	158,3
15	214	40	196,1	65	176,4	90	153,3
20	210,5	45	192,3	70	172,1	95	148,1

FILTRATION OF SAMPLES

- **Always check with the lab and local guidances**
- **Some general guidelines**
 - Reference values made for filtered water: filter the samples
 - Metals: filtration in the field
 - Orthophosphate: filtration in the field
 - CN: filtration in the field
 - Other nutrients: no filtration
 - Volatiles: NO filtration
 - Mineral oil: no filtration



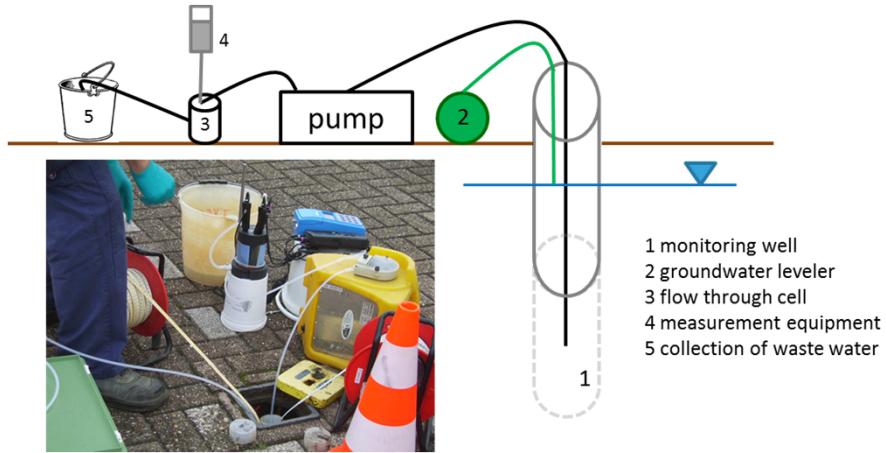
GENERAL GUIDELINES FOR GROUNDWATER SAMPLING

- Sampling order: least polluted to most polluted well
- Sampling tubing needs to be replaced before each sampling
- Don't leave sampling tubings in the well
- Wear a fresh pair of gloves for each well
- Fill the recipient in a single go without air bubbles
- Topping up recipients for volatile parameters is prohibited
- Overfilling a recipient that contains a conservative: start again with a new recipient
- Clean or replace all the tubings and parts of the pump that have been in contact with the groundwater
- Filling order recipients
 - No conservatives
 - Solid conservatives
 - Fluid conservatives

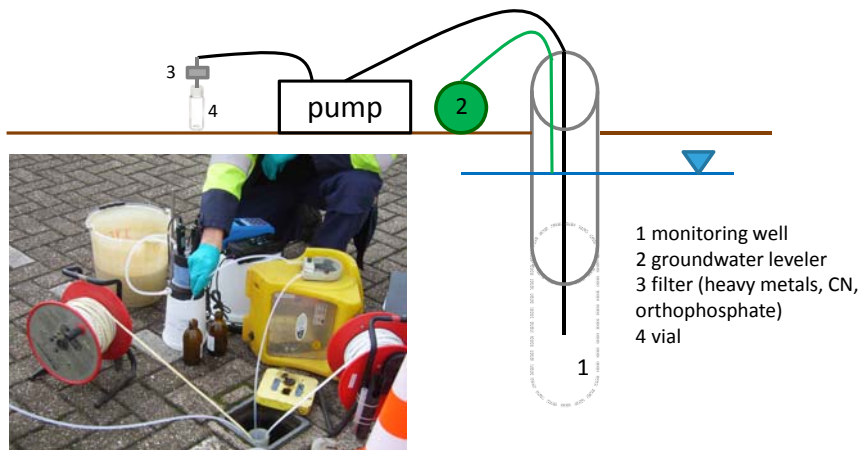
GENERAL GUIDELINES FOR GROUNDWATER SAMPLING

- Avoid turbulence during the filling of the recipient
 - Flowrate : 0,1 to 0,2 l/min
 - Tubing in recipient (max 0,5cm in sample)
 - Bring the tubing up while recipient fills
 - Recipient with conservatives: cut off the part of the tubing that was in touch with the sample
- Label the sample
 - Code groundwater well
 - Code location
 - Date of sampling!
- Store chilled from the moment of sampling until deliverance to the laboratory

LOW FLOW WELL REFRESHMENT



LOW FLOW SAMPLING





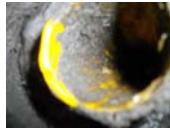
DON'TS



inappropriate "flow through" cell



Never sample dirty well



use proper vials



Waste water has to be collected and properly disposed



avoid head space



No "dripping"



After sampling, remove tubings



Store samples in cool box

Photography
Joris Tallon (OVAM)

USING DIVERS FOR GROUNDWATER LEVEL MONITORING

- Divers
 - Groundwater level
 - Temperature
 - Conductivity
 - Dissolved oxygen
 - ...
- Programmable to monitor the groundwater over an extended period of time
- Divers used at VITO:
 - Water pressure (= water level + barometric pressure)
 - Water pressure + conductivity
 - Barometric pressure



USING DIVERS FOR GROUNDWATER LEVEL MONITORING

- Tips for programming the diver
 - Use a barometric diver if the diver measures total pressure
 - Start all the divers at the same time (programmable start in the future)
 - Program the divers in advance, record which diver was installed in which monitoring well
 - Take into account the maximum amount of measurements before the memory overflows
 - Groundwater: measuring every 15 mins is ok

- Use the diver in slug tests:
 - Measure every 1 or 0,5 sec
 - Short monitoring time, no barometric diver needed

Passive sampling techniques to measure solute fluxes in the subsurface

Inspiration workshop – 7 March 2018

Goedele Verreydt - iFLUX

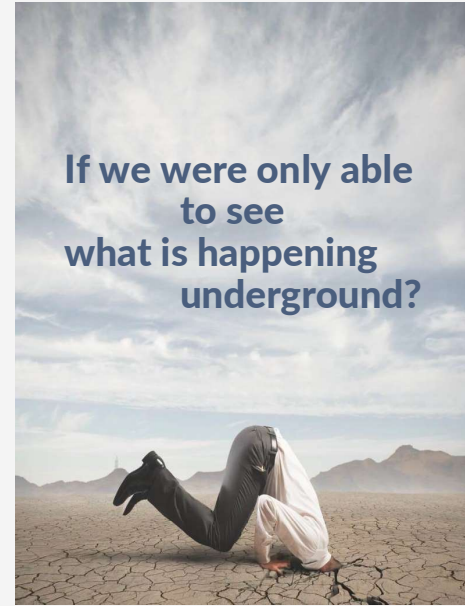
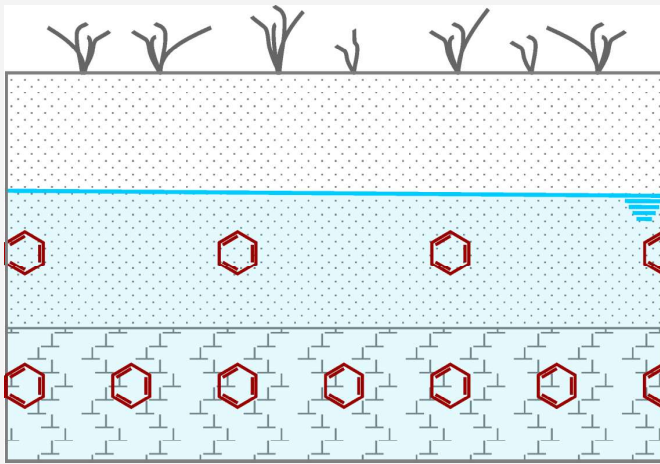


Overview of presentation

1. **What is solute mass flux?**
2. Why determine mass flux?
3. How to determine solute mass flux?
4. Passive sampling
5. Passive flux sampling
6. iFLUX sampler
7. Some case studies
8. How about regulation? CMF approach
9. Take home points

1. What is solute mass flux?

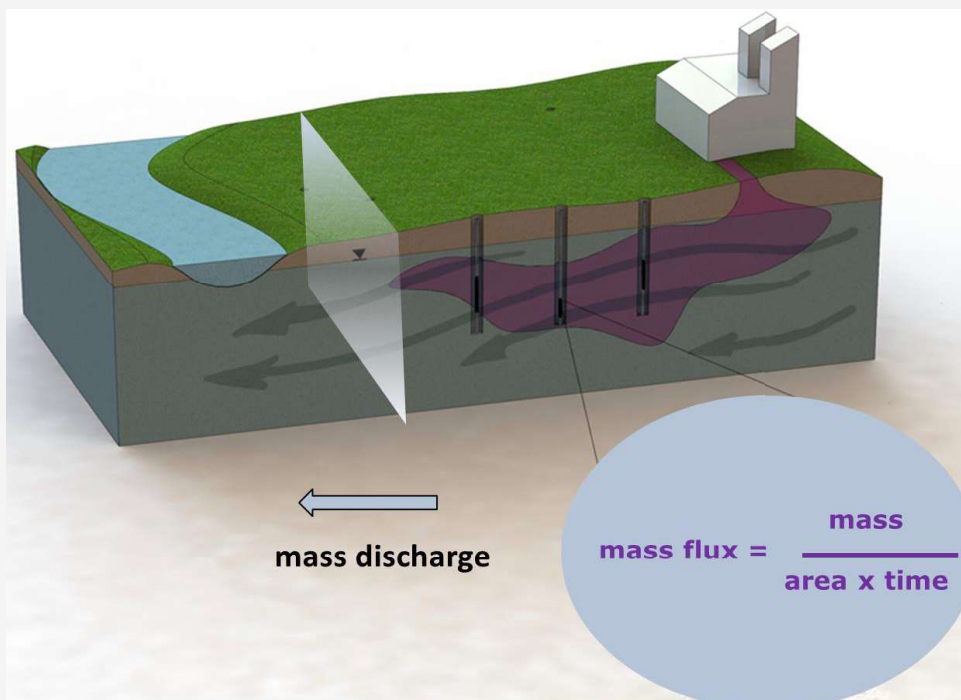
What presents the highest risk?



3



1. What is solute mass flux?



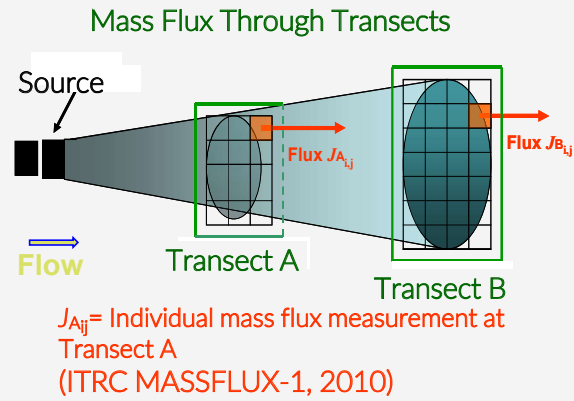
4



1. What is solute mass flux?

- **Solute mass flux (J)**

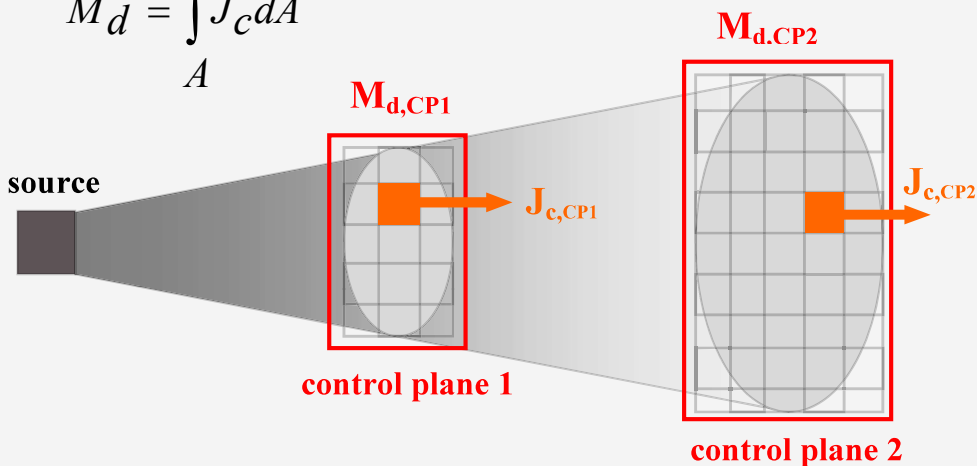
- The speed at which a 'solute moves through a defined plane, a particle of the cross-section 'through the plume'
- The solute mass flux is a vectorial quantity
- Mass per unit of area per unit of time [$M/L^2/T$]



1. What is solute mass flux?

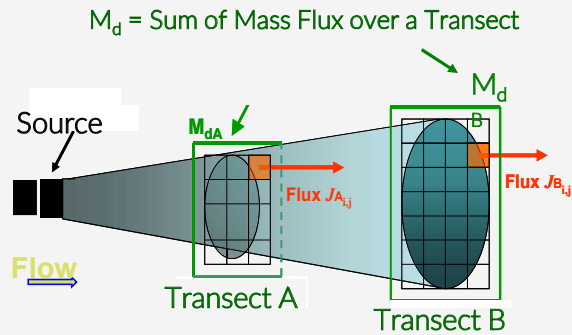
Solute mass flux J_c → solute mass discharge M_d

$$M_d = \int_A J_c dA$$



1. What is solute mass flux?

- **Solute mass discharge (M_d)**
 - The integration of all solute mass fluxes through a control plane in a plume
 - M_d is vectorial quantity
 - Mass per unit of time [M/T]
- Source or plume strength



J_{Aij} = Individual mass flux measurement at Transect A
(ITRC MASSFLUX-1, 2010)

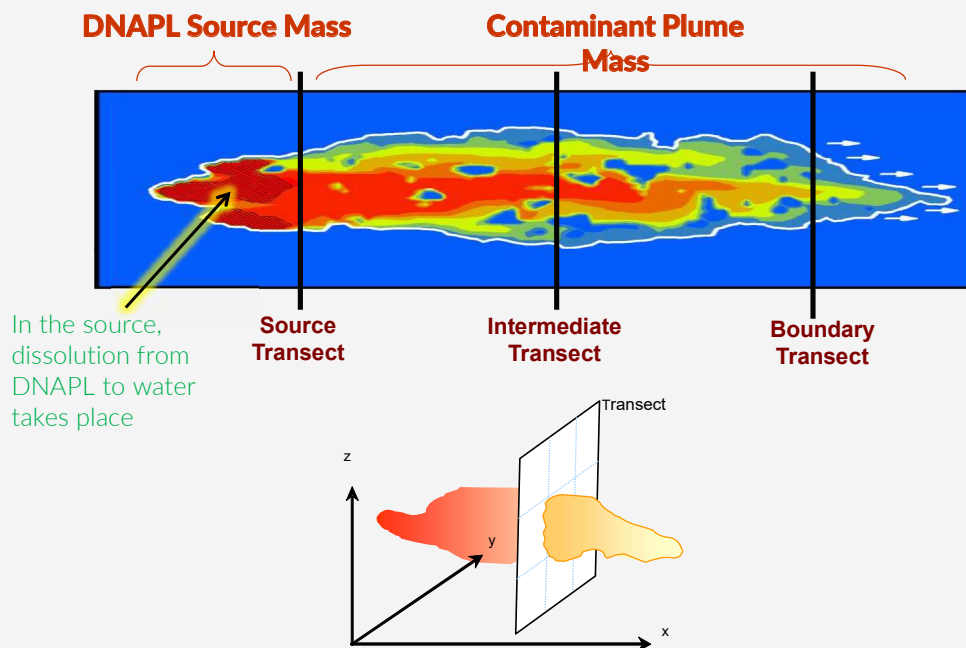
M_{dA} = Mass discharge at transect A

$$M_{dA} = \sum [J_{Aij} \times A]$$



1. What is solute mass flux?

FLUX based concept

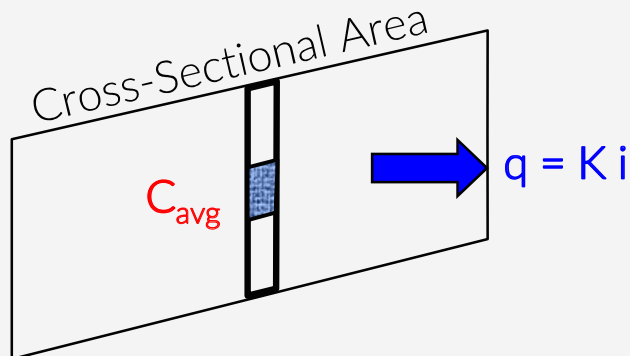


Solute mass fluxes versus solute concentrations

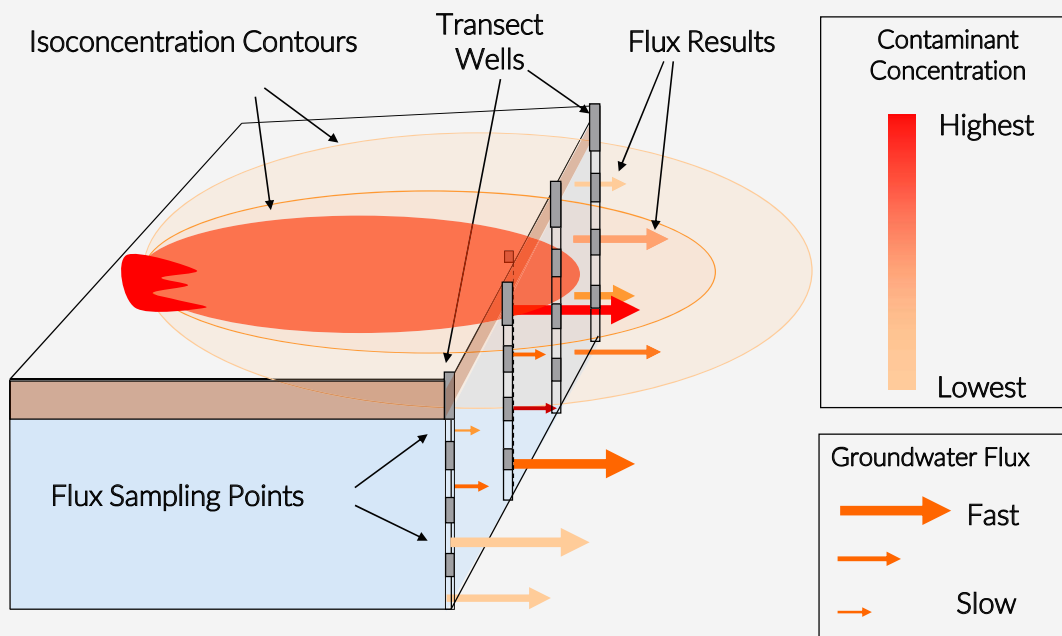
1. Water flux: $q = K \times i$ [L/T] or [L³/L²/T]

2. Average solute concentration: C_{avg} [M/L³]

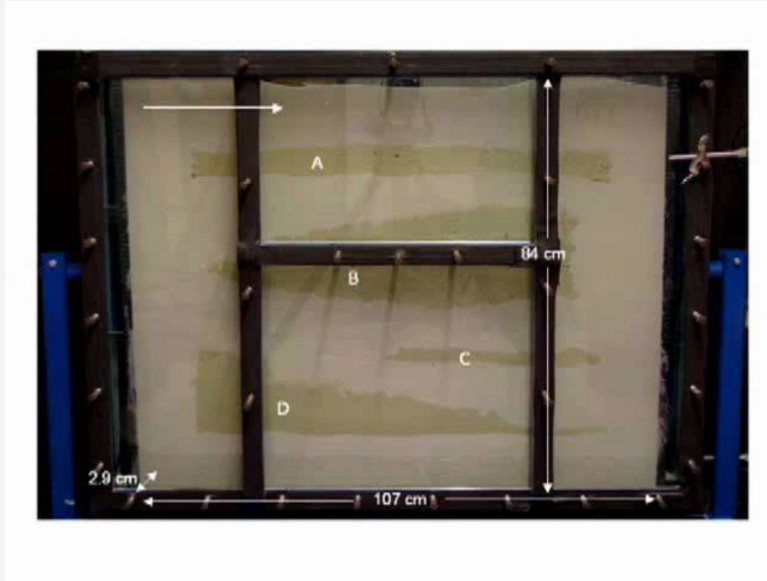
3. Solute mass flux: $J = q \times C_{avg}$ [M/L²/T]



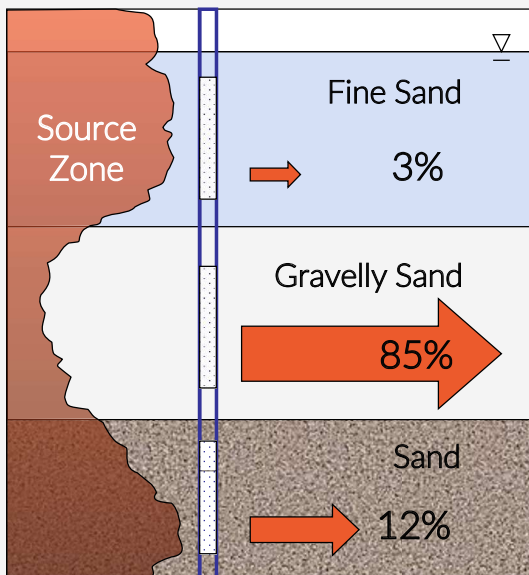
Solute mass fluxes can vary



Solute mass fluxes can vary



Mass fluxes and concentrations



$$\text{Mass Flux } (J) = qC = KiC$$

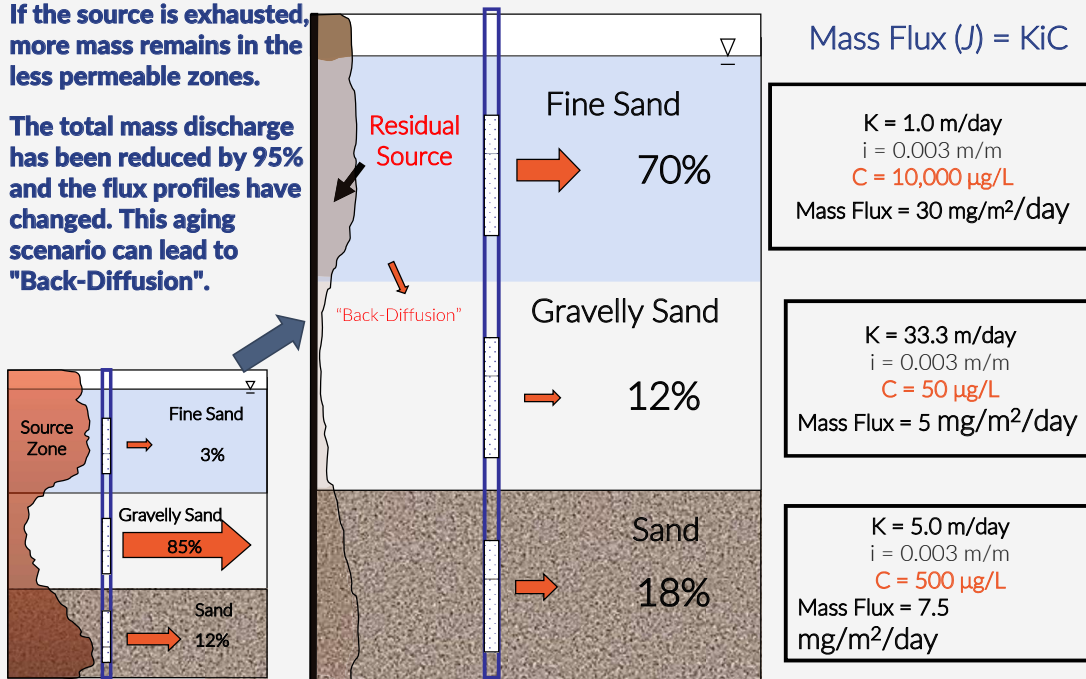
$K = 1.0 \text{ m/day}$
 $i = 0.003 \text{ m/m}$
 $C = 10,000 \text{ } \mu\text{g/L}$
 Mass Flux = $0.03 \text{ g/m}^2/\text{day}$

$K = 33.3 \text{ m/day}$
 $i = 0.003 \text{ m/m}$
 $C = 10,000 \text{ } \mu\text{g/L}$
 Mass Flux = $1 \text{ g/m}^2/\text{day}$

$K = 5.0 \text{ m/day}$
 $i = 0.003 \text{ m/m}$
 $C = 10,000 \text{ } \mu\text{g/L}$
 Mass Flux = $0.15 \text{ g/m}^2/\text{day}$

Mass fluxes and concentrations AT AGED contamination

- If the source is exhausted, more mass remains in the less permeable zones.
- The total mass discharge has been reduced by 95% and the flux profiles have changed. This aging scenario can lead to "Back-Diffusion".



13



Overview of presentation

1. What is solute mass flux?
2. Why determine mass flux?
3. How to determine solute mass flux?
4. Passive sampling
5. Passive flux sampling
6. iFLUX sampler
7. Some case studies
8. How about regulation? CMF approach
9. Take home points

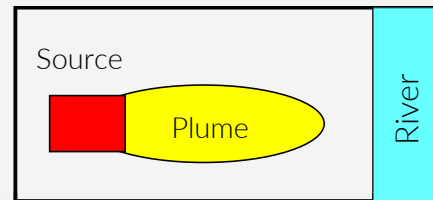
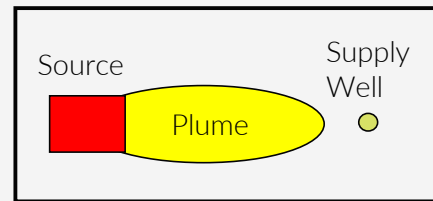
14



Why determining solute mass flux?

Better insight leads to smarter solutions!

- Addition to concentrations, no replacement
 - Does the contamination move?
 - Extra 'line of evidence'
- Optimizing remediation strategies
 - Most flux passes through a small fraction of the aquifer!
 - More targeted remediation, better focus
- Meaningful performance figures
- Effect of (partial) (source) remediation
- Calibration of existing groundwater models
- Risk-based management



Downstream risk depends on mass discharge and not on concentration!



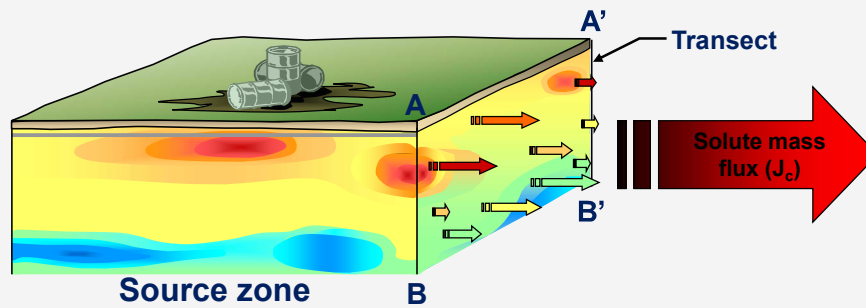
Overview of presentation

1. What is solute mass flux?
2. Why determine mass flux?
3. **How to determine solute mass flux?**
4. Passive flux measurement
5. Passive sampling
6. Passive flux sampling
7. iFLUX sampler
8. Some case studies
9. How about regulation? CMF approach
10. Take home points

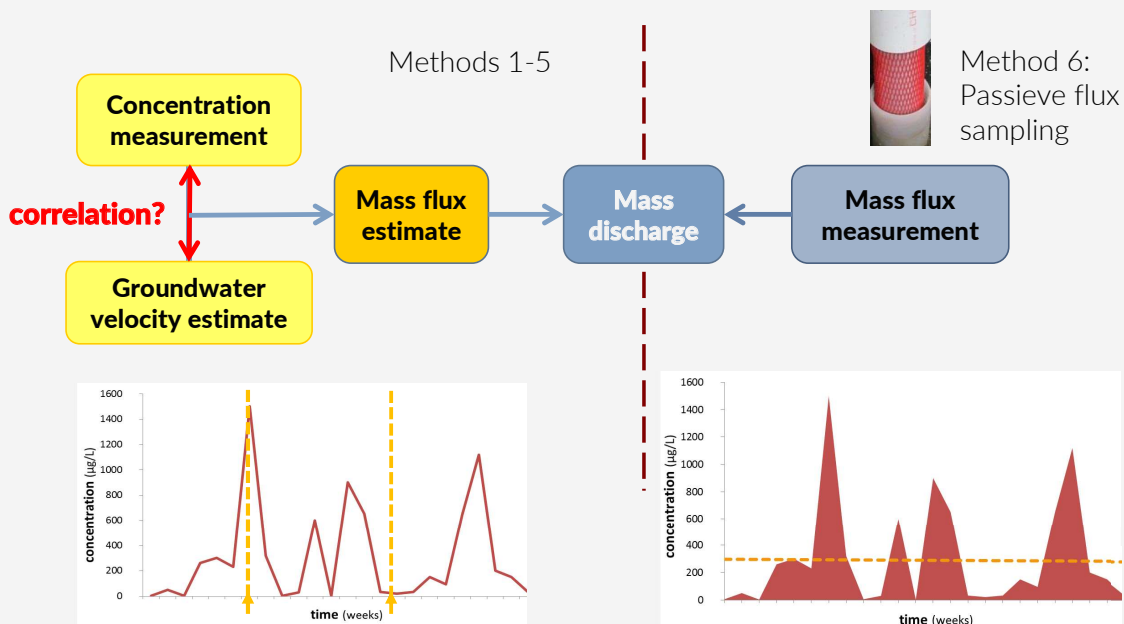


Determination of contaminant mass fluxes

- 6 methods
 - » Method 1: Transects
 - » Method 2: Existing historical data
 - » Method 3: Solute Transport Models
 - » Method 4: Well Capture/Pump Tests
 - » Method 5: Finite Volume Point Dilution Method
 - » Method 6: Passive flux sampling



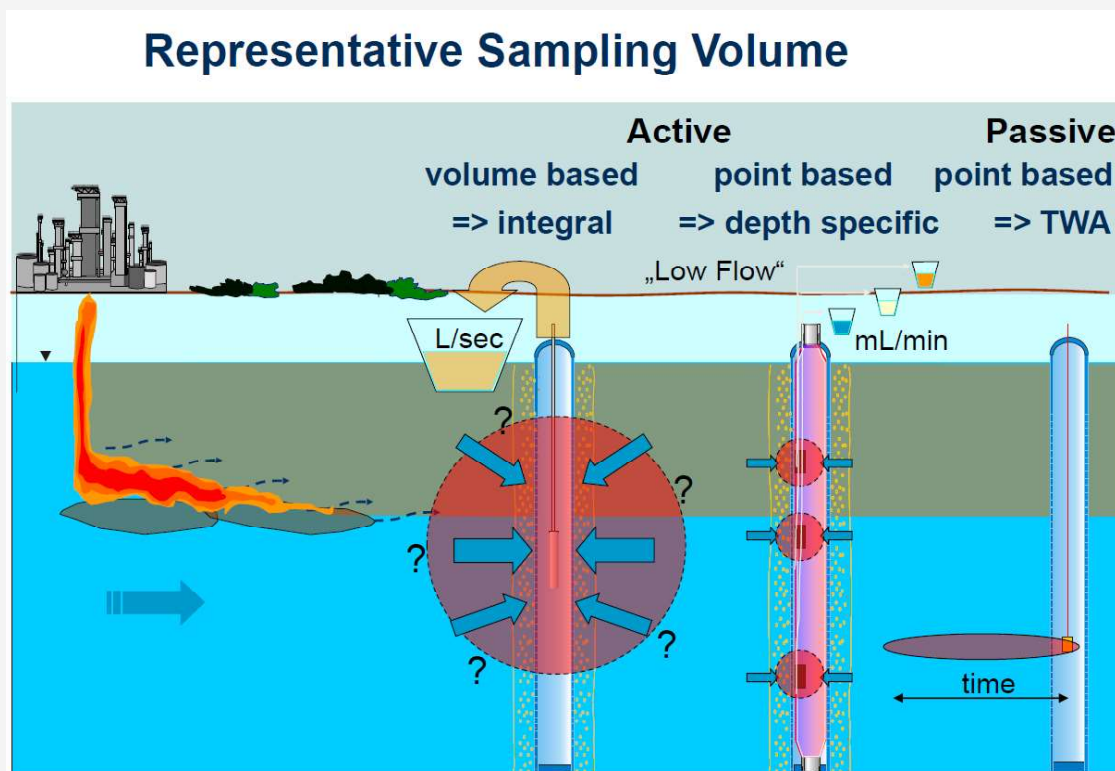
Determination of mass flux and mass discharge



Overview of presentation

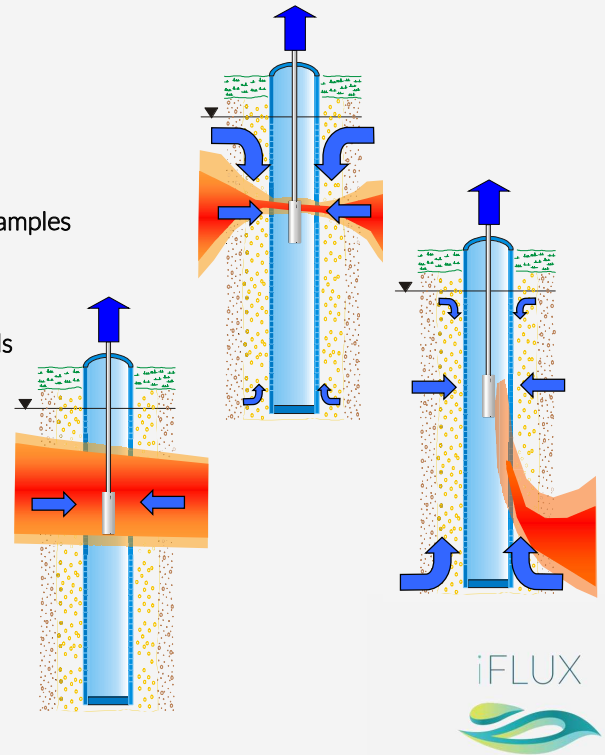
1. What is solute mass flux?
2. Why determine mass flux?
3. How to determine solute mass flux?
4. **Passive sampling**
5. Passive flux sampling
6. iFLUX sampler
7. Some case studies
8. How about regulation? CMF approach
9. Take home points

4. Passive sampling



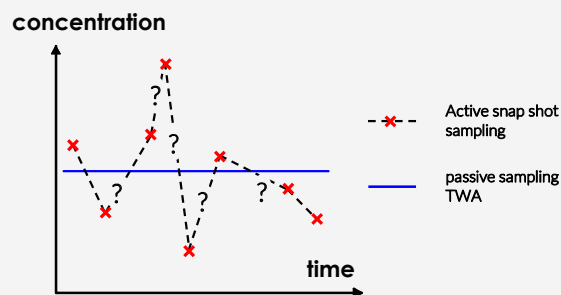
Advantages compared to conventional active monitoring

- No power supply or heavy and bulky equipment necessary
- No limitations through depth
- No disposal of contaminated water
- Small effort for sampling, transport, cooling and storing of the samples
- No filtration necessary
- No losses through sorption to pump tubing and sampling vessels
- No or little losses of high volatile compounds during sampling process
- No danger of cross contamination
- No influence regarding the hydraulic flow situation of groundwater



Advantages of time integrative sampling

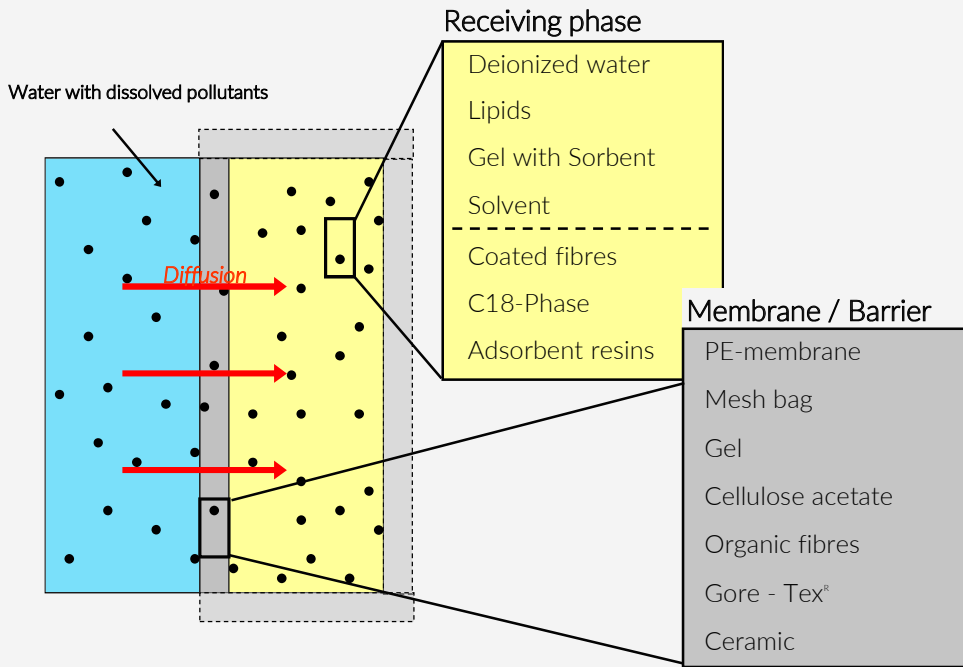
- Detectability through accumulation
- Time-weighted average (TWA) of concentration fluctuations



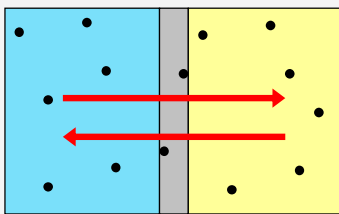
Disadvantages (sampler specific)

- Sampling rate influenced by flow velocity or turbulence and temperature
- Influence of biofouling and/or biofilms
- Low sampling rates result in low sensitivity or long sampling times

Design



Classification (simplified)

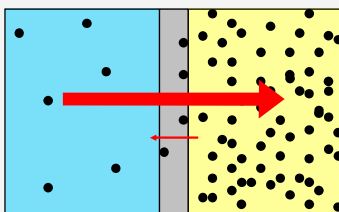


Water Receiving phase
Membrane / Barrier

Equilibrium passive samplers

Equilibrium conditions between surrounding water and receiving phase are reached

➡ Information on the concentration at the end of sampler exposure

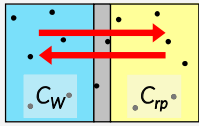


Non-equilibrium / Kinetic passive samplers

Non-equilibrium conditions achieved by high capacities of the receiving phase leading to an „infinite sink“ for substances in the surrounding water

➡ Information on the average aqueous concentration during sampler exposure (TWA)

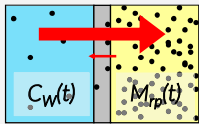
Classification (specified)



Equilibrium passive samplers

$$C_W = C_{rp} / K$$

Water Membrane / Barrier Receiving phase



Non-equilibrium / Kinetic passive samplers

Linear uptake $\rightarrow C_W(t) = M_{rp}(t) / R t$

Sampling rate $R = \frac{D_e \cdot A}{\Delta x}$ [mL / day]

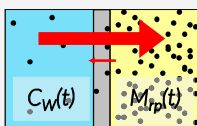
Volume of water cleared of analyte per unit of sampling time by the sampler

$C_W(t)$ = time-weighted average concentration in water
 $M_{rp}(t)$ = accumulated mass in receiving phase in t
 t = sampling time

D_e = effective diffusion coefficient
 A = surface area of the barrier
 Δx = thickness of the barrier



Classification (specified)



Non-equilibrium / Kinetic passive samplers

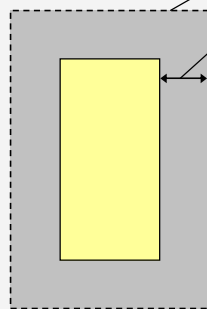
Sampling rate

$$R = \frac{D_e \cdot A}{\Delta x}$$

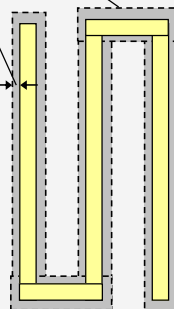
A = surface area of the barrier
 Δx = thickness of the barrier

$\frac{A}{\Delta x} = \text{low}, R = \text{low}$

„Diffusion samplers“



Low sampling rates: few mL / day



$\frac{A}{\Delta x} = \text{high}, R = \text{high}$

„Permeation samplers“

High sampling rates: few 100- 1000 mL / day

Influence of water flow velocity and turbulence, biofouling??, temperature??








low

high

PRCs



Selection of passive samplers

Sampler		Substances	Type	Sampling time
Passiv-Diffusions-Bag (PDB)		High volatile organic compounds VOCs: BTEX, CHCs	equilibrium	min. 2 weeks
Dialysis- Membrane-Sampler (DMS)		Anions, cations, trace metals, explosives, VOCs	equilibrium	1 - 14 days
Ceramic-Dosimeter & Toximeter		PAHs, BTEX, CHCs & toxicity level	TWA	weeks - months
Semi-Permeable-Membran-Device (SPMD)		Hydrophobic, semi-volatile organic compounds	TWA	about 1 month
MESCO (Membrane Enclosed Sorptive Coating)		Hydrophobic organic compounds: PAHs, PCBs, Organochloro pesticides	TWA	2 weeks
Chemcatcher		Polar and non-polar organics	TWA	2 - 4 weeks
POCIS (Polar Organic Chemical Integrative Sampler)		Herbicides and pharmaceuticals	TWA	2 days - 2 months

27



- a) Passive Flux Meter
- b) Ceramic Dosimeter
- c) Sorbi sampler
- d) MESCO sampler
- e) Gaiasafe passive sampler



28



Overview of presentation

1. What is solute mass flux?
2. Why determine mass flux?
3. How to determine solute mass flux?
4. Passive sampling
- 5. Passive flux sampling**
6. iFLUX sampler
7. Some case studies
8. How about regulation? CMF approach
9. Take home points

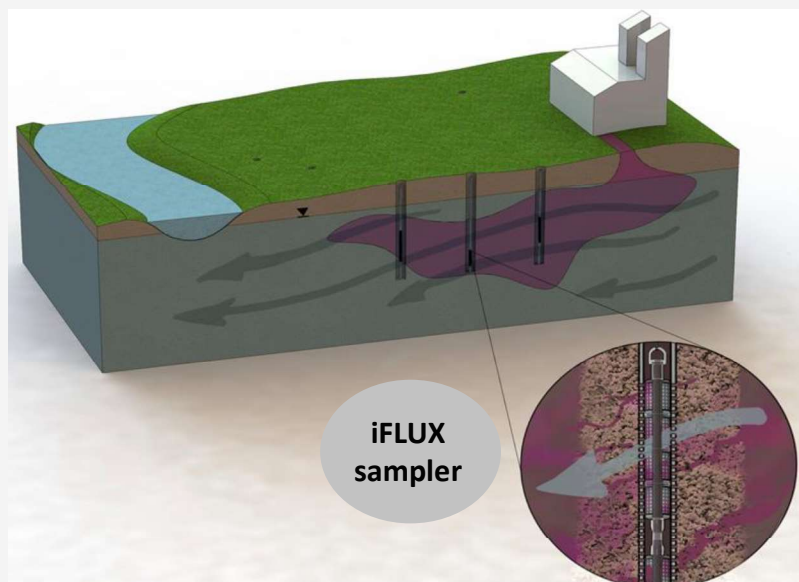


29

5. Passive flux sampling

Bepalen van pollutentfluxen en vuilvrachten

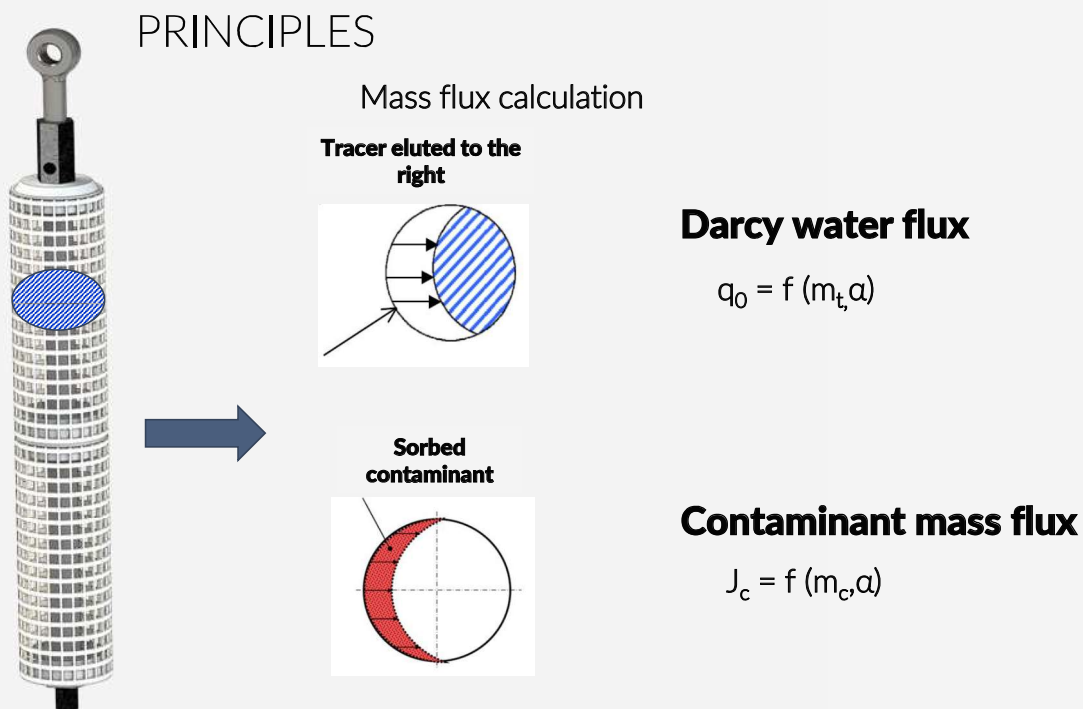
- Method 6: Passive flux sampling



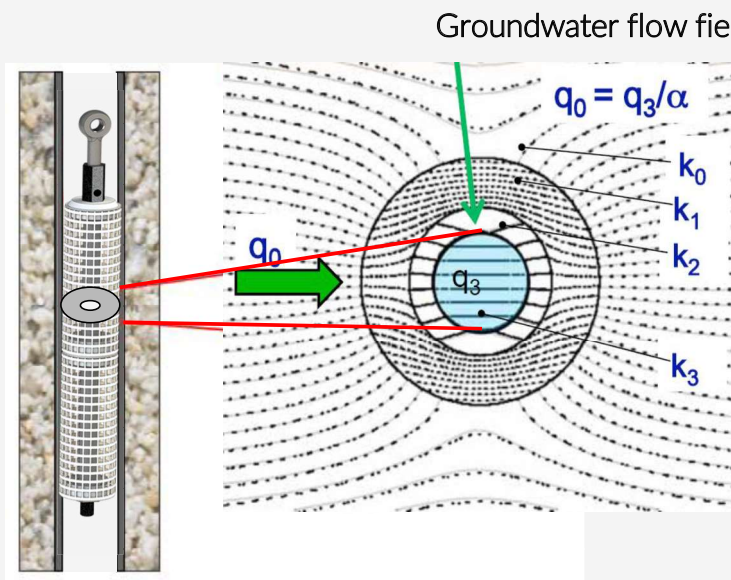
30

Determination of solute mass flux

- Method 6: Passive flux sampling
 - Advantages
 - simultaneous evaluation of both water and contaminant fluxes under natural gradient conditions
 - cumulative measurement → less sensitive to daily fluctuations in groundwater flow or contaminant concentrations
 - only two site visits required
 - measurement of vertical variations in horizontal fluxes
 - no electrical power or pumping required
 - measured mass flux profiles indirectly reflect the distribution of a soil contamination and directly reflect the mobility of the contaminants present
 - Points of attention
 - Depends on groundwater flow distortion through the monitoring well



PRINCIPLES



$$\alpha = \frac{q}{q_0}$$

$$\alpha = f(k_0, k_F, k_S, k_P, r_1, r_2, r_3)$$



PRINCIPLES

contaminant mass flux → contaminant mass discharge

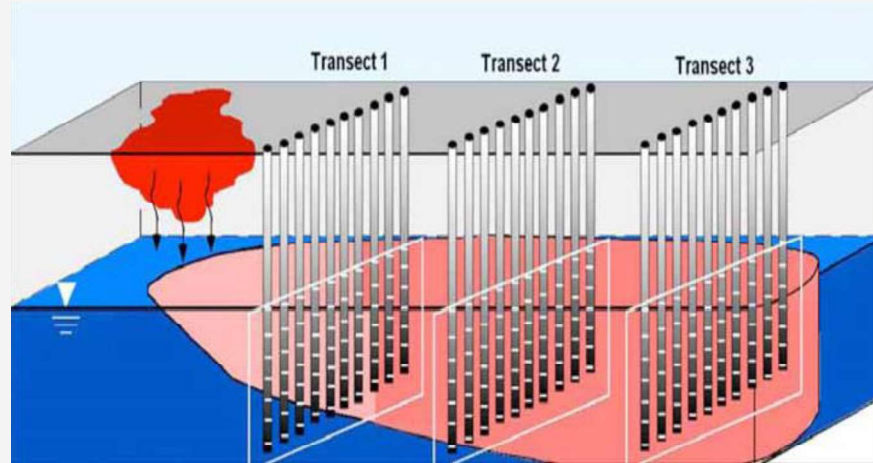
Interpolation

- *Methods*
 1. Nearest neighbour
 2. Thiessen Polygon
 3. Kriging
- *Tools*
Mass flux toolkit, Surfer, Groundwater Modeling Software (GMS)
- *Uncertainty analysis* ~ confidence intervals



PRINCIPLES

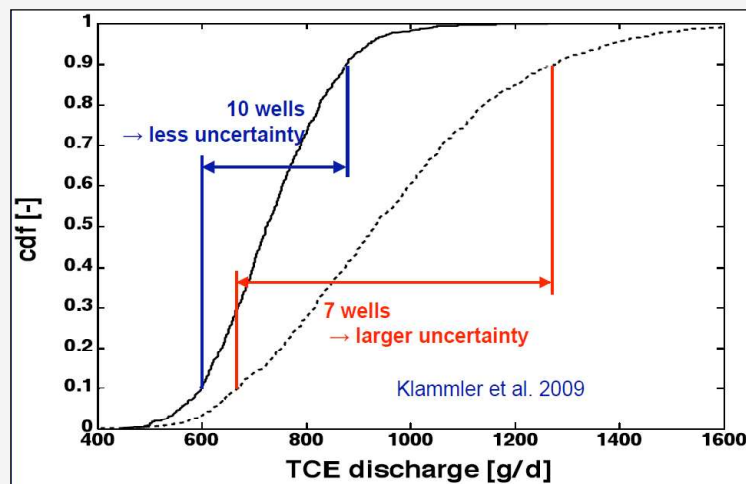
How many passive flux samplers per control plane?



(Kübert en Finkel, 2006)

PRINCIPLES

Probability distribution of the solute mass discharge



Overview of presentation

1. What is solute mass flux?
2. Why determine mass flux?
3. How to determine solute mass flux?
4. Passive sampling
5. Passive flux sampling
- 6. iFLUX sampler**
7. Some case studies
8. How about regulation? CMF approach
9. Take home points

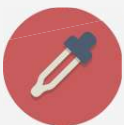


37

6. iFLUX sampler

iFLUX technology

- Based on fundamental and applied research and product development.



Patented and
validated



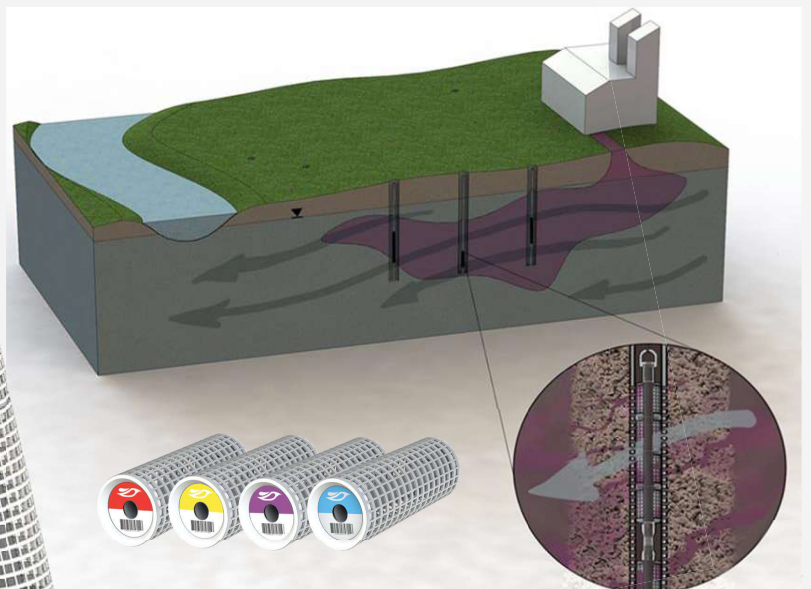
Captures 90% of
all pollution
types



Accurate
measurement of
speed and
direction



Potential cost
reduction up to
30%



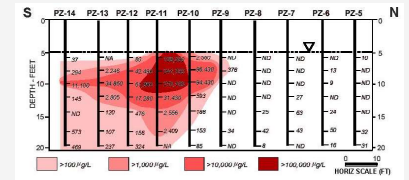
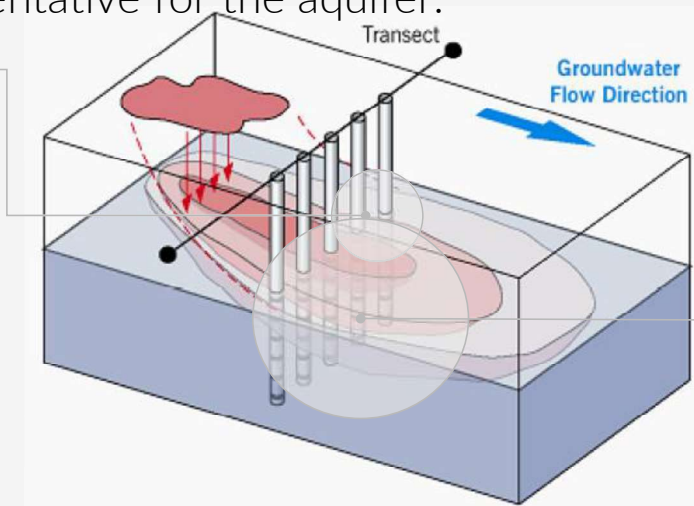
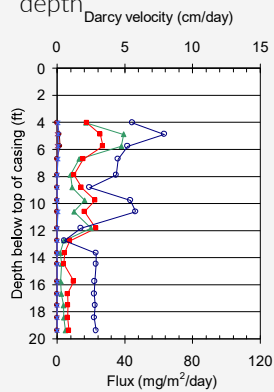
38

iFLUX technology

- End report includes interpreted flux results representative for the aquifer.

Well info

Every data point represents accurate flux results versus depth



Control plane info

Interpolation and integration of flux point results delivers mass flux discharge



iFLUX Project

iFLUX offers an integrated solution in close cooperation with the Environmental Consultant to guarantee accurate flux results. A typical project includes 4 milestones.



1 – Field design

Based on preliminary site investigation and customer input, a detailed monitoring campaign is developed.



2 – Sampler installation on site

An authorized field team will guarantee a precise installation of the selected iFLUX samplers on site.



3 – Retrieval and lab analysis

After retrieval, dedicated transport from site to our partner laboratory is taken care of. A certified lab analysis will provide us the raw flux data measured.



4 – Data analysis and reporting

Validated flow field distortion calculations deliver detailed and reliable flux data in the aquifer. Our end report contains comprehensible graphs and maps of the designated field.



Overview of presentation

1. What is solute mass flux?
2. Why determine mass flux?
3. How to determine solute mass flux?
4. Passive sampling
5. Passive flux sampling
6. iFLUX sampler
7. **Some case studies**
8. How about regulation? CMF approach
9. Take home points



41

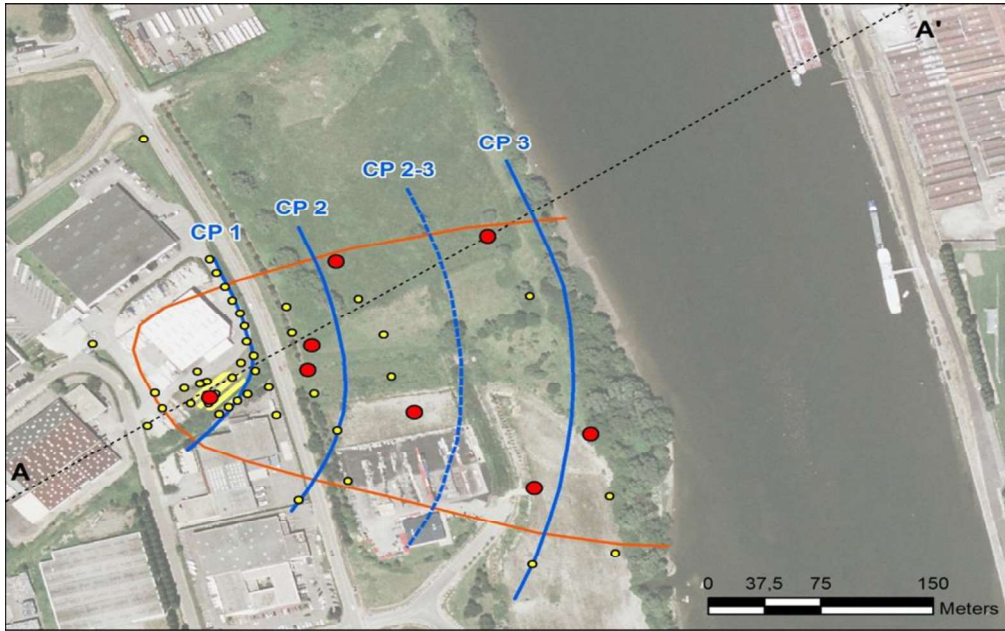
7. Some case studies

Case studies



7. Some case studies

Case 1: Spreading of a CAH plume to the Seine



Legend

- Monitoring well equipped with PFMs
- Monitoring well
- Plume zone: chlorinated solvents
- Cross section
- Control planes
- ▨ Source area: chlorinated solvents

Company : Burgeap
Project : Evaluation and spreading of a CAH plume

- ✓ CAHs
- ✓ Spreading risk
- ✓ Mass discharge calculation
- ✓ 50 samplers, 6 cartr./sampler
- ✓ Near tidal river



- Field site near Seine river, France
- Chemical storage/distribution – out of activity
- Chlorinated solvent source zone near company shed
- PCE; TCE; 1,1,1-TCA; 1,1,2-TCA; 1,1-DCE; VC in groundwater
- Source zone: size roughly 20 x 30 m with a depth of a least first 25 meters in the sandy aquifer down to the substratum which might be between 40 to 60 m deep
- Plume zone at least 20 m deep and 100 m long - deliniation ongoing
- Total of 64 monitoring wells; 26 long filterscreen wells, placed in 2009
- Site complexity:
 - Site geology – erratic distribution pattern – vertical distribution?
 - Plume shifting
 - Tidal effects in monitoring wells

Company : Burgeap
Project : Evaluation and spreading of a CAH plume

7. Some case studies

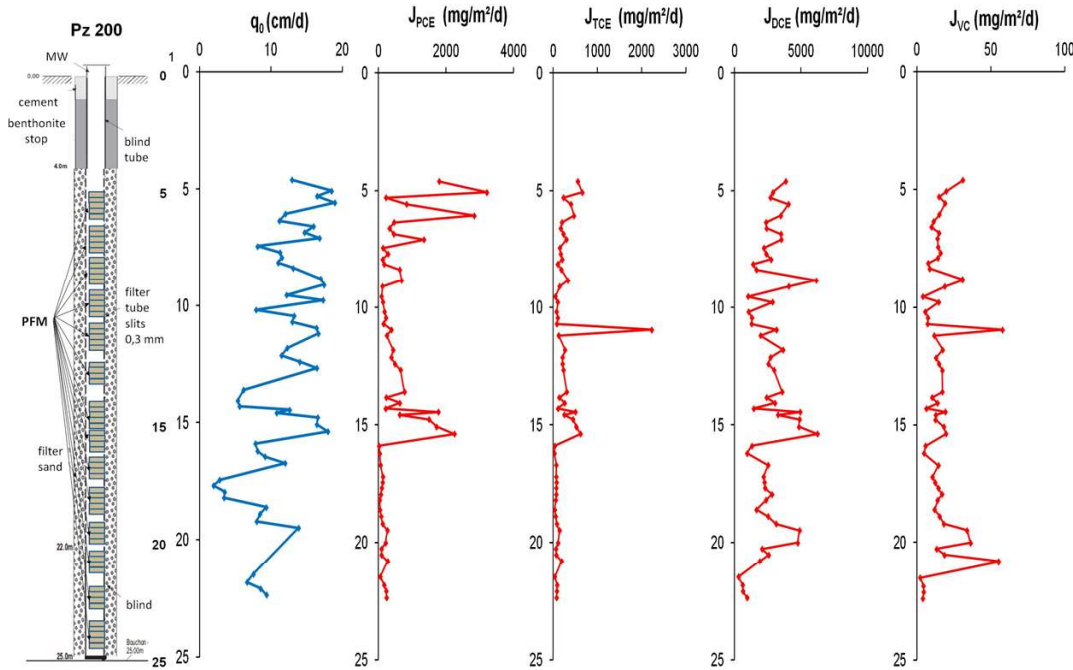
Case 1: Spreading of a CAH plume to the Seine

- ✓ CAHs
- ✓ Spreading risk
- ✓ Mass discharge calculation
- ✓ 50 samplers, 6 cartr./sampler
- ✓ Near tidal river



7. Some case studies

Case 1: Spreading of a CAH plume to the Seine



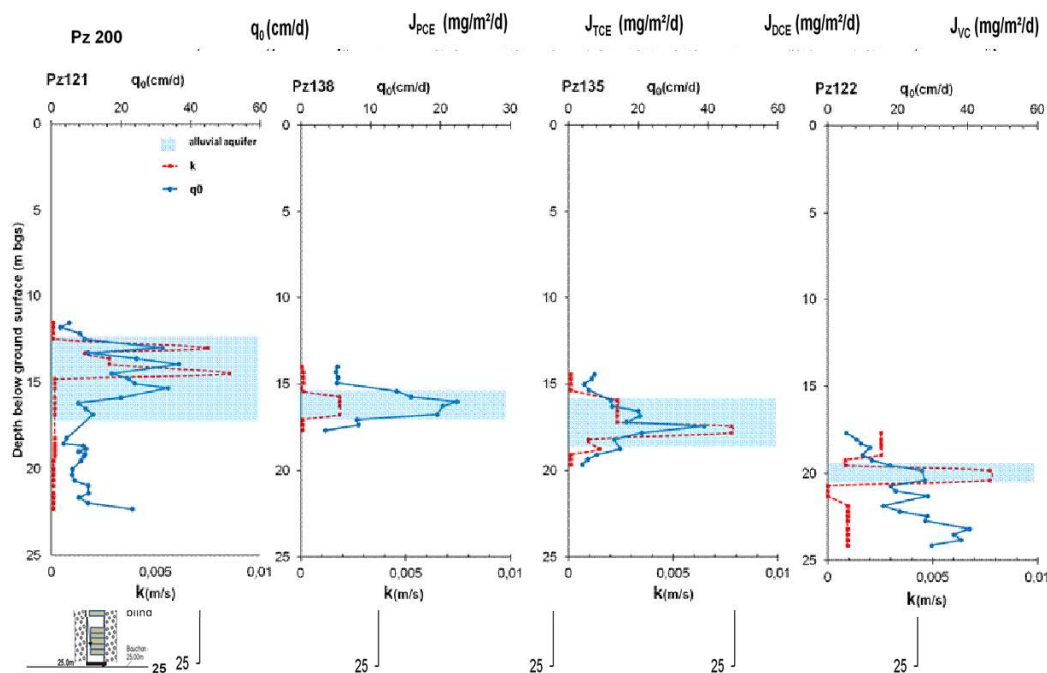
Company : Burgeap
Project : Evaluation and spreading of a CAH plume



- ✓ CAHs
- ✓ Spreading risk
- ✓ Mass discharge calculation
- ✓ 50 samplers, 6 cartr./sampler
- ✓ Near tidal river

7. Some case studies

Case 1: Spreading of a CAH plume to the Seine

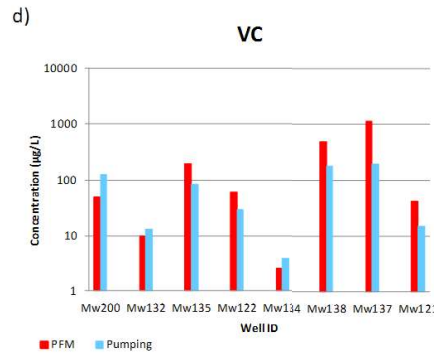
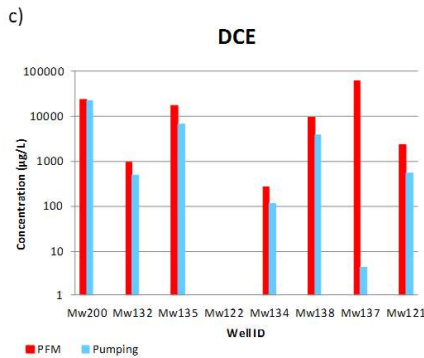
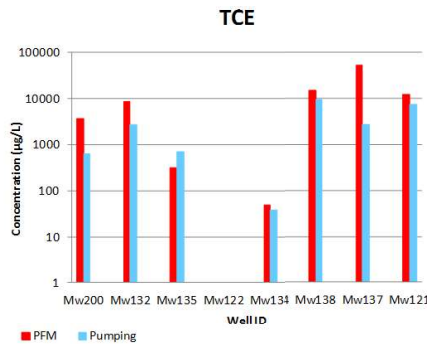
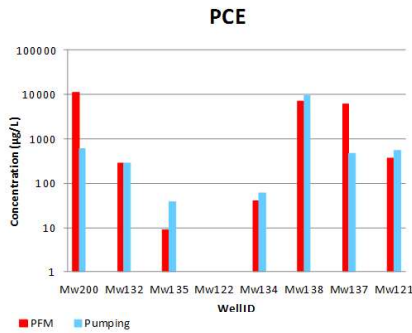


Company : Burgeap
Project : Evaluation and spreading of a CAH plume



- ✓ CAHs
- ✓ Spreading risk
- ✓ Mass discharge calculation
- ✓ 50 samplers, 6 cartr./sampler
- ✓ Near tidal river

Case 1: Spreading of a CAH plume to the Seine



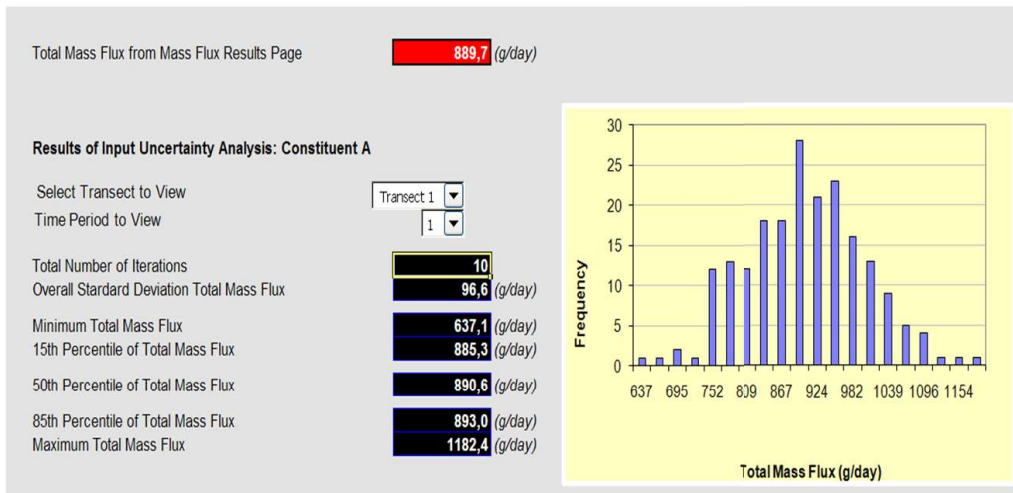
Company : Burgeap
Project : Evaluation and spreading of a CAH plume



- ✓ CAHs
- ✓ Spreading risk
- ✓ Mass discharge calculation
- ✓ 50 samplers, 6 cartr./sampler
- ✓ Near tidal river

Contaminant Mass Discharge (CMD) at CP2

- » Mass Flux Toolkit - Nearest Neighbour interpolation
- » Q_c, CP_1 (total VOC) = **890 g/day** or **325 kg/year**



Company : Burgeap
Project : Evaluation and spreading of a CAH plume



Case 1: Spreading of a CAH plume to the Seine

- ✓ CAHs
- ✓ Spreading risk
- ✓ Mass discharge calculation
- ✓ 50 samplers, 6 cartr./sampler
- ✓ Near tidal river

Context

Why passive flux samplers? Contaminant mass flux determination

- Better characterization of **source areas, transfer routes, plume edge conditions**
- Evaluation of **natural attenuation rates**
- Better choice and optimization of **remediation techniques**

Current bottlenecks

- **No direct flux measurement:** groundwater sampling + Darcy water velocity estimation

Objectives of the Passiflux project: code of best practice for passive flux sampling

- **Installation and retrieval**
- **Evaluation & interpretation of the results:** concentrations and contaminant mass fluxes
- **Multilevel sampling**

Collaboration with Chlorokarst project (2014-2017) and iFLUX/VITO/University of Antwerp

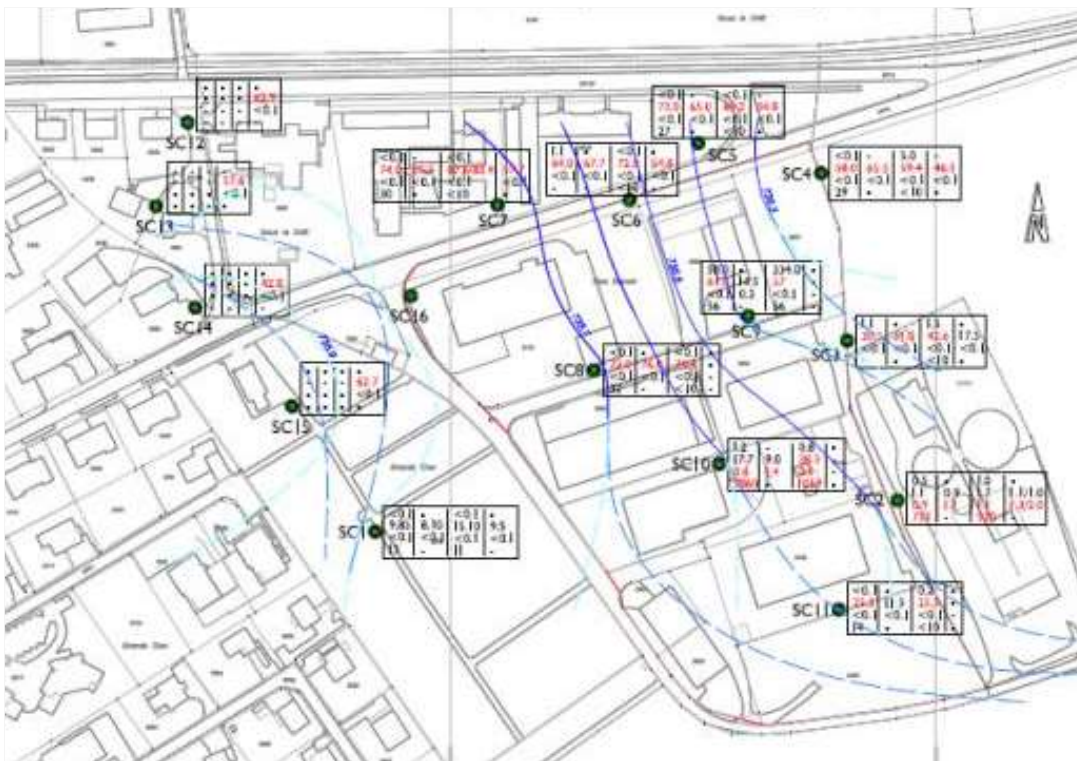
- CHYN (Centre d'Hydrogéologie et de Géothermie de Neuchâtel, P. Renard)
- 2 BE (eOde, H. Demougeot-Renard et MFR, A. Bapst)

Partner : Ineris
Project : PASSIFLUX

7. Some case studies

Case 2: Passiflux project

- ✓ Chlorinated solvents
- ✓ High groundwater flow (variability)
- ✓ Plume zone
- ✓ 40 flux samplers (2 cartr./sampler)
- ✓ 4 fases
- ✓ Code of best practices



Partner : Ineris
Project : PASSIFLUX

7. Some case studies

Case 2: Passiflux project

- ✓ Chlorinated solvents
- ✓ High groundwater flow (variability)
- ✓ Plume zone
- ✓ 40 flux samplers (2 cartr./sampler)
- ✓ 4 fases
- ✓ Code of best practices

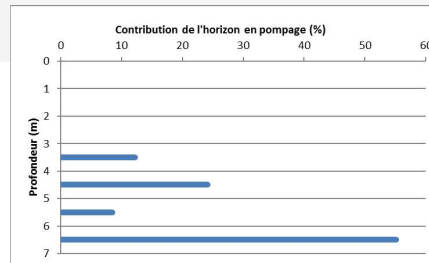
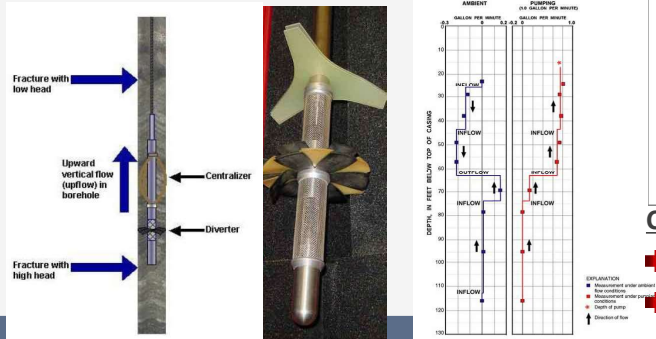


Flowmeter measurements

7. Some case studies

Vertical natural fluxes and contributions of the pumped horizons : heat pulse flowmeter

- ➔ Vertical natural fluxes
 - Homogenization of concentrations within the well filter during pumping: possibility of multi-level flux layering within different horizons?
- ➔ Contribution of the groundwater of the pumped horizons
 - Interpretation of the results/conventional sampling (average concentration within the screened interval)



Cost elements

- Flowmeter purchase: ≈ 25 k€
- Measurement : 3h/10m screened

Case 2: Passiflux project

- ✓ Chlorinated solvents
- ✓ High groundwater flow (variability)
- ✓ Plume zone
- ✓ 40 flux samplers (2 cartr./sampler)
- ✓ 4 fases
- ✓ Code of best practices

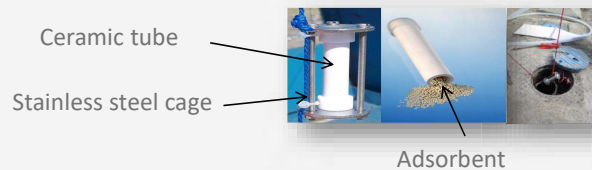


Partner Project : Ineris PASSIFLUX

Field exposure of the passive flux samplers

7. Some case studies

- ➔ 4 measurement campaigns: 2/3 months – summer/winter
 - Exposure of iFLUX samplers + Ceramic Dosimeters in one long sampling chain
 - Conventional groundwater sampling before and after exposure
 - Tests of detection limits of mass fluxes and concentrations in groundwater



- ➔ Interpretation of the results
 - Evaluation of concentrations : iFLUX samplers/Ceramic dosimeters/conventional sampling

Cost elements (Passiflux configuration)

- Conventional sampling: 1h – 1h30 / Pz
- Flux sampling + analyses : ≈ 800 – 1 000 €
- Installation /retrieval: 15 - 30 min / Pz



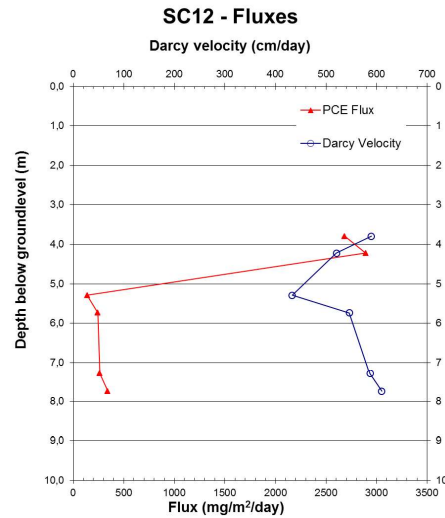
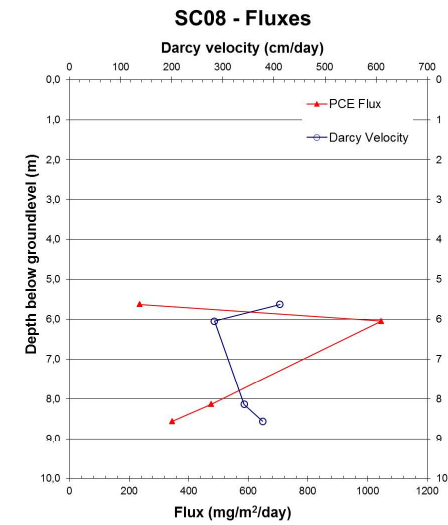
Case 2: Passiflux project

- ✓ Chlorinated solvents
- ✓ High groundwater flow (variability)
- ✓ Plume zone
- ✓ 40 flux samplers (2 cartr./sampler)
- ✓ 4 fases
- ✓ Code of best practices



Case 2: Passiflux project

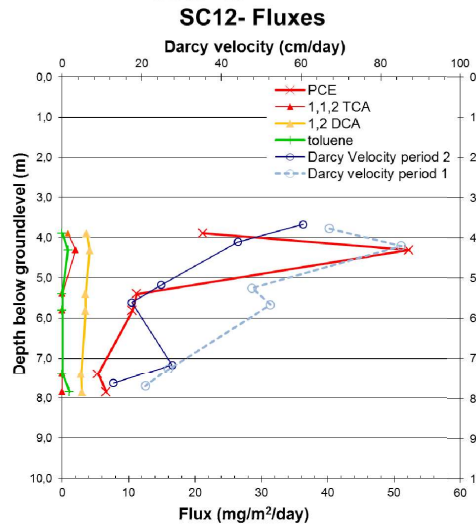
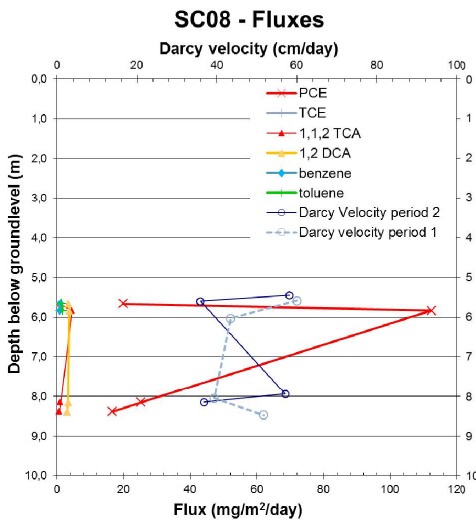
- ✓ Chlorinated solvents
- ✓ High groundwater flow (variability)
- ✓ Plume zone
- ✓ 40 flux samplers (2 cartr./sampler)
- ✓ 4 fases
- ✓ Code of best practices



Partner : Ineris
Project : PASSIFLUX

Case 2: Passiflux project

- ✓ Chlorinated solvents
- ✓ High groundwater flow (variability)
- ✓ Plume zone
- ✓ 40 flux samplers (2 cartr./sampler)
- ✓ 4 fases
- ✓ Code of best practices

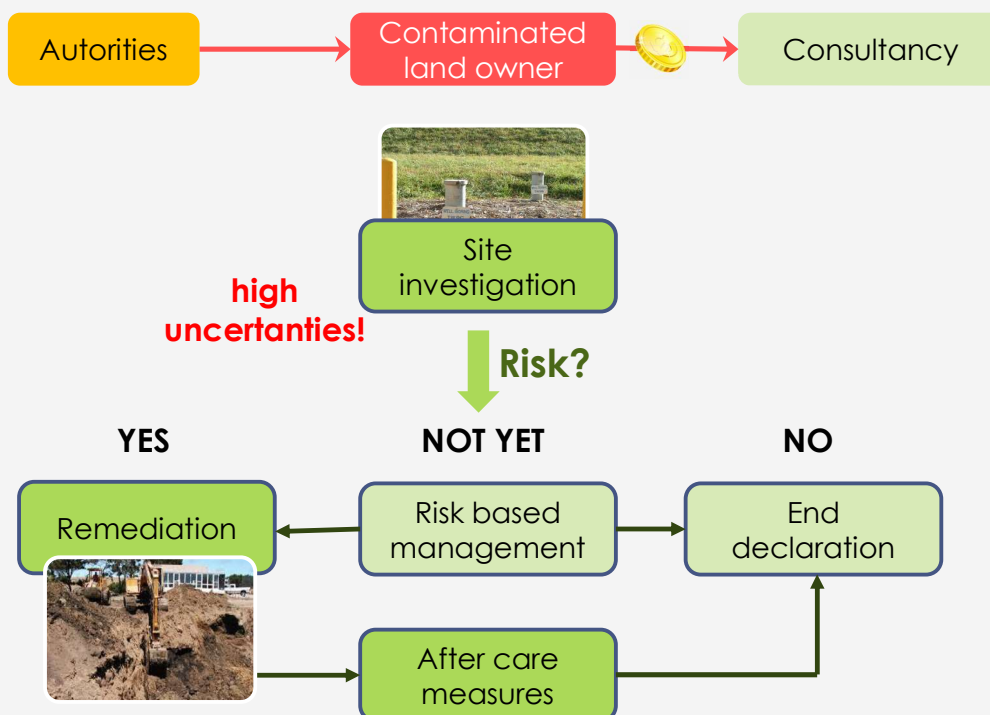


Partner : Ineris
Project : PASSIFLUX

Overview of presentation

1. What is solute mass flux?
2. Why determine mass flux?
3. How to determine solute mass flux?
4. Passive sampling
5. Passive flux sampling
6. iFLUX sampler
7. Some case studies
8. How about regulation? CMF approach
9. Take home points

8. How about regulation? CMF approach



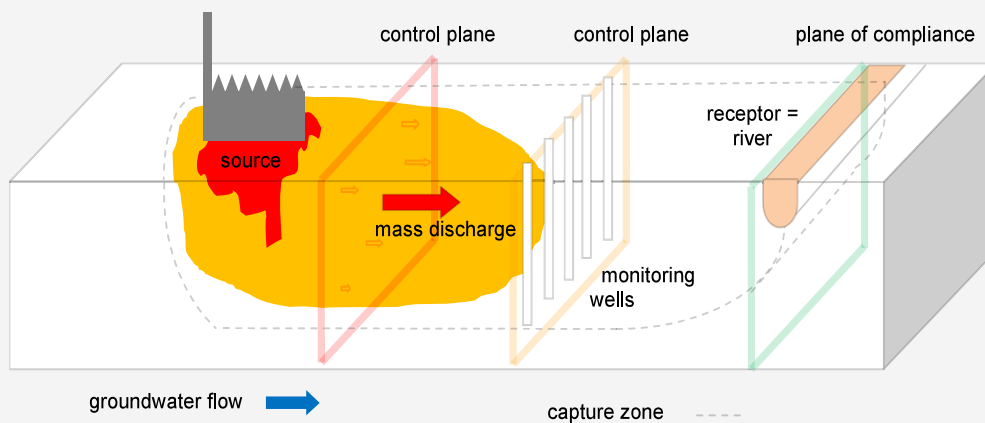
How about regulation?

- Passive flux measurements are new, there is no regulation or manual for it. Inclusion in a code of good practice is indicated.
- How do solute mass fluxes and mass discharges link to risk and exposure?
- How do solute mass fluxes correlate with standard criteria such as concentration levels?
- → **CMF approach** can be a first step towards the use of solute mass fluxes and discharges in risk management

57



CMF approach



→ **CMD_{max} = maximum contaminant mass discharge**

58



CMF approach

$$CMD_{max,0,static} = \text{risk level} \cdot Q_0 \quad \longleftrightarrow \quad CMD_{max,0,dynamic} \sim \text{risk level}, Q, DF$$

$CMD_{max,0}$ = maximum allowed contaminant mass discharge at plane of compliance [mg/m².d]

Risk level = concentration threshold value, defined by legislation or risk assessment [mg/m³]

Q_0 = daily flux that reaches the receptor [m³/d]

DF = dilution factor for the impact of the groundwater pollution on the surface water [-]

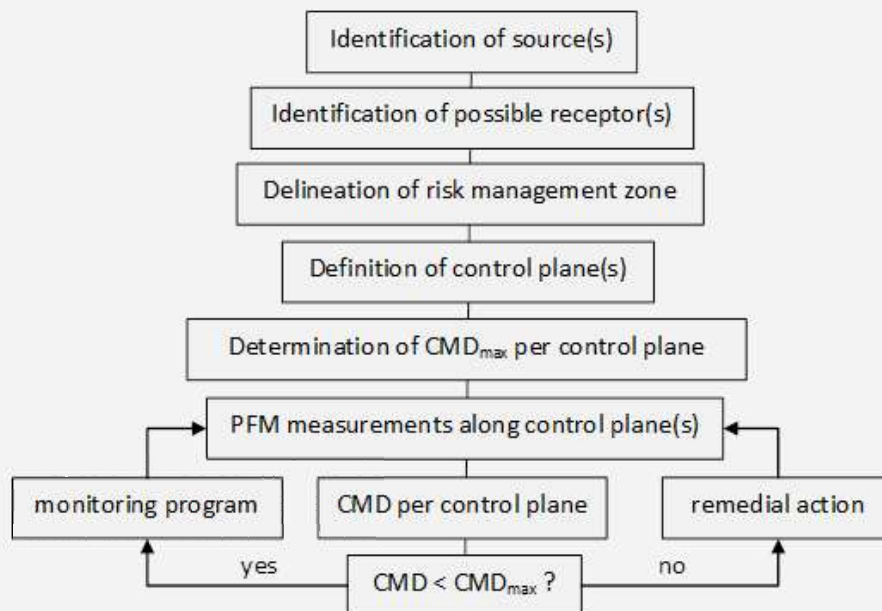
$$CMD_{max,x} = CMD_{max,0} \cdot f_d$$

$CMD_{max,x}$ = maximum allowed contaminant mass discharge at control plane x [mg/m².d]

f_d = distance factor, ratio between the $CMD_{max,0}$ at the plane of compliance and corresponding modeled mass discharge at the considered control plane at the same time $CMD_{max,0}$ is exceeded [-]



CMF approach

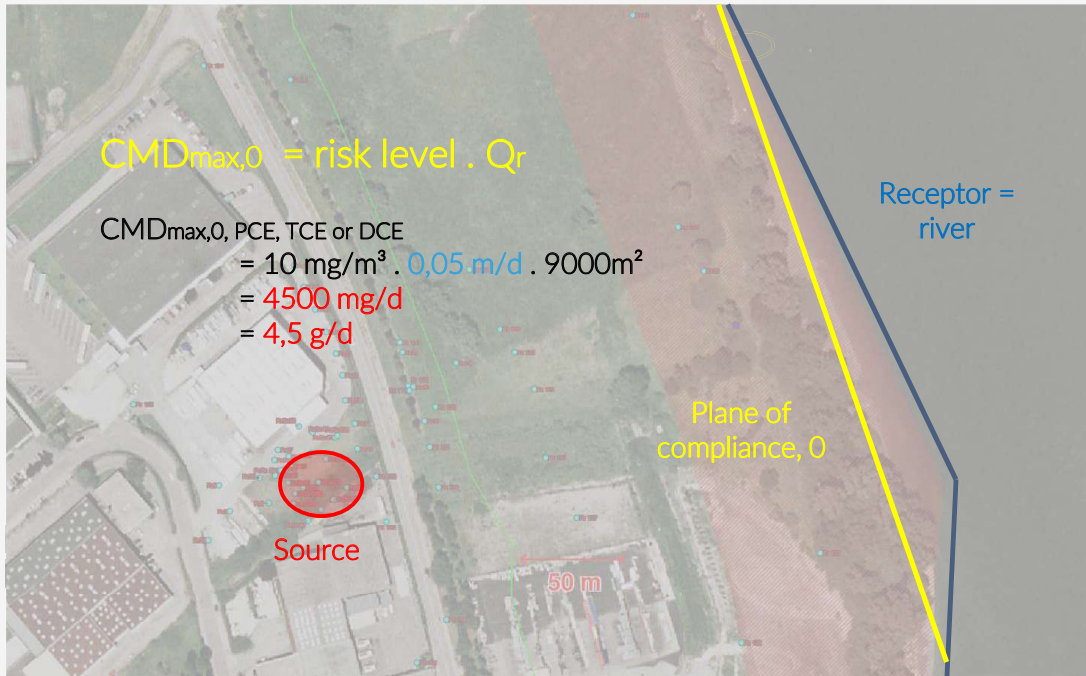


CMF approach

- objective flux-based risk management approach for contaminated land
- clear strategy
- based on the source-pathway-receptor approach
- includes the direct measurement of contaminant mass fluxes along a control plane with the iFLUX technology
- states the derivation of the maximum allowed contaminant mass discharge (CMDmax) per control plane
- cost-effective and efficient
- should lead to more integrated and more controlled handling and management of soil and groundwater contamination in the near future

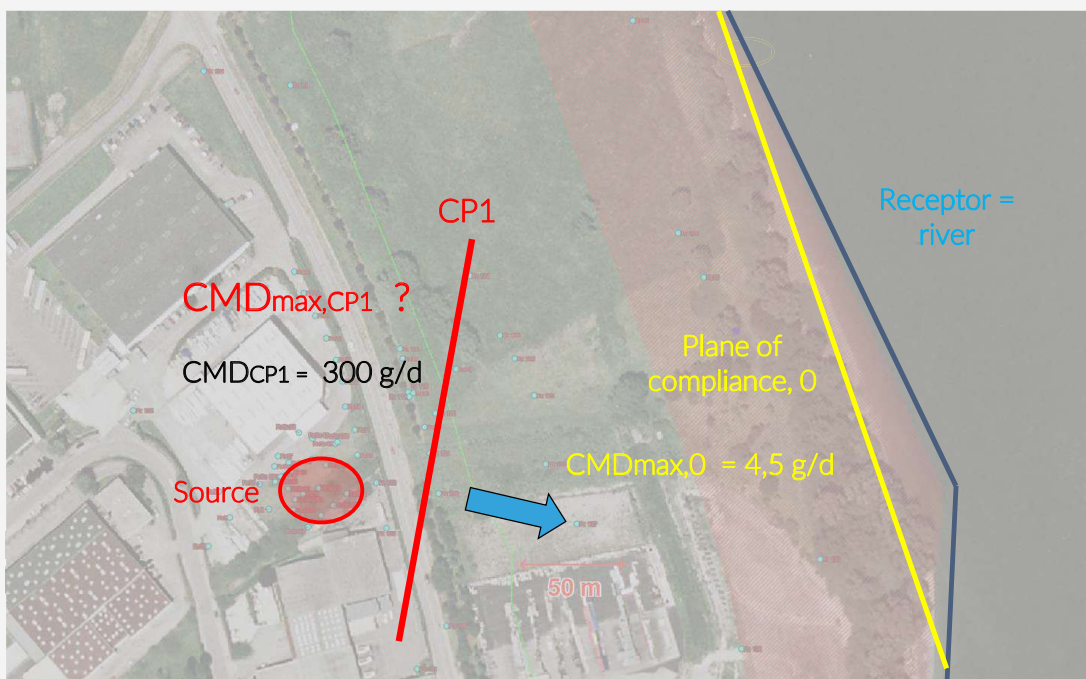


8. How about regulation? CMF approach



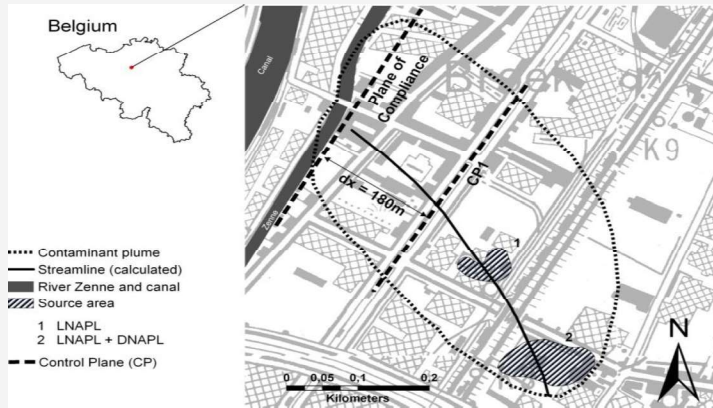
63

8. How about regulation? CMF approach



64

Goedele Verreydt



Pollutant	Risk level ($\mu\text{g L}^{-1}$)	f_d [-]	$\text{CMD}_{\text{max},0}$ (g d^{-1})		$\text{CMD}_{\text{max},\text{CP}1}$ (g d^{-1})		$\text{CMD}_{\text{CP}1}$ (g d^{-1})
			no DF	with DF	no DF	with DF	
perchloroethylene	10	20.6	8	4308	81	44425	5
trichloroethylene	10	20.6	8	4308	81	44425	10
cis + trans dichloroethylene	10	2.9	8	4308	11	6139	36
vinylchloride	10	1.5	8	4308	6	3231	21
benzene	10	20.6	8	4308	81	44425	5

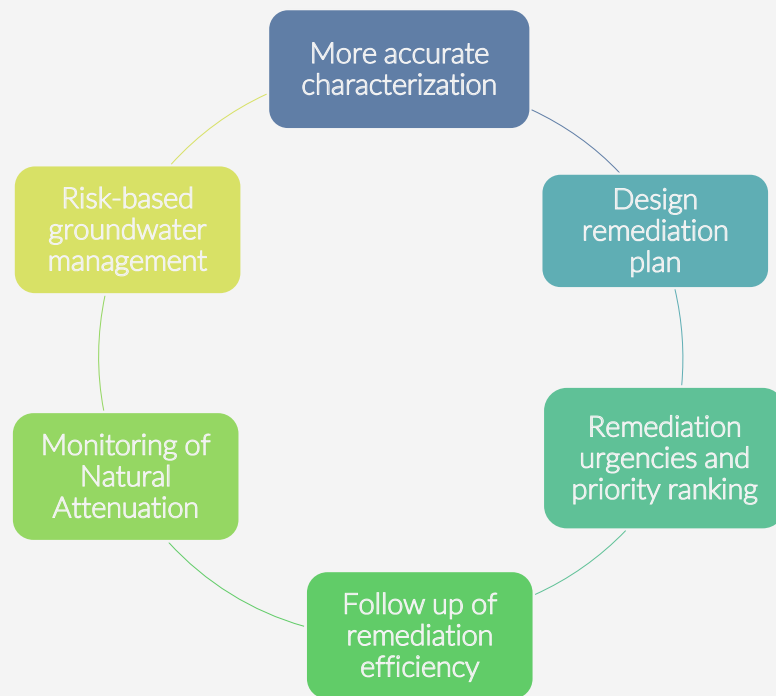


Overview of presentation

1. What is solute mass flux?
2. Why determine mass flux?
3. How to determine solute mass flux?
4. Passive sampling
5. Passive flux sampling
6. iFLUX sampler
7. Some case studies
8. How about regulation? CMF approach
9. **Take home points**

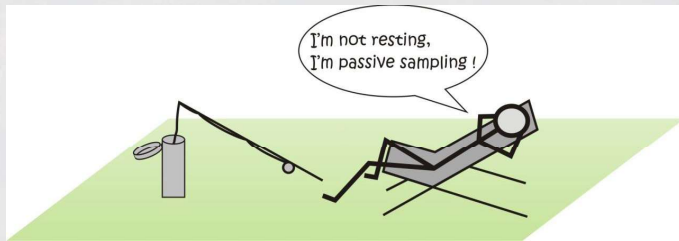


When to apply flux measurements?



Take home points


- Alternative research techniques such as passive samplers and passive flux samplers are a very valuable addition to the current measurements
- Flux measurements improve conceptual site models
- Better source characterization and increase of remediation efficiency
- Good standard in risk-based soil and groundwater management




Thank you! Questions?

 tim@ifluxsampling.com

 goedele@ifluxsampling.com

 +32 499 53 92 91

 +32 473 83 64 62

www.ifluxsampling.com

Innovative methods for solute flux measurement in the subsurface environment, with technology demonstration and practical field training

Using tracers to assess the movement of solutes in the subsurface environment

Serge Brouyère

Université de Liège, Urban & Environmental Engineering (UEE)

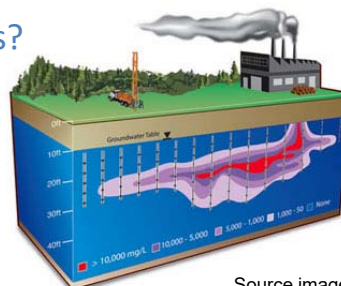
Department of Engineered Architecture, Geology, Environment and Constructions
Hydrogeology & Environmental Geology

Serge.Brouyere@uliege.be

www.inspirationitn.eu

In most groundwater pollution studies, a sound characterization relies on a good understanding of the fate of dissolved pollutants in groundwater....

- Groundwater & pollutants fluxes?
- Occurrence and magnitude of transport processes?
- Degradation – transformation mechanisms?



Source image:
<http://www.solinst.com/Prod/660/660d2.html>

Tracer technologies can be efficient tools
to answer to these questions

The transport of contaminants in the subsurface is governed by complex, overlapping physicochemical processes

effective porosity	Koc, foc Kd kinetics	diffusion coefficient longitudinal / transverse dispersivity	Source strength and behaviour
mobile water	sorption	diffusion dispersion	source
$\frac{\partial(\theta_m C)}{\partial t} + \frac{\partial(\theta_{im} C_{im})}{\partial t} + \rho_b \frac{\partial(C_s)}{\partial t} = -\nabla \cdot (v_D C) + \nabla \cdot (\theta_m \underline{D}_h \cdot \nabla C) - \lambda(\theta_m C + \theta_{im} C_{im}) + qC'$			
physical retardation	advection	degradation	
diffusion dual porosity first order constant	Darcy fluxes	chemical reaction constants biodegradation potential	
...			

If we want to solve the groundwater pollution issue, we need first to solve this equation...

... And in this context, different questions may arise

Are we able to identify the processes affecting the fate of contaminants in the subsurface and to differentiate them from other producing similar effects?

Can we quantify the parameters associated to these ongoing processes?

In some cases, can we evaluate their dynamics /evolution with time or space?

Lab experiments are nice, but what about the issues of heterogeneity and scale?

...

We can “trace” the information from the subsurface by ...

Monitoring the contaminants by themselves

Concentration evolution in time and space, co-reactive compounds, ...

Investigating other compounds present in the subsurface

Natural or environmental tracers: stable isotopes ...

Most often, poor control on the source of pollution (when, where, strength, composition...)



The “do it yourself” option

Apply tracers with known characteristics, in controlled conditions, with specific objectives in mind

Presentation outline

1. General aspects on applied tracer techniques with different examples of applications in the field
2. The Finite Volume Point Dilution Method for monitoring groundwater fluxes (FVPDM)

GENERAL ASPECTS ON APPLIED TRACER TECHNIQUES

7

Applied tracers: definition

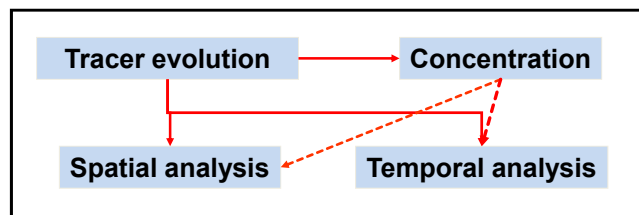
Any chemical compound / any product

- Of **known** chemical composition or physical properties
- **Voluntarily introduced** in groundwater (in the subsurface) :
generally a known quantity on a short duration at a selected location
- With the idea in mind of **identifying** and/or **quantifying properties / characteristics of groundwater or the subsurface medium in general**, such as groundwater flow directions, hydrodispersive properties, subsurface reactivity ...

Applied tracers: basic concept

Tracer injection at one location (e.g. piezometer, sinkhole ...)

Monitoring tracer at one or more locations (e.g. sampling at recovery well, spring, downgradient piezometer)



How do we proceed?

In theory, very easy, just dissolve the tracer in water and inject it into the subsurface / aquifer



In practice, experimental protocols can be sophisticated and experimental conditions can have a significant influence on the results and interpretation

From an operational perspective, classifying applied tracer techniques is not just a matter of fact ...

		Groundwater flow conditions	
		Natural	Forced-gradient
Number of piezometers / well required	1	Point dilution / FVPDM	Push-Pull / Dipole flow
	2 or more	Natural gradient	Many! In particular radially-converging flow

Potentially, we have an infinite number of tracers at our disposal

Practically, a limited number of products are commonly used
 Detection limit, background concentration, costs, health and environmental risks, non-conservative behaviour, interactions / interferences ...

Inorganic compounds (salts)

Most common : chloride, bromide, iodide, nitrate, lithium...

Fluorescent organic compounds

Uranine (fluoresceine), rhodamines, tinopal, naphthionate, eosin Y...

Non-fluorescent organic compounds

labelled contaminants, lactate, acetate, ...

“Others”

microspheres, nanotracers ...

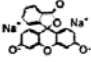
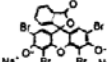
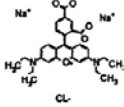
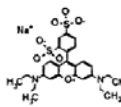
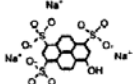
Saline tracers

- As soluble as possible (most often Na or K salts)
 - Low backgrounds in groundwater
 - Anions usually more conservative than cations
 - Quantities usually on the order of kgs to tens of kgs
-
- Most commonly used:
 - iodide I^- → 3-10 ppb
 - bromide Br^- → ~100 ppb?
 - lithium Li^+ → 3-10 ppb
 - chloride Cl^-
 - nitrate NO_3^-
 - Potassium K^+
 - Sodium Na^+
 - Strontium Sr^{2+}
- } Strongly background dependent
(usually applied on short distances
or in specific cases)

Fluorescent organic compounds

Source: P.Meus (EWTS)

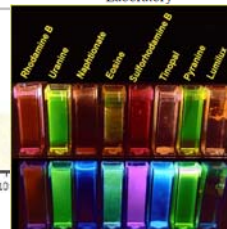
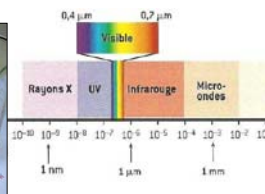
Table 1. Physical and Chemical Characteristics of Fluorescein, Eosine, Rhodamine WT, Sulforhodamine B, and Pyranine

Dye	Fluorescein ^a (Acid Yellow 73)	Eosine (Acid Red 87)	Rhodamine WT (Acid Red 388)	Sulforhodamine B (Acid Red 52)	Pyranine (Solvent Green 7)
Group	Xanthenes	Xanthenes	Rhodamines	Rhodamines	Aromatic hydrocarbons
Structure ^b					
Formula ^c	$C_{20}H_{10}O_5Na_2$	$C_{20}H_6Br_4O_5Na_2$	$C_{29}H_{29}N_7O_5Na_2Cl$	$C_{27}H_{30}N_2O_7S_2Na_2$	$C_{16}H_7O_{10}S_3Na_3$
Molecular weight (g/mol)	376	692	566	604	524
Detection limit ^d (ppb)	0.002	0.01	0.006	0.007	0.008
Excitation/emission wavelength (nm) ^e	492/513	515/535	558/583	560/584	460/512
Log K_{ow} ^b	-0.39	-1.33	-1.33	-2.02	-0.68
Provider	Kingscote Chemicals	Ozark Underground Laboratory	Formulabs	Ozark Underground Laboratory	Ozark Underground Laboratory

^aKnown as Uranine in Europe.

^bField et al. (1995).

^cBehrens (1986).



We can also classify our tracers according to the way they generally behave in the underground ...

The referential for that is most often (ground)water
(water is a very sorptive compound!)

“Ideal” tracers

Tracers that are supposed to behave just like water in the underground

Conservative tracers

Tracer that do not sorb or react in the subsurface
In practice, mostly a myth!

Reactive tracers

Probably 99% of the applied tracers react somehow!

Common domains of applications of applied tracer technologies

Groundwater pollution studies

Measurements of groundwater / pollutant mass fluxes & identification and quantification of solute transport mechanisms

Hydrogeological assessment

Groundwater pathways, recharge processes, time lags...

(Delineation of groundwater protection zones)

Determination of tracer travel times in groundwater

(Reactive transport and degradation processes)

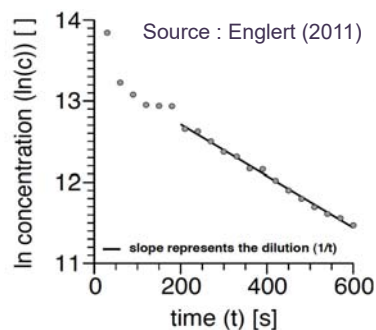
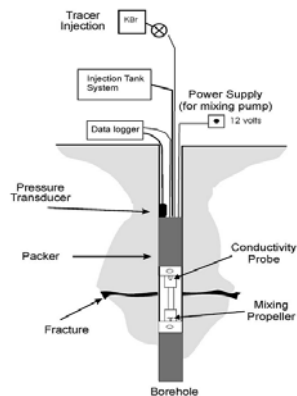
Use of reactive tracers to evidence sorption / degradation / partitioning processes

MEASURING AND MONITORING GROUNDWATER FLUXES

17

Measuring groundwater fluxes is essential because this is the main driver of pollutants

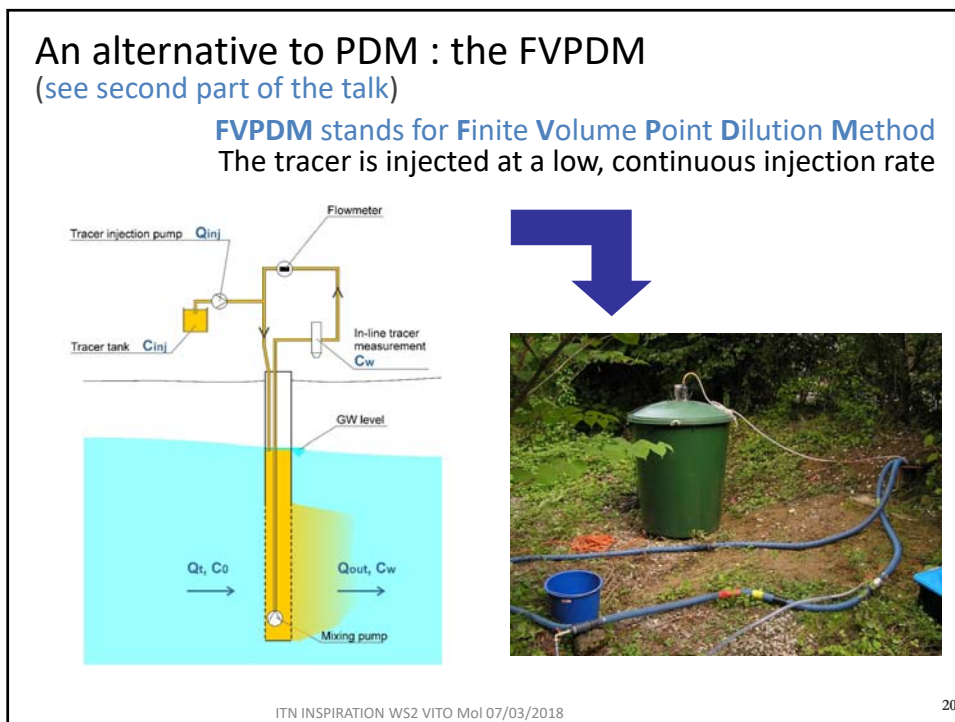
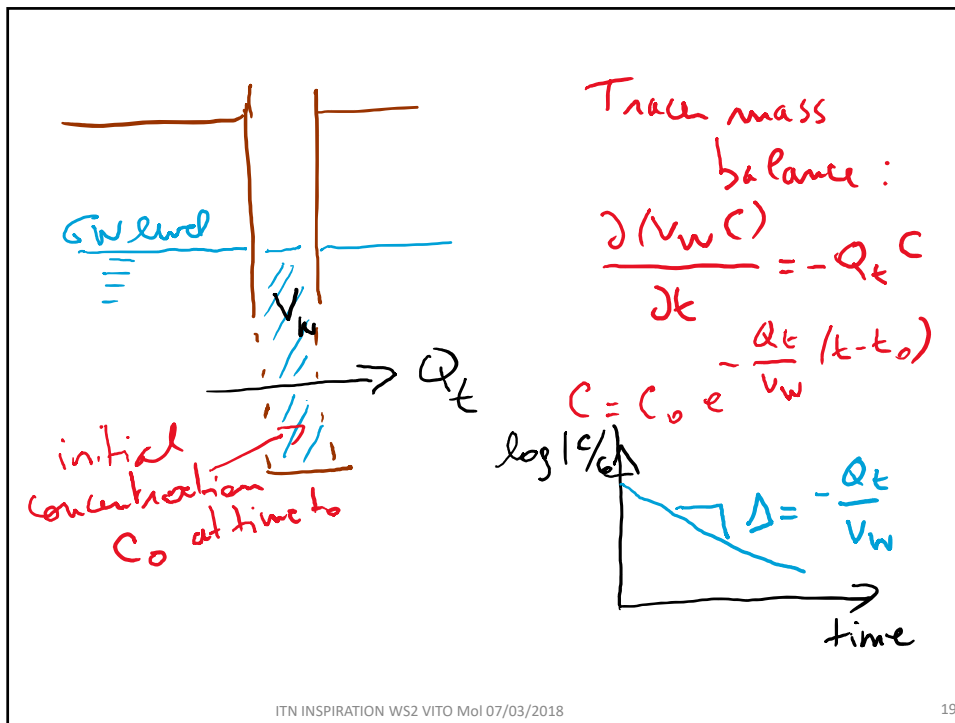
Most common tracer technique : the **Point Dilution Method**
Monitoring concentration exponential decline in the column of water located in a piezometer due to groundwater flow across the screens



K. Nowakowski et al. / Journal of Contaminant Hydrology 82 (2006) 44-60

ITN INSPIRATION WS2 VITO MoI 07/03/2018

18



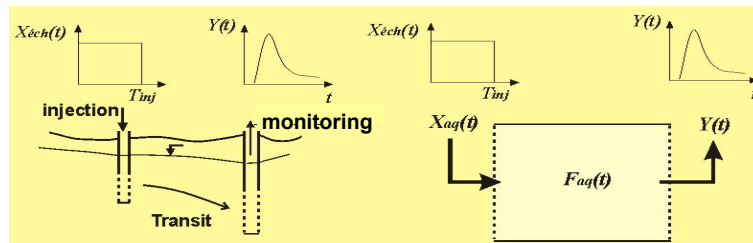
IDENTIFICATION AND QUANTIFICATION OF SOLUTE TRANSPORT MECHANISMS

21

We can also use applied tracers as surrogates of contaminants ...

Tracers are injected in controlled conditions (quantity, duration, injection rate, groundwater flow conditions...) at selected locations

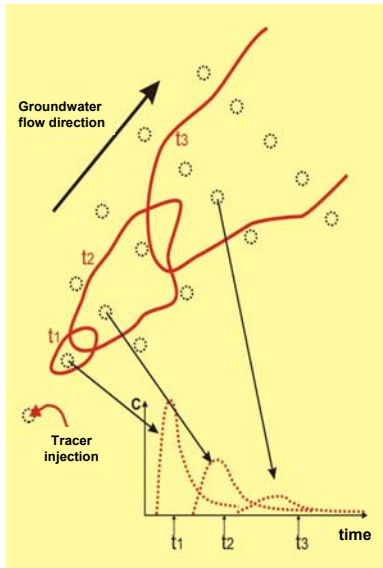
Concentration evolutions monitored down gradient from the injection is used to determine and quantify transport processes



Two main categories

Natural flow and radially converging flow tracer experiments

Natural flow experiments are more representative of groundwater pollution problems



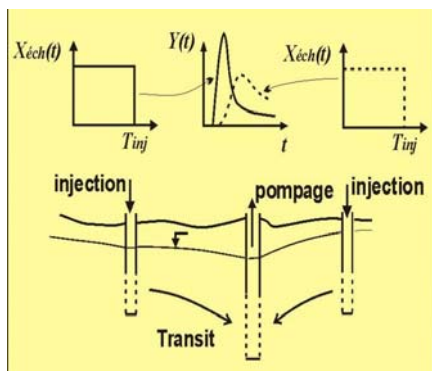
Advantages and drawbacks

- Natural groundwater flow conditions
- Groundwater not pumped, just sampled
- Monitoring system potentially costly
- Interpretation not straightforward (moment analysis)



Cape Cod, MA, USA (USGS)

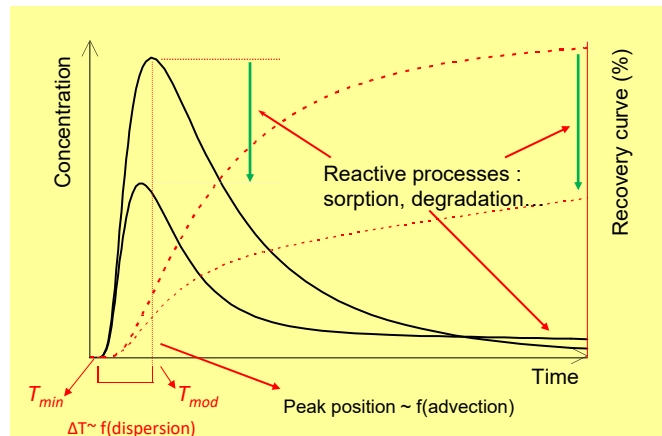
Radially converging flow tracer experiments provide more quantitative results



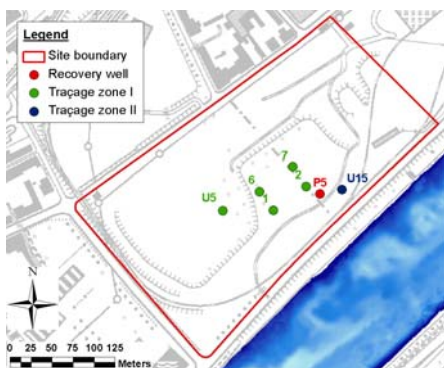
Advantages and drawbacks

- Quantitative interpretation based on concentration evolution and tracer mass recovery
- Faster because of forced gradient
- Abstracted groundwater = further costs + restrictions on where to perform on contaminated sites
- Modified groundwater flow conditions

The breakthrough curve is a record of subsurface transport processes



Lessons from a tracer experiment in a brownfield



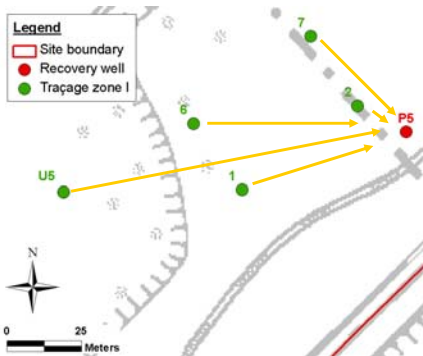
Tracer experiments performed in radially converging flow conditions around P5 (located in a uncontaminated groundwater sector)

Objectives: to obtain information on solute transport processes and parameters for the site

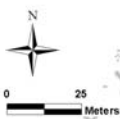
Battle-Aguilar et al., J. Hydrol (2008)
Battle-Aguilar, PhD thesis, ULg (2008)



2 injection phases performed

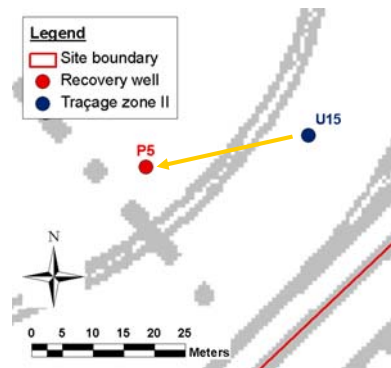


- Pz 1: Li⁺ (1.39 kg)
- Pz 2: NO₃⁻ (12.16 kg) + sulpho B (0.10 kg)
- Pz 6: I⁻ (3.28 kg)
- Pz 7: Naphtionate (1 kg)
- Pz U5: Fluorescein (0.2 kg)



Pz U15

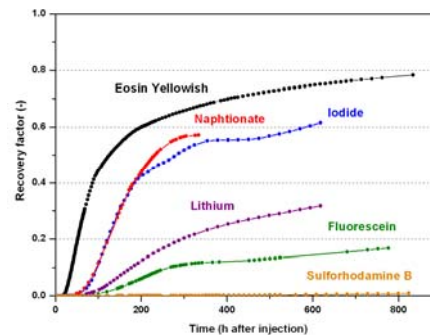
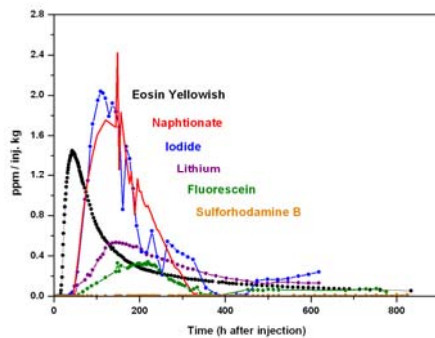
- Eosin Yellowish (1 kg)
- Naphtionate (0.01 kg)
- Sulpho B (0.01 kg)
- Fluorescein (0.01 kg)
- Li⁺ (0.6 kg)
- I⁻ (0.76 kg)



Very contrasted results ...!

- Phase 1: **No arrival of the tracers** injected upgradient in the site ...
- Phase 2: **Different breakthrough curves** (concentration and mass recovery) for the different salt and dye tracers, injected in the same piezometer (U15)

⇨ ≠ physico-chemical properties



ITN INSPIRATION WS2 VITO MoI 07/03/2018

29

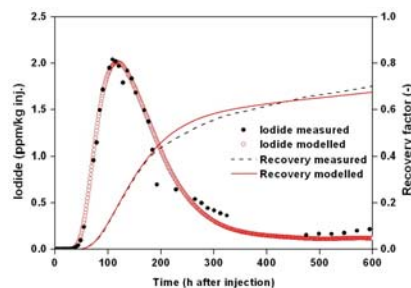
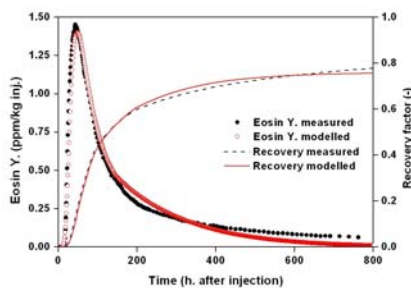
MT3DMS (Zheng and Wang, 1999)

Paramètres hydrodispersifs

Effective porosity (θ_m) (-)	0.03 – 0.045
Long. dispersivity (α_L) (m)	1.5 – 2.5
Trans. dispersivity (α_T) (m)	0.3 – 0.5

Effets de retard

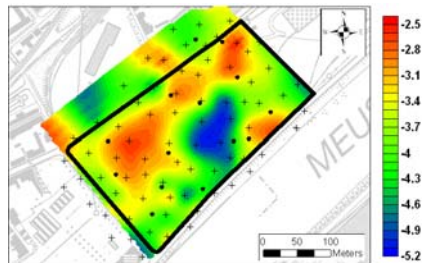
Immobile water porosity (θ_{im}) (-)	0.05 – 0.1
1 st order coefficient (α) (s ⁻¹)	2×10^{-7} - 8×10^{-8}



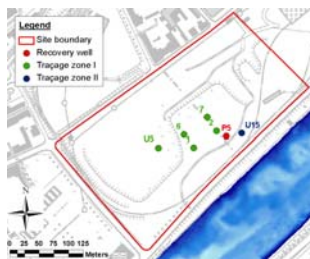
ITN INSPIRATION WS2 VITO MoI 07/03/2018

30

Tracer experiments are better explained considering the heterogeneity of the alluvial deposits



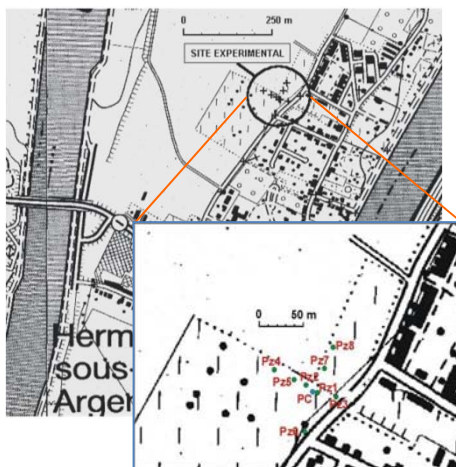
K-field heterogeneity highlighted through modelling of variations in groundwater levels with changes in river stage, using a pilot point approach



Pz1 Pz2 Pz6 Pz7 U5 not recovered because of a low pervious zone on the way to P5

U15 : recovery at P5 which drained most probably water from the Meuse River

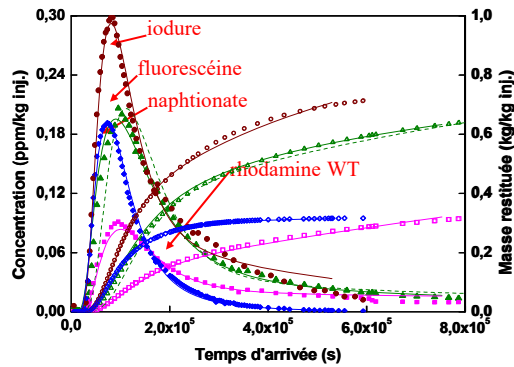
Tracer experiment at Hermalle\Argenteau (Liège region)



Alluvial aquifer of the Meuse River
1 pumping well ($Q = 52.6 \text{ m}^3/\text{h}$)
8 piezometers (4→50m)
tracer tests in the saturated zone

- Influence of tracer injection protocol
- Specific physico-chemical behaviour of tracers

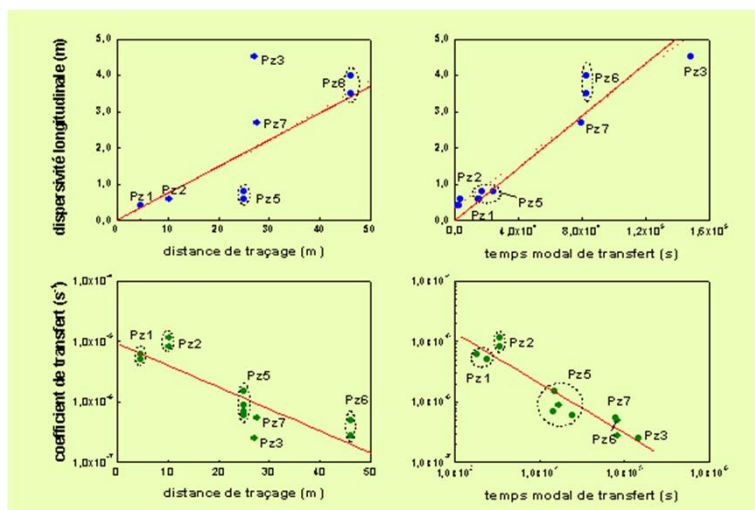
Hermalle s/Argenteau: injection of tracers at Pz6 (46m from the pumping well at $Q = 50 \text{ m}^3/\text{h}$)



- Iodure: conservative
- Naphionate: degradation
- Fluoresceine: sorption
- Rhodamine WT: strong sorption

Modelling breakthrough curves with SUFT3D finite element code
Iodide : advection-dispersion + immobile water effect
 $\theta_m = 0.085, \alpha_L = 3.5 \text{ m}, \theta_{im} = 0.13, \alpha = 5.0 \times 10^{-7} \text{ s}^{-1}$

Transport parameters affected by scale effects / non-fickian processes...
 Effective porosity and immobile water porosity: not pronounced
 longitudinal dispersivity and transfer coefficient: evident



HYDROGEOLOGICAL ASSESSMENT: RECHARGE PROCESSES IN FRACTURED ROCKS

35

Context : nitrate in excess in many fractured aquifers used for groundwater abstraction in Wallonia

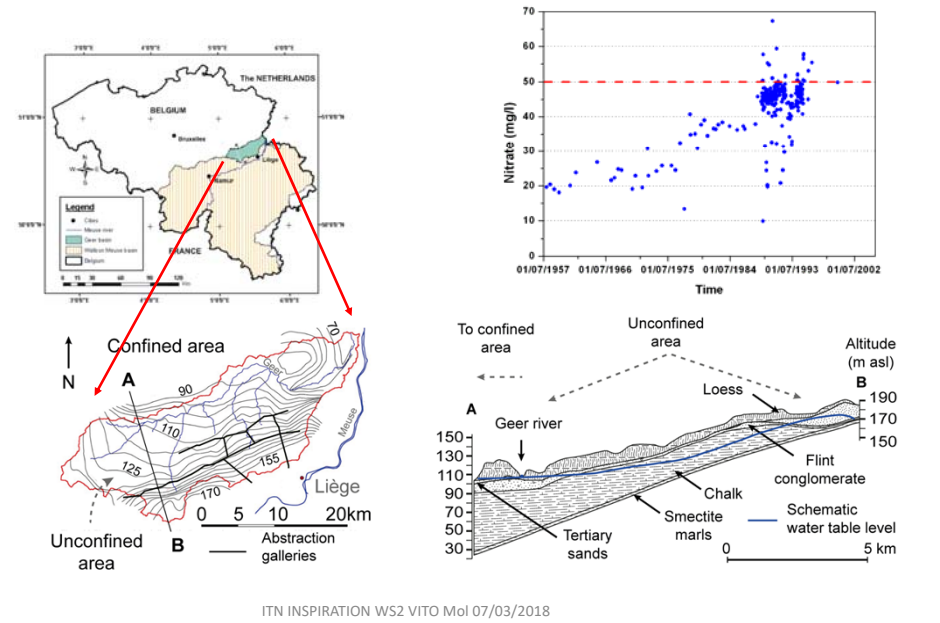
→ What are pollutants **recharge mechanisms** across the unsaturated zone above those aquifers?

→ **How fast do pollutants migrate** vertically across the unsaturated zone and what are the **expected time lags** (e.g. for trend reversal) ?

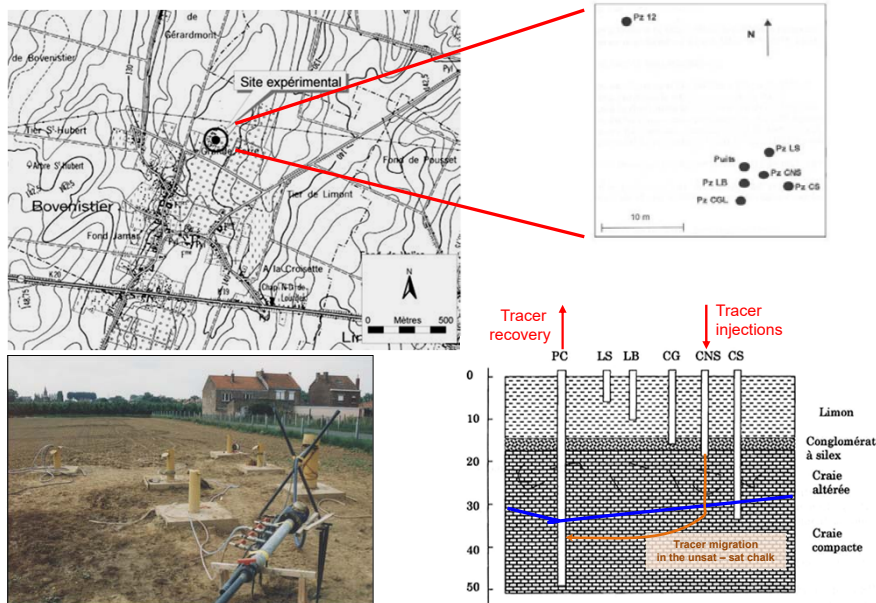
Two case studies:

1. Tracer experiments in unsaturated cretaceous chalks overlain by thick eolian loess deposits
2. Tracer experiments in unsaturated carboniferous limestone overlain by shallow soils

Case study II : Geer watershed – Hesbaye region (Belgium)



Tracer experiments in the unsaturated chalk



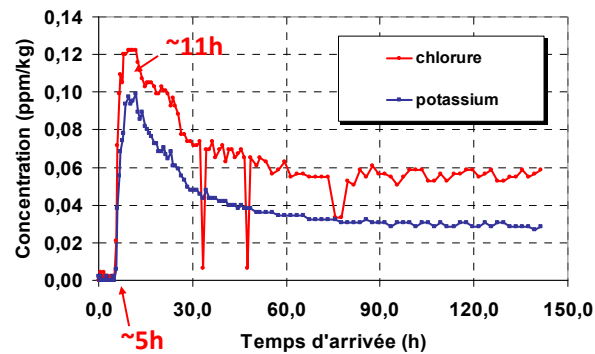
Tracer experiments across the unsaturated chalk (1/2)

Pz CNS → PC, horizontal distance : 6m

Vertical distance (thickness of unsat. chalk) : 10m

Tracer injection in Pz CNS **under artificial recharge conditions**

Tracer: KCl
Q rate at PC : 6,5
m³/h
M_{inj}: 100 kg
V_{inj}: 300 L
T_{inj}: ~1 h
Q_{ch}: ~300 L/h



**Short travel times and very strong tailing
(delayed recovery of injected tracers)**

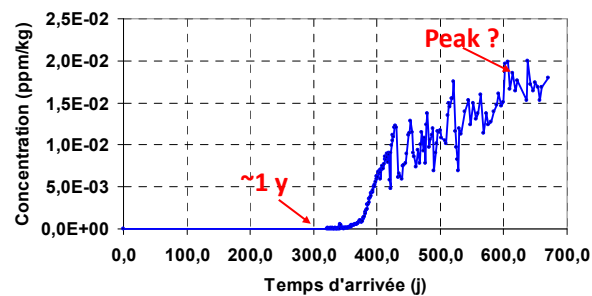
Tracer experiments across the unsaturated chalk(2/2)

Pz CNS → PC, horizontal distance : 6m

Vertical distance (thickness of unsat. chalk) : 10m (at beginning of exp.)

Tracer injection in Pz CNS **under natural recharge conditions** (no water added after tracer injection)

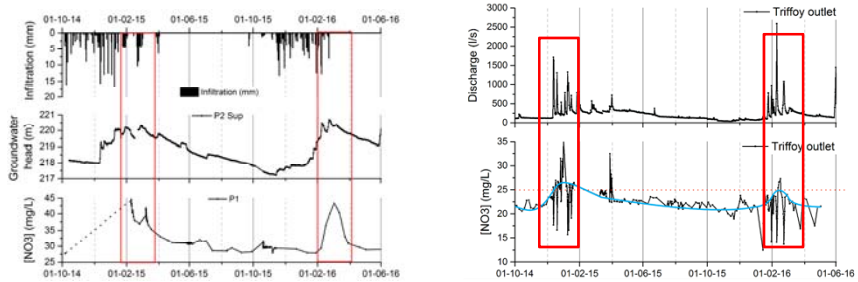
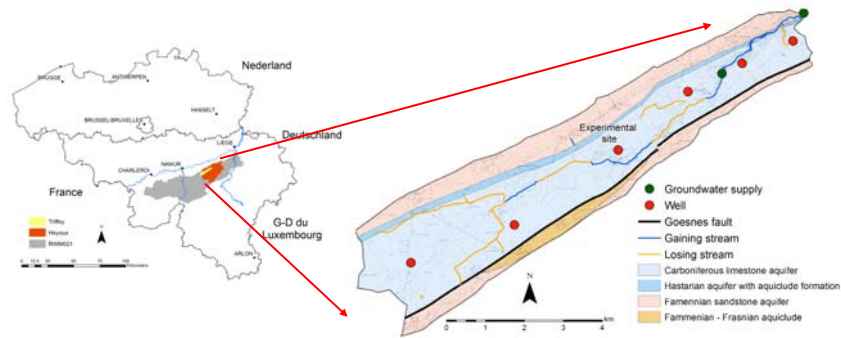
Tracer: iodide (in KI)
Qrate at PC : 3 to 6m³/h
M_{inj}: 10 kg
V_{inj}: 30 litres
T_{inj}: 6 min
Q_{ch}: 0 m³/h



Very long traver time!

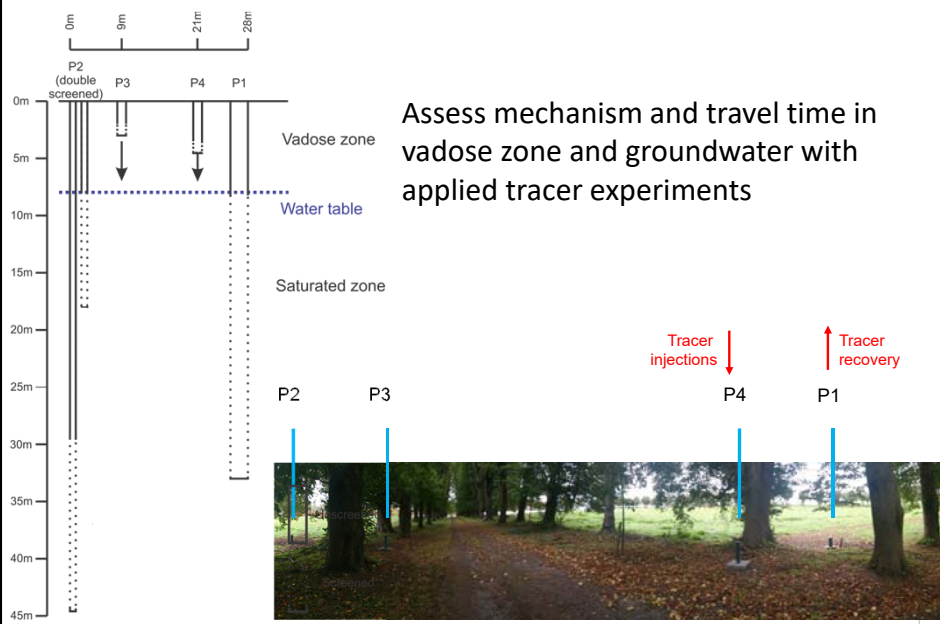
Knowing that a rise in groundwater level was observed during that period, facilitating the recovery of the tracer!

Case study I : Triffoz watershed – Condroz region (Belgium)



ITN INSPIRATION WS2 VITO Mol 07/03/2018

Experimental site



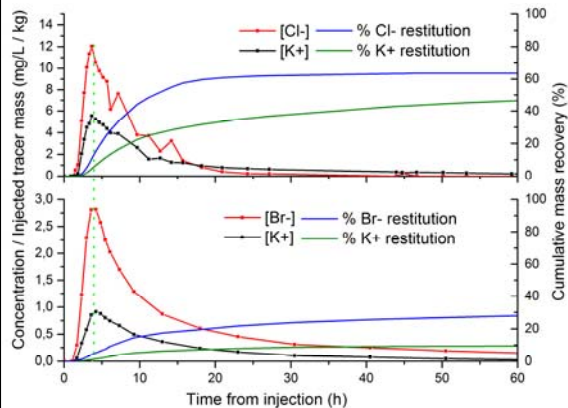
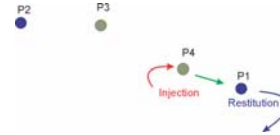
Assess mechanism and travel time in vadose zone and groundwater with applied tracer experiments

ITN INSPIRATION WS2 VITO Mol 07/03/2018

Mechanism and travel time : vadose zone

Two tracer injections in P4 :

- (1) KCl with water pounding (recharge) in the injection piezometer
- (2) KBr with no water recharge



In both case :

- 1st arrival : 1h30 / Modal time : 4h
- Short travel time in vadose zone ($v_{\max} = 1.33$ m/h, $v_{\text{mod}} = 2$ m/h)
- No impact of water pounding on travel time

→ Fast preferential flow

Conclusions on recharge processes

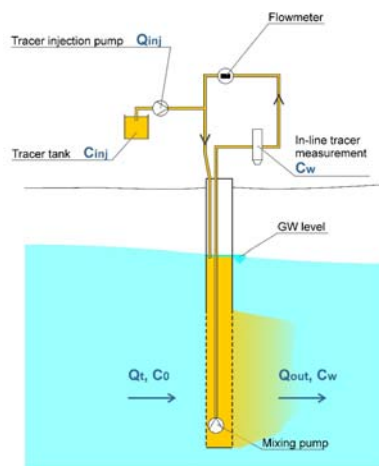
- Hesbaye dual-porosity chalk overlain by **thick loess soils**
- **Inhibited preferential pathways** because of buffering effect of low K loess formation and long travel times
- **Slow groundwater and NO₃ transfer mechanisms** across deep unsaturated zone
- **On a short term, low aquifer vulnerability to pollution** occurring on the land surface
- However, on a long term perspective, **strong time lags and delays to recover better groundwater quality levels**
- Triffoy Carbonifereous limestone overlain by **shallow soils**
- **Preferential flow paths** through fractures and short travel times
- **Fast groundwater and NO₃ transfer mechanisms** across limestone unsaturated zone
- **On a short term, strong aquifer vulnerability** to pollution occurring on the land surface
- However, one may expect **shorter time lags and delays to recover better groundwater quality levels**

The Finite Volume Point Dilution Method FOR MONITORING GROUNDWATER FLUXES

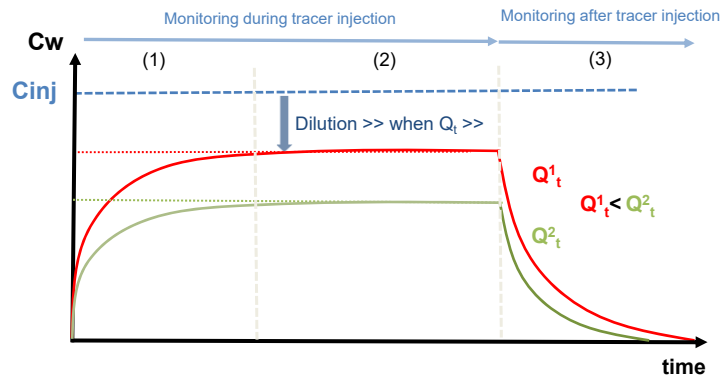
45

An alternative to PDM : the FVPDM (developed by HGE-ULiège)

FVPDM stands for **F**inite **V**olume **P**oint **D**ilution **M**ethod
The tracer is injected at a low, continuous injection rate



The Finite Volume Point Dilution Method: 3 steps



1. Transient when tracer concentration rises
 - C_w is a function of Q_t and V_w
2. Stabilized at equilibrium between injection and discharge in the aquifer
 - dilution C_w/C_{inj} is a function of Q_t only
3. Exponential decline (= classical PDM)

ITN INSPIRATION WS2 VITO MoI 07/03/2018

The concentration evolution is obtained using a tracer mass-balance in the injection well

Water conservation

$$\frac{\partial V_w(t)}{\partial t} = \pi r_w^2 \frac{\partial h_w}{\partial t} = Q_{inj}(t) + Q_t(t) - Q_{out}(t)$$

Further details in Brouyère (2001) and Brouyère et al. (2008)

Tracer mass conservation

$$\frac{\partial M_t}{\partial t} = \frac{\partial}{\partial t} (V_w C_w) = r_w^2 \left(C_w \frac{\partial h_w}{\partial t} + h_w \frac{\partial C_w}{\partial t} \right) = Q_{inj} C_{inj} + Q_t C_t - Q_{out} C_{out}$$

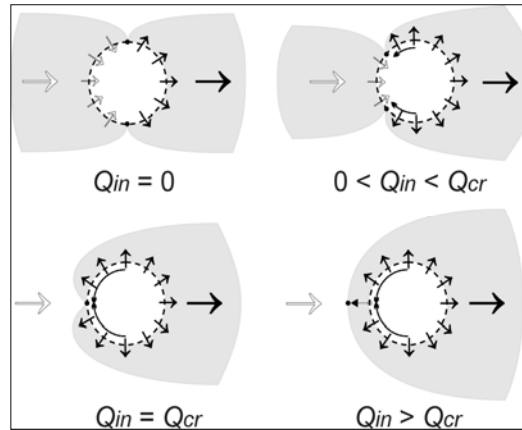
Concentration evolution in the injection well

$$C_w(t) = \frac{Q_{inj} C_{inj} - (Q_{inj} C_{inj} - Q_{out} C_{w,0}) \exp\left(-\frac{Q_{out}}{V_w} (t - t_0)\right)}{Q_{out}} \quad Q_t = Q_{out} - Q_{inj}$$

ITN INSPIRATION WS2 VITO MoI 07/03/2018

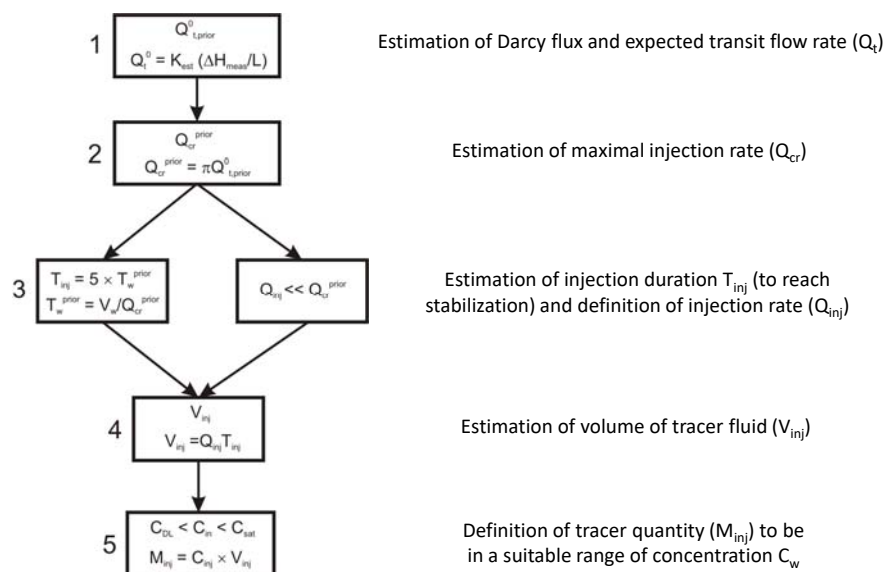
48

The success of the experiment relies on a controlled, low injection rate



It can be shown that the maximal injection rate (Q_{inj}) should be less than 3 times the transit flow rate (Q_t) that we try to quantify

FVPDM dimensioning strategy

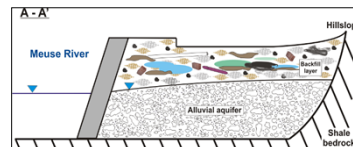
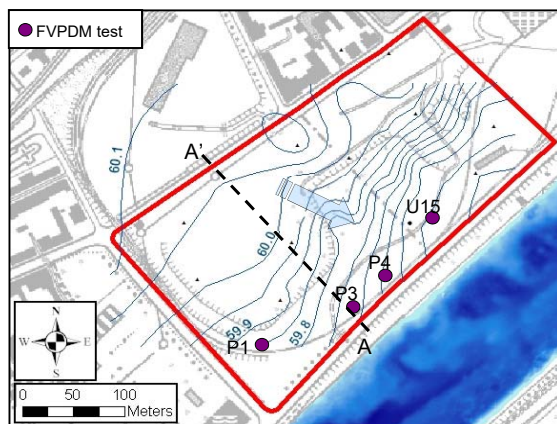


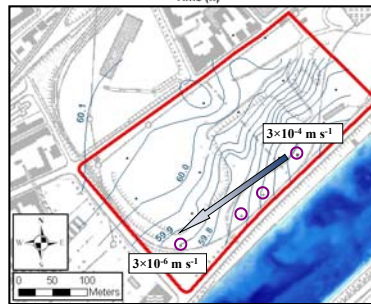
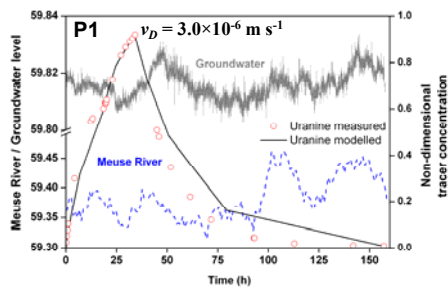
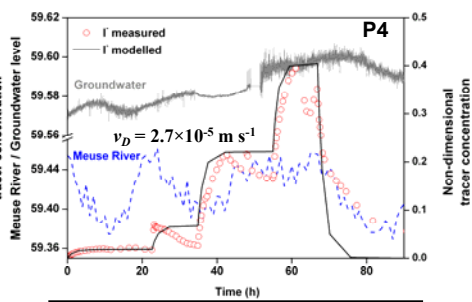
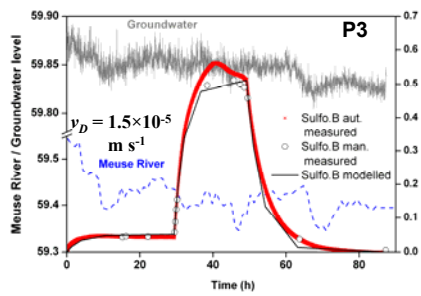
FVPDM APPLICATIONS IN THE FIELD

51

The FVPDM was first successfully applied in piezometers located in the border of a contaminated brownfield

The objective was to measure groundwater discharge rates from a contaminated alluvial aquifer to the Meuse river (Liège, Belgium)



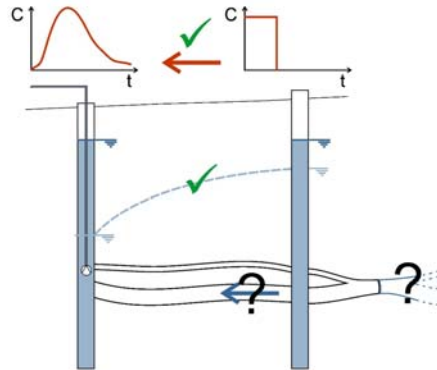


FVPDM packer application in open-boreholes

Identified fracture

Verified hydraulic connexion (pumping test, tracer test ...)

Groundwater flow ?



Work done in collaboration
with Geosciences URennes

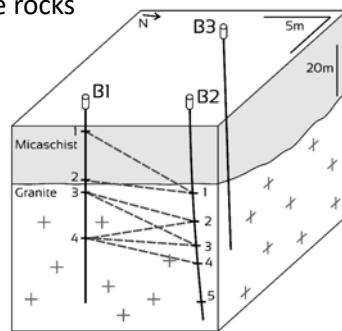
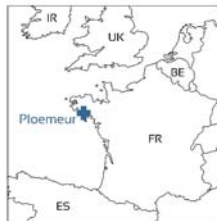
ITN INSPIRATION WS2 VITO MoI 07/03/2018

Experimental site: fractured granite of Brittany

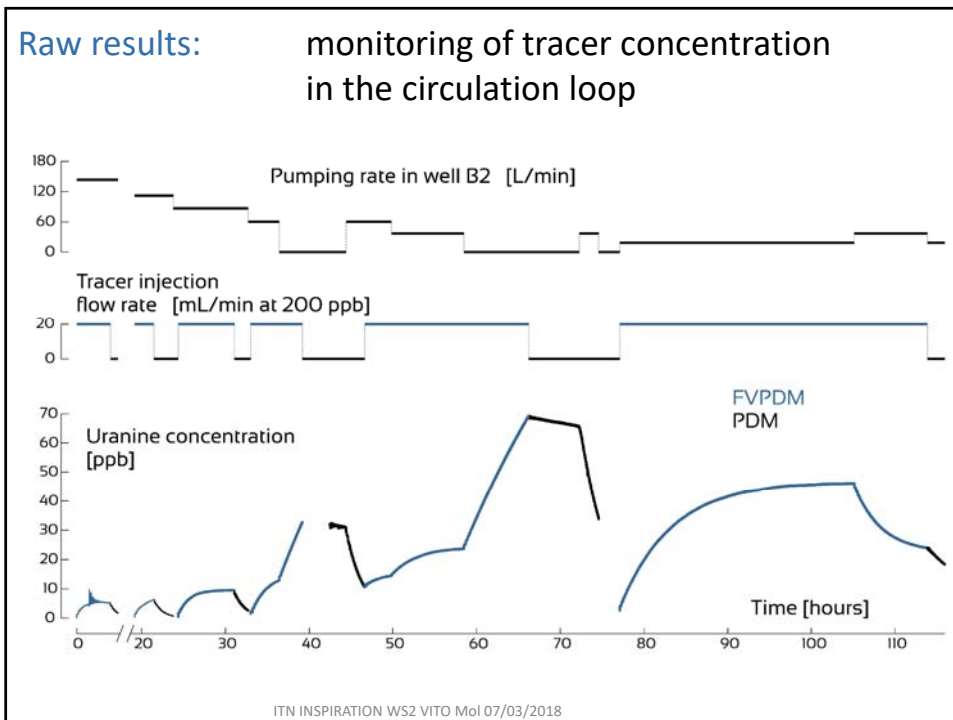
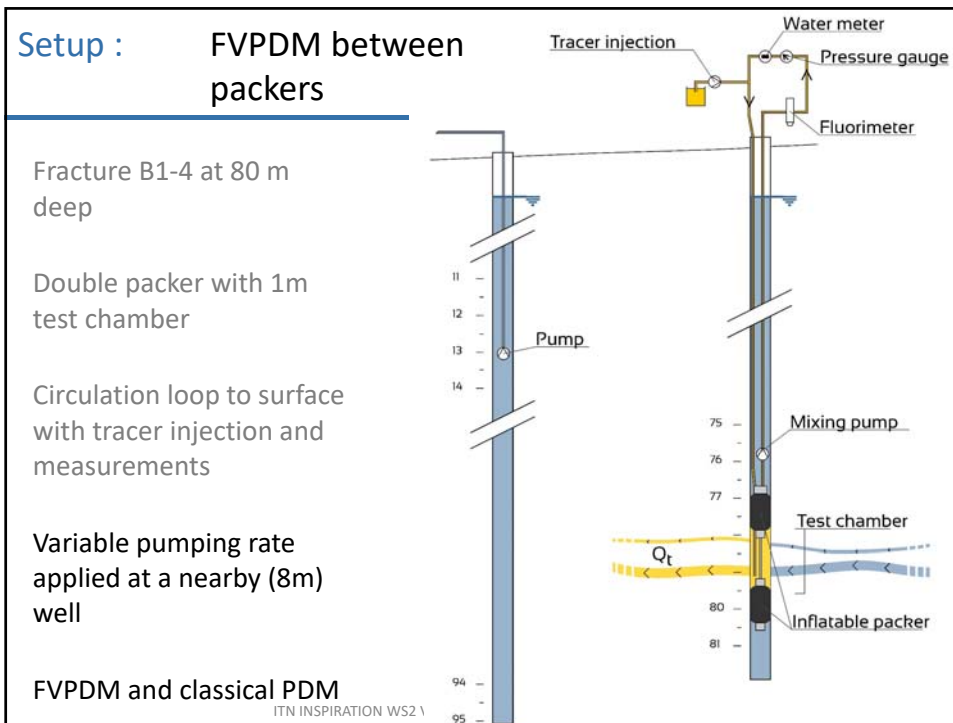
Ploemeur, Brittany, France

Productive aquifer within fractured crystalline rocks

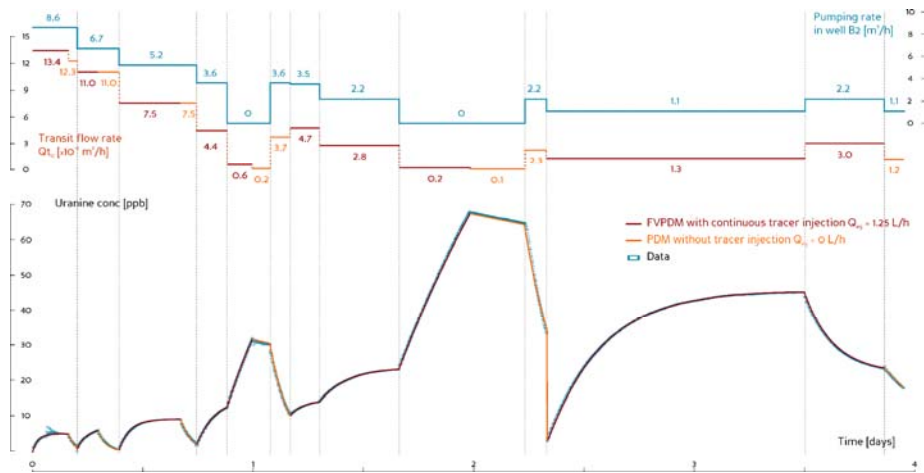
Three uncased wells of 90+ m deep



ITN INSPIRATION WS2 VITO MoI 07/03/2018



Interpretation using the FVPDM analytical solution



ITN INSPIRATION WS2 VITO MOI 07/03/2018

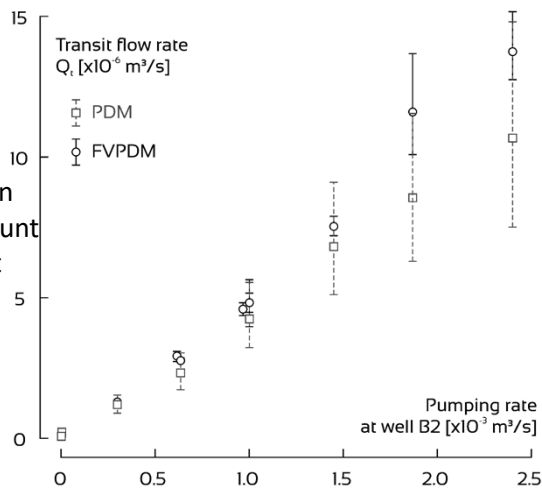
Interpretation : Comparison of transit flow rates for different pumping rates applied at the nearby well

Same conclusions for all the tests performed

FVPDM more precise than PDM after $5 t^*$

PDM underestimate Q_t because geometric estimation of V_w does not take into account part of the fracture zone that play a role in tracer mixing

Linear evolution of Q_t with pumping in B2



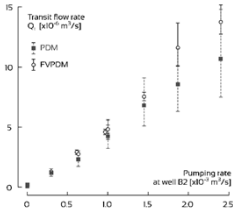
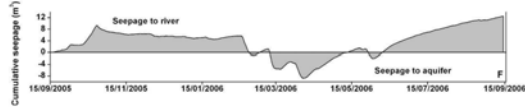
ITN INSPIRATION WS2 VITO MOI 07/03/2018

Next step with FVPDM: monitoring transient groundwater fluxes because ...Nature is transient!

Hydrogeological contexts intrinsically show transient groundwater fluxes...

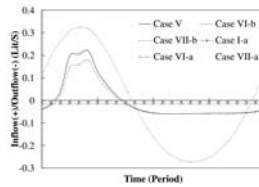
GW – Surface water interactions

"Darcy fluxes change continuously in time because of frequent changes in the difference of head between the river and its alluvial aquifer." Batlle-Aguilar, PhD thesis. 2008



Nearby pumping wells

"The change of pumping rate at the nearby well induced changes in the groundwater flow velocity that were recorded by continuous groundwater flux measurement." Jamin et al., J. of Contam. Hydrol. 2015



High recharge zones

"Intensive rainfall [...] can also provide substantial recharge to the aquifer locations considered as discharge areas. [...] certain areas may change from recharge to discharge status, depending on the temporal variability of fluxes." Lubczynska & Gurwinb, J. of Hydrology. 2005

Tidal effects

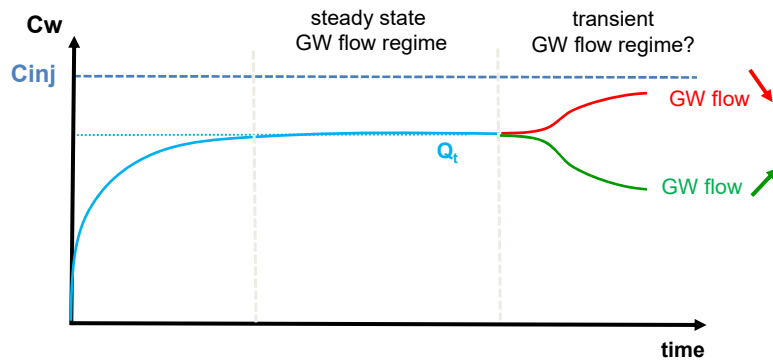
"The tidal oscillations [...] have an influence on regional groundwater flow." Ataie-Ashtiani et al., Hydrological Processes. 2001

ITN INSPIRATION WS2 VITO MoI 07/03/2018

The FVPDM: Monitoring of variable GW fluxes

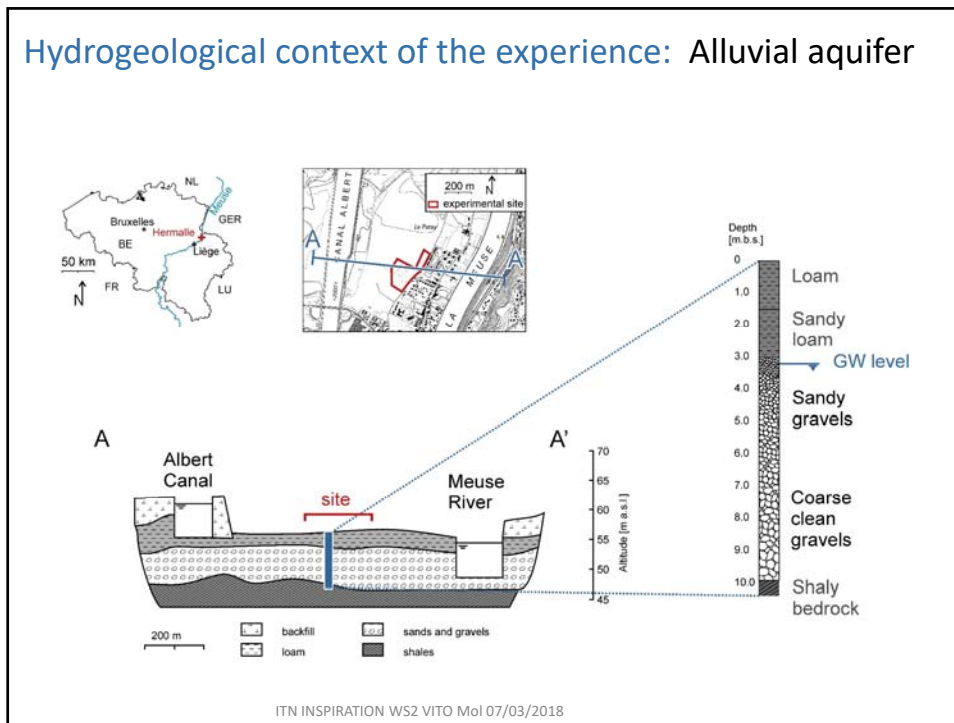
Constant injection of tracer and mixing during the monitoring time

Tracer concentration in the tested piezometer varies according to the GW flux (more/less dilution)

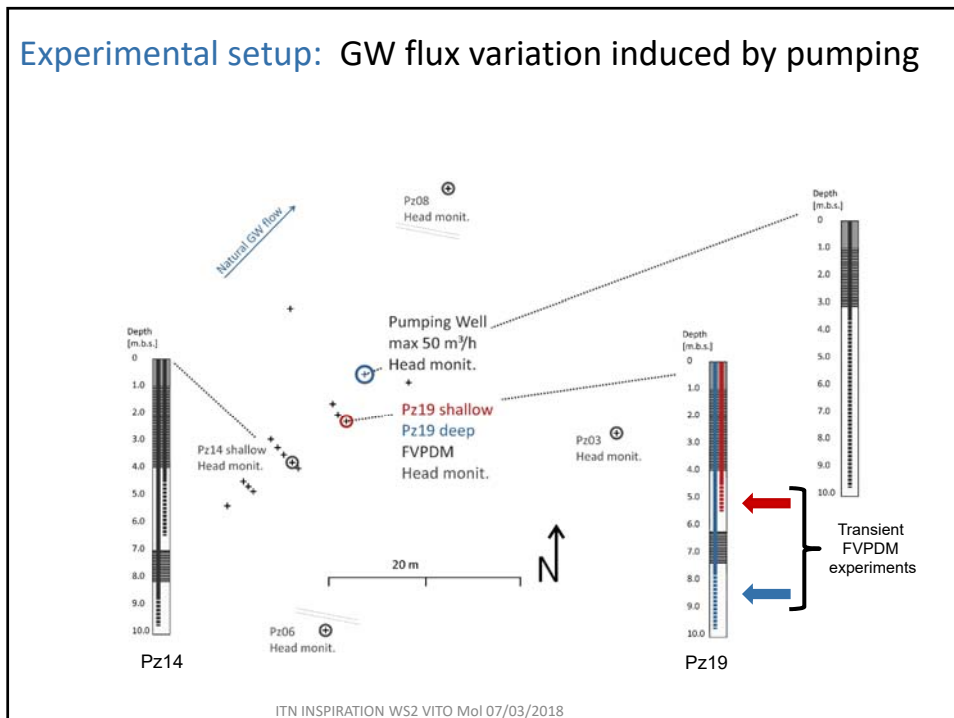


ITN INSPIRATION WS2 VITO MoI 07/03/2018

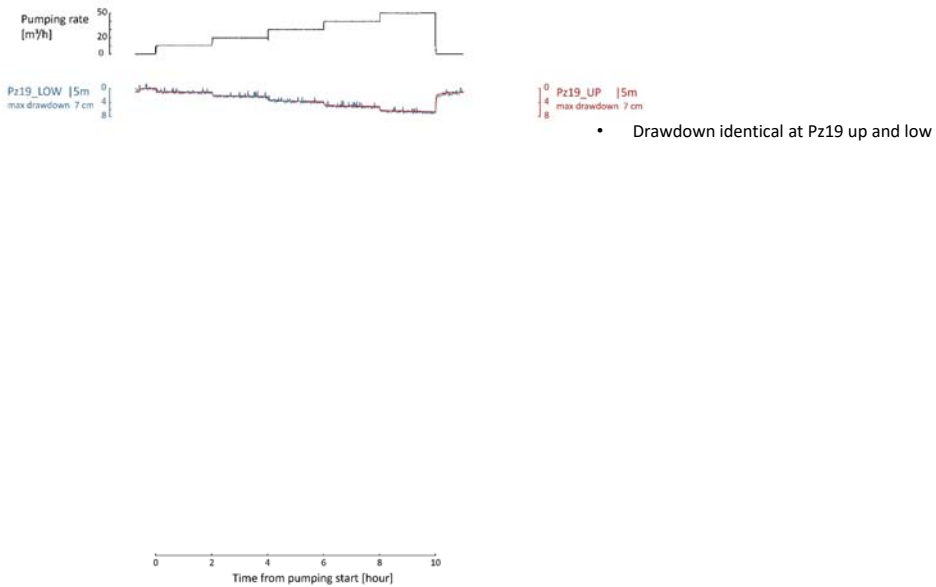
Hydrogeological context of the experience: Alluvial aquifer



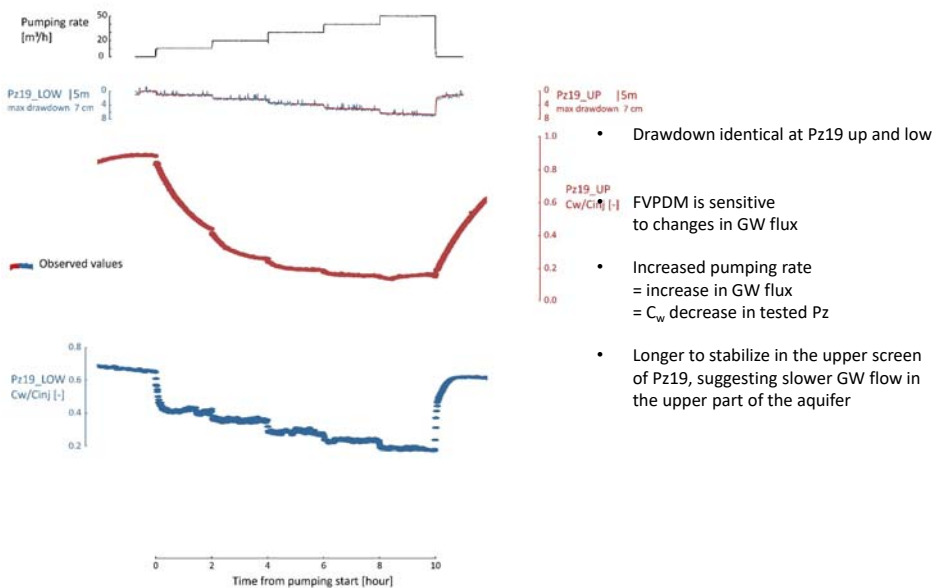
Experimental setup: GW flux variation induced by pumping



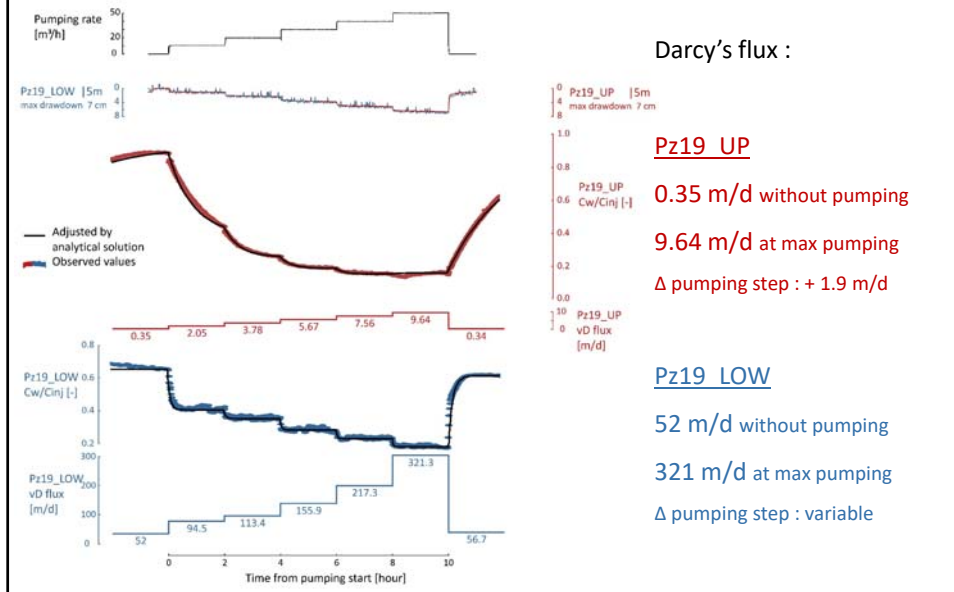
FVPDM results: Drawdown



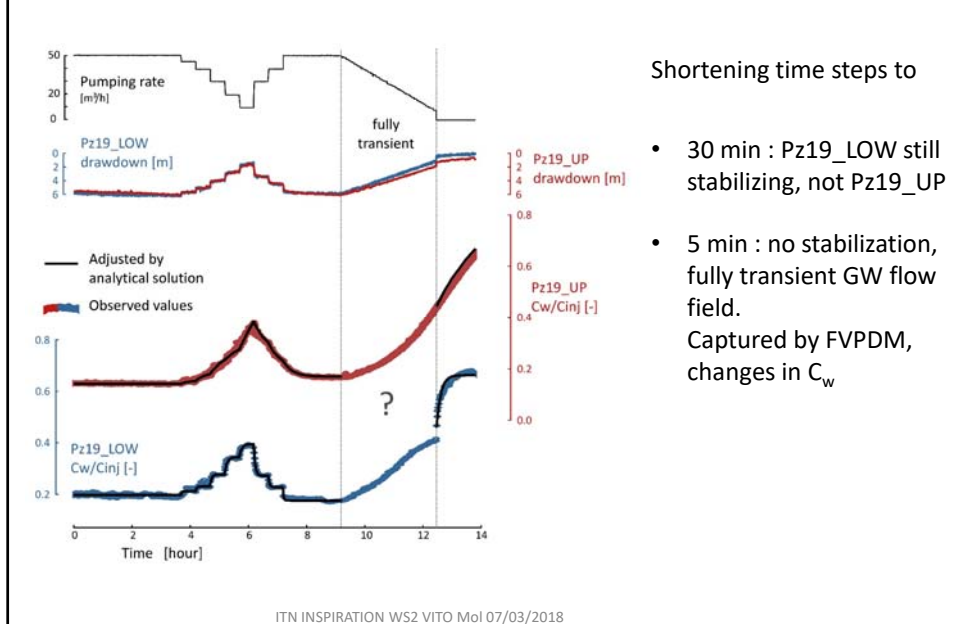
FVPDM results: GW flux higher in the lower part of aquifer



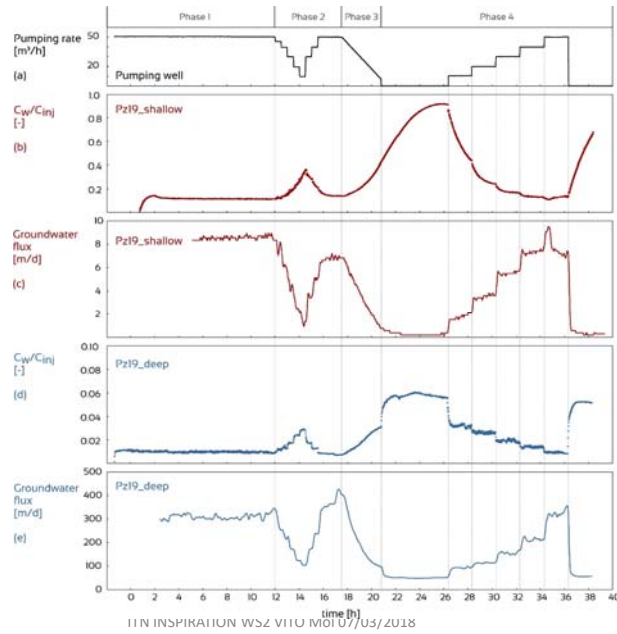
FVPDM results: GW flux higher in the lower part of aquifer



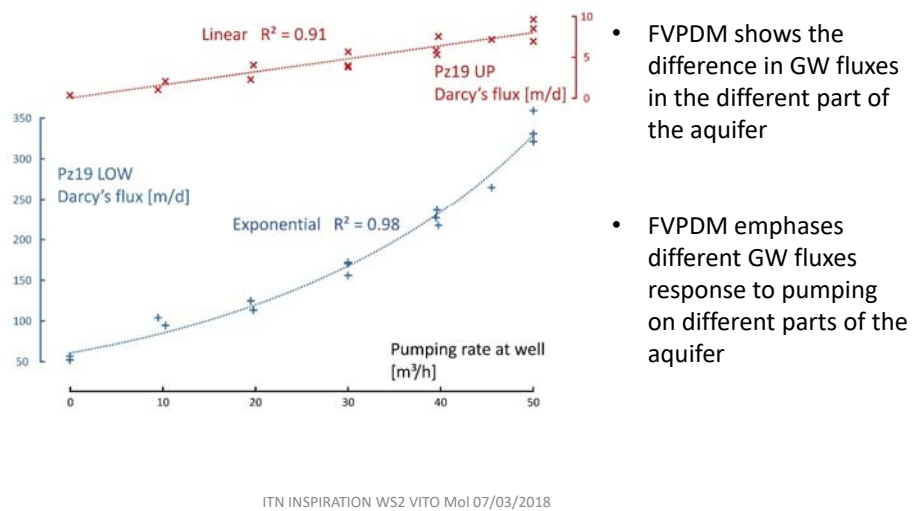
FVPDM abilities: Simulated transient GW fluxes



FVPDM transient: Calculation of transient GW fluxes



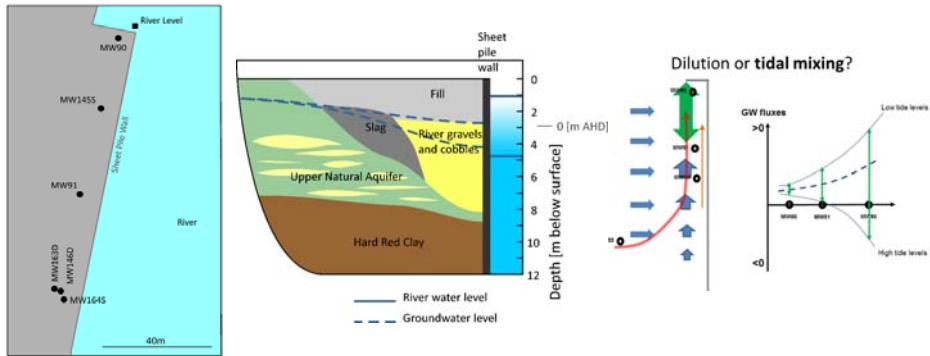
Contribution of FVPDM: Flow regimes in the aquifer



- FVPDM shows the difference in GW fluxes in the different part of the aquifer
- FVPDM emphasizes different GW fluxes response to pumping on different parts of the aquifer

Monitoring changes in groundwater fluxes and pollutant mass fluxes in a dynamic groundwater system (connected groundwater – estuary)

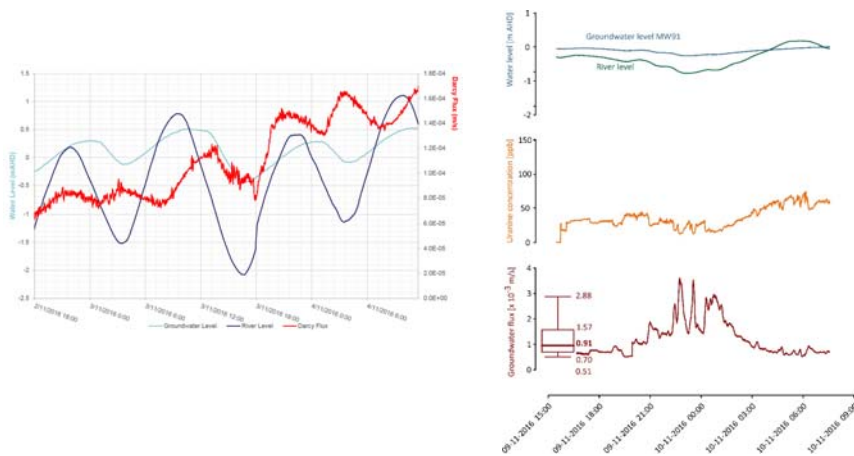
- Context: coastal aquifer hydraulically linked to tidal estuary
-> complex transient groundwater flow
- Heavy metal contamination of GW (Mn, Zn, Cd, Pb)
-> risk to estuarian ecosystems



ITN INSPIRATION WS2 VITO MoI 07/03/2018

Result 1: No inversion of GW flow direction

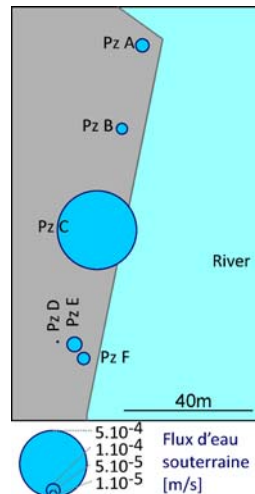
- The GW fluxes coming from upgradient are so important that we observed no inversion of GW flow during high river level



ITN INSPIRATION WS2 VITO MoI 07/03/2018

Result 2: The benefits of mass fluxes measurements

- Ranges of groundwater fluxes



ITN INSPIRATION WS2 VITO MoI 07/03/2018

Few tracer tests papers...

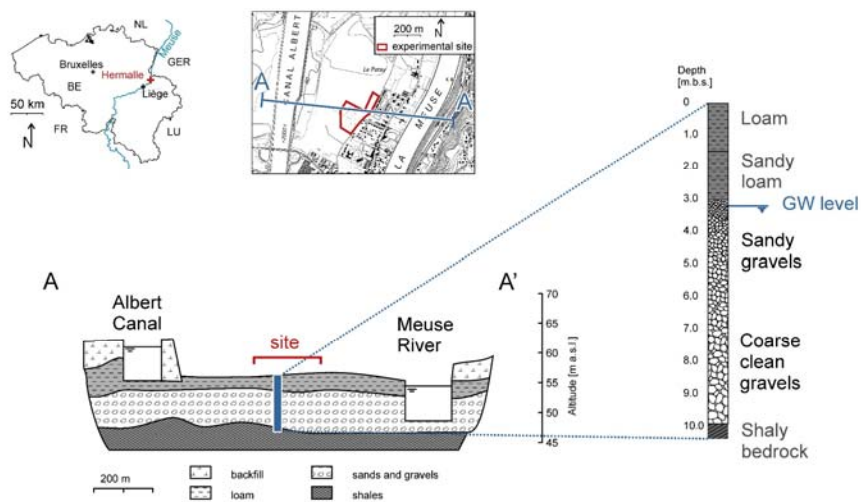
- Brouyère, S. (2003). Modeling tracer injection and well-aquifer interactions: A new mathematical and numerical approach. *Water Resources Research*, 39(3). <http://hdl.handle.net/2268/2321>
- Brouyère S., Dassargues A. and Hallet V., 2004. *Migration of contaminants through the unsaturated zone overlying the Hesbaye chalky aquifer in Belgium: a field investigation*. *Journal of Contaminant Hydrology* 72 (2004) 135-164. <http://hdl.handle.net/2268/2335>
- Brouyère, S., Carabin, G., & Dassargues, A. (2005). Influence of injection conditions on field tracer experiments. *Ground Water*, 43(3), 389-400. <http://hdl.handle.net/2268/3306>
- Brouyère S., Battle-Aguilar J., Goderniaux P. and Dassargues A, 2008. *A new tracer technique for monitoring groundwater fluxes: The finite volume point dilution method*. *Journal of Contaminant Hydrology* 95 (2008) 121 – 140. <http://hdl.handle.net/2268/1308>
- Battle-Aguilar J., Brouyère S., Dassargues A., Morasch B., Hunkleler D., Hohener P., Diels L., Vanbroekhoven K, Seuntjens P and Halen H, 2009. Benzene dispersion and natural attenuation in an alluvial aquifer with strong interactions with surface water. *Journal of Hydrology*, 369, 305-317. <http://hdl.handle.net/2268/9140>
- Goderniaux, P., Brouyère, S., Gutierrez, A., & Baran, N. (2010). Multi-tracer tests to evaluate the hydraulic setting of a complex aquifer system (Brévilles spring catchment, France). *Hydrogeology Journal*. <http://hdl.handle.net/2268/69365>
- Wildemeersch, S., Jamin, P., Orban, P., Hermans, T., Klepikova, M., Nguyen, F., Brouyère, S., & Dassargues, A. (2014). Coupling heat and chemical tracer experiments for estimating heat transfer parameters in shallow alluvial aquifers. *Journal of Contaminant Hydrology*, 169, 90-99. <http://hdl.handle.net/2268/171944>
- Jamin, P., Goderniaux, P., Bour, O., Le Brogne, T., Englert, A., Longuevergne, L., & Brouyère, S. (2015). Contribution of the Finite Volume Point Dilution Method for measurement of groundwater fluxes in a fractured aquifer. *Journal of Contaminant Hydrology*, 244–255. <http://hdl.handle.net/2268/185541>
- Natalia Fernández de Vera, Jean Beaujean, Pierre Jamin, Vivien Hakoun, David Caterina, Ofer Dahan, Marnik Vanclooster, Alain Dassargues, Frédéric Nguyen, Serge Brouyère; Tracer Experiment in a Brownfield Using Geophysics and a Vadose Zone Monitoring System. *Vadose Zone Journal* ; 16 (1): 1–15. doi: <https://doi.org/10.2136/vzj2016.06.0051>

ITN INSPIRATION WS2 VITO MoI 07/03/2018

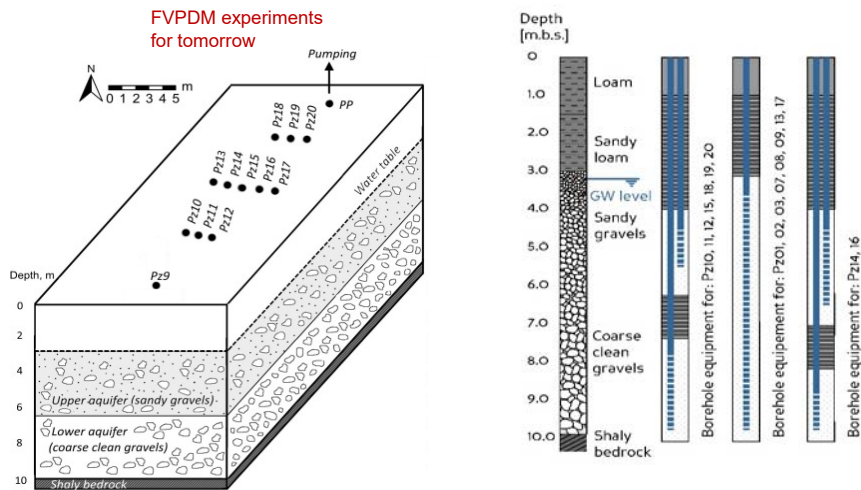
77

FIELD EXPERIMENTS TOMORROW IN HERMALLE-SOUS-ARGENTEAU

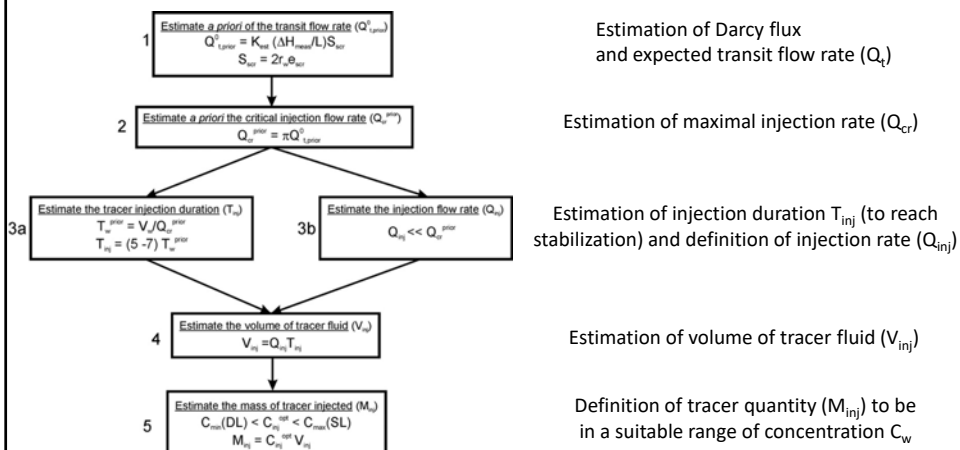
Hermalle-sous-Argenteau experimental site



Hermalle-sous-Argenteau experimental site



FVPDM dimensioning strategy



For your information: $C_{inj} = 5000$ ppb (tracer solution already prepared by Pierre Jamin 😊)



2. FIELD TRAINING (08/03/2018)

2.1 SCHEDULE

	Gwflux	iFlux-S	iFlux-P	Volume based	Low Flow
10.30	Team1	Team 3	Team 2	Team 4	
11.30	Team 3	Team1	Team 4	Team 2	
12.30	<i>Lunch</i>				
13.15	Team 2	Team 4	Team 1	Team 3	
14.15	Team 4	Team 2	Team 3	Team 1	
15.15	<i>Coffeebreak</i>				

2.2 TEAMS

Team 1	Team 2	Team 3	Team 4
Amoah-Antwi Collins	Ariza Carricondo Cristina	Banerjee Priyanka	Dhaese Kristiaan
Bujak Izabela	Damala Polyxeni	Debin Mao	Gill Richard
Ezzati Golnaz	Geukens Lana	Giber Alexandra	Nikolenko Olha
Gillett Andrew	Naert Martijn	Neyens Cas	Soria Penafiel Rosa Isabel
Tegenbos Julie	Quaglia Gisela	Saputra Bastian	Weatherl Robin
Yendell Alan	Van Humbeeck Thomas	von Chamier Julia	

2.3 EXERCISES

- Groundwater flux measurement (Pierre Jamin)
- Application of iFlux sampler – prospector (Goedele Verreydt)
- Volume based groundwater sampling (Johan Vos / Ilse Van Keer)
- Low flow sampling (Johan Vos / Ilse Van Keer)

2.4 EXPERIMENTAL FIELD SITE

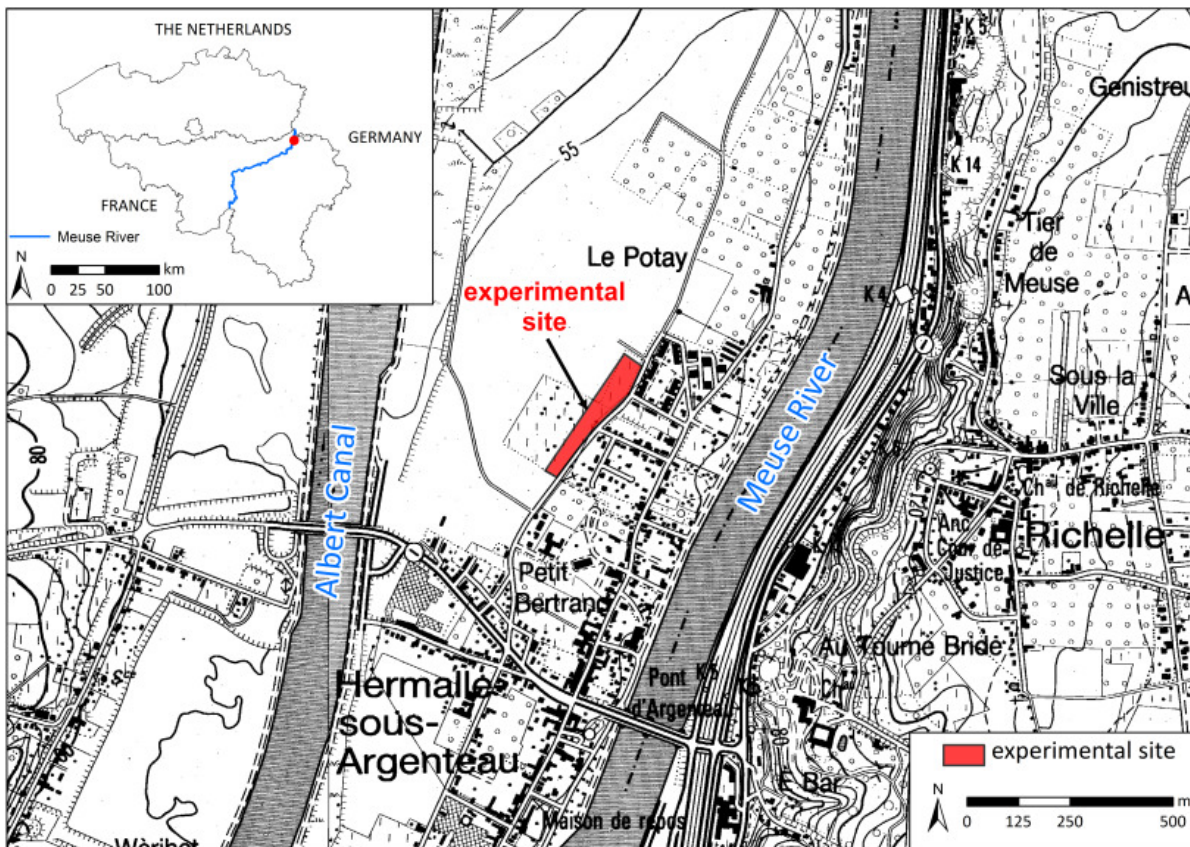
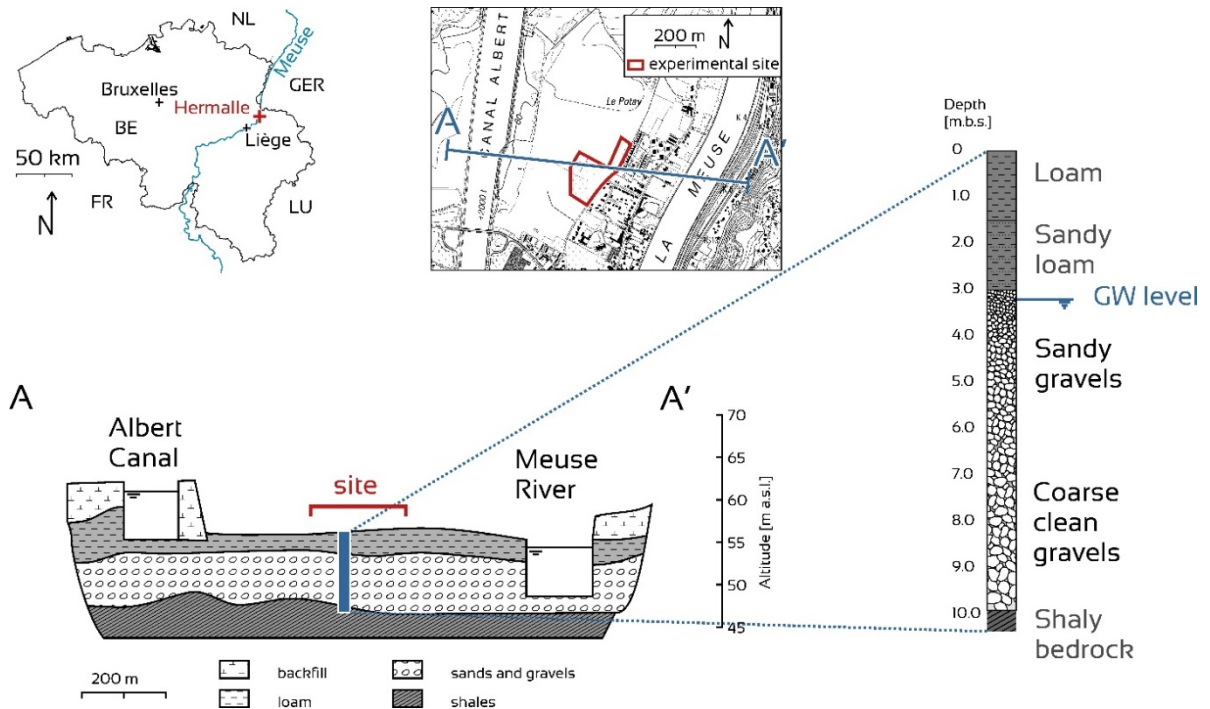


Figure 1: location of the HssA test site.

The experimental site is located in the small village of Hermalle-sous-Argenteau, 13 km north-east of the city of Liège in Belgium. The site consists in a vast meadow lying on the alluvial plain of the Meuse River (**Error! Reference source not found. 2**). The alluvial deposits can be divided into four different units. The upper layer is 1 to 1.5 m thick and is composed of loam with clay lenses. The second unit consists of sandy loam with millimetric gravels which proportion increases with depth down to 3 m depth. From 3 to 10 m below ground surface, the third layer is mainly made of alluvial sand and gravels. The gravels to sand ratio increases progressively with depth to reach at the bottom a zone of clean pebbles frequently more than 0.2 m in diameter. This third layer contains the main mostly unconfined alluvial aquifer. The groundwater table is located approximately 3.2 m below land surface when not artificially disturbed. The annual fluctuation of the water level in the aquifer is approximately 0.5 m with the highest levels observed during the month of January. Below the alluvial deposits, low permeability carboniferous shale and sandstone formations are considered as the basement of the alluvial aquifer.



The test site is located between the Albert Canal and the Meuse River. The alluvial aquifer is recharged with water by direct infiltration of rainfall but also from the Albert Canal which basement is not perfectly impervious. The Meuse River imposes the base hydraulic head and constitutes the outflow for the alluvial aquifer. The topography of the site is almost flat and the natural hydraulic gradient in the alluvial aquifer is on the order of 0.06 % directed toward the north-east. Pumping and tracer tests performed in 1999 (Brouyère, 2001; Brouyère, 2003) showed a mean hydraulic conductivity for the alluvial aquifer ranging from 2×10^{-2} m/s to 7×10^{-2} m/s, a longitudinal dispersivity ranging between 0.5 to 5 m and an effective porosity from 4 to 8 %. The groundwater flux measured under natural flow conditions is around 52 m/day in the lower part of the aquifer and around 0.35 m/day in the upper part of the aquifer.

The experimental site includes 1 pumping well and 18 piezometers in total. The pumping well is 0.152 m of internal diameter and is screened from 3 to 9.5 m depth. Six piezometers were installed during the years 1980's. They are equipped with PVC tubes of 0.05 m in diameter and screened within the alluvial gravels. More recently (June 2012), twelve new piezometers were specifically drilled for the purpose of this research. They are located upgradient from the pumping well and organized as three transverse control planes across the main groundwater flow direction, at respective distances of 17, 12 and 5 m from the pumping well. Laterally, the piezometers are separated of approximately 1m. An injection piezometer is also implanted 20 m upgradient the pumping well. Nine of the new piezometers are double-screened with a 2 m lower screen level set at the bottom of the aquifer between 8 and 10 m depth and an upper screen level placed between 5 and 6 m depth. The most upgradient injection piezometer and two lateral piezometers from the second (central) transverse control plane are fully screened from 3 to 10 m depth. Fully screened piezometers were used to monitor the experiment with cross borehole electrical resistivity tomography.

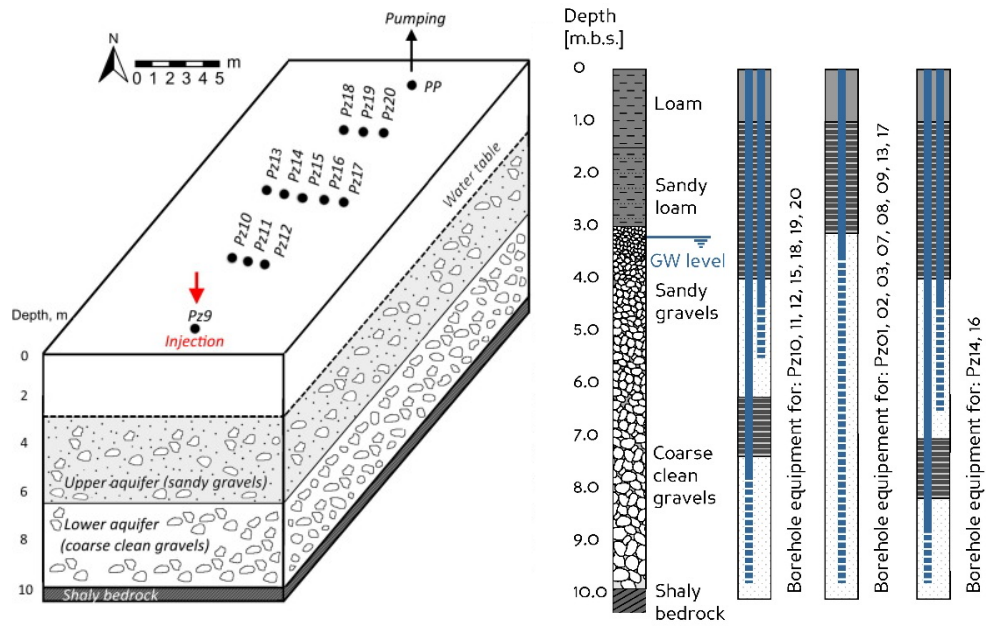


Figure 3: piezometers equipment.

Table 1: Well Characteristics

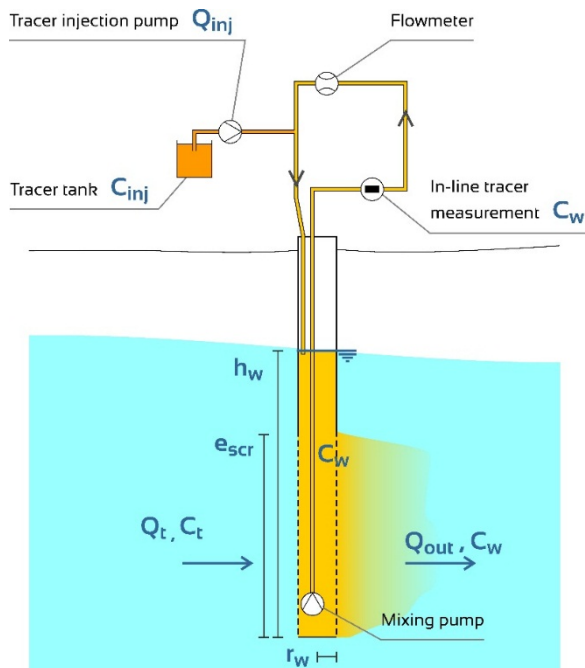
Name	X Lambert 72 [m]	Y Lambert 72 [m]	Z internal tubing [m asl]	Distance from PP [m]	Diameter internal tubing [mm]	Top filter depth [m bgs]	Bottom filter depth [m bgs]
PP	242671.37	157150.14	56.628	0.000	150	3	10
Pz2	242663.64	157156.97	56.597	10.315	50	3	10
Pz7	242683.99	157174.69	56.034	27.604	50	3	10
Pz8	242694.19	157197.27	55.817	52.364	50	3	10
Pz9	242657.06	157136.29	56.594	19.915	50	3	10
Pz10 - shallow	242658.97	157138.67	56.59	16.891	50	4.8	5.8
Pz10 - deep	242658.97	157138.67	56.589	16.891	50	8	10
Pz11 - shallow	242659.4	157138.2	56.597	16.907	50	4.7	5.7
Pz11 - deep	242659.4	157138.2	56.588	16.907	50	8.1	10.1
Pz12 - shallow	242659.68	157137.88	56.554	16.940	50	4.9	5.9
Pz12 - deep	242659.68	157137.88	56.508	16.940	50	8.1	10.1
Pz13	242661.62	157143.21	56.542	11.962	50	3.1	9.6
Pz14 - shallow	242662.27	157142.34	56.443	11.985	50	4	6
Pz14 - deep	242662.27	157142.34	56.467	11.985	50	8.3	9.3
Pz15 - shallow	242662.92	157141.59	56.442	12.021	50	4.5	5.5
Pz15 - deep	242662.92	157141.59	56.431	12.021	50	7.8	9.8
Pz16 - shallow	242663.75	157140.81	56.412	12.046	50	4.9	6.9
Pz16 - deep	242663.75	157140.81	56.403	12.046	50	8.5	9.5
Pz17	242664.36	157140.11	56.411	12.237	50	2.9	9.4
Pz18 - shallow	242668.02	157146.91	56.491	4.654	50	4.6	5.6
Pz18 - deep	242668.02	157146.91	56.488	4.654	50	8	10
Pz19 - shallow	242668.59	157145.82	56.43	5.137	50	4.7	5.7
Pz19 - deep	242668.59	157145.82	56.419	5.137	50	7.7	9.7
Pz20 - shallow	242669.37	157145.19	56.44	5.339	50	4.2	5.2
Pz20 - deep	242669.37	157145.19	56.44	5.339	50	7.8	9.8

2.5 FINITE VOLUME POINT DILUTION METHOD TO MEASURE GROUNDWATER FLUX ON HERMALLE-SOUS-ARGENTEAU EXPERIMENTAL TEST SITE (PIERRE JAMIN)

The aim of the fieldwork is to calculate the mass discharge of selected solute in an aquifer through different type of measurements. Since groundwater flow is the vector that transports the solutes in aquifers, it is essential to have an accurate and precise measurement of the Darcy flux at the location where the mass discharge has to be calculated. To reach this objective, the FVPDM will be used to perform a direct measurement of groundwater flux at two piezometers located in the experimental test site of Hermalle-sous-Argenteau.

The Finite Volume Point Dilution Method

The aim of a single borehole dilution test is to perform a direct measurement of groundwater fluxes. Point dilution methods (PDM) relate the concentration evolution of a tracer previously injected in a borehole as a function of the intensity of groundwater flow through the screen of the borehole. The result of such test is a groundwater flux, which depends on the hydraulic conditions within the geological formation and in the vicinity of the tested borehole. Since the first use of PDM in 1916, many PDM configurations have been tested, including experiments which uses inflatable packers to limit the vertical extension of the investigated zone. The tracer can be salt species, fluorescent dyes or radio isotopes.



The Finite Volume Point Dilution Method (FVPDM) generalizes the PDM to more advanced tracer injection scenarios. The FVPDM is performed by continuously injecting a tracer fluid into a well and monitoring the evolution of the tracer concentration into the same well. During all the experiment, the water column within this well is mixed to ensure a homogeneous repartition of the tracer mass. This method is originally based on a mathematical and a numerical model of tracer injection into a well, considered as a mass balance of the injection of tracer fluid and transit groundwater flow passing through the well screen. An analytical solution obtained from this model (Equation 1) was further applied as a single well tracer technique, enabling an accurate estimation of Darcy fluxes.

Figure 4 : FVPDM experimental setup. The water volume within the well is constantly mixed using a pump and circulated to the surface, where tracer is injected using a dosing pump. Concentration of tracer in the loop is monitored using a field fluorometer placed in the line.

$$C_w(t) = \frac{Q_{inj} \times C_{inj} - (Q_{inj} \times C_{inj} - Q_{out} \times C_{w,0}) \times e^{-\frac{Q_{out}}{V_w} \times (t-t_0)}}{Q_{out}} \quad \text{with} \quad Q_{out} = Q_{inj} + Q_t \quad (1)$$

The tracer concentration within the well $C_w(t)$ [ML-3] can be calculated at each time t [T] using the parameters defined by the experimental setup C_{inj} [ML-3] the tracer concentration in the injection solution, $C_{w,0}$ [ML-3] the tracer concentration within the well at initial time t_0 [T], Q_{inj} [L3T-1] the tracer fluid injection flow rate and V_w [L3] the volume of water in the injection well, assumed to be constant. Q_{out} [L3T-1], the flow rate leaving the well through the screen, carrying tracer at concentration C_w and representing the sum of Q_{in} and Q_t [L3T-1] the transit flow rate intercepted by the well screen. As for other single well tracer dilution techniques, the FVPDM allows for the calculation of an apparent Darcy flux (q_D) [LT-1], which depends on the well characteristics. The apparent Darcy flux q_D is calculated using the transit flow rate (Q_t), which is measured during the FVPDM test and divided by the flowing section (S_w) [L²] perpendicular to the groundwater flow (Equation 2) equal to the well screen length (es_{scr}) [L] and multiplied by the well diameter ($2r_w$) [L].

$$q_D = \frac{Q_t}{S_w} = \frac{Q_t}{2r_w es_{scr}} \quad (2)$$

Finally, the mixing volume can be estimated using the geometric properties of the tested well and of the circulation loop as detailed in Equation 3.

$$V_w = \pi r_w^2 (D_{well} - D_{gwt}) + \pi r_{loop}^2 L_{loop} \quad (3)$$

Where r_w is the radius of the circulation loop, D_{well} the total depth of the tested well, D_{gwt} the depth of the groundwater table, r_{loop} the radius of the circulation loop and L_{loop} the length of the circulation loop.

Note that the dimensioning of a FVPDM experiment required an a priori estimation of a critical injection rate Q_{cr} [L3T-1] (Equation 4). If the tracer injection flow rate Q_{inj} exceeds Q_{cr} , it induces a hydraulic loading of the well, which completely cancels the transit flow rate, making the experiment invalid.

$$Q_{cr} = \pi Q_t \quad (4)$$

During the experiment, the tracer concentration first increases in the injection well, until reaching a plateau when steady state conditions are observed between the rate of tracer injection and the rate of tracer that is carried out of the well by the groundwater flow. The experiment can thus be divided into three phases (Figure 5). The first phase corresponds to transient concentrations and its duration is a function of the mixing volume V_w and the transit flow rate Q_t . The steady state conditions are reached faster if the mixing volume is small and the transit flow rate is high. The second phase begins when the concentration C_w in the well has stabilized, corresponding to steady state conditions. At this moment, C_w only depends on the tracer injection flow rate and on the transit flow rate (Equation 5). As a consequence, the interpretation of a FVPDM test consists in (1) calculating the transit flow rate from the steady state C_w and (2) in adjusting the mixing volume (V_w) to fit the transient phase of the experiment. Allowing the system to reach this steady state strongly increases the precision of the FVPDM interpretation because the two unknown parameters of the FVPDM equation (V_w and Q_t) can be determined independently on different parts of the experimental curve. At the end of the experiment, the injection of tracer is stopped and this last phase corresponds to a classical dilution.

$$C_{w,stab} = C_{inj} \frac{Q_{inj} + Q_t}{Q_{inj}} \quad (5)$$

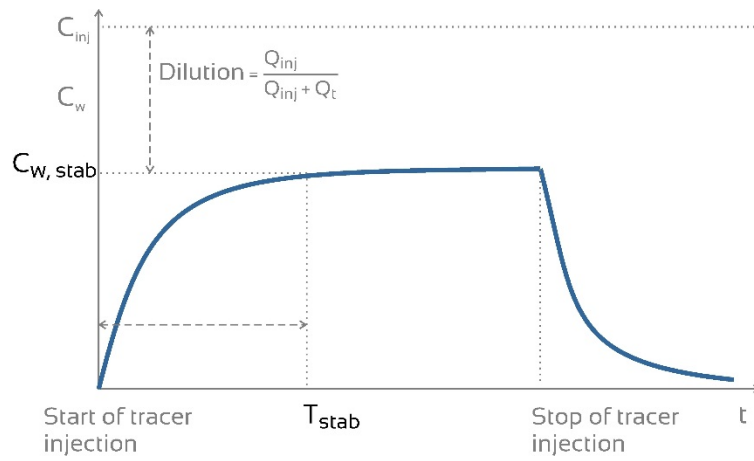


Figure 5 : Typical temporal evolution of tracer concentration in a well, which is tested by FVPDM.

Application of the FVPDM on the field

You will use the FVPDM method to measure the Darcy flux in piezometers of the HssA test site. To do so, you will follow these steps:

1) Based on the available data, you will dimension an FVPDM experiment; i.e. define the injection flow rate (Q_{inj}) and injection time (T_{inj}) according to the dimensioning flow chart available in Brouyère et al. 2008 (see below) and considering an tracer injection concentration (C_{inj}) of 5000 ppb.

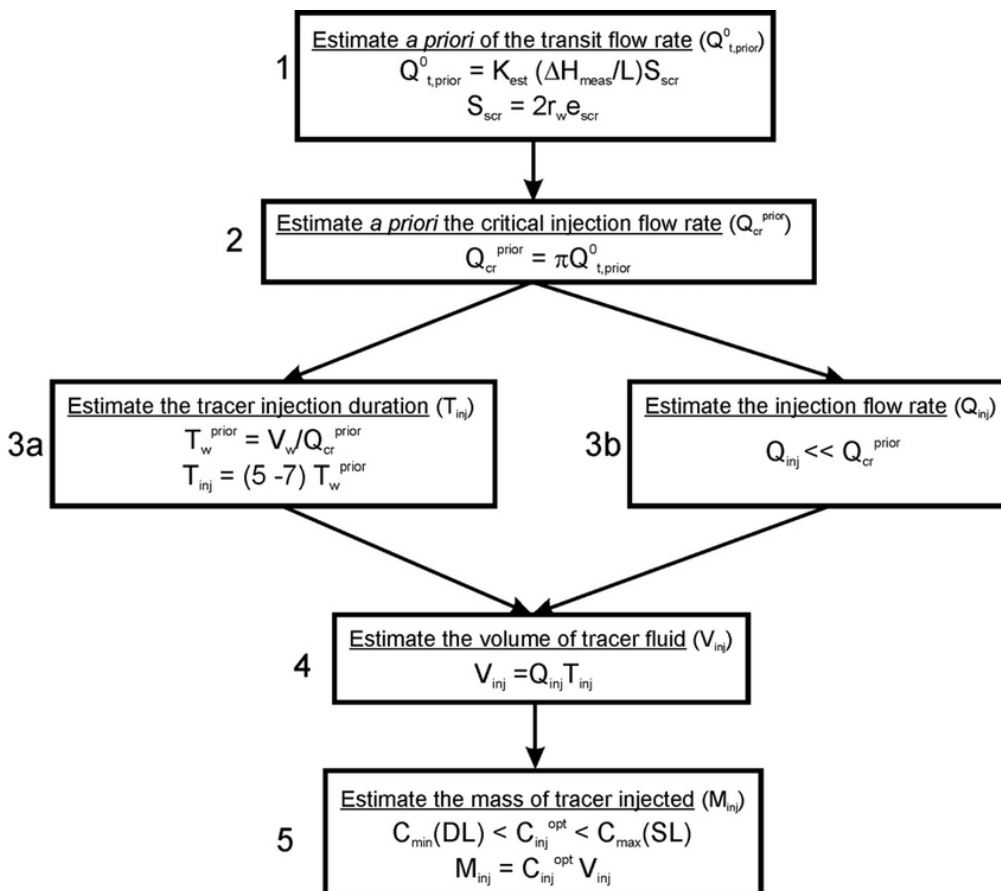


Figure 6: Flowchart for the definition of the optimal FVPDM injection profile

2) You will install the experimental setup in the piezometer to be tested, verify and calibrate the injection flow rate (Q_{inj}) and the circulation flow rate (Q_{mix}) to perform the FVPDM experiment. During the experiment, you will check regularly the tracer concentration in the tested well thanks to direct in situ measurements and take the appropriate decisions to ensure a successful test.

On Friday 09/03 you will interpret the results obtained. More information of the FVPDM method and heat tracer tests is given in chapter 4.

Table 2: Field document

Well parameters			
Borehole depth (m)			
Water column h_w (m)			
Well radius r_w (m)			
Well Volume V_w (m ³)			
Screen length e_{scr} (m)			

FVPDM dimensioning			
q_D prior mean (m s ⁻¹)			
Flow surface S_w (m ²)			
Estimated Q_{t_prior} (m ³ s ⁻¹)			
Estimated Q_{cr} (m ³ s ⁻¹)			
Q_{inj} (m ³ s ⁻¹)			
T_{inj} (s)			
V_{inj} (m ³)			
M_{inj} (mg) for C_{inj} 5000 ppb			

Field notes			
Start injection (time)			
C_{inj} (ppb)			
Q_{inj} (mL min ⁻¹)			
Q_{rec} (L min ⁻¹)			
Fluorometer serial 211 or 814			

Table 3: HssA – Major ions

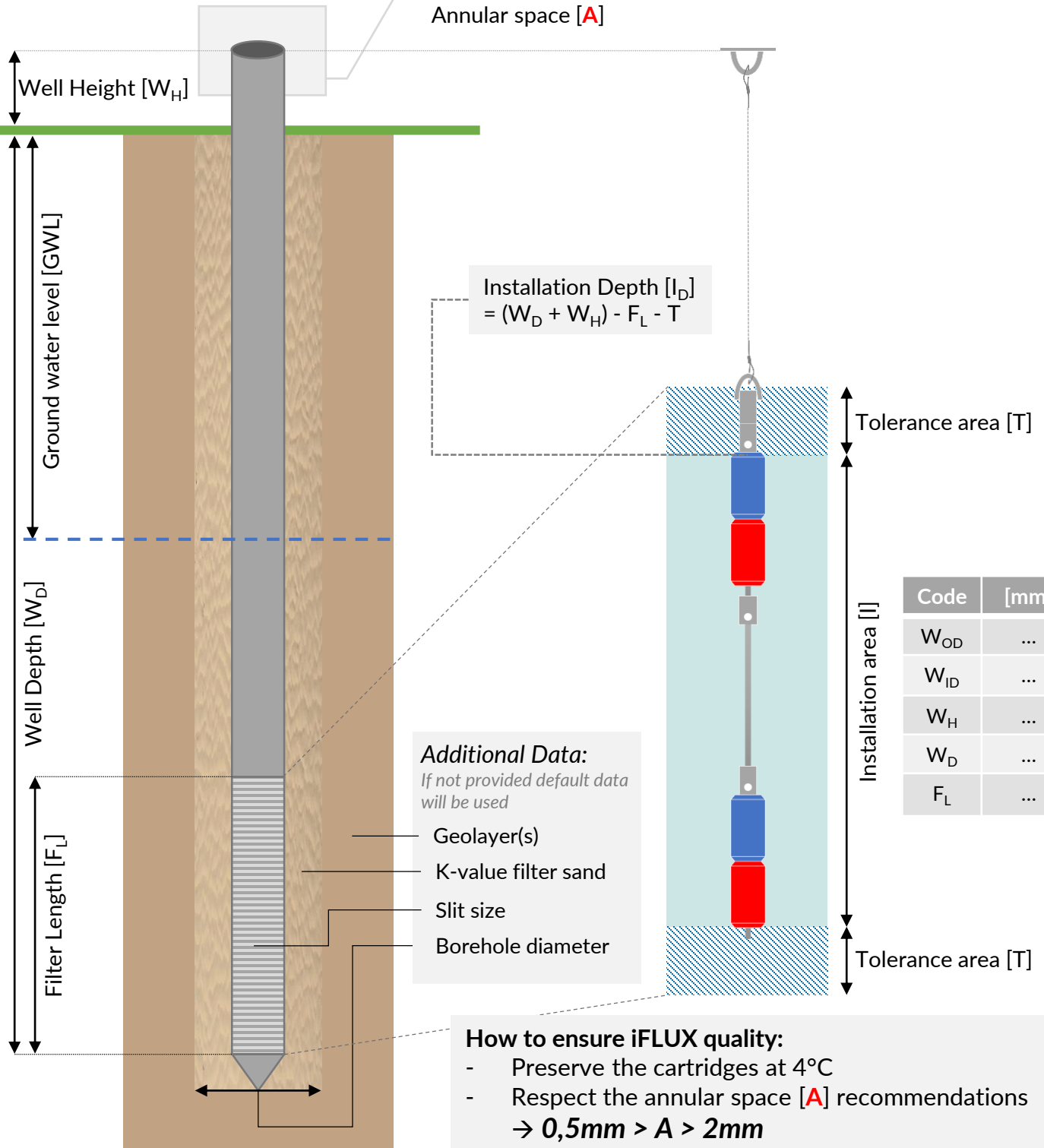
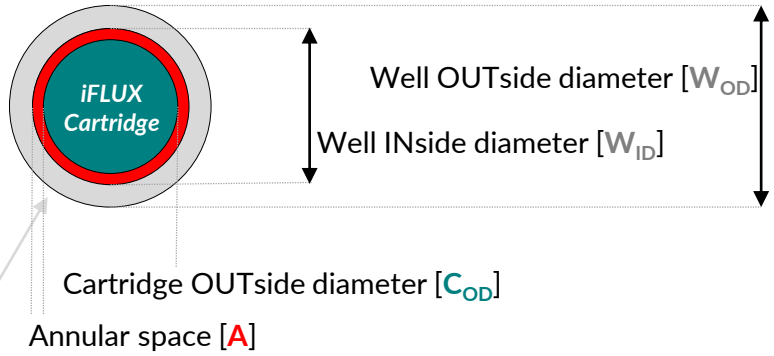
A L'ATTENTION DE :		PROJECT : Inspiration Workshop			JOB772	DATE : 8/03/2018					
Computer reference Sample ID Remarks		D7626 Puits Pompe	D7627 Pz 11 Sup	D7628 Pz 11 Prof	Computer reference Sample ID Remarks		D7626 Puits Pompe	D7627 Pz 11 Sup	D7628 Pz 11 Prof		
Conductivity @ 25°C	µS/cm	POT	760,3	760,3	756,8	← carbonates					
Resistivity @ 25°C	Ω.cm		1315,3	1315,3	1321,4	OH ⁻	mg/L	CAL	0,00	0,01	0,00
Temperature	°C	POT	20,7	20,7	20,9	CO ₃ ²⁻	mg/L	CAL	0,45	0,49	0,47
pH		POT	7,44	7,47	7,46		meq/L		0,01	0,01	0,01
pHs (de saturation)		CAL	7,07	7,1	7,1	HCO ₃ ⁻	mg/L	CAL	299,18	300,33	296,70
LANGELIER's index		CAL	0,37	0,4	0,4		meq/L		4,90	4,92	4,86
Caractère			CACO ₃ ∇	CACO ₃ ∇	CACO ₃ ∇	CO ₂ libre	mg/L	CAL	7,60	7,12	7,20
total hardness	°f	CAL	31,8	31,4	31,5	SiO ₂	mg/L	AA	15,23	17,46	15,96
permanent hardness	°f	CAL	7,2	6,7	7,1	Cations total	meq/L		8,14	8,15	8,07
temporary hardness	°f	CAL	24,6	24,7	24,4	Anions total	meq/L		8,09	8,11	7,97
TA	°f	CAL	0,0	0,0	0,0						
TAC	°f	TIT	24,6	24,7	24,4						
CATIONS											
Ca ²⁺	mg/L	TIT	108,78	107,61	107,66						
	meq/L		5,43	5,37	5,37						
Fe ³⁺ soluble	mg/L	AA	0,07	0,05	0,07						
	meq/L		0,00	0,00	0,00						
Fer total	mg/L	AA	0,07	0,05	0,07						
K ⁺	mg/L	CIA	4,18	3,79	3,89						
	meq/L		0,11	0,10	0,10						
Mg ²⁺	mg/L	CIA	11,41	10,98	11,30						
	meq/L		0,94	0,90	0,93						
Mn ²⁺ soluble	mg/L	AA	0,00	0,00	0,00						
	meq/L		0,00	0,00	0,00						
Mn total	mg/L	AA	0,00	0,00	0,00						
Na ⁺	mg/L	CIA	37,25	40,39	37,49						
	meq/L		1,62	1,76	1,63						
NH ₄ ⁺	mg/L	CIA	0,85	0,48	0,76						
	meq/L		0,05	0,03	0,04						
ANIONS											
Br ⁻	mg/L	CIA	0,00	0,00	0,00						
	meq/L		0,00	0,00	0,00						
Cl ⁻	mg/L	CIA	50,20	50,78	49,48						
	meq/L		1,41	1,43	1,39						
F ⁻	mg/L	CIA	0,00	0,00	0,00						
	meq/L		0,00	0,00	0,00						
H ₂ PO ₄ ⁻	mg/L	CIA	0,00	0,00	0,00						
	meq/L		0,00	0,00	0,00						
NO ₂ ⁻	mg/L	CIA	0,00	0,00	0,00						
	meq/L		0,00	0,00	0,00						
NO ₃ ⁻	mg/L	CIA	16,03	14,98	14,83						
	meq/L		0,26	0,24	0,24						
SO ₄ ²⁻	mg/L	CIA	72,13	72,56	70,60						
	meq/L		1,50	1,51	1,47						

2.6 APPLICATION OF IFLUX SAMPLER – PROSPECTOR

During this exercise both the iFLUX sampler and the prospector will be installed properly and retrieved after a certain exposure time.

CRITICAL WELL INFORMATION

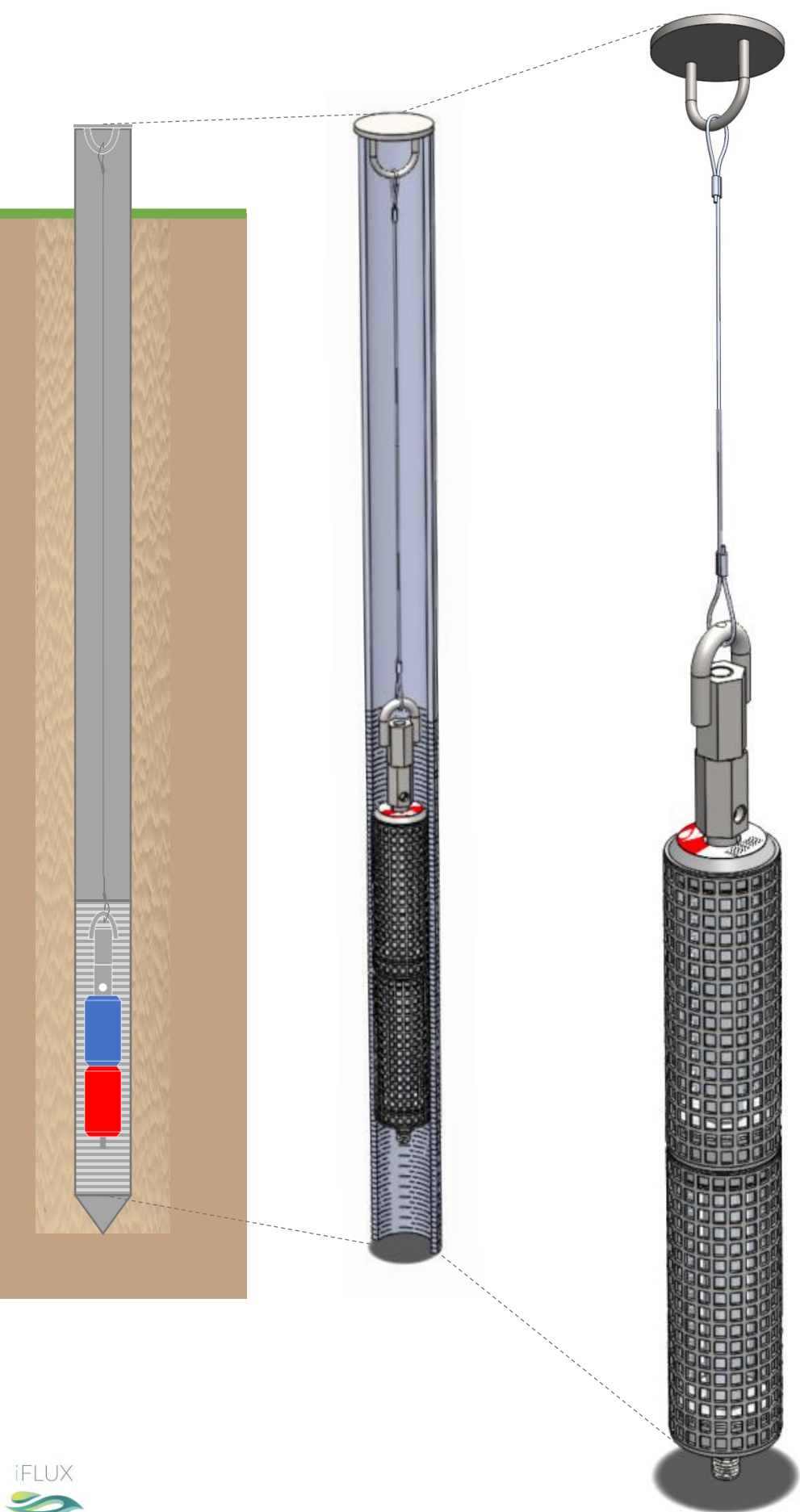
Name: ...
Location: ...



How to ensure iFLUX quality:

- Preserve the cartridges at 4°C
- Respect the annular space [A] recommendations
→ $0,5mm > A > 2mm$
- Don't revise the cartridges
- Provide all needed information (this sheet)

EXAMPLE INSTALLATION



The cable, in combination with the well cap and eyebolt, is preassembled at the right length



Example of the cartridge assembly on the rod with a securing nut.



*Locking pin is used to avoid sudden drop in the well

iFLUX



Install & Retrieval Manual

This booklet provides all the information you need to install and retrieve iFLUX Samplers.



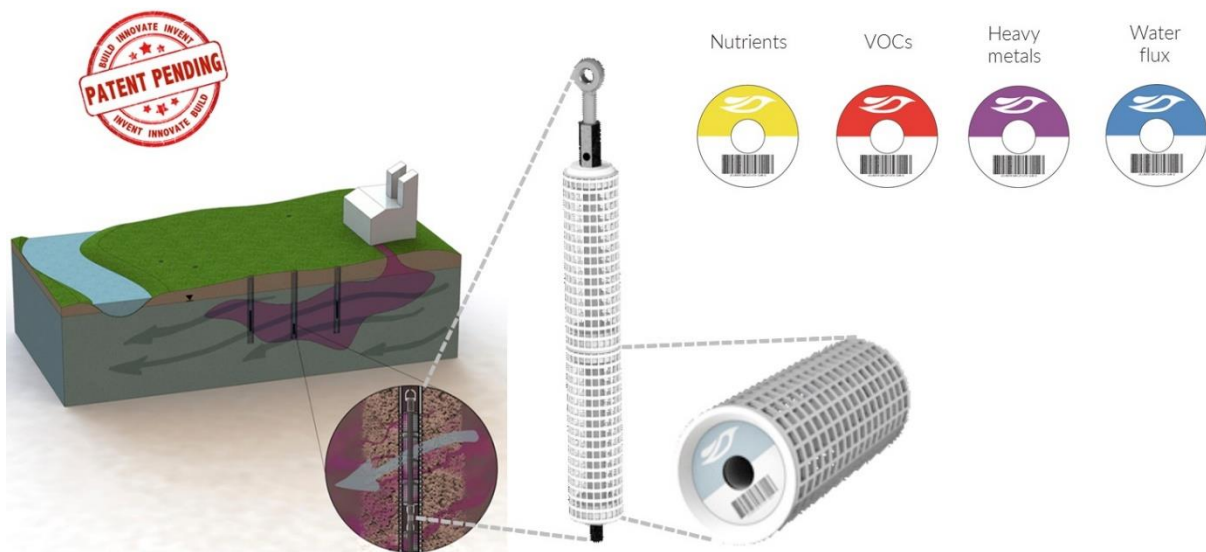
ENVISION WATER IN MOTION

Summary – What is iFLUX?

iFLUX is a new player on the market of measuring techniques, more specifically measurements regarding groundwater and pollution fluxes. Our technology is based and validated through years of research at the university of Antwerp and VITO.

Our product, the iFLUX Sampler, can be composed modularly with different types of cartridges, which makes it possible to measure different pollution groups (nutrients, VOCL's and heavy metals) over a long period of time. The iFLUX Samplers will be typically installed in 63mm wells by attaching them on a stainless steel structure. During a few weeks up till a few months the iFLUX Samplers will stay in the wells to be subsequently analysed in a certificated lab.

Measuring groundwater- and pollution fluxes results in mapping the pollution plume more accurate and reliable, to minimize and optimise remediation procedures.



Workflow – What's the process like?

The first step to conduct a iFLUX measuring campaign is the **monitoring plan**. This is where we will combine our expertise in measuring fluxes and the site characteristics to come up with a plan to accurately map the underground situation on site. The monitoring plan results in a total amount of cartridges, where and at which depths to install them, an installation and retrieval date when the iFLUX Samplers will be installed.

The **on-site installation** of the iFLUX Samplers is the implementation of the monitoring plan; placing the iFLUX Cartridges at the right depth in the well and report following the 'On Site Sheet'. Depending on the size of the project, this takes half a day up to one day.

The **retrieval** of the iFLUX Samplers, where the cartridges are being retrieved, is a double check for the data on the 'On Site Sheet'. Checking the data twice ensures the quality of our iFLUX Report. After the retrieved iFLUX Cartridges are packaged they are sent to SGS, our partnering laboratory, for **analysis**.

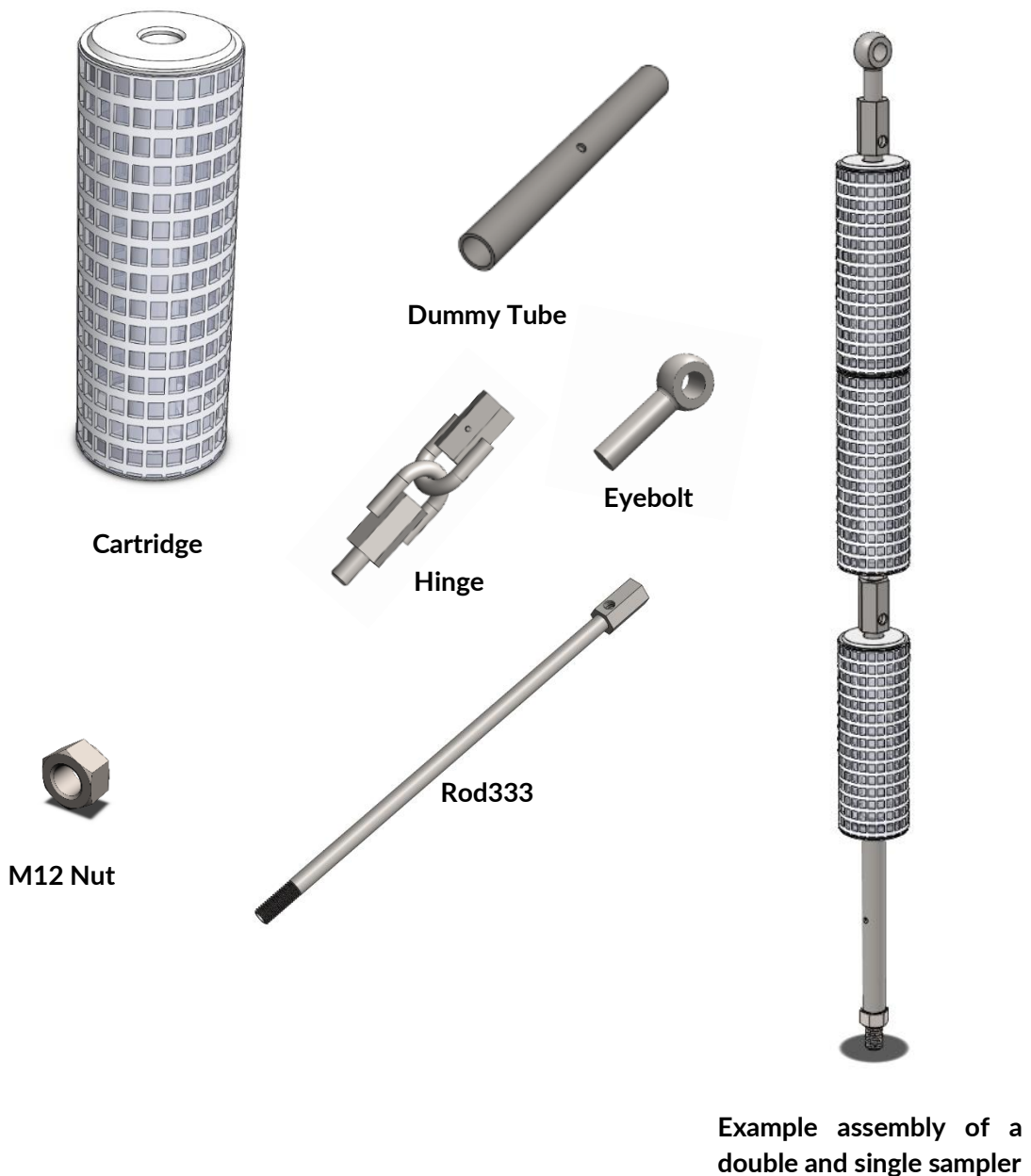
Generating the iFLUX **Report** is the last step of the process. By combining the data of the 'On Site Sheet', the raw analysis data of SGS and our in-house expertise, we generate a final document with the findings. This report will also be deliberated with the client to ensure clear communication.

iFLUX Parts & Tools

The iFLUX Samplers consists the Cartridges that are mounted on stainless steel rods. Each rod can contain two Cartridges, a single Cartridge is possible by using a dummy tube.

When measuring in a multilevel set-up, the rods will also act as spacers between the different Samplers. Hinges every two meters will provide some flexibility to the whole string of rods. The upper Sampler (or rod) will be attached to the well cap via a cable attached to a mounted eyebolt.

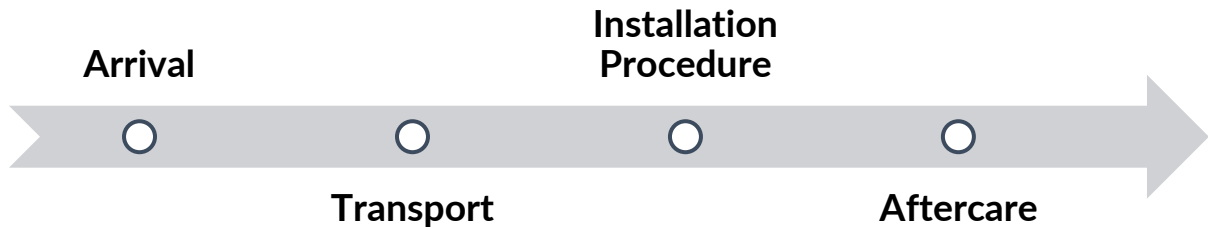
To assemble a Sampler two Cartridges (or one Cartridge and a dummy tube) can be slid onto a Rod and secured by a M12 nut by using a SW19 wrench. More specific information about the install can be found in the next chapter.



Installation

In this part of the booklet the installation of iFLUX Samplers will be thoroughly explained. It is important to install the iFLUX Cartridges correctly, to avoid malfunctions or inadequate measurements.

The installation consists of four main steps. First the arrival on site where safety precautions must be taken and the equipment must be gathered. Next is the transportation to the well, followed by the installation procedure. The last step is the aftercare where the equipment and waste must be managed.



Equipment

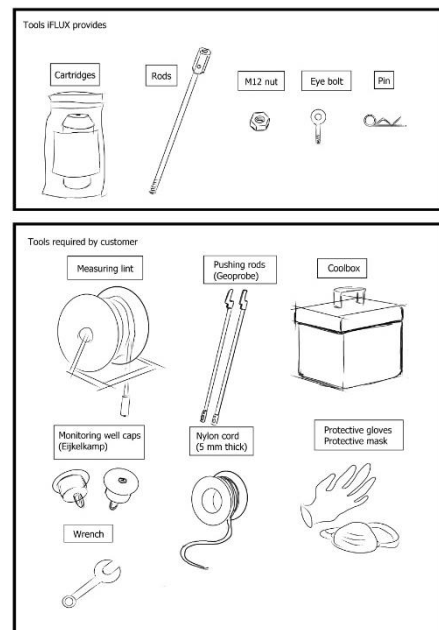
The tools and equipment needed for the installation of iFLUX Cartridge is listed underneath. These tools ease the installation on the one hand, but some of them are indispensable and are must-haves during installation. The equipment list does not take the iFLUX Cartridges in account, as they are project specific.

iFLUX Tools (provided by iFLUX)

- iFLUX Rods333
- iFLUX Rods666
- iFLUX Hinges
- iFLUX Eyebolt
- iFLUX Well Cap
- iFLUX 'on site sheet' + 'installation plan'
- Stainless steel locking pins
- Stainless steel cable + clamps
- Stainless steel M12 nuts

Equipment

- Insulated transport crate (storing the cartridges at a stable temperature)
- Klauke Micro with fully charged battery (or substitute)
- Water level meter
- Push tool (Katimex or substitute)
- Field cart (for transport)
- Measuring tape (min 30m)
- Wrench SW19 (at least 2)
- Toolbox with general tooling as backup tooling
- Waste bin/bag



Waste management is also critical during fieldwork and must be managed carefully; you are working with (potentially) contaminated components. Cross contamination must be avoided at all cause!

Personal protection gear (PBM)

Each person on site has to wear his/hers PBM's, safety is always a priority!



Depending on the site, more severe precautions can be imposed. These site-specific regulations must be followed otherwise the site manager can abort the installation.

1 - Arrival

When arrived on site notify the client, in some cases a safety instruction movie or presentation must be attended in order to get permission to proceed. Additional protective equipment like e.g. an explosion gauge can be provided by the client, depending on the characteristics of the site.

2 - Transport

Off course it is desirable to park your vehicle as near as possible, but keep in mind legal restrictions and terrain characteristics when parking a van or other vehicle.

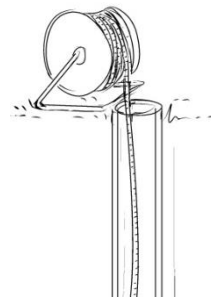
The last part of transporting all the equipment will be done manually, a field cart can ease this job. Keep in mind the restricted areas that are prohibited to access in case of possible danger or health risks.

3 - Installation Procedure

Before starting the installation, check the monitoring plan provided by the iFLUX Monitoring Expert. This document shows how many iFLUX Cartridges must be installed at what depths in which well.

After opening the well (keys must be provided by the client in case of a lock) the first thing to do is measuring the water level and the total depth of the well. Afterwards it is required to clean the apparatus (as dictated in the CMA) to avoid cross contamination. It is important that there are no sharp edges on the well tube, this implies a possible risk of ripping the cartridges and a malfunctioning measurement. To avoid this, deburring is advised!

In case the upper cartridge will not be submerged when installed according to the monitoring plan, contact (call Goedele Verreydt +32 473 83 64 62) the iFLUX Expert; an advisable solution will be provided. Changing the monitoring plan without proper communication towards iFLUX will diminish the quality of the iFLUX Report.

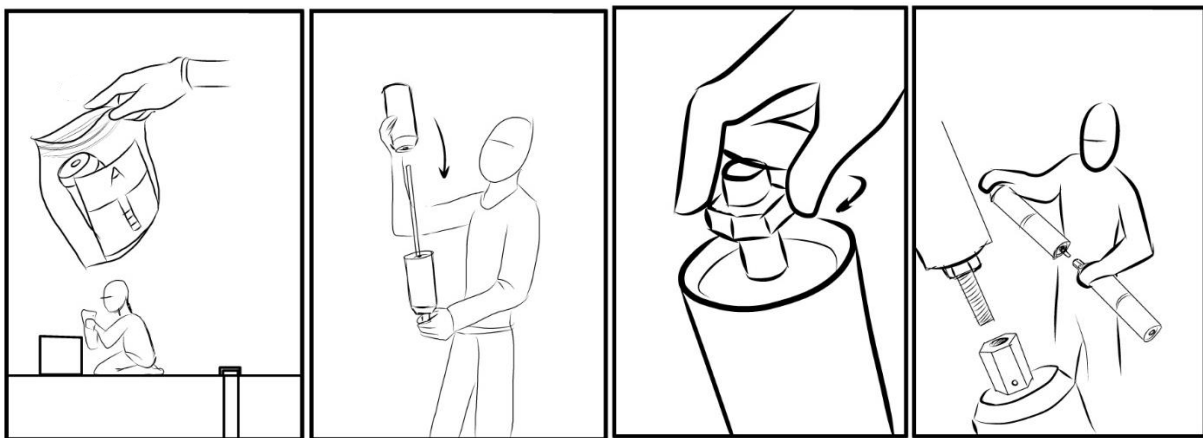


The (stainless steel) cable that suspends the iFLUX Rods and consequently the iFLUX Cartridges must be prepared according to the length mentioned in the monitoring plan. To secure the cable to the eyebolt and Well Cap, it is advisable to use the Klauke Micro crimping tool and its clamps or a comparable apparatus.

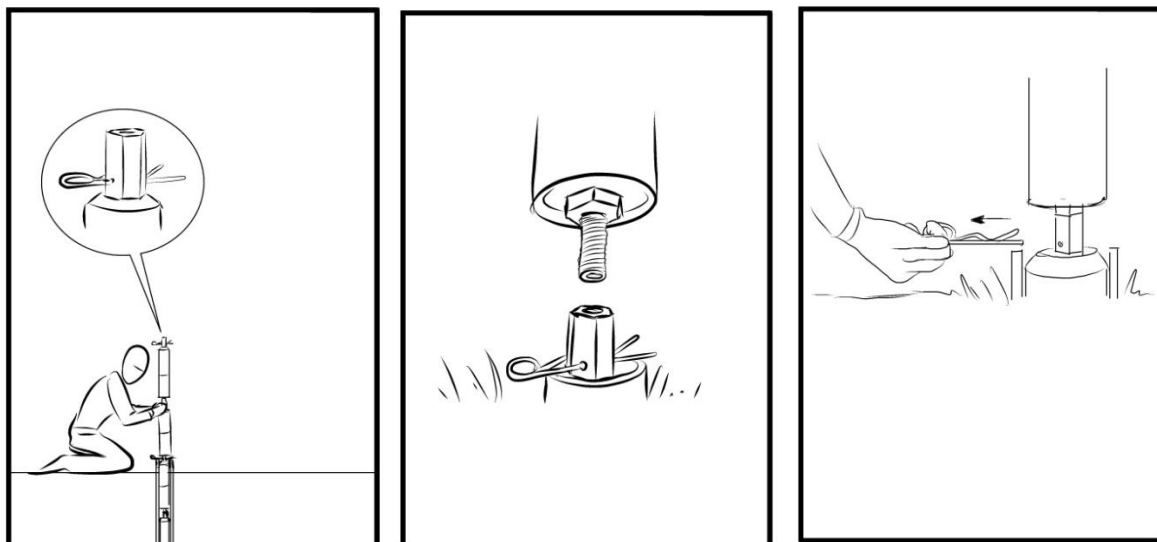


The next step is to put the cartridges onto the iFLUX Rods, starting with the lowest ones. Register the cartridge ID's that were used on the 'On Site Sheet'.

Unpack the iFLUX Cartridges and slide them over the iFLUX Rod333. Secure them by tightening the nut at the lower end of the rod. Attach the next Sampler or Rod following the same procedure, it is not advised to use more than three segments at once to avoid large structures and possible product (structural) failures. The iFLUX Rod666 is only used as an extension rod between Samplers and not for attaching Cartridges.

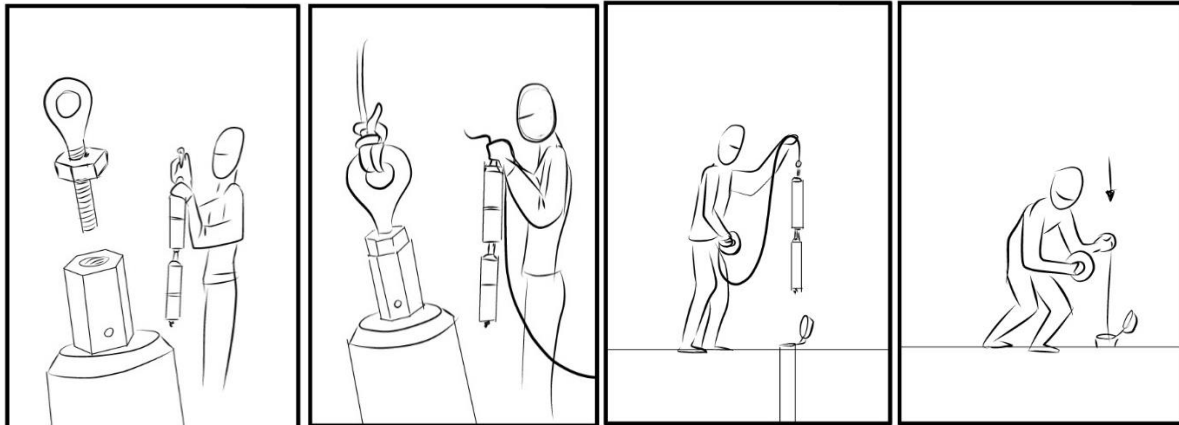


Before lowering the Samplers into the well put the Safety Pin through the drainage hole of the rod, this avoids the Samplers sliding down into the well and potentially losing them. Again watch out for sharp edges on the top of the well, it is favourable to remove them first.

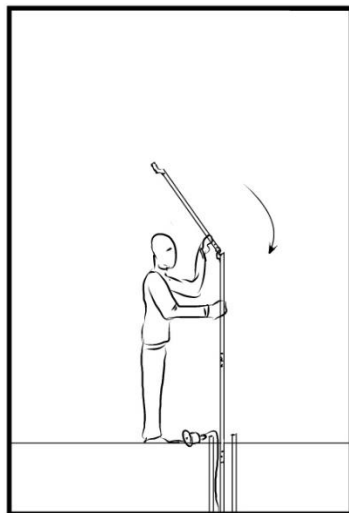


Attach the next iFLUX Sampler or Rods following the previous procedure. Put the safety pin in the upper rod and pull out the safety pin out of the lowest rod and lower the whole structure. It is not advised to use more than three iFLUX Segments to avoid large structures and possible product failures. The monitoring plan will also state where to install the Hinges to allow a more flexible structure in the well.

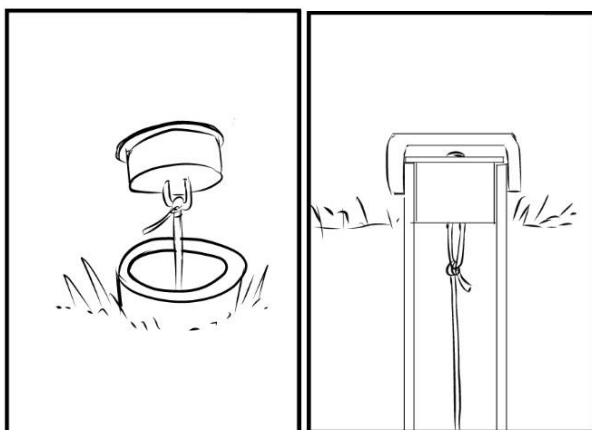
Iterate this process, according to the monitoring plan, until the upper Sampler and eventually the eyebolt with the cable attached is reached.



When having troubles with lowering the iFLUX Samplers, use the push tool or a similar apparatus. This allows you to push down the whole structure in an easy way. When reaching an obstacle, instead of a obstruction, it is wise to pull the string of Samplers back up and lower it again. If other more severe problems occur, contact the iFLUX Expert to find a suitable solution.



The installation is done when the Well Cap reaches the edge of the well and the weight of the iFLUX Samplers is transferred to the Well Cap. Finally the well is sealed by a cap to avoid above ground influences in case the well is exposed.

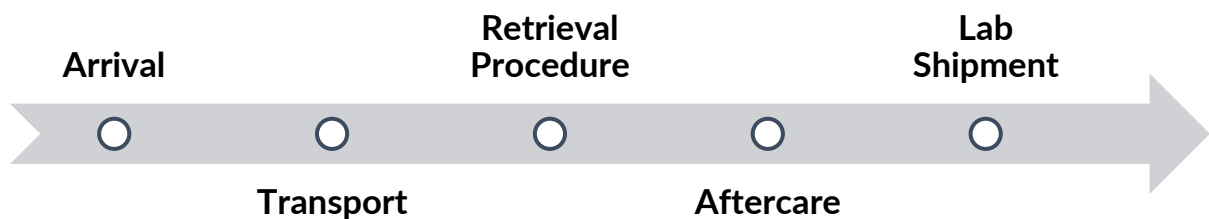


4 - After Care

When the installation of the whole monitoring plan is completed, check whether all data of the 'On Site Sheet' is registered. It is important to gather all the remaining tools and equipment, gather all waste (e.g. packaging) used during the installation and leave the site as it was before.

Retrieval

The sequence of different steps during retrieval is similar to the installation. First the arrival on site, where the monitoring plan has to be checked to verify which cartridges have to be retrieved. Next is the transport and the retrieval procedure itself. Finally the shipment to SGS, our partnering lab, to analyse the cartridges.



Equipment

The tools to retrieve the iFLUX Samplers are a less in amount in comparison to the installation retrieval.

- iFLUX On Site Sheet
- Water level meter
- SW 19 Wrench (at least two)
- Locking pins (at least two)
- Post-measurement Packaging
- Insulated transport crate
- Field cart (for transport)
- Waste Bin

Personal Protection Gear

Analogue to Install procedure you have to wear the appropriate safety gear.



1 - Arrival

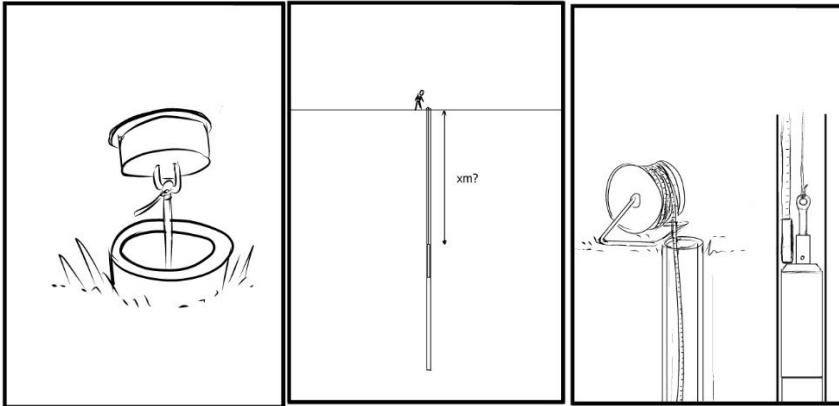
The First thing to do is to verify which iFLUX Cartridges must be retrieved. In accordance with the site manager, the site can be entered. When unfamiliar with the site at retrieval, a safety instruction movie or presentation must be attended in order to get permission to proceed. As of this moment protective gear is indispensable.

2 - Transport

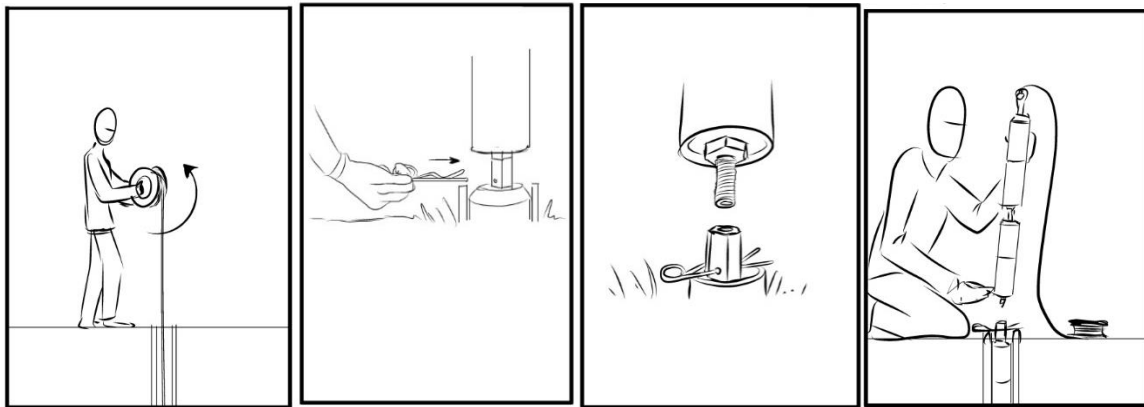
Similar to the installation, transportation must be within the safe or free to access areas on site. A field cart can ease the job.

3 - Retrieval Procedure

When arrived at the well, check the well name/code and verify the water level.



Afterwards take the Well Cap and pull up **GENTLY** the iFLUX Samplers. As the centre tube is limited in diameter this cannot be rushed, hurrying this job can cause product failures and has to be avoided at all cause. Slow and steady does the job.



When the first three segments are retrieved, block the string of sampler with the locking pin before unbolting the rods above. Separate the rods and unfasten the nut, during these tasks verify the sequence of the cartridge ID's and check with the previous filled in 'On Site Sheet'. Store the cartridges (individually) in post-measurement bags as prescribed (to ensure the shipping quality). Eventually collect the packaged cartridges in an insulated crate to store them at a stable temperature.



The remaining iFLUX Parts must be collected to ship back to iFLUX, they will take care of proper cleaning and maintenance for reuse purposes.

4 - Aftercare

When the retrieval of the whole monitoring plan is completed, check whether all data of the 'On Site Sheet' is registered. It is important to gather all the remaining tools and equipment, gather all waste (e.g. packaging) used during the installation and leave the site as it was before.

5 - Shipment

After retrieval the cartridges must be stored in a cool environment, shipment must be done as soon as possible. The cartridges must be packaged in an insulated box, preferably with ice packs, and sent to following address. iFLUX must be notified of these actions.

SGS Nederland BV

Spoorstraat 12 - 4431 NK - 's-Gravenpolder - Holland

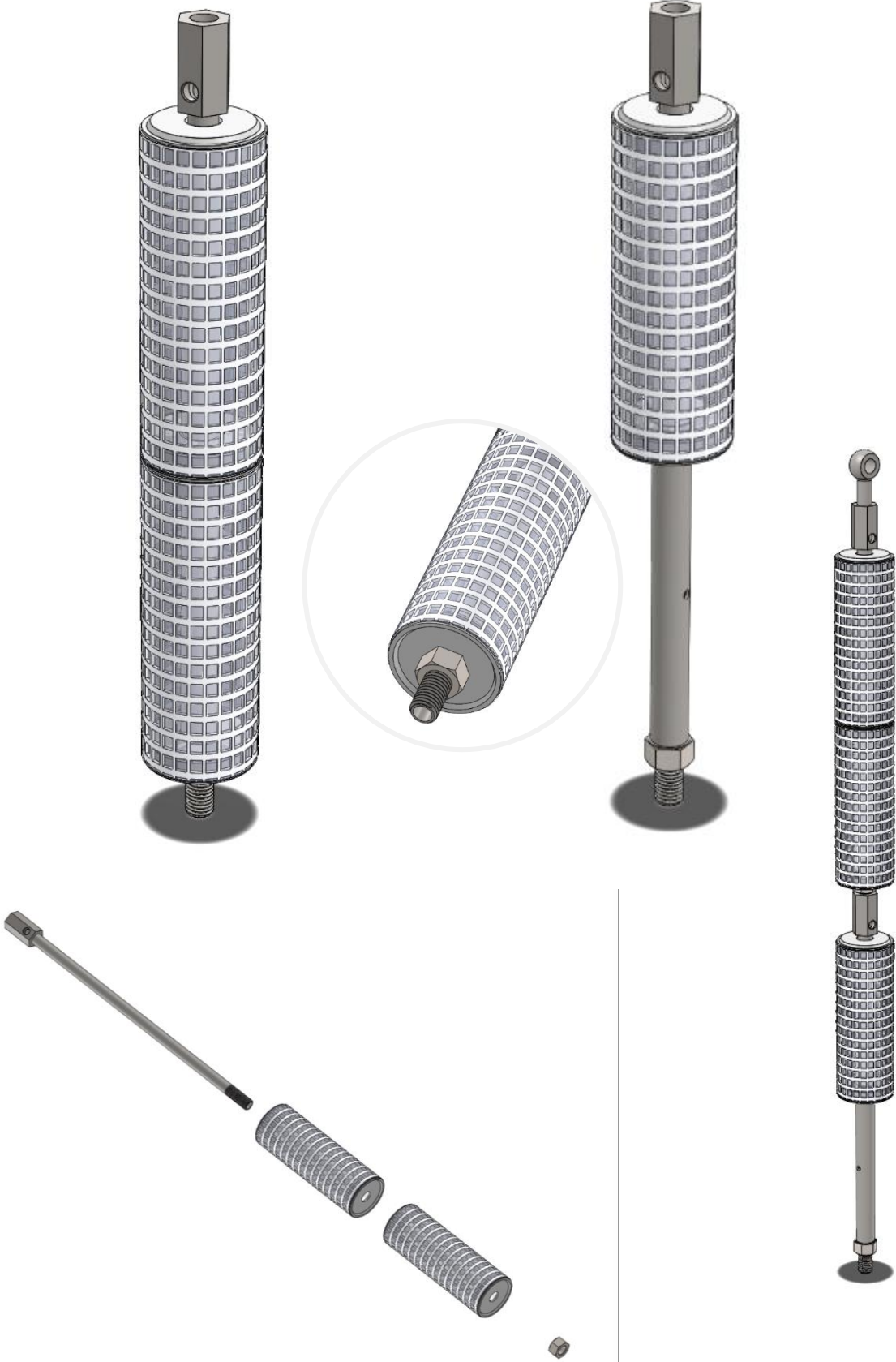
The remaining iFLUX tools must be send back in the same box as you received to following address:

iFLUX, Science Park Antwerp University

Galileilaan 15, 2845 Niel, Belgium

Building Darwin C0.05

Appendix I - Images



Appendix II – Tool list Installation

Listing all the tools in detail needed for the installation of iFLUX Samplers (+ images)

Pending...

Appendix III – Tool list Retrieval

Listing all the tools in detail needed for the retrieval of iFLUX Samplers (+images)

Pending...

2.7 VOLUME BASED & LOW FLOW GROUNDWATER SAMPLING (JOHAN VOS / ILSE VAN KEER)

2.7.1 GOAL

Proper groundwater sampling in function of the research question

2.7.2 MATERIAL

- Centrifugal submersible pump
- Staalnameslang
- Measuring tape
- Flow through cell
- Diver
- Filters
- Handheld pH and oxygen meter
- Handheld conductivity, redox and temperature meter
- Portable turbidity meter
- Portable photometer
- Measure
- vials

2.7.3 WELL CHARACTERISTICS

- Date of installment: 01/06/2012
- No additional water was used during the installment
- Filter depth: cf. table 1
- No sand trap

2.7.3.1 Procedure

- Control measurement depth monitoring well
- Measurement of field parameters
 - Groundwater level
 - pH
 - conductivity
 - dissolved oxygen
 - redox
 - temperature
 - turbidity
- Proper sampling of target analytes:
 - Chlorinated aliphatic hydrocarbons
 - Mineral oil
 - Heavy metals

Sampling groundwater	Well ID	
Well depth (m-bgs)		
Ground water level (m-bgs)		
Well diameter		
Flow rate refreshment		
Flow rate sampling		
Remarks		

Conductivity					
pH					
ORP					
temperature					
O ₂ -concentration					
Turbidity					
Others					

Sampling groundwater	Well ID	
Well depth (m-bgs)		
Ground water level (m-bgs)		
Well diameter		
Flow rate refreshment		
Flow rate sampling		
Remarks		

Conductivity					
pH					
ORP					
temperature					
O ₂ -concentration					
Turbidity					
Others					

3. EVALUATION & DISCUSSION OF FIELD MEASUREMENTS

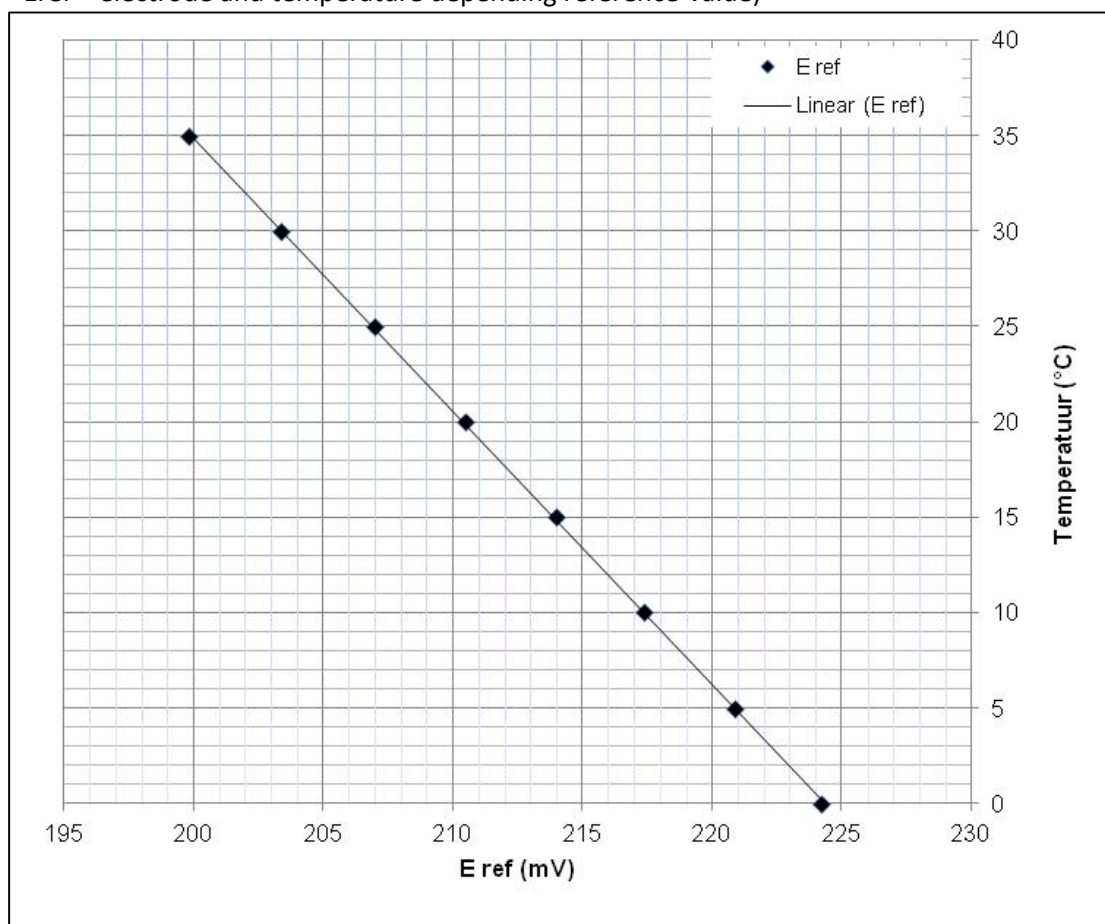
3.1 GROUNDWATER SAMPLING

3.1.1 CORRECTION MEASURED ORP TO H₂-ELECTRODE

The measured ORP needs to be recalculated to a H₂-electrode according to the following formula:

$E_H = E_m + E_{ref}$ with

- E_H = ORP relative to a H₂-electrode
- E_m = ORP measured with an Ag/AgCl(3M)-electrode
- E_{ref} = electrode and temperature depending reference-value)



T (°C)	E _{ref}	T (°C)	E _{ref}	T (°C)	E _{ref}	T (°C)	E _{ref}
0	224,2	25	207	50	188,4	75	167,7
5	220,9	30	203,4	55	184,4	80	163,1
10	217,4	35	199,8	60	180,3	85	158,3
15	214	40	196,1	65	176,4	90	153,3
20	210,5	45	192,3	70	172,1	95	148,1

3.1.2 DIVERS, PROGRAMMING – READ OUT

Demonstration will be given on how to recalculate the raw diver data to barometric compensation.

3.2 EVALUATION FVPDM RESULTS – CALCULATION OF GROUNDWATER FLUX

You have to interpret the result of your experiment, the evolution with time of tracer concentration* in the tested piezometer using a spread sheet where you will code the Equation 1 given below. Knowing the parameters of the experimental setup and by adjusting the mixing volume (V_w) and the Darcy flux (q_D), you will fit the curve calculated by the analytical solution of the FVPDM on the observed curve.

$$C_w(t) = \frac{Q_{inj} \times C_{inj} - (Q_{inj} \times C_{inj} - Q_{out} \times C_{w,0}) \times e^{-\frac{Q_{out}}{V_w} \times (t-t_0)}}{Q_{out}} \quad \text{with } Q_{out} = Q_{inj} + Q_t \quad (1)$$

a) Import the time series from the field fluorometer (tracer single VS time). The signal corresponding the tracer used is from the led F3 (mV). To convert fluorimeter signal in to concentration in ppb, use the calibration coefficient here below according to the fluorimeter you used on the field. Plot the tracer concentration VS time to have a look at the FVPDM curve.

Fluo 814	ppb=3.3685 x mV
Fluo 211	ppb=5.3281 x mV

b) Use the analytical solution (Eq 1) and the experimental parameters (C_{inj}, Q_{inj}) to calculate the theoretical tracer concentration evolution with time that corresponds to the groundwater flow rate (Q_{out}) and the mixing volume (V_w) you estimated for the dimensioning. Plot the resulting curve along with the observations.

c) Adjust manually Q_{out} and V_w to fit the calculated FVPDM curve to the observed tracer concentration and calculate the corresponding Darcy flux (q_D).

$$Q_{out} = Q_{inj} + Q_t \quad \text{and} \quad q_D = Q_t / S_w$$

Interpretation of FVPDM experiment

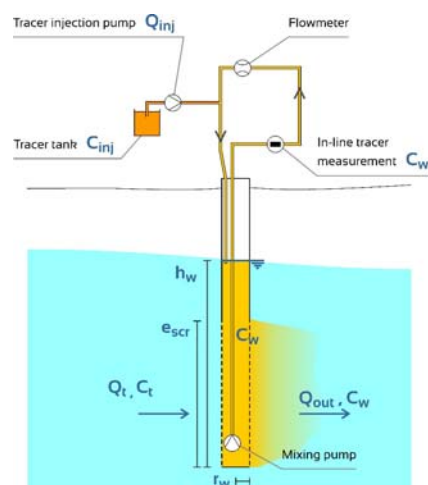


Pierre JAMIN



Setup : Illustration of the terms of
the tracer mass balance equation

- 1 pump for mixing the water column (not needed for the calculation of Darcy's flux)
- 1 pump to inject the tracer at a flow rate Q_{inj} and at a concentration C_{inj}

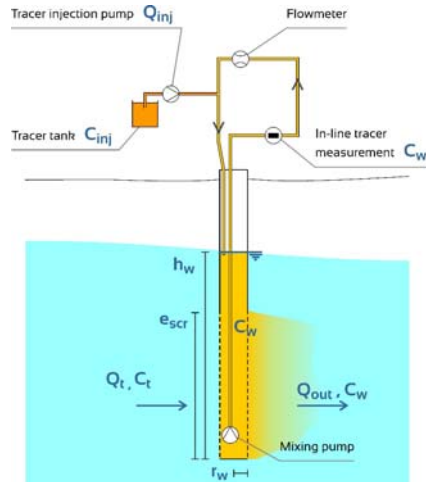


Interpretation : Analytical solution of the tracer mass balance equation

$$C_w(t) = \frac{Q_{inj} \times C_{inj} - (Q_{inj} \times C_{inj} - Q_{out} \times C_{w,0}) \times e^{-\frac{Q_{out}}{V_w} \times (t-t_0)}}{Q_{out}} \quad \text{with } Q_{out} = Q_{inj} + Q_t$$

Parameters from the experimental setup :

- C_{inj}
- Q_{inj}
- $C_{w,0}$



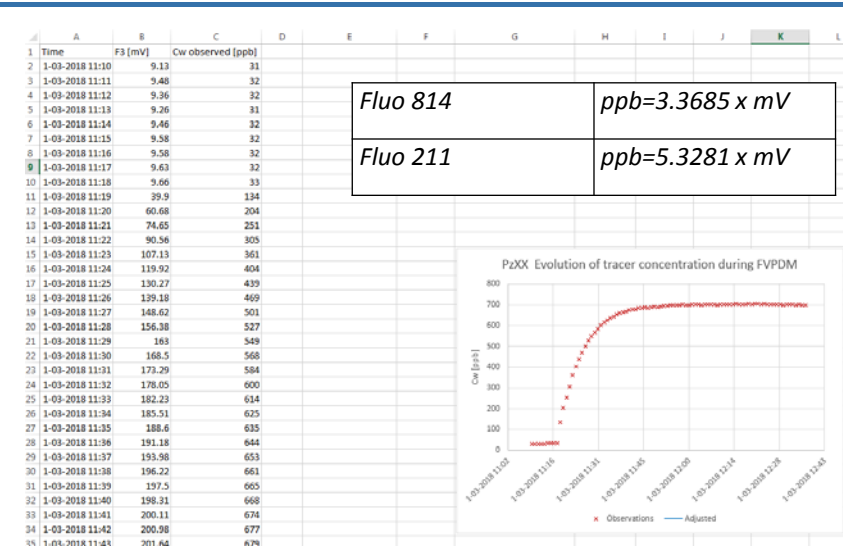
Parameters to be adjusted :

- Q_{out}
- V_w

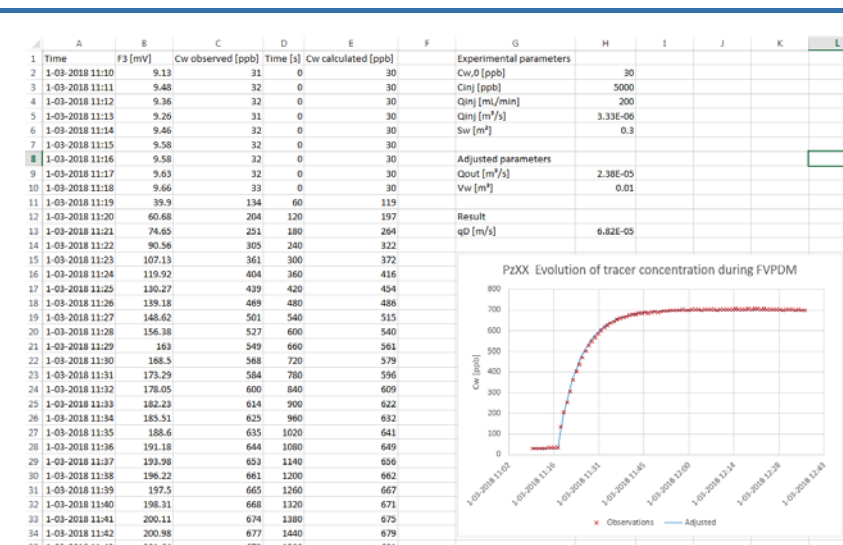
Importation of the time series : Time + F3 signal

	A	B	C	D	E	F	G	H
1	Timestamp	Timestamp	T [°C]	F1 [mV]	F2 [mV]	F3 [mV]	F4 [mV]	Vbat [V]
2	Thu 2018-03-01 11:10:00 GMT+00:00	1519902600	8.42	18.41	9.05	9.13	383.63	12.13
3	Thu 2018-03-01 11:11:00 GMT+00:00	1519902660	8.5	18.12	8.17	9.48	312	12.13
4	Thu 2018-03-01 11:12:00 GMT+00:00	1519902720	8.57	18.06	9.04	9.36	296.03	12.14
5	Thu 2018-03-01 11:13:00 GMT+00:00	1519902780	8.63	17.71	17.53	9.26	309.69	12.14
6	Thu 2018-03-01 11:14:00 GMT+00:00	1519902840	8.69	17.34	20.49	9.46	267.94	12.13
7	Thu 2018-03-01 11:15:00 GMT+00:00	1519902900	8.74	16.99	8.9	9.58	253.36	12.13
8	Thu 2018-03-01 11:16:00 GMT+00:00	1519902960	8.79	16.76	7.74	9.58	227.31	12.14
9	Thu 2018-03-01 11:17:00 GMT+00:00	1519903020	8.83	16.54	7.85	9.63	209.35	12.13
10	Thu 2018-03-01 11:18:00 GMT+00:00	1519903080	8.87	16.25	9.34	9.66	193.05	12.13
11	Thu 2018-03-01 11:19:00 GMT+00:00	1519903140	8.89	16.15	12.81	39.9	193.74	12.13
12	Thu 2018-03-01 11:20:00 GMT+00:00	1519903200	8.91	15.9	8.57	60.68	179.89	12.13
13	Thu 2018-03-01 11:21:00 GMT+00:00	1519903260	8.93	15.73	7.21	74.65	176.14	12.13
14	Thu 2018-03-01 11:22:00 GMT+00:00	1519903320	8.96	15.49	7.27	90.56	167.5	12.13
15	Thu 2018-03-01 11:23:00 GMT+00:00	1519903380	8.98	15.51	7.23	107.13	148.17	12.13
16	Thu 2018-03-01 11:24:00 GMT+00:00	1519903440	9	15.3	9.81	119.92	144.71	12.13
17	Thu 2018-03-01 11:25:00 GMT+00:00	1519903500	9.02	15.23	11.85	130.27	135.58	12.13
18	Thu 2018-03-01 11:26:00 GMT+00:00	1519903560	9.03	15.14	6.99	139.18	131.55	12.13
19	Thu 2018-03-01 11:27:00 GMT+00:00	1519903620	9.04	15.04	6.77	148.62	124.46	12.13
20	Thu 2018-03-01 11:28:00 GMT+00:00	1519903680	9.05	15.04	6	156.38	120.78	12.13
21	Thu 2018-03-01 11:29:00 GMT+00:00	1519903740	9.07	14.95	9.57	163	120.64	12.13
22	Thu 2018-03-01 11:30:00 GMT+00:00	1519903800	9.08	14.87	8.34	168.5	119.15	12.11
23	Thu 2018-03-01 11:31:00 GMT+00:00	1519903860	9.09	14.79	6.9	173.29	115.07	12.11
24	Thu 2018-03-01 11:32:00 GMT+00:00	1519903920	9.11	14.75	6.59	178.05	110.66	12.13
25	Thu 2018-03-01 11:33:00 GMT+00:00	1519903980	9.12	14.72	6.59	182.23	106.91	12.13
26	Thu 2018-03-01 11:34:00 GMT+00:00	1519904040	9.13	14.68	6.99	185.51	105.6	12.13
27	Thu 2018-03-01 11:35:00 GMT+00:00	1519904100	9.14	14.67	9.52	188.6	103.73	12.13
28	Thu 2018-03-01 11:36:00 GMT+00:00	1519904160	9.15	14.59	7.08	191.18	99.75	12.11
29	Thu 2018-03-01 11:37:00 GMT+00:00	1519904220	9.16	14.57	6.38	193.98	97.89	12.13
30	Thu 2018-03-01 11:38:00 GMT+00:00	1519904280	9.17	14.5	6.34	196.22	98.53	12.13
31	Thu 2018-03-01 11:39:00 GMT+00:00	1519904340	9.18	14.43	6.54	197.5	96.38	12.11
32	Thu 2018-03-01 11:40:00 GMT+00:00	1519904400	9.18	14.53	7.57	198.31	96.63	12.13
33	Thu 2018-03-01 11:41:00 GMT+00:00	1519904460	9.18	14.47	6.8	200.11	97.06	12.13

Convert signal to tracer concentration and plot

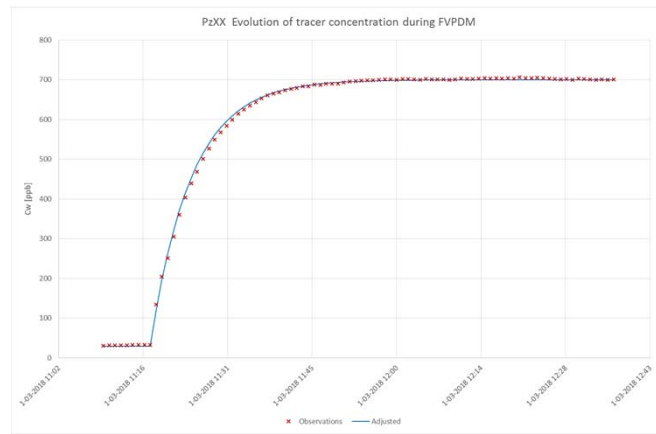


Write FVPDM equation and parameters to model a curve



Adjust Q_{out} , V_w and calculate the corresponding Darcy flux

Manual adjustment of Q_{out} to fit the stabilized C_w value
Manual adjustment of V_w to fit the curvature at the beginning of the tracer injection

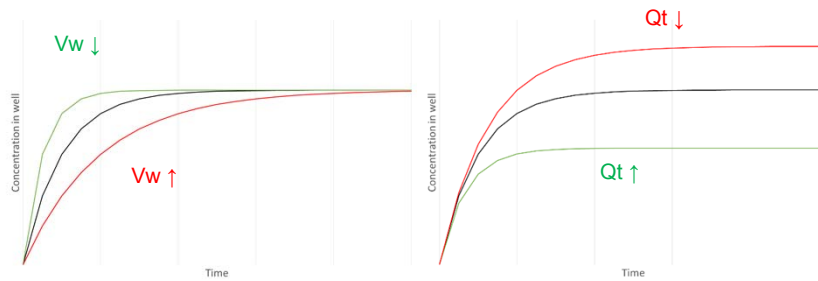


$$Q_{out} = Q_{inj} + Q_t$$

$$q_D = Q_t / S_w$$

Adjust Q_{out} , V_w and calculate the corresponding Darcy flux

Manual adjustment of Q_{out} to fit the stabilized C_w value
Manual adjustment of V_w to fit the curvature at the beginning of the tracer injection



$$Q_{out} = Q_{inj} + Q_t$$

$$q_D = Q_t / S_w$$

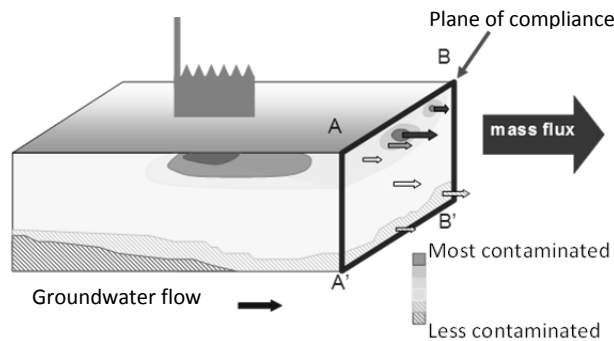
3.3 EVALUATION RESULTS IFLUX – CALCULATION OF MASS FLUXES

CONTAMINANT MASS FLUX

Contaminant mass flux (Eq.1) is defined as the total amount of contaminant, expressed as mass, passing per unit area per unit time through a well-defined control plane or plane of compliance that is orthogonal to the mean groundwater flow direction.

$$J_c = C.v = \frac{m}{A.t} \quad (2)$$

where J_c is the contaminant mass flux [$\text{g m}^{-2} \text{day}^{-1}$], C is the mean concentration of the contaminant in the groundwater [g m^{-3}], v is the Darcy groundwater flux [$\text{m}^3 \text{m}^{-2} \text{day}^{-1}$], m is the mass of contaminant [g], A is a well-defined plane of compliance ($AA'B'B$), orthogonal to the groundwater flow direction [m^2] and t is the time [day]. Figure 1 shows the concepts of a contaminant flux at a plane of compliance between source and receptor.



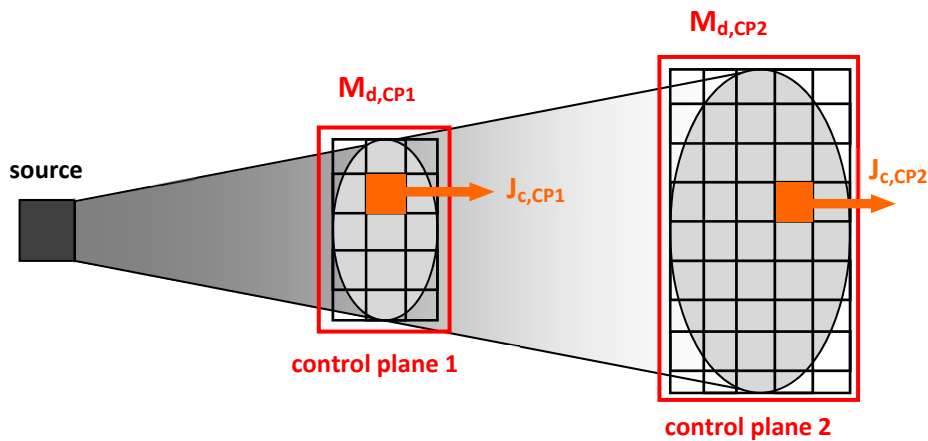
Concept of a contaminant mass flux at a plane of compliance (after EPA, 2003)

CONTAMINANT MASS DISCHARGE

Contaminant mass discharge (M_d) is the spatial integration of the contaminant mass fluxes (i.e., the sum of all mass flux measures across an entire plume) and thus represents the total mass of any contaminant transported by groundwater through a defined plane. Contaminant mass discharge is expressed as mass per time.

$$M_d = \int_A J_c dA \quad (3)$$

where A is the area of the plane of compliance [m^2] and J_c is the spatially variable contaminant flux [$\text{g m}^{-2} \text{day}^{-1}$]. Figure 2 shows the concept of contaminant mass flux and contaminant mass discharge.



Concept of mass flux (J_c) and mass discharge (M_d) (after ITRC, 2010)

Contaminant mass flux can be determined directly or indirectly using passive sampling devices (Goltz et al., 2007; Verreydt et al., 2010), while contaminant mass discharge requires a calculation, estimation or modeling approach.

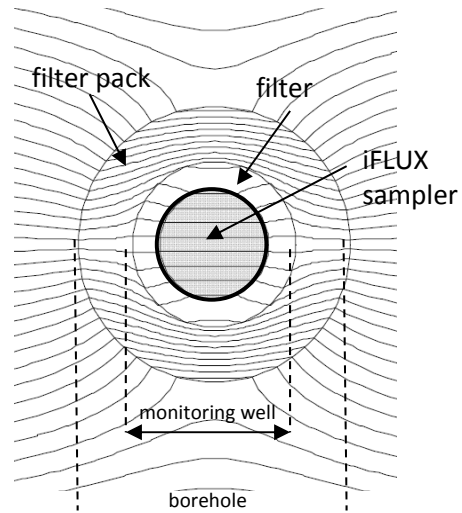
GROUNDWATER FLOW FIELD DISTORTION

The groundwater flow field around a monitoring well, whether or not equipped with an iFLUX sampler, will be disturbed because of the different hydraulic conductivities of the well filter, flux measurement device and surrounding aquifer (Fig.3). Therefore, flux measurements performed in a monitoring well should always be corrected for this flow field distortion (Verreydt et al., 2014).

The water flux (q) through the iFLUX sampler or monitoring well [$\text{m}^3 \text{m}^{-2} \text{day}^{-1}$] is directly proportional to the water flux (q_0) in the aquifer [$\text{m}^3 \text{m}^{-2} \text{day}^{-1}$]. This is expressed in:

$$q_0 = \frac{q}{\alpha} \quad (4)$$

where α is the flow field distortion of the groundwater flow in the vicinity of a monitoring well with or without an iFLUX sampler installed [-]. If a monitoring well is equipped with an iFLUX sampler, α can be calculated from the potential theory (Klammler et al., 2007). The potential theory assumes a uniform flow field in a homogeneous domain. If $\alpha < 1$, the groundwater flow field shows a convergence, if $\alpha > 1$, divergence of the groundwater flow takes place.



Converging and diverging flow lines in a uniform groundwater flow field due to the presence of a monitoring well with filter pack and iFLUX sampler (horizontal cross-section, Verreydt, 2012).

4. ADDITIONAL INFORMATION FVPDM & HEAT TRACER TEST

Modeling tracer injection and well-aquifer interactions: A new mathematical and numerical approach

Serge Brouyère

Hydrogeology, Department of Georesources, Geotechnologies and Building Materials, University of Liège, Liège, Belgium

Received 30 October 2002; accepted 4 February 2003; published 26 March 2003.

[1] A new mathematical and numerical approach is presented to model solute exchange between a well and the surrounding aquifer for the interpretation of field tracer tests. On the basis of water and tracer mass balance equations integrated over the volume of water in the well, the approach allows for finite volumes of tracer fluid and water flush. It deals with tracer mixing and capturing in the well bore, local distortion of the flow field around the well, and possible tracer back-migration into the well. A numerical solution, implemented in the three-dimensional finite element groundwater flow and transport simulator SUFT3D, is proposed that allows for modeling nonuniform distributions of tracer mass fluxes along the well screens related to variations in aquifer hydraulic conductivity. Showing its ability to reproduce concentration evolutions monitored in a well during field tracer experiments, considering various injection conditions, validates the approach. *INDEX TERMS:* 1831 Hydrology: Groundwater quality; 1832 Hydrology: Groundwater transport; *KEYWORDS:* tracer techniques, tracer injection, groundwater transport modeling

Citation: Brouyère, S., Modeling tracer injection and well-aquifer interactions: A new mathematical and numerical approach, *Water Resour. Res.*, 39(3), 1070, doi:10.1029/2002WR001813, 2003.

1. Introduction

[2] Tracer experiments are frequently performed to identify aquifer transport processes and to quantify the governing hydrodispersive parameters. Many physical factors, related to experimental conditions and well-aquifer interactions, may lead to a tracer input function that departs strongly from commonly assumed instantaneous or step injection profiles. If not explicitly considered, this can lead to severe misinterpretation of the results. In particular, *Gelhar et al.* [1992] mention that in terms of dispersivity assessment, a clear definition and control of the tracer input function are important factors for classifying the tracer experiment as reliable. Nevertheless, little attention is usually given to this experimental step or to the accuracy of mathematical or numerical representations of the tracer injection.

[3] A new physically based approach is developed in order to accurately model tracer injection in a well. It is able to account for finite volumes and flow rates of tracer fluid, untraced water flush, mixing and capturing in the well bore, and complex well-aquifer interactions. The possibility of accounting for the influence of aquifer heterogeneity close to the injection well is also discussed. The implementation of the numerical scheme in a groundwater flow and transport numerical simulator (here, in the SUFT3D code) is described. For validation of these developments, the model

is used to fit concentration evolutions monitored in a well during field tracer experiments.

2. Main Factors Influencing the Injection Process

[4] When the tracer is injected in a well, its actual input function in the aquifer may be influenced by several factors. First of all, the duration and flow rates associated with the tracer injection and the water flush can play an important role [*Guvanasen and Guvanasen*, 1987; *Brouyère and Rentier*, 1997]. However, the experimenter can control these factors. Other key factors, related to well configuration and well-aquifer interactions, are not directly controlled and are often disregarded.

[5] When the volume V_{inj} (L^3) of tracer is injected, a dilution occurs with the volume of water V_w (L^3) in the well. In spite of the injection of a water flush, a quantity of tracer may remain temporarily captured in the well bore. These so-called mixing effects that potentially result in lower recovery peaks at observation or pumping wells [*Novakowski*, 1992a; *Moench*, 1989] are usually quantified with a non-dimensional mixing factor $V_{inj}^* = V_{inj}/V_w$.

[6] When injection operations are completed, the remaining quantity of tracer in the well is progressively released to the aquifer due to the natural-gradient transit flow rate crossing well screens. This flow rate is affected by well bore skin effects, which are often considered by means of a nondimensional lumping distortion coefficient α_w , expressing the ratio between the actual water flow rate crossing the well section orthogonal to the main flow direction and the theoretical flow rate that would transit across the same

section if the well was not present [e.g., *Drost et al.*, 1968; *Hall*, 1996]:

$$\alpha_w = \frac{Q_t^0}{2r_w e_{scr} |v_D|}. \quad (1)$$

Q_t^0 is the flow rate crossing the well screens ($L^3 T^{-1}$) in natural flow conditions, r_w is the screen casing radius (L), e_{scr} is the screen length (L), and $|v_D|$ is the mean Darcy flux ($L T^{-1}$) that would prevail close to the well in the absence of flow distortion.

[7] Finally, because of the heterogeneity of the aquifer, the distribution of water fluxes along the screens may lead to a nonuniform tracer spreading in the aquifer, in the vicinity of the injection well.

3. Mathematical Model

3.1. Existing Approaches

[8] *Guvanasen and Guvanasen* [1987] have developed a semianalytical solution that deals with a finite volume of tracer fluid and water flush but does not consider well-bore mixing and skin effects. The analytical solutions of *Novakowski* [1992a] allow for tracer column displacements, considering mixing effects in reservoirs connected to column inlet and outlet, but are limited to the one-dimensional case. The analytical solution of *Moench* [1989], applied to radially converging tracer tests, considers well-bore mixing effects in the injection and extraction wells, but a Dirichlet-type boundary condition is used to link concentrations in the well bore and in the surrounding aquifer. *Novakowski* [1992b] determined that from a physical point of view, the third-type boundary conditions better represent experimental data. Aside from proposing a correction to the solution proposed by *Moench* [1989] (see correction to *Moench* [1989]), *Zlotnik and Logan* [1996] discuss concentration-based and mass flux-based boundary conditions applied at the interface between the injection well and the aquifer, with the assumption that the tracer injection rate is small and therefore does not alter the velocity distribution in the aquifer around the injection well. Thus actual injection conditions dealing with a finite volume of tracer and water cannot be considered. Several approaches have also been proposed for modeling wells using one-dimensional highly conductive finite elements [e.g., *Sudicky et al.*, 1995; *Wu et al.*, 1996]. Being one-dimensional, these elements do not consider the influence of skin effects on the flow field pattern close to the well.

[9] It appears that none of the existing approaches is able to deal with the full complexity associated with the tracer injection process and actual field conditions. In what follows, a new mathematical model is presented that allows for the tracer injection operations actually encountered in the field to be modeled.

3.2. Mass Balance Equations Applied to Water and Tracer in the Well Bore

[10] The model is based on mass balance equations applied to water and solute, integrated over the volume of water V_w in the well bore (Figure 1). Flow rate terms account for different possible exchanges between the well and its environment: the injection flow rate Q_{in} , the transit

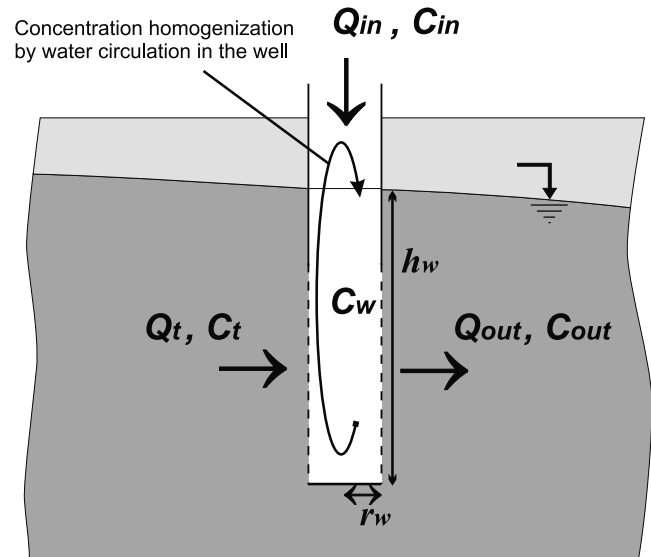


Figure 1. Schematic representation of the well-aquifer system and exchanged fluxes.

flow rate Q_t entering the well through the screens, and the flow rate Q_{out} leaving the well through the screens. Tracer concentrations associated with these flow rates and in the injection well are C_{in} , C_t , C_{out} , and C_w , respectively. All these terms may vary with time. The well radius is r_w , and the length of the water column in the well is h_w . If density effects, due to the presence of a solute in the water, are neglected, the mass balance equation applied to water within the well can be written as follows:

$$\frac{\partial V_w(t)}{\partial t} = Q_{in}(t) + Q_t^{in}(t) - Q_{out}(t), \quad (2)$$

where $V_w = \pi r_w^2 h_w$ is the volume of water in the well at time t and the superscript “in” appearing in Q_t^{in} reflects a dynamic link with Q_{in} (see section 3.3).

[11] The hypothesis of perfect mixing of the tracer and water in the well bore is assumed. This may be facilitated by pumping water from the bottom part of the well and discharging it at the upper part of the water column. On the basis of that, $C_w(t)$ represents the mean concentration in the well at time t . It is also assumed that the tracer concentration C_{out} is equal to the concentration C_w in the well.

[12] Finally, the mass balance equation applied to the tracer within the well is given by

$$\begin{aligned} \frac{\partial M(t)}{\partial t} &= \frac{\partial}{\partial t} (V_w C_w) = \pi r_w^2 \left(C_w \frac{\partial h_w}{\partial t} + h_w \frac{\partial C_w}{\partial t} \right) \\ &= Q_{in} C_{in} + Q_t^{in} C_t - Q_{out} C_w \end{aligned} \quad (3)$$

3.3. Evaluation of the Transit Flow Rate and Concentration

[13] The transit flow rate depends on the injection rate. If Q_{in} is low, Q_t^{in} is close to natural flow conditions (Figure 2a). As Q_{in} is increased, it progressively diminishes Q_t^{in} (Figure 2b). For a critical value $Q_{in} = Q_{cr}$, Q_t^{in} is exactly canceled (Figure 2c). Above the critical injection

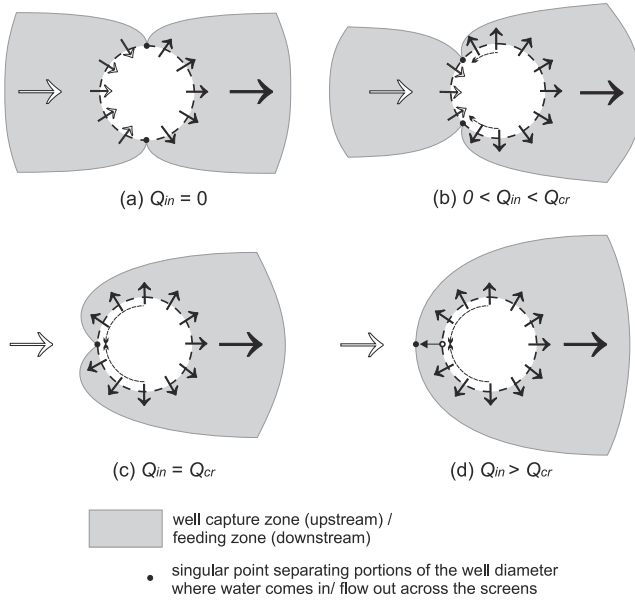


Figure 2. Modification of groundwater flow lines in the vicinity of the well, according to the injection flow rate Q_{in} .

rate ($Q_{in} > Q_{cr}$), all water leaving the well through the screens is injected water, this water being spread in all directions around the injection well (Figure 2d). To account for the continuous variation of Q_t^{in} according to injection conditions, an analytical formulation has been deduced from the potential theory presented by *Bidaux and Tsang* [1991]. It can be shown that the resulting equation is given by

$$Q_t^{in} = 2r_w e_{scr} \alpha_w |\underline{v}_D| \sin(\arccos Q_{in}^*) - \frac{Q_{in}}{2\pi} (2 \arccos Q_{in}^*), \quad (4)$$

where $Q_{in}^* = Q_{in}/Q_{cr}$ with $Q_{cr} = 2\pi r_w e_{scr} \alpha_w |\underline{v}_D|$ the critical injection rate.

[14] If $Q_{in}^* = 0$, equation (4) simplifies to the expected expression for the natural transit flow rate:

$$Q_t = Q_t^0 = \alpha_w S_w |\underline{v}_D| = 2e_{scr} r_w \alpha_w |\underline{v}_D|. \quad (5)$$

Equation (4) assumes that locally all fluxes reach equilibrium almost instantaneously (i.e., $\partial h_w / \partial t = 0$). This assumption is not valid if the injection rate is very high or if the aquifer hydraulic conductivity or well bore skin permeability is low. However, in this situation, it is likely that the transit flow rate would be canceled.

[15] To evaluate the natural transit flow rate (equation (5)), Darcy velocities prevailing in the aquifer close to the injection well have to be estimated without the influence of any source/sink term applied in the injection well. In a homogeneous aquifer, this can be based on an estimation of the local hydraulic conductivity and gradient. If pure radially converging flow conditions prevail, the following expression can be used:

$$|\underline{v}_D| = \frac{Q_P}{2\pi d e_{aq}}. \quad (6)$$

Q_P is the extracted flow rate at the pumping well, d is the distance between pumping and injection wells, and e_{aq} is the mean saturated thickness of the aquifer.

[16] During injection and water flush, the transit mass flux ($f_{Mt} = Q_t^{in} C_t$) is set to zero. Indeed, it can be expected that either $Q_{in} > Q_{cr}$ in which case Q_t is equal to zero, or Q_{in} is low and the transit flux does not carry tracer (i.e., $C_t = 0$). When Q_{in} is set to zero (tracer injection or water flush completed), it is assumed that $C_t = C$, the latter being the mean concentration in the aquifer around the injection well.

[17] Introducing equation (2), expressed in terms of Q_{out} , in equation (3) and considering the different assumptions presented above, the general equation used for modeling tracer injection is

$$\pi r_w^2 h_w \frac{\partial C_w}{\partial t} = Q_{in} (C_{in} - C_w) + Q_t^{in} (C - C_w). \quad (7)$$

Equation (7) shows that the well-aquifer system acts similarly to a dual-porosity system. The injection can thus have some influence on tracer test results due to the capture of tracer in the well bore and gradual release into the aquifer. This may lead to artificially enhanced concentration attenuation and tailing at the observation well [Brouyère, 2001].

4. Numerical Model

4.1. Finite Difference Approximation

[18] Equation (7) is evaluated numerically, using classical finite difference approximations:

$$C_w \approx \tilde{C}_w = \omega_w C_w(t + \Delta t) + (1 - \omega_w) C_w(t) \quad (8)$$

$$\frac{\partial C_w(t)}{\partial t} \approx \frac{C_w(t + \Delta t) - C_w(t)}{\Delta t}, \quad (9)$$

where ω_w is a time weighting factor, an implicit scheme ($\omega_w = 1$) being used to guaranty the stability of the numerical computations, and Δt is the computation time step.

[19] From the groundwater flow simulation performed prior to execution of the transport problem, the variation of water level in the injection well is linearized on the time step Δt , as follows:

$$h_w \approx \tilde{h}_w = \omega_w h_w(t + \Delta t) + (1 - \omega_w) h_w(t), \quad (10)$$

where $h_w(t)$ and $h_w(t + \Delta t)$ are the water levels in the well computed at time t and $t + \Delta t$.

[20] These approximations are introduced in equation (7), giving the following expression:

$$\begin{aligned} & \left[\frac{\pi r_w^2 \tilde{h}_w}{\Delta t} + \omega_w (Q_{in} + Q_t^{in}) \right] C_w(t + \Delta t) \\ & = \left[\frac{\pi r_w^2 \tilde{h}_w}{\Delta t} - (1 - \omega_w) (Q_{in} + Q_t^{in}) \right] C_w(t) + Q_{in} C_{in} + Q_t^{in} C \end{aligned} \quad (11)$$

With the initial condition for C_w and the appropriate values for the injection rate and concentration on the computation

Table 1. Description of the Injections Performed in Well Pz5

Tracer	Phase	V_{inj} , m ³	T_{inj} , s	Q_{inj} , m ³ /s	V_{fl} , m ³	T_{fl} , s	Q_{fl} , m ³ /s
Naphionate	I	0.007	100	7.0×10^{-5}	0.014	240	5.75×10^{-5}
	II	0.003	52	5.77×10^{-5}	0.100	268	3.73×10^{-4}
	III	0.048 + 0.152	2400 + 9900	$2.0 \times 10^{-5} + 1.54 \times 10^{-5}$	-	-	-

time step, equation (11) fully determines the time evolution of tracer concentration in the injection well.

4.2. One-Dimensional Representation of the Injection Well

[21] In some cases, well screens extend over several meters, along which the hydraulic conductivity may vary by orders of magnitude, leading to a nonuniform distribution of injected water and tracer fluxes. In the SUFT3D finite element code [Carabin and Dassargues, 1999; Brouyère, 2001], the approach proposed by Sudicky *et al.* [1995], for modeling wells using one-dimensional finite elements, is used for distributing the injected water “naturally” among the well nodes. From flow computational results on the current time step, if n_w nodes connect the injection well and the aquifer, the different flow rates terms are split into n_w components. For example, the injection rate Q_{in} is split into n_w terms q_{in}^K , with $Q_{in} = \sum_{K=1}^{n_w} q_{in}^K$. Considering these distributed flow rates, equation (11) can be written

$$C_w(t + \Delta t) = \frac{1}{R_w} \left(Q_{in} C_{in} + \sum_K q_t^K C_K(t) + B_w C_w(t) \right), \quad (12)$$

with

$$R_w = \frac{\pi r_w^2 \tilde{h}_w}{\Delta t} + \omega_w \sum_K (q_t^K + q_{in}^K)$$

$$B_w = \frac{\pi r_w^2 \tilde{h}_w}{\Delta t} - (1 - \omega_w) \sum_K (q_t^K + q_{in}^K).$$

$C_K(t)$ is the concentration in the transit flow rate q_t^K at node K connecting the aquifer and the well. It is taken to be in a fully explicit form in order to relax the dependency of computed concentrations in the aquifer at one connecting node on concentrations in the aquifer at other connecting nodes. This does not influence the stability of the numerical scheme, as the explicit evaluation is performed on a source term and not directly in the transport equation. In this case, Darcy fluxes are computed at the nodes located at the well-aquifer interface, based on flow conditions prevailing before injection begins.

[22] Using a general operator $T_{3D}(C)$ to represent the numerical form of the transport equation in the aquifer, the following expression describes the implementation of the injection well in the 3-D simulator as a simple source/sink term:

$$T_{3D}(C) - \sum_{K=1}^{n_w} (q_{out}^K C_w - q_t^K C_K(t)) = 0. \quad (13)$$

5. Experimental Validation

[23] Typical concentration evolutions monitored in the field during field tracer experiments in alluvial deposits and

subsequently modeled with SUFT3D are presented as an illustration of the adequacy and accuracy of the modeling approach with respect to field observations.

[24] The studied site is located in the alluvial aquifer of the river Meuse, near Liège, in Belgium. A detailed hydrogeological study including groundwater flow and transport modeling was conducted to study the influence on tracer test results of the injection procedure, local flow conditions, and

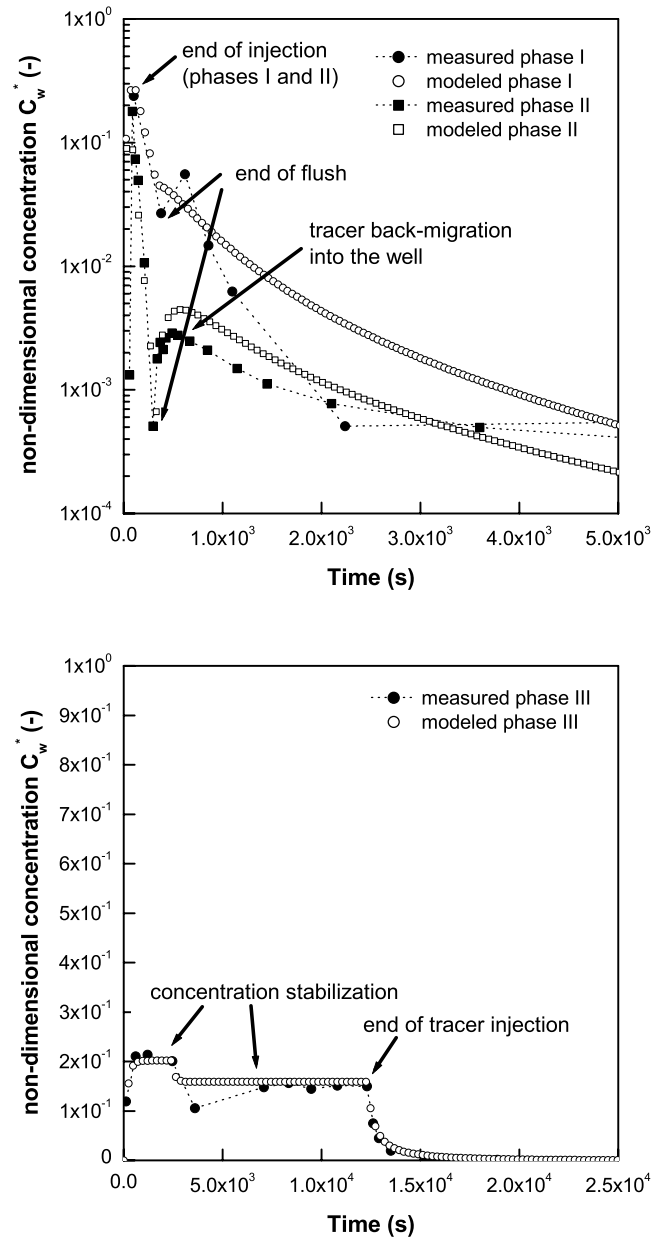


Figure 3. Comparison between concentration evolutions monitored in Pz5 and modeled with the SUFT3D code.

tracer characteristics [Brouyère, 2001]. Eight injection wells, located at distances ranging from 4.5 to 50 m from the pumped well (extraction rate, 52.6 m³/h) were used for the tracer experiments. Injections wells have a radius r_w of 2.5 cm, and the average length of the water column h_w in the wells was 7 m ($V_w \approx 13.7$ l). During each injection, a water circulation was performed in order to homogenize the tracer concentration and to obtain samples at the injection point. To illustrate the proposed methodology, results are presented for well Pz5, located 25 m away from the pumping well (for details, see Brouyère [2001]). Table 1 summarizes information relative to these injections. Figure 3 shows concentration evolutions monitored in Pz5 together with corresponding profiles computed with SUFT3D. Concentrations are normalized with respect to the concentration in the injected tracer fluid.

[25] During phase I, small volumes and flow rates were used for both the tracer injection and the water flush. During phase II the flush volume and rate were relatively large. During phase III it was decided to perform a “long duration injection,” without any flush afterward. For technical reasons, the injection rate was reduced during the injection. Concentration evolutions were adjusted considering r_w and α_w as fitting parameters. For r_w , a value of 2.5 cm was used, equal to the actual well radius, while for the distortion coefficient α_w , a value of 11.5 was found. This last value is relatively high. However, the distortion coefficient may be viewed as a “correction” factor used to fit the actual transit flow rate across well screens. Furthermore, all injection wells were drilled with a bit diameter ($d_{drill} = 11.5$ cm) larger than the casing ($d_{casing} = 5$ cm). The annular space, filled with a gravel pack of high hydraulic conductivity, may induce a strong convergence of flow lines around the well.

[26] For phases I and II the maxima of concentrations observed at the end of the tracer fluid injection and the decrease of concentration observed during the water flush are well reproduced. During phase II the tracer back-migration observed in Pz5 is also well reproduced. During phase III, the concentration in Pz5 stabilizes at a value lower than in the injected fluid ($C_w^* < 1$), indicating that a transit flow rate exists and contributes to flush the tracer. When the injection rate is reduced, the transit flow rate is increased, contributing to enhanced dilution of the tracer in the injection well and the stabilization of concentration at a lower level. In addition, the computed concentration evolution remarkably reproduces the dynamic variation of concentration with respect to the equilibrium between injection and transit flow rates, suggesting that equation (4), linking the injection and transit flow rates, is accurate.

6. Conclusions

[27] A new conceptual and mathematical approach is proposed for modeling tracer concentration evolution in wells and the solute mass flux leaving or crossing the well

at the screen level. It is validated by modeling concentration evolutions monitored in the field during tracer experiments. Contrary to previous approaches, this physically based model considers all processes that can have some influence on solute exchange between a well and the surrounding aquifer: finite volumes of tracer and flush, mixing and skin effects, back-migration of the tracer in the well bore, and heterogeneity of aquifer materials close to the injection well.

[28] **Acknowledgments.** The Ph.D. research of S. Brouyère was supported by a 4-year grant provided by the Funds for Scientific Research of Belgium. The author would thank Rob McLaren, Ed Sudicky, and René Therrien for their help during a stay in the Department of Earth Sciences of the University of Waterloo, with a travel grant provided by the Ministry of Education and Scientific Research of the French-Speaking Community Government of Belgium, and Jean Houard, Varut Guvanasen, and Allen Moench for their review of the English and their comments.

References

- Bidaux, P., and C.-F. Tsang, Fluid flow patterns around a well bore or an underground drift with complex skin effects, *Water Resour. Res.*, 27(11), 2993–3008, 1991.
- Brouyère, S., Study and modelling of transport and capturing of solutes in variably saturated media (in French), Ph.D. thesis, 572 pp., Fac. of Appl. Sci., Univ. of Liège, Liège, Belgium, 2001.
- Brouyère, S., and C. Rentier, About the influence of the injection mode on tracer test results, in *Tracer Hydrology 97*, edited by A. Kranjc, pp. 11–17, A. A. Balkema, Brookfield, Vt., 1997.
- Carabin, G., and A. Dassargues, Modeling groundwater with ocean and river interaction, *Water Resour. Res.*, 35(8), 2347–2358, 1999.
- Drost, W., D. Klotz, K. Arnd, M. Heribert, F. Neumaier, and W. Rauer, Point dilution methods of investigating groundwater flow by means of radioisotopes, *Water Resour. Res.*, 4(1), 125–146, 1968.
- Gelhar, L. W., C. Welty, and K. R. Rehfeldt, A critical review of data on field-scale dispersion in aquifers, *Water Resour. Res.*, 28(7), 1955–1974, 1992.
- Guvanasen, V., and V. M. Guvanasen, An approximate semianalytical solution for tracer injection tests in a confined aquifer with a radially converging flow field and a finite volume of tracer and chase fluid, *Water Resour. Res.*, 23(8), 1607–1619, 1987.
- Hall, S. H., Practical single-well tracer methods for aquifer testing, in *Tenth National Outdoor Action Conference and Exposition*, Natl. Groundwater Assoc., Columbus, Ohio, 1996.
- Moench, A. F., Convergent radial dispersion: A Laplace transform solution for aquifer tracer testing, *Water Resour. Res.*, 25(3), 439–447, 1989. (Correction, *Water Resour. Res.*, 32(5), 1457, 1996.)
- Novakowski, K., An evaluation of boundary conditions for one-dimensional solute transport, 1, Mathematical development, *Water Resour. Res.*, 28(9), 2399–2410, 1992a.
- Novakowski, K., An evaluation of boundary conditions for one-dimensional solute transport, 2, Column experiments, *Water Resour. Res.*, 28(9), 2411–2423, 1992b.
- Sudicky, E. A., A. J. A. Unger, and S. Lacombe, A noniterative technique for the direct implementation of well-bore boundary conditions in three-dimensional heterogeneous formations, *Water Resour. Res.*, 31(2), 411–415, 1995.
- Wu, Y. S., P. A. Forsyth, and H. Jiang, A consistent approach for applying numerical boundary conditions for multiphase subsurface flow, *J. Contam. Hydrol.*, 23, 157–184, 1996.
- Zlotnik, V. A., and J. D. Logan, Boundary conditions for convergent radial tracer tests and effect of well bore mixing volume, *Water Resour. Res.*, 32(7), 2323–2328, 1996.

S. Brouyère, Hydrogeology, Department of Georesources, Geotechnologies and Building Materials, University of Liège, Building B52/3, 4000 Liège, Belgium. (serge.brouyere@ulg.ac.be)

A new tracer technique for monitoring groundwater fluxes: The Finite Volume Point Dilution Method

Serge Brouyère^{a,b,*}, Jordi Batlle-Aguilar^a, Pascal Goderniaux^{a,c}, Alain Dassargues^a

^a Department ArGENCo, Hydrogeology Unit, University of Liège, Building B52/3, 4000 Sart Tilman, Belgium

^b Aquapôle, University of Liège, Building B52/3, 4000 Sart Tilman, Belgium

^c National Funds for Scientific Research of Belgium, Belgium

Received 17 May 2007; received in revised form 16 August 2007; accepted 7 September 2007

Available online 15 September 2007

Abstract

Quantification of pollutant mass fluxes is essential for assessing the impact of contaminated sites on their surrounding environment, particularly on adjacent surface water bodies. In this context, it is essential to quantify but also to be able to monitor the variations with time of Darcy fluxes in relation with changes in hydrogeological conditions and groundwater—surface water interactions. A new tracer technique is proposed that generalizes the single-well point dilution method to the case of finite volumes of tracer fluid and water flush. It is called the Finite Volume Point Dilution Method (FVPDM). It is based on an analytical solution derived from a mathematical model proposed recently to accurately model tracer injection into a well. Using a non-dimensional formulation of the analytical solution, a sensitivity analysis is performed on the concentration evolution in the injection well, according to tracer injection conditions and well-aquifer interactions. Based on this analysis, optimised field techniques and interpretation methods are proposed. The new tracer technique is easier to implement in the field than the classical point dilution method while it further allows monitoring temporal changes of the magnitude of estimated Darcy fluxes, which is not the case for the former technique. The new technique was applied to two experimental sites with contrasting objectives, geological and hydrogeological conditions, and field equipment facilities. In both cases, field tracer concentrations monitored in the injection wells were used to fit the calculated modelled concentrations by adjusting the apparent Darcy flux crossing the well screens. Modelling results are very satisfactory and indicate that the methodology is efficient and accurate, with a wide range of potential applications in different environments and experimental conditions, including the monitoring with time of changes in Darcy fluxes.

© 2007 Elsevier B.V. All rights reserved.

Keywords: Tracer technique; Single well; Darcy flux; Experimental setup; Analytical solution

1. Introduction

In many practical applications in hydrogeology, it is necessary to estimate groundwater fluxes, or even to be

able to monitor their evolution with time. For groundwater remediation, because of the concomitant and opposite effects of contaminant mobility and contaminant retardation or reaction, estimating Darcy fluxes and contaminant effective velocity in groundwater is essential for assessing the natural attenuation capacity of the subsurface (Valocchi, 1985; Brusseau, 1994; Li et al., 1994). Darcy fluxes are also required for dimensioning remediation systems such as reactive barriers, because their feasibility and efficiency mainly depend on the magnitude of

* Corresponding author. Department ArGENCo, Hydrogeology Unit, University of Liège, Building B52/3, 4000 Sart Tilman, Belgium. Tel.: +32 43662377; fax: +3243669520.

E-mail address: Serge.Brouyere@ulg.ac.be (S. Brouyère).

groundwater and contaminant fluxes in the aquifer (e.g. Morrison et al., 2002; Hatfield et al., 2004). Recently, important research efforts have also been devoted to better understanding and quantifying, at local and catchment scales, the mechanisms that govern the interactions between groundwater and surface water. These mechanisms play an important role on riparian ecosystems, on the fate of trace metals and organic contaminants, particularly in the hyporheic zone and, from a more general perspective, they have to be well understood to efficiently protect and manage water resources (Kalbus et al., 2006). A good perception of hydrogeologic systems requires knowledge of the local groundwater flow paths, the rates of exchange between stream and groundwater and the dynamics of such exchanges with varying river stage conditions (Wroblicky et al., 1998; Arntzen et al., 2006).

The most basic approach to estimating groundwater fluxes is to use Darcy's law with estimates of hydraulic conductivity (e.g. from pumping tests) and hydraulic gradients. However, doing so provides a rough estimate of the Darcy flux, subject to large errors (Devlin and McElwee, 2007), and only valid at the scale of the distance between the observation wells used to calculate the hydraulic gradient or at the scale of the pumping test used to determine the hydraulic conductivity.

The Point Dilution Method — PDM (e.g. Havelly et al., 1967; Drost et al., 1968; Klotz et al., 1978; Hall, 1996) allows to locally estimate groundwater fluxes based on the concentration decline monitored with time in an injection well. However, the injection is difficult to perform because the tracer must be instantaneously and uniformly mixed in the well bore water at the beginning of the test, without perturbation of the flow pattern around the well. Furthermore, this technique just provides an estimate of the Darcy flux at a given time, and it cannot be used to monitor changes in Darcy fluxes with time.

Recently, Brouyère (2003) presented a new mathematical and numerical approach to accurately model tracer injection into a well, considering injection conditions, such as the volume of tracer fluid and water flush, the flow rates or the injection duration and well-aquifer interactions, such as the flow rate that is actually crossing the screens due to motion of water in the aquifer. This model was used by Brouyère et al. (2005) in order to determine how and to what extent the tracer injection can influence the shape of the breakthrough curve and its interpretation. In that article, an analytical solution was derived and used to perform a detailed analysis of the evolution of the tracer input function in the aquifer for a better identification and understanding of factors that actually govern the influence of injection conditions on tracer test results.

Here, the same analytical solution is used to develop a new single-well tracer technique, called the Finite Volume Point Dilution Method (FVPDM) that generalizes the PDM to almost any kind of tracer injection scenario, and particularly to the case of a finite volume of tracer fluid and water flush. It can be used to locally estimate Darcy fluxes at the injection point for any type of tracer experiment. This new method allows for an easier experimental setup than the PDM and it has the further advantage over the PDM that it can be used for monitoring variations with time of the Darcy fluxes.

In the next chapters, the analytical solution obtained by Brouyère et al. (2005) is briefly reviewed, putting the accent on some mathematical aspects required to understand the specificity of the FVPDM. A non-dimensional formulation of the analytical solution is then used to perform a sensitivity analysis of the concentration evolution in the well during and after the tracer injection. Based on this analysis, several methodologies and interpretation formulas are proposed and discussed. The FVPDM technique was applied successfully in two case studies with contrasting scientific objectives and experimental conditions. The results of these experiments are used here to illustrate the adequacy and usefulness of the new tracer technique and to prove its applicability in the field. The potential for further developing the tracer technique to monitor transient Darcy fluxes, for example for changing river stage or piezometry, is also discussed.

2. The mathematical basis for FVPDM

The analytical solution obtained by Brouyère et al. (2005) for calculating the concentration evolution in the injection well is:

$$C_w(t) = \frac{Q_{in}C_{in} - (Q_{in}C_{in} - Q_{out}C_{w,0}) \exp\left(-\frac{Q_{out}}{V_w}(t - t_0)\right)}{Q_{out}} \quad (1)$$

with,

$$Q_{out} = Q_{in} + Q_t^{in} \quad (2)$$

In Eqs. (1) and (2), C_w , C_{in} and C_w^0 are tracer concentrations ($M L^{-3}$) in the well, in the injection water, and in the injection well at time t_0 , respectively. The injection rate is Q_{in} ($L^3 T^{-1}$), Q_t^{in} ($L^3 T^{-1}$) is the rate of water intercepted by the well at the screen level (transit flow rate) and Q_{out} ($L^3 T^{-1}$) is the flow rate that leaves the well through the screens, carrying tracer at concentration C_w . The superscript 'in' in the transit flow rate Q_t^{in} indicates the fact that this flow rate dynamically depends on the injection rate Q_{in} (see next section).

The term $V_w = \pi r_w^2 h_w$ is the volume of water in the injection well, where h_w (L) and r_w (L) represent the height of the water column in the well bore and the radius of the injection well, respectively. The volume of water in the injection well is assumed to be constant. This assumption is valid if a packer system is used in the well to isolate the injection level from the rest of the well bore and if variations in water level are small compared to the height of the water column in the well. Furthermore, as discussed later, the FVPDM should be performed using a low injection rate, which increases the chances to keep a constant water level in the well.

Eq. (1) extends the classical PDM to the case of finite volumes of tracer fluid and finite duration of tracer injection. Because the PDM relies on limiting assumptions of an instantaneous injection and a complete mixing of tracer diluted into an infinitesimal volume of water, Eq. (1) is a major improvement since it generalizes the former technique to experimental conditions that are more realistic and easier to perform in the field (Brouyère, 2001).

2.1. Evaluation of the transit flow rate Q_t^{in}

The physical process behind the FVPDM is dilution by mixing of the different flow rate components (Q_{in} and Q_t^{in}), which is similar to the standard dilution technique commonly used in hydrology to calculate flow rates in streams (Gilman, 1977a,b; Australian Government, 2006; Ruehl et al., 2006).

The FVPDM is, however, more complex than the dilution technique because the relationship between the injection flow rate Q_{in} and the transit flow rate Q_t^{in} is non-linear, as it depends on the flow patterns around the injection well and on the well geometry. As explained in

Brouyère (2003), the transit flow rate Q_t^{in} is maximum when the injection rate is equal to zero and it progressively decreases as the injection rate increases. For a critical value of the injection rate $Q_{in} = Q_{cr}$, the transit flow rate Q_t^{in} is exactly zero. Above the critical injection rate, only injection water leaves the well screen. This implies that the FVPDM should be performed with a tracer injection rate which is less than a critical injection rate (Q_{cr}) above which the transit flow rate crossing the screens of the injection well could not be determined because it would be cancelled. The key for developing the FVPDM is thus to accurately express the dependency of Q_t^{in} on Q_{in} and to evaluate as accurately as possible the critical injection rate (Q_{cr}).

Using the principle of superposition, Bidaux and Tsang (1991) developed equations to compute steady-state potential and stream functions near a well for purely regional flow, purely radial flow or a combination of both. Their equations allow calculation of Darcy flux components $v_r(r, \theta)$ and $v_\theta(r, \theta)$ in a (r, θ) coordinates system centred on the well (Fig. 1) and the output flow rate Q_{out} leaving the well screen. For the more general case of combined regional and radial flow, $v_r(r, \theta)$ and $v_\theta(r, \theta)$ are given by:

$$v_r(r, \theta) = -\hat{K}(r) \left[a(r)r^{\alpha(r)-1} - \frac{b(r)}{r^{\alpha(r)+1}} \right] \cos \theta + \frac{Q_{in}}{2\pi e_{scr} r_w} \tag{3a}$$

$$v_\theta(r, \theta) = \alpha(r)\hat{K}(r) \left[a(r)r^{\alpha(r)-1} + \frac{b(r)}{r^{\alpha(r)+1}} \right] \sin \theta \tag{3b}$$

where all coefficients are given in Bidaux and Tsang (1991).

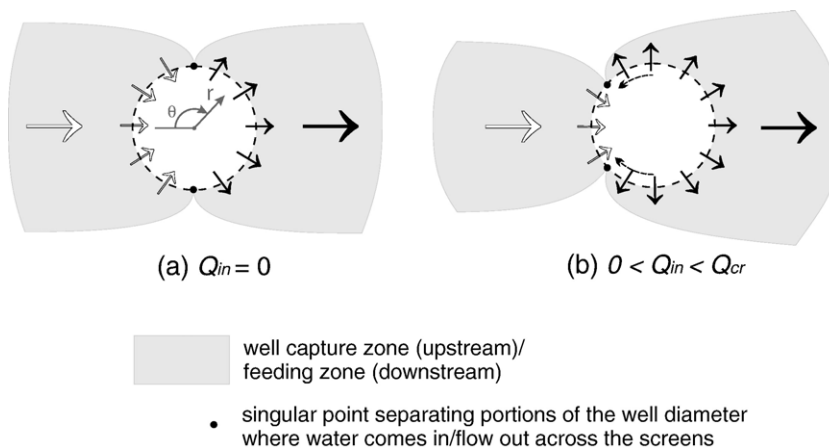


Fig. 1. Flow patterns around the injection well (a) in natural flow conditions, (b) modified by the injection of water in the well and radial coordinate system used to calculate the components of Darcy flux at the vicinity of the injection well (adapted from Brouyère, 2003).

At the well radius, the Darcy flux components (L T^{-1}) evaluated with expressions (3a) and (3b) are given by,

$$v_\theta(r_w, \theta) = 0 \quad (4a)$$

$$v_r(r_w, \theta) = -v_{ap} \cos \theta + \frac{Q_{in}}{2\pi e_{scr} r_w} \quad (4b)$$

where $v_{ap} = \alpha_w |\underline{v}_D|$ is the apparent Darcy flux measured at the well, α_w is a non-dimensional correction factor (distortion coefficient), $|\underline{v}_D|$ is the magnitude of the mean Darcy flux (L T^{-1}) that would prevail close to the well in the absence of flow distortion, e_{scr} (L) is the screen length of the well and r_w (L) is the radius of the injection well.

If the hydraulic conductivity field is homogeneous, α_w reflects the possible distortion of the flow field around the injection well (Drost et al., 1968; Hall, 1996; Brouyère, 2003). The flux component for the θ coordinates is always equal to zero (Eq. (4a)) and the Darcy flux field is purely radial for all values of pumping or injection rate in the well.

The flow rate Q_{out} leaving the well can be evaluated using the expression for v_r (Eq. (4b)). The screen section through which water is leaving the well corresponds to values of θ where $v_r(r_w, \theta) > 0$. In natural flow conditions, when the injection rate $Q_{in} = 0$, Eq. (4b) gives the following inequality,

$$v_r(r_w, \theta) = -v_{ap} \cos \theta \geq 0 \quad (5)$$

which is valid if $\cos \theta \leq 0$, so if $\frac{\pi}{2} \leq \theta \leq \frac{3\pi}{2}$. Therefore, in the absence of any injection ($Q_{in} = 0$), groundwater enters the well along the upstream segment of the screen which corresponds to, and leaves from the half downstream segment, as expected (Fig. 1a). The flow rate dq_{out} leaving the well between angles θ and $\theta + d\theta$ is given by:

$$dq_{out} = r_w e_{scr} v_r(r, \theta) d\theta = -r_w e_{scr} v_{ap} \cos \theta d\theta \quad (6)$$

Integrating Eq. (6) over half of the well circumference provides the following expression:

$$\begin{aligned} Q_{out} &= Q_t^0 = \int_{\pi/2}^{3\pi/2} dq_{out} \\ &= r_w e_{scr} \int_{\pi/2}^{3\pi/2} (-v_{ap} \cos \theta) d\theta = 2r_w e_{scr} v_{ap} \\ &= 2r_w e_{scr} \alpha_w |\underline{v}_D| \end{aligned} \quad (7)$$

As expected, the flow rate leaving the well is the product between the apparent Darcy flux (v_{ap}) and the

section of the injection well orthogonal to the main flow direction ($2r_w e_{scr}$).

For the more general case, when water is injected in the well at a rate $Q_{in} > 0$ (Fig. 1b), the solution of Eq. (8) gives the portion of the well circumference where water leaves the well.

$$\cos \theta \leq \frac{Q_{in}}{2\pi r_w e_{scr} v_{ap}} \quad (8)$$

Because of the condition $-1 \leq \cos \theta \leq 1$, for injected water, the bounding value $\cos \theta = 1$ provides the mathematical expression for the critical injection rate (Q_{cr}):

$$Q_{cr} = 2\pi r_w e_{scr} v_{ap} = 2\pi r_w e_{scr} \alpha_w |\underline{v}_D| \quad (9)$$

For an injection rate $Q_{in} > Q_{cr}$, all water leaving the well through the screen is injected water, the transit water flow rate Q_t being exactly offset by the injection flow rate Q_{in} . Bidaux and Tsang (1991) draw the same conclusions by computing the stream function rather than Darcy fluxes at the well circumference.

A comparison of the natural transit flow rate Q_t^0 (Eq. (7)) and the critical injection rate Q_{cr} (Eq. (9)) shows that they are related as follows:

$$Q_{cr} = \pi Q_t^0 \quad (10)$$

The factor π simply comes from the difference between the flow section associated to these two flow rates, which is the well diameter ($2r_w$) for Q_t^0 and the well circumference ($2\pi r_w$) for Q_{cr} .

If $Q_{in} \leq Q_{cr}$, the cosine inequality (Eq. (8)) allows defining the portion of circumference where the water leaves the well:

$$\arccos \left(\frac{Q_{in}}{Q_{cr}} \right) \leq \theta \leq 2\pi - \arccos \left(\frac{Q_{in}}{Q_{cr}} \right) \quad (11)$$

Using the limits defined in Eq. (11), the flow rate Q_{out} leaving the well through the screen is given by:

$$\begin{aligned} Q_{out} &= \int_{\arccos \frac{Q_{in}}{Q_{cr}}}^{2\pi - \arccos \frac{Q_{in}}{Q_{cr}}} \left(-r_w e_{scr} v_{ap} \cos \theta + \frac{Q_{in}}{2\pi} \right) d\theta \\ &= 2r_w e_{scr} v_{ap} \sin \left(\arccos \frac{Q_{in}}{Q_{cr}} \right) \\ &\quad + \frac{Q_{in}}{2\pi} \left(2\pi - 2 \arccos \frac{Q_{in}}{Q_{cr}} \right) \end{aligned} \quad (12)$$

where $Q_{in}^* = Q_{in}/Q_{cr}$

Finally, the expression for the transit flow rate is given by:

$$Q_t^{\text{in}} = Q_{\text{out}} - Q_{\text{in}} = 2r_w e_{\text{scr}} v_{\text{ap}} \sin\left(\arccos Q_{\text{in}}^*\right) - \frac{Q_{\text{in}}}{2\pi} \left(2 \arccos Q_{\text{in}}^*\right) \quad (13)$$

Using Eq. (13) assumes that the different flow rates (Q_{in} , Q_t^{in} , Q_{out}) reach equilibrium almost instantaneously during tracer injection, such that $Q_{\text{out}} = Q_{\text{in}} + Q_t^{\text{in}}$. This assumption is generally not valid if the injection rate is very high or if the hydraulic conductivity near the injection well is very low. However, with such injection rate or hydraulic conductivity, it is likely that the transit flow rate would be zero ($Q_{\text{in}}^* > 1$).

2.2. Non-dimensional formulation of the injection model

As shown by Brouyère et al. (2005), a more general form of Eq. (1) can be obtained using non-dimensional variables, by normalizing concentration, volume, flow rates and time variables according to the concentration in the tracer fluid C_{inj} , the volume of water in the injection well V_w , the critical injection flow rate Q_{cr} and the time T_w needed to replace the water in the well at this critical injection rate ($T_w = V_w / Q_{\text{cr}}$), respectively. The non-dimensional form of Eq. (1) can be written as:

$$C_w^*(t^*) = \frac{Q_{\text{in}}^* C_{\text{in}}^* - (Q_{\text{in}}^* C_{\text{in}}^* - Q_{\text{out}}^* C_{w,0}^*) \exp(-Q_{\text{out}}^* t^*)}{Q_{\text{out}}^*} \quad (14)$$

The following section presents a sensitivity analysis for the evolution of concentration in the injection well during and after tracer injection, based on non-dimensional Eq. (14). It will allow for a better understanding of practical conditions under which the new single-well tracer experiment has to be performed in order to obtain useful results and to propose interpretation methods and formulas. For the sake of generality, the non-dimensional formulation is used, but the methodology, the reasoning and the conclusions are valid for the corresponding dimensional variables as well.

3. Sensitivity analysis of the concentration evolution on tracer injection and local groundwater flow conditions

The most general way of performing a tracer injection is as follows. A quantity M_{inj} (M) of tracer is diluted in a volume V_{inj} (L^3) of water, at a concentration $C_{\text{in}} = C_{\text{inj}} =$

$M_{\text{inj}}/V_{\text{inj}}$ ($M L^{-3}$). The tracer fluid is injected during a period T_{inj} (T) at an injection flow rate is $Q_{\text{in}} = Q_{\text{inj}} = V_{\text{inj}}/T_{\text{inj}}$ ($L^3 T^{-1}$). Sometimes, the tracer injection is followed by a flush with clear (untraced) water ($C_{\text{in}} = 0$) to accelerate the transfer of the tracer from the injection well to the surrounding aquifer. This flush is performed with a volume of water V_{fl} (L^3), injected over a period T_{fl} , at an injection rate $Q_{\text{in}} = Q_{\text{fl}} = V_{\text{fl}}/T_{\text{fl}}$ ($L^3 T^{-1}$). When tracer injection and subsequent flushing are completed, some tracer remains in the injection well, from where it is progressively released in the aquifer, as a result of the transit flow rate Q_t^0 ($L^3 T^{-1}$) crossing the well screens in natural flow conditions. Table 1 summarizes the dimensional and the non-dimensional terms for the different possible steps of tracer injection operations. In the following section, the evolution of concentration in the injection well during the various phases of tracer injection is performed and analysed to propose in the next section the most efficient methodology for the FVPDM.

3.1. Concentration evolution during tracer injection

If one assumes that, at the beginning of tracer injection, there is no tracer in the well ($C_{w,0}^* = 0$) and that appropriate values are used for the flow rate variables (see Table 1), Eq. (14) can be written:

$$C_w^*(t^*) = \frac{Q_{\text{inj}}^* \left(1 - \exp(-Q_{\text{out}}^* t^*)\right)}{Q_{\text{out}}^*} \quad (15)$$

The concentration evolution in the injection well $C_w^*(t^*)$, as computed according to Eq. (15), is presented in Fig. 2. Each continuous curve corresponds to a constant injection rate Q_{inj}^* , moving along a curve corresponding to increasing tracer volumes V_{inj}^* and injection durations t_{inj}^* . Concentrations increase for larger injection rates and longer injection duration, thus for larger injection volumes.

The curve $C_w^*(Q_{\text{in}}^* = 1)$ divides the diagram into two contrasting domains. If the injection rate is higher than the critical injection rate ($Q_{\text{inj}}^* > 1$, Fig. 2, domain 1), the concentration in the well approaches the concentration in the injected tracer fluid ($C_w^* \rightarrow 1$) when the volume of tracer is large ($V_{\text{inj}}^* \approx 5$). If the injection rate is lower than the critical injection rate ($Q_{\text{inj}}^* < 1$, Fig. 2, domain 2), the concentration in the well never approaches that in the injected tracer fluid ($C_w^* < 1$), whatever the volume of tracer fluid injected because the transit flow rate crossing the screens contributes to tracer dilution in the well. In this case, provided that the injection duration is long enough, the concentration in the well approaches a value $C_{w,\text{stab}}^*$ which is all the lower as the injection rate is low, thus as the transit flow rate is high.

Table 1

Dimensional and non-dimensional values taken by the different variables for the different phases of the tracer injection process

Dimensional variables					
	C_{in}	V_{in}	Q_{in}	Q_t^{in}	Q_{out}
Tracer injection	C_{inj}	V_{inj}	Q_{inj}	Q_t^{inj}	$Q_{inj} + Q_t^{inj}$
Tracer flush	0	V_{fl}	Q_{fl}	Q_t^{fl}	$Q_{fl} + Q_t^{fl}$
Natural release of the tracer	0	0	0	Q_t^0	Q_t^0
Non-dimensional variables					
	$C_{in}^* = C_{in}/C_{inj}$	$V_{in}^* = V_{in}/V_w$	$Q_{in}^* = Q_{in}/Q_{cr}$	$Q_t^{in*} = Q_t^{in}/Q_{cr}$	$Q_{out}^* = Q_{out}/Q_{cr}$
Tracer injection	$C_{inj}^* = 1$	V_{inj}^*	Q_{inj}^*	Q_t^{inj*}	$Q_{inj}^* + Q_t^{inj*}$
Tracer flush	0	V_{fl}^*	Q_{fl}^*	Q_t^{fl*}	$Q_{fl}^* + Q_t^{fl*}$
Natural release of the tracer	0	0	0	$Q_t^{0*} = 1/\pi$	$Q_t^{0*} = 1/\pi$

The stabilized concentration level in the well can be computed as follows:

$$C_{w,stab}^* = \lim_{t_{inj}^* \rightarrow \infty} \left(\frac{Q_{inj}^* (1 - \exp(-Q_{out}^* t_{inj}^*))}{Q_{out}^*} \right) = \frac{Q_{inj}^*}{Q_{out}^*} = \frac{Q_{inj}^*}{Q_{inj}^* + Q_t^{inj*}} = \frac{Q_{inj}}{Q_{inj} + Q_t^{in}} \quad (16)$$

From a practical point of view, Eq. (16) allows estimation of the transit flow rate Q_t^{in} by performing a low-rate tracer injection of long duration, which is as close to the natural transit flow rate Q_t^0 as the injection rate is low (see practical examples in the next section).

In Fig. 2, the dotted lines correspond to envelope curves of the maximum concentration reached in the well at the end of tracer injection, for variable tracer volumes V_{inj}^* . If $Q_{inj}^* \geq 1$ (Fig. 2, domain 1), the concentration reached in the well at the end of tracer injection is independent of the injection duration t_{inj}^* (concentration plateau at the beginning of each envelope curve). If $Q_{inj}^* < 1$ (Fig. 2, domain 2), the concentration level reached in the well at the end of tracer injection decreases with the injection duration t_{inj}^* . In the first case, the transit flow rate is cancelled and the only contribution to tracer dilution comes from the mixing between untraced water initially present in the well bore (V_w) and the tracer fluid (V_{inj}), quantified by the mixing factor $V_{inj}^* = V_{inj}/V_w$. In the second case, the

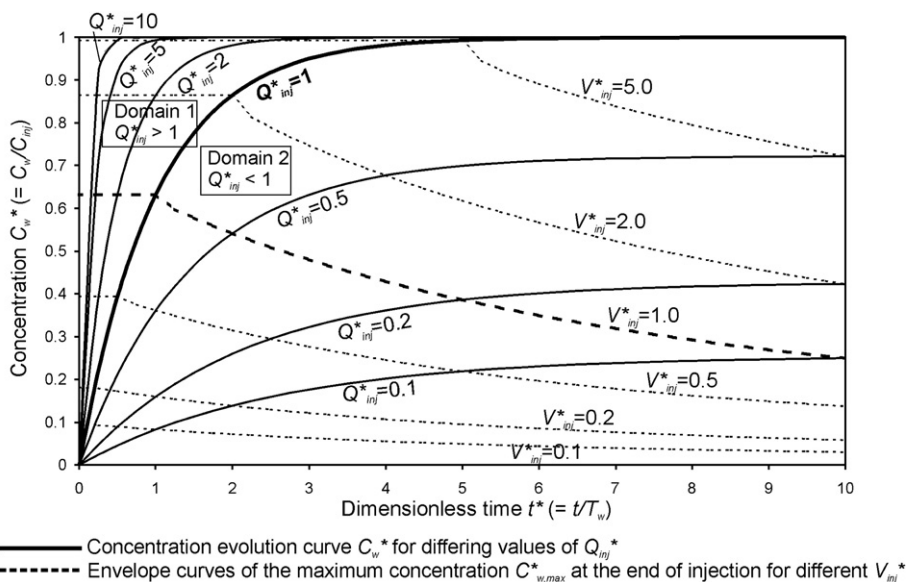


Fig. 2. Dimensionless representation of concentration evolution in the well according to injection conditions.

existing transit flow rate also contributes to tracer dilution in the well bore.

These observations can be obtained mathematically using Eq. (15), by calculating the concentration in the well at the end of tracer injection (for $t^* = t_{inj}^*$):

For $Q_{inj}^* > 1$, $C_{inj}^* = 1$, $C_{w,0}^* = 0$, $Q_{out}^* = Q_{inj}^*$ and $Q_{inj}^* t_{inj}^* = V_{inj}^*$:

$$C_{w,e_{inj}}^* = \frac{Q_{inj}^* (1 - \exp(-Q_{out}^* t_{inj}^*))}{Q_{out}^*} = 1 - \exp(-V_{inj}^*) \tag{17a}$$

For $Q_{inj}^* < 1$, $Q_{out}^* = Q_{inj}^* + Q_t^{inj*}$:

$$C_{w,e_{inj}}^* = \frac{Q_{inj}^* (1 - \exp(-(V_{inj}^* + Q_t^{inj*} t_{inj}^*)))}{Q_{out}^*} = \frac{Q_{inj}^* (1 - \exp(-(V_{inj}^* + V_t^*)))}{Q_{out}^*} \tag{17b}$$

In Eq. (17a), $C_{w,e_{inj}}^*$ depends only on the mixing factor V_{inj}^* . In Eq. (17b), $C_{w,e_{inj}}^*$ still depends on the mixing factor V_{inj}^* , but also on the transit flow rate Q_t^{inj*} and on the injection duration t_{inj}^* , with the product $Q_t^{inj*} t_{inj}^* = V_t^*$ being the volume of groundwater that flows across the well screen during tracer injection. This means that the rising part, as well as the stabilized part of the concentration evolution in the injection well can be used to evaluate Q_t^{inj} and Q_t^0 provided that $Q_{inj} < Q_{cr}$. As

mentioned already, Q_t^{inj} is calculated using Eq. (13), knowing the injection rate Q_{inj} .

If $Q_{inj} \geq Q_{cr}$, thus if $Q_{inj}^* \geq 1$, $Q_{out} = Q_{inj}$ and Eq. (17a) allows one to check if the mixing volume of water V_w^{mix} , defined as the volume of water actually involved in the injection and mixing processes, differs from the actual volume of water stored in the well bore $V_w = \pi r_w^2 h_w$ (i.e. based on the geometry of the well). Discrepancies can be expected between V_w^{mix} and V_w . A smaller mixing volume of water may be expected if the mixing procedure does not involve the whole column of water in the well. On the contrary, a bigger mixing volume of water may be observed if either the well casing is deteriorated or if groundwater located around the well is directly involved in the mixing process.

3.2. Concentration evolution after tracer injection

When the injection of the tracer fluid is completed, a water flush is frequently performed in the well by injecting untraced water ($C_{fl}^* = C_{fl}/C_{inj} = 0$) at a rate Q_{fl} to accelerate the transfer of the tracer from the well into the aquifer around. During this phase, Eq. (14) can be written:

$$C_w^* = C_{w,0}^* \exp(-Q_{out}^* t^*) \tag{18}$$

where $C_{w,0}^*$ is the non-dimensional concentration in the well at the beginning of the flush (usually at the end of the tracer fluid injection).

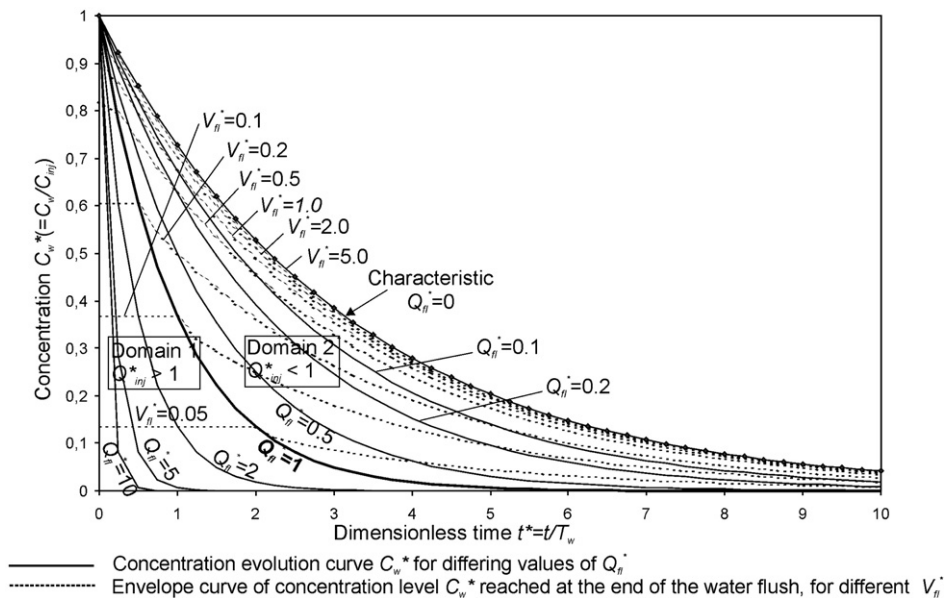


Fig. 3. Dimensionless graphical representation of concentration evolution in the well during water flush or natural release of the tracer.

Eq. (18) expresses that the concentration in the injection well decreases exponentially, at a rate which is proportional to $Q_{\text{out}}^* = Q_{\text{fl}}^* + Q_t^{\text{fl}*}$.

The concentration evolution in the well during the flush, as computed with Eq. (18), is presented in Fig. 3, assuming $C_{w,0}^* = 1$ at the beginning of the water flush. The time scale refers to the beginning of the flush. Each continuous curve corresponds to a constant flush rate Q_{fl}^* , moving along a curve corresponding to increasing water flush volumes V_{fl}^* and flush durations t_{fl}^* . Concentrations decrease for higher flushing rates and longer flush duration or larger flush volumes. In a semi-log diagram ($t, \log C_w^*$), these curves would plot as straight lines of negative slope equal to Q_{out}^* .

The dotted lines correspond to envelop curves of the concentration reached in the well at the end of the flush, for variable flush volumes V_{fl}^* . If $Q_{\text{fl}}^* > 1$ (Fig. 3, domain 1), the concentration level $C_{w,\text{en}}^*$, reached in the well at the end of the flush, depends only on the flush mixing factor $V_{\text{fl}}^* = V_{\text{fl}}/V_w$ (and on the initial concentration in the well $C_{w,0}^*$). If $Q_{\text{fl}}^* < 1$ (Fig. 3, domain 2), $C_{w,\text{en}}^*$ decreases with the flush duration (t_{fl}^*).

These observations can be obtained mathematically from Eq. (18), by calculating the concentration in the well at the end of the tracer flush (for $t^* = t_{\text{fl}}^*$):

If $Q_{\text{fl}}^* > 1$, $Q_{\text{out}}^* = Q_{\text{fl}}^*$, thus $Q_{\text{fl}}^* t_{\text{fl}}^* = V_{\text{fl}}^*$ and,

$$\begin{aligned} C_{w,\text{fl}}^* &= C_{w,0}^* \exp\left(-Q_{\text{fl}}^* t_{\text{fl}}^*\right) \\ &= C_{w,0}^* \exp\left(-V_{\text{fl}}^*\right) \end{aligned} \quad (19a)$$

If $Q_{\text{fl}}^* < 1$, $Q_{\text{out}}^* = Q_{\text{fl}}^* + Q_t^{\text{fl}*}$ and,

$$C_{w,\text{en}}^* = C_{w,0}^* \exp\left(-\left(V_{\text{fl}}^* + Q_t^{\text{fl}*} t_{\text{fl}}^*\right)\right) \quad (19b)$$

As for the equivalent case during tracer injection, if $Q_{\text{fl}}^* \geq 1$, $Q_{\text{out}} = Q_{\text{fl}}$, and Eq. (19a) allows one to check if the mixing volume of water in the well V_w^{mix} differs from the actual volume of water V_w located in the well bore.

If $Q_{\text{fl}} < Q_{\text{cr}}$, Eq. (19b) can be used to calculate the total flow rate Q_{out} leaving the well through the screens, thus the transit flow rate Q_t^{fl} crossing the screens during the water flush:

$$Q_t^{\text{fl}} = -\frac{\Delta_{ch} V_w}{\log e} - Q_{\text{fl}} \quad (20)$$

where Δ_{ch} is the slope of the decrease of concentration plotted in a semi-log diagram ($t, \log C_w^*$) and $\log e = 0,43429$.

If a flush is not performed ($Q_{\text{fl}}^* = 0$), the tracer is flushed from the well because of the transit flow rate

Q_t^{0*} crossing the screens in natural flow conditions. This comes to the interpretation formula used for the classical point dilution method.

$$\begin{aligned} C_w^*(t^*) &= C_{w,\text{en}}^* \exp\left(-Q_t^{0*} t^*\right) \\ &= C_{w,\text{en}}^* \exp\left(-t^*/\pi\right) \end{aligned} \quad (21)$$

where $C_{w,\text{en}}^*$ is the concentration of the tracer remaining in the well at the end of the injection.

4. Field applications

The Finite Volume Point Dilution Method was applied in two case studies. The results obtained during these experiments are used here to show the accuracy of the mathematical concepts and of the analytical solution on which the tracer technique relies. More information about these experiments is available in technical reports (Batlle-Aguilar and Brouyère, 2005, 2006; Goderniaux and Brouyère, 2006).

The first case study consists in tracer experiments between piezometers and a spring line system in a small (11.7 km²) catchment located in the north west of France (Val d'Oise — Brévilles springs). The saturated aquifer is located in sandy layers overlain by unsaturated fractured marly limestones (unsaturated zone). The objectives of the tracer experiments were to highlight vertical variations in mostly horizontal groundwater fluxes in the sandy aquifer, related to vertical variations in grain size distribution and hydraulic conductivity, to estimate contaminant travel times from several locations in the catchment to the Brévilles springs and to identify transport processes affecting the fate of solute contaminants in the saturated part of the aquifer. Considering these objectives, monitoring the concentration evolutions at the injection points was performed (1) to check that the tracers did not remain captured close to the injection point, as discussed in Brouyère et al. (2005), (2) to obtain local estimates of Darcy fluxes in the aquifer, which is a useful complementary information with regards to the general objectives of the experiments.

The field conditions in Brévilles did not offer the possibility of obtaining a power supply, an unlimited quantity of water and a protection of the equipment against vandalism. These conditions did not allow to apply the most advanced experimental setup of the FVPDM, as described further in section 4.1. Long-duration tracer injections were not possible and the tests had to be dimensioned in a “shorter version”. For each test, only the beginning of the rising concentration curves was monitored and modelled, using several steps of increasing injection rates. Furthermore, due to recovery

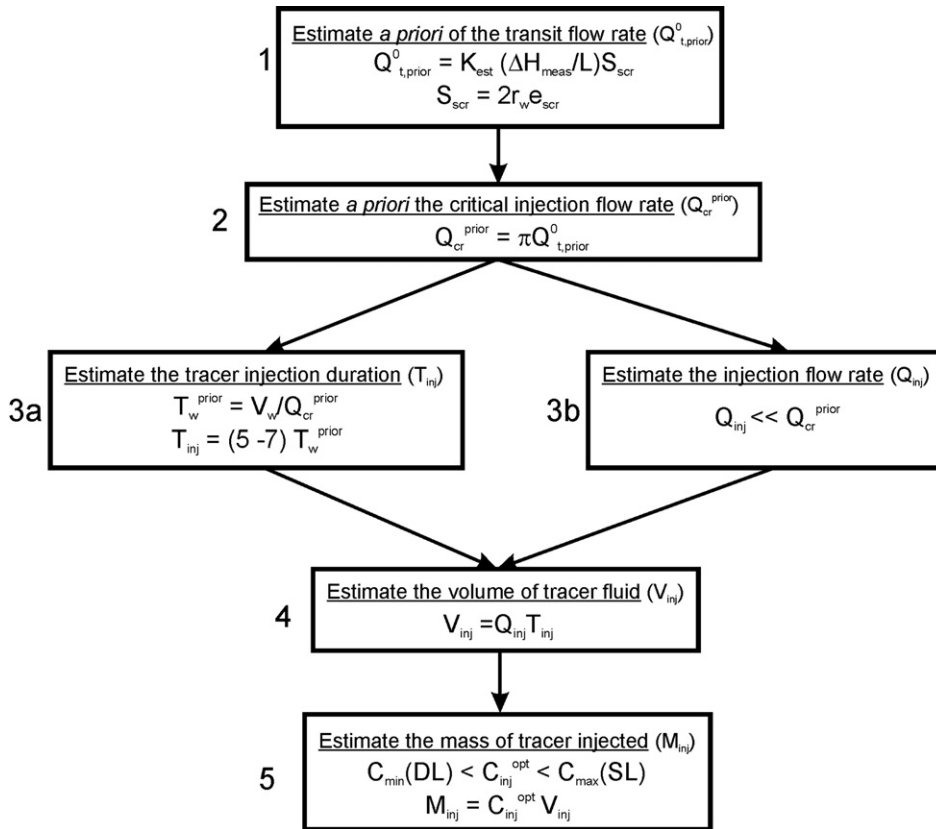


Fig. 4. Flowchart for the definition of the optimal FVPDM injection profile.

objectives at the Brévilles spring, the required quantity of tracer was large and the resulting high concentrations in the injection tracer fluid made handling operations less comfortable.

The second test site (further called site A) is a brownfield of 7.3 ha corresponding to a former cokery. It is located 30 m from the Meuse River, on the north bank, upstream of the city of Liège, Belgium. Groundwater is contaminated by inorganic (mainly sulphates and heavy metals) and organic pollutants (BTEX and PAH). The main objective of the tracer experiments was to evaluate groundwater fluxes discharging in the Meuse River. It was decided to apply the FVPDM in several observation wells located at the boundary of the site, near the river. At this site, the experimental conditions allowed to define and to use the most adequate and sophisticated experimental setup for monitoring tracer experiments over a long period so as to optimize the chances of reaching stabilization of concentration in the injection wells.

In the following sections, the FVPDM methodology, as used in actual field practice, is described first. After a brief description of the tracer experiments performed in

the two contrasting experimental sites, modelling results of the concentration evolutions using Eq. (1) are presented and discussed.

4.1. The FVPDM as performed in the field

Generally, the objectives of the study and the conditions prevailing in the field are the main constraining factors for dimensioning the tracer experiments, which will be illustrated by the results of the two case studies presented here. However, based on the theory, it is possible to propose a very structured methodology for dimensioning the FVPDM experiment prior to going to the field. This is summarized in Fig. 4 in the form of a flowchart which is described in details below.

As already mentioned, an essential condition for the FVPDM to be valid is that the injection rate should be less than the critical injection rate ($Q_{inj}^* < 1$). If that condition is not met, the concentration in the injection well (C_w) would become equal to the concentration of the injected tracer (C_{inj}) and the monitored evolution of concentration in the well could not provide an estimation of Darcy fluxes in the vicinity of the well.

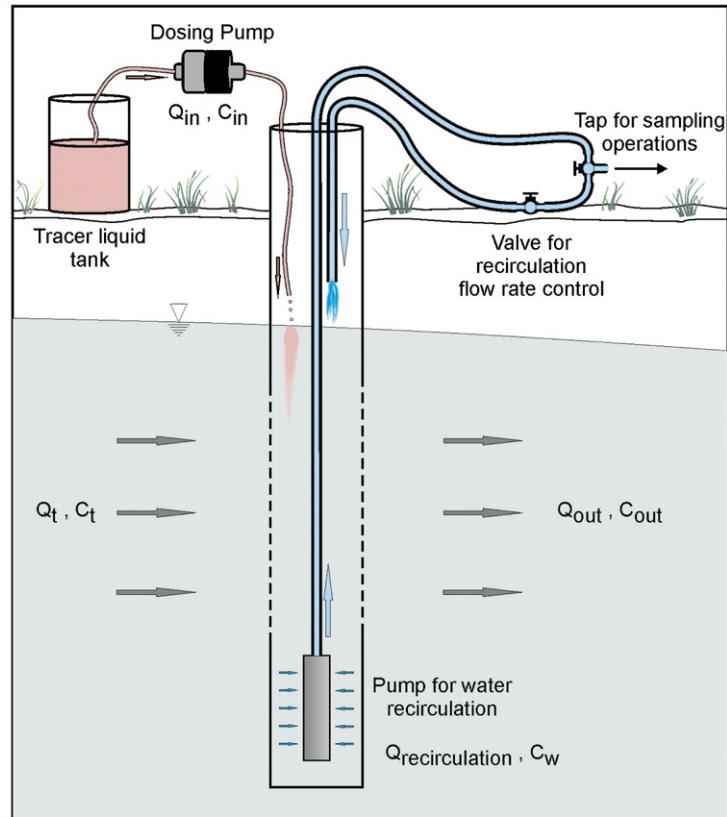


Fig. 5. Schematic experimental device (above) and real experimental device in the field (below).

The first step in setting up the experiment is thus to estimate *a priori* the critical injection rate Q_{cr} by applying Darcy's law with estimated hydraulic conductivity and hydraulic gradient (Fig. 4, step 1). Values of hydraulic conductivity and hydraulic gradient can be

obtained from pumping test results and from groundwater levels measured in the vicinity of the injection well, respectively.

When the critical injection rate Q_{cr} is estimated from Q_t (Fig. 4, step 2), one can define the injection profile

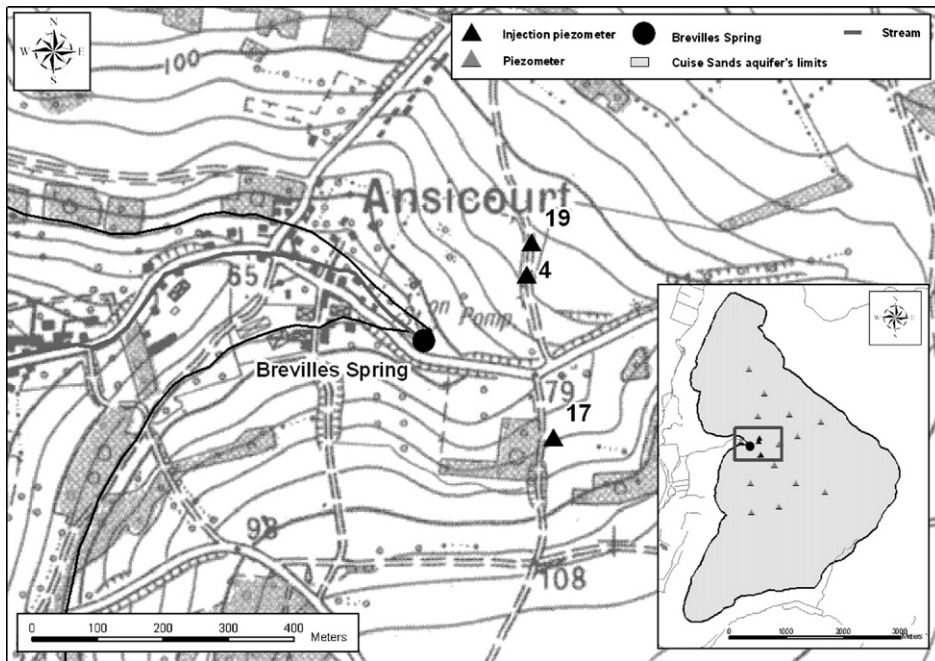


Fig. 6. Global view of the Brévilles test site and detail of the spring area (injection area).

(Q_{inj} , V_{inj} , T_{inj} , C_{inj} , ...) as follows. Theoretically, a single injection step at a constant rate Q_{inj} is sufficient to obtain a concentration evolution that is useful for the FVPDM interpretation. Here, it was however decided to perform, for each injection, various injection steps with increasing injection rates, the idea being to check that the relationship between Q_{inj}^{inj} and Q_{inj} remains valid for different values of Q_{inj} . It can also be expected that the resulting multi-step concentration evolution can provide a more reliable estimation of Darcy fluxes. Using increasing injection rates reduces also the risk of injecting the tracer at a rate that is larger than the critical injection rate.

Based on Fig. 2, one can estimate that the concentration evolution in the injection well stabilizes after a minimal injection duration T_{inj} equal to five times T_w . Knowing Q_{cr} and V_w , one can estimate T_w and then T_{inj} (Fig. 4, step 3a). At the same time, the prior estimate of Q_{cr} allows one to define an optimal value of Q_{inj} , as low as possible as compared to Q_{cr} (Fig. 4, step 3b). Having defined Q_{inj} and T_{inj} allows then to determine the volume of tracer fluid V_{inj} (Fig. 4, step 4).

The quantity of tracer has to be defined so as to have concentrations in the injection fluid (C_{inj}) and in the injection well (C_w) that are higher than the detection limit ($C_{inj} > C_{DL}$), to be easily detected and monitored, but still low enough to avoid adverse problems such as saturation of monitoring devices or density effects ($C_{inj} < C_{SL}$). So, the final step consists in defining the

quantity of tracer M_{inj} such that concentrations in the injection fluid C_{inj} and in the injection well C_w are within this acceptable interval (Fig. 4, step 5). During the experiment, ‘real-time’ measurements of the electrical conductivity or the fluorescence is recommended to monitor ‘on-line’ the concentration evolution and to check that the injection rate remains lower than the critical injection rate ($Q_{inj} < Q_{cr}$). Of course, if the FVPDM is performed in conjunction with another tracer experiment, like in Brévilles (see after), the quantity of tracer should be defined such that the tracer is likely to be recovered at the downstream monitoring point(s) in the aquifer.

Fig. 5 shows the basic experimental devices and their layout in the field. At each site, the tracer was injected using a peristaltic pump for injection rates lower than 3.4 l/h or a dosing pump for injection rates up to 40 l/h. Groundwater circulation was performed in each injection well in order to homogenize the tracer concentration in the well and to obtain samples at the injection point. This was accomplished using an immersed pump, with a circulation rate ranging between 0.3 and 3 m³/h.

4.2. Experimental validation in a small catchment (Brévilles, France)

The aquifer of the Brévilles spring is located in the Val d’Oise (France), 80 km north west of Paris. This

Table 2

Experimental setup data specific to injections performed on the Brévilles spring test site (\mathcal{V}_D : Darcy's flow; Q_{cr} : critical value of injection rate; M_{inj} : mass tracer injected; V_{inj} : volume tracer injected; C_{inj} : tracer concentration in the injection solution; Q_{inj} : injection rate; Q_{rec} : recirculation rate)

	Pz4	Pz19	Pz17b	Pz17c
Borehole depth (m)	28	28.4	16	21
Water column h_w (m)	14.31	9.93	5.81	11.07
Well radius r_w (m)	0.040	0.040	0.040	0.040
Well volume V_w (m ³)	0.071	0.078	0.030	0.051
Screen length e_{scr} (m)	8.9	11.9	2.9	2.9
K_{mean} (pumping test) (m s ⁻¹)	2.75×10^{-4}	4.00×10^{-4}	8.67×10^{-4}	2.75×10^{-4}
Estimated \mathcal{V}_D (m s ⁻¹)	1.1×10^{-5}	1.5×10^{-5}	1.9×10^{-5}	0.6×10^{-5}
Estimated Q_{cr} (m ³ s ⁻¹)	2.6×10^{-5}	4.6×10^{-5}	1.5×10^{-5}	4.7×10^{-6}
	(93.6 l h ⁻¹)	(165.6 l h ⁻¹)	(54.0 l h ⁻¹)	(16.9 l h ⁻¹)
Tracer	Li ⁺	Sulforhodamine B	I ⁻	Uranine
Total M_{inj} (kg)	6.6	10	19.2	5
Total V_{inj} (m ³)	0.16	0.098	0.16	0.045
C_{inj} (kg m ⁻³)	41.3	102.0	120.0	111.1
Q_{rec} (m ³ h ⁻¹)	≈ 1.0	≈ 1.0	≈ 1.0	≈ 1.0

	Injection step	Pz4			Pz19			Pz17b				Pz17c				
		1	2	Total	1	2	Total	1	2	3	4	Total	1	2	3	Total
Injection parameters	Q_{inj} (l h ⁻¹)	23.5	40.9		23.5	35.3		9.4	21.4	32.6	39.9		5.8	15.9	32.6	
	Time (min)	79	51	130	82	99	181	59	35	30	25	149	101.5	31	16	149
	Volume (m ³)	0.031	0.035	0.066	0.032	0.066	0.098	0.009	0.013	0.016	0.017	0.055	0.010	0.008	0.009	0.027
	Tracer mass (kg)	1.28	1.45	2.73	3.26	6.73	10.00	1.08	1.56	1.92	2.04	6.60	1.11	0.88	0.99	2.98
Results	Calculated \mathcal{V}_D (m.s ⁻¹)		9.8×10^{-6}		1.0×10^{-5} – 3.0×10^{-5}					2.5×10^{-5}				4.0×10^{-5}		
	Calculated Q_{cr} (m ³ s ⁻¹)		2.18×10^{-5}		3.01×10^{-5} – 9.04×10^{-5}					1.82×10^{-5}				2.91×10^{-5}		
			(78.5 l h ⁻¹)		(108.4–325.4 l h ⁻¹)					(65.5 l h ⁻¹)				(104.8 l h ⁻¹)		

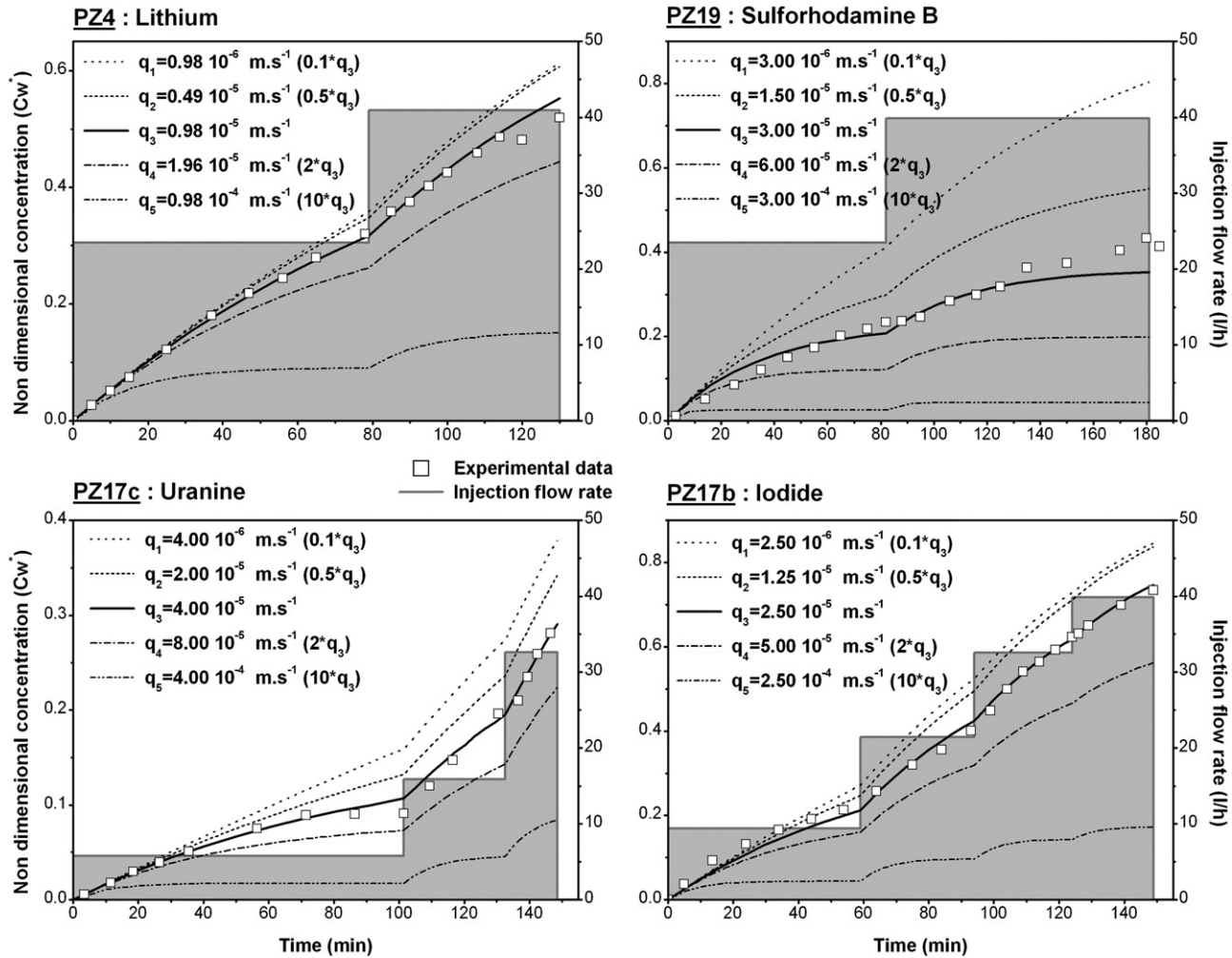


Fig. 7. Monitored and modelled concentration evolution and injection flow rates (Brévilles spring test site experiments).

catchment has been studied for years by BRGM because of a problem with atrazine at the spring (Morvan et al., 2006; Roulier et al., 2006). The aquifer is mainly located in the Cuisian sandy formation limited at its base by a low permeability clay (Fig. 6). These sands are medium in the upper part of the formation to very fine in the lower part. The aquifer system is assumed unconfined and extends over approximately 11.6 km². Several springs are observed along the boundary between the sands and the clay. The Brévilles spring is the most important of them and it is considered as the main outlet of the aquifer (Fig. 6).

4.2.1. Description of the injections

Four tracer injections were performed in November 2005, in PZ4, PZ19, PZ17b and PZ17c (Fig. 6). All the details about these injections are provided in Table 2. PZ4 is screened in the lower part of the aquifer where the flow is assumed to be slower. PZ19 is screened over the whole thickness of the aquifer. PZ17 consists of three piezometric boreholes about 2 m distant from each other. The three boreholes are screened at 3 different levels in the aquifer, in the Lutetian limestone lying above the sands (PZ17a), in the upper (PZ17b) and in the lower part (PZ17c) of the Cuise sands, respectively. Tracer quantities were defined to increase the chances of detecting the tracers at the Brévilles spring, which explains the high tracer concentrations that could appear atypical and unnecessarily high for a single FVPDM monitoring. For each experiment, successive steps of constant injection rate were performed. During each injection, samples were collected in

the injection well at an approximate frequency of 1 sample every 5 min. Generally, 2 to 4 injection steps were performed, after which the remaining quantity of tracer was injected in a short time to finalize the tracer injection in a reasonable time.

Table 2 presents data on the tracer injections and the technical characteristics of the injection wells. Fig. 7 shows the injection steps together with the concentration evolutions in the four injection wells.

4.2.2. Modelling results

Simulated concentrations were adjusted by modifying only the apparent Darcy flux v_{ap} . The other terms appearing in Eq. (1) were defined based on the experimental conditions only (Q_{inj} , C_{inj} , V_{inj} , ...).

Fig. 7 allows comparison of monitored concentrations and adjusted concentrations, using the FVPDM method. In each diagram, the solid thick curve corresponds to the best adjustment of Darcy flux ($v_{ap} = q_3$). The other curves were calculated for v_{ap} equal to $10 \times q_3$, $2 \times q_3$, $0.5 \times q_3$ and $0.1 \times q_3$, respectively, to check the sensitivity of the method to the magnitude of the Darcy flux. Fig. 7 shows that the calculated curves almost perfectly match experimental data. Small differences can however be observed for PZ19 probably due to the difficulty in controlling injection conditions because of the very high tracer concentration required. There were problems to keep the concentration of the tracer fluid perfectly homogeneous in the container. It is thus possible that, during the first injection steps, the tracer concentration in

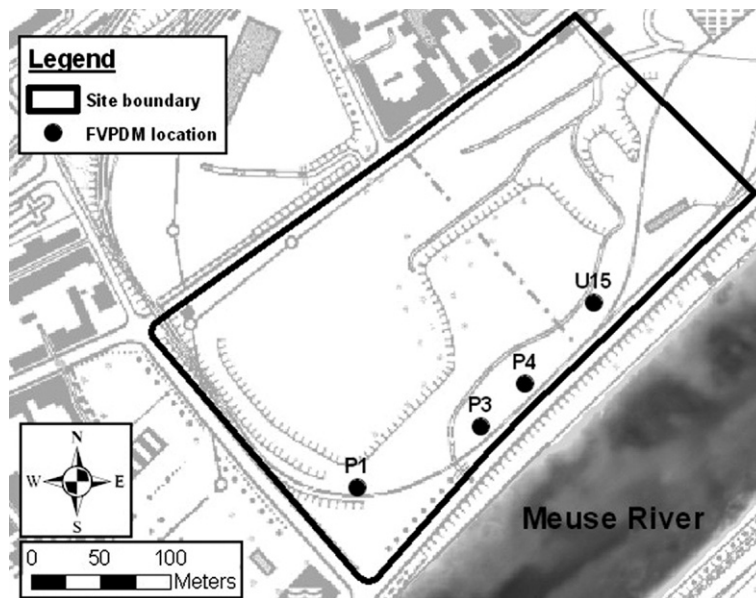


Fig. 8. Location map of wells used in field tracer injections in site A.

Table 3

Characteristics of wells used during injections and experimental set-up characteristics of tracer injections performed in site A (v_D : Darcy's flow; Q_{cr} : critical value of injection rate; M_{inj} : mass tracer injected; V_{inj} : volume tracer injected; C_{inj} : tracer concentration in the injection solution; Q_{inj} : injection rate; Q_{rec} : recirculation rate)

		U15				P4				P3			P1			
Borehole depth (m)		14.2				15.5				15.0			18.2			
Water column h_w (m)		6.66				7.32				7.03			10.11			
Well radius r_w (m)		0.05				0.075				0.075			0.075			
Well volume V_w (m ³)		0.05				0.13				0.12			0.18			
Screen length e_{scr} (m)		3.0				5.5				4.25			4.25			
K_{mean} (pumping test) (m s ⁻¹)		3.3×10^{-3}				1.1×10^{-3}				4.0×10^{-4}			2.7×10^{-4}			
Estimated v_D (m.s ⁻¹)		1.1×10^{-5}				4.8×10^{-6}				9.8×10^{-7}			5.6×10^{-7}			
Estimated Q_{cr} (m ³ s ⁻¹)		1.1×10^{-5}				1.3×10^{-5}				1.9×10^{-6}			1.1×10^{-6}			
		(39.6 l h ⁻¹)				(46.8 l h ⁻¹)				(6.84 l h ⁻¹)			(3.96 l h ⁻¹)			
Tracer		Br ⁻				Γ				Sluforhodamine B			Uranine			
Total M_{inj} (kg)		2.69				2.77				4.45×10^{-5}			4.25×10^{-5}			
Total V_{inj} (m ³)		0.46				0.98				0.50			0.50			
C_{inj} (ppm)		5818				2775				0.088			0.085			
Q_{rec} (m ³ h ⁻¹)		0.3				3.0				1.0			0.3			
	Injection step	1	2	3	Total	1	2	3	4	Total	1	2	Total	1	2	Total
Injection parameters	Q_{inj} (l h ⁻¹)	9.3	32.9	20.3		1.5	5.4	19.2	39.4		1.7	22.8		10.5	20.1	
	Time (h)	3.00	9.58	5.92	18.50	23.4	12.62	20.73	12.30	69.05	29.37	19.83	49.20	19.08	14.92	34.00
	Volume (m ³)	0.028	0.315	0.120	0.463	0.035	0.068	0.398	0.485	0.986	0.050	0.450	0.500	0.200	0.300	0.500
Results	Tracer mass (kg)	0.16	1.83	0.70	2.69	0.10	0.19	1.12	1.36	2.77	4.4×10^{-6}	4.0×10^{-5}	4.4×10^{-5}	1.7×10^{-5}	2.5×10^{-5}	4.2×10^{-5}
	Darcy's flow V_D (m.s ⁻¹)	$2.05 - 3.1 \times 10^{-4}$				2.7×10^{-5}				1.5×10^{-5}			3.0×10^{-6}			
	Calculated Q_{cr} (m ³ .s ⁻¹)	$1.93 \times 10^{-4} - 2.92 \times 10^{-4}$				7.0×10^{-5}				3.02×10^{-5}			6.02×10^{-6}			
		(694.8–1051.2 l h ⁻¹)				(252.0 l h ⁻¹)				(108.7 l h ⁻¹)			(21.6 l h ⁻¹)			

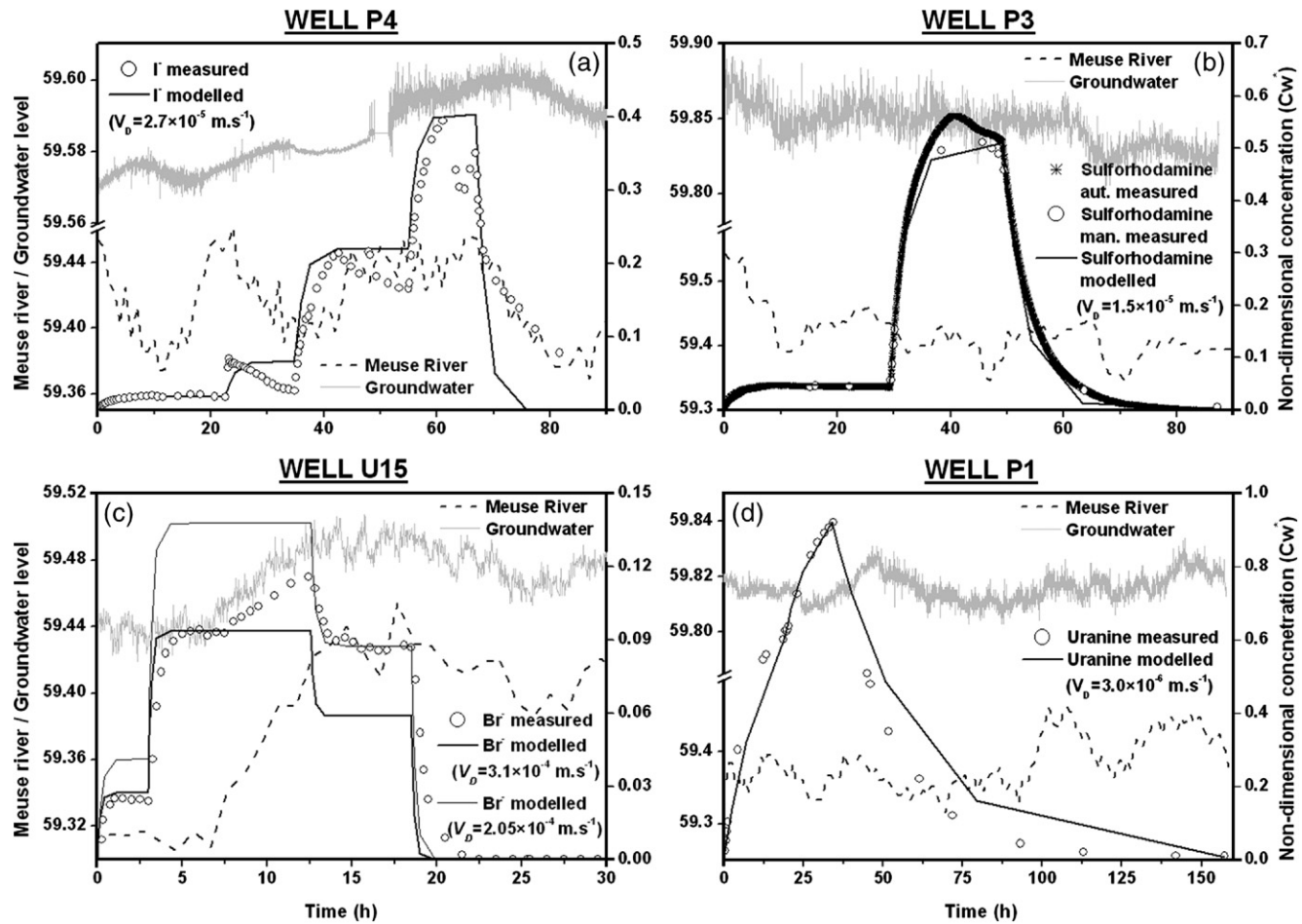


Fig. 9. Comparison between concentration evolutions monitored and modelled in site (V_D is the Darcy's flow) and representation of the Meuse River level and groundwater level in site A.

the injected fluid was lower than expected, the remaining quantity of tracer being injected afterwards.

All the adjustment results are summarized in Table 2. The Darcy fluxes estimated using the FVPDM technique are in good agreement with a priori estimates obtained using the pumping test results and the application of Darcy's law between the injection point and the spring.

4.3. Experimental validation in a brownfield test site (Walloon Meuse basin, Belgium)

The brownfield under investigation corresponds to a former cokery whose activities during the 20th Century have heavily contaminated the soil, subsoil, alluvial deposits and groundwater. The main aquifer is located in the fluvial gravels sediments deposited by the Meuse River overlying the low permeability carboniferous substratum made of shale and sandstone, from 7 m depth to the bedrock (~ 14 m depth). The topography is flat and the mean hydraulic gradient is low with a value approximately equal to 0.1%.

This test site has been the subject of many investigations during the last 15 years. In this context, many complementary investigations have been performed: borehole drilling, soil and subsoil sampling, hydrogeological investigations such as groundwater monitoring, pumping tests, infiltration tests, etc. This site being fenced, protected and very well equipped (power supply, water available etc), it was possible to define a more advanced protocol and experimental device than in Brévilles.

Various tracer experiments were performed at the site, including FVPDM tests performed in 4 observation wells (U15, P4, P3 and P1) located at the border of the site, at distances ranging from 30 m to 50 m to the Meuse River (Fig. 8). The characteristics of the injection wells are summarized in Table 3.

4.3.1. Description of the injections

Tracer solutions were stored in 500 l barrels. At this site, the volume of tracer fluid and the injection durations were determined to optimize the chances of reaching the stabilization of concentration in the injection well for each injection step, as explained in Fig. 4. Tracers were continuously injected and monitored in each well during several days. Iodide was injected in well P4 using four steps of increasing injection rates, sulforhodamine B in well P3 using two steps of increasing injection rates, bromide in well U15 using two steps of increasing injection rates followed by one step with a decreased injection rate, and uranine in the well P1 using two steps

of increasing injection rates. The characteristics of each injection are summarized in Table 3.

With the saline tracers (iodide and bromide), the evolution of concentration was continuously monitored by measuring the electrical conductivity with a YSI 600 XLM probe in the circulation water compared to the electrical conductivity measured in the injection fluid. With fluorescent tracers, a field fluorometer (GGUN-FL30 #1370) was used to monitor the evolution of concentration during the experiment. During each experiment, samples were also taken using an ISCO 6700 automatic sampler and manually (control samples) in order to be analyzed in the laboratory. Groundwater level and temperature were also continuously monitored in the injection wells (every 2 min) using a pressiometric TrollLevel probe.

Fig. 9 shows the concentration evolutions in the injection wells during and after the tracer injections, together with water levels monitored in the injection well and in the Meuse River. Most often, the various injection steps were clearly identifiable, but the monitored concentrations in the injection wells hardly reached stability, as expected by the FVPDM theory for long-duration injections. The reason is that the injection wells are very near the Meuse River and river stage variations generate a pressure wave which is propagated into the aquifer (Workman et al., 1997; Barlow and Moench, 1998; Barlow et al., 2000; Srivastava et al., 2006), as revealed by the continuous monitoring of groundwater and surface water levels performed in the test site. River stage variations generate indirectly local changes in the hydraulic gradients in the aquifer and thus changes in groundwater fluxes close to the injection wells. This phenomenon was observed during most of the injection experiments. During the "transient" phase of the evolution of concentration in the injection well, at the beginning of each tracer injection step, the influence of the changes in groundwater fluxes is not as visible because it overlaps with the "normal" rise of concentration. On the contrary, when the tracer concentration has stabilized in the injection well, changes in groundwater fluxes induce variations in the transit flow rate across of the screens and thus variations in the tracer concentration in the well. This perturbation is clearly visible when looking at the concomitant changes in water levels in the Meuse River and the "anomalies" in concentration monitored in the injections wells. In Fig. 9a and in the second injection step of the Fig. 9b, the observed decreases in Meuse levels are systematically associated with observed decreases in concentrations in the well because the hydraulic gradient and Darcy fluxes are increased in the vicinity of the injection well. On the contrary, during the stabilized phase

of the second step of bromide injection in well U15 (Fig. 9c), an increase in tracer concentration is observed, corresponding to a rise in water levels in the Meuse because the hydraulic gradient and Darcy fluxes are reduced close to U15.

4.3.2. Modelling results

Using Eq. (1), calculated evolutions of concentrations were fitted to the monitored ones by modifying the apparent Darcy flux v_{ap} (Fig. 9). Similar to Brévilles tests, all other terms appearing in Eq. (1) were defined based on the experimental conditions (Q_{inj} , C_{inj} , V_w ...). The results are summarized in Table 3. Considering that the influence of changes in water levels in the Meuse was not taken into account directly in the interpretation, one can consider that tracer concentration evolutions calculated with the analytical solution are very close to the measured ones. As explained before, for the injection performed in U15, the strong deviation of concentration observed during injection in step 2 is related to a rise of about 15 cm in the Meuse water level during the FVPDM experiment. For a Darcy flux of $3.1 \times 10^{-4} \text{ m s}^{-1}$, the first injection step and the beginning of the second step are well reproduced, but not the third for which the calculated concentration is too low. These results are consistent with the fact that the rise in Meuse water level has reduced the gradient and thus Darcy fluxes in the gravel aquifer near the river bank. The third step was adjusted separately, using a lower Darcy flux equal to $2.05 \times 10^{-4} \text{ m s}^{-1}$.

The estimated Darcy fluxes are similar in P3 and P4, on the order of $2 \times 10^{-5} \text{ m s}^{-1}$ while in the vicinity of well P1, they are 10 times lower, around $3 \times 10^{-6} \text{ m s}^{-1}$. In the vicinity of well U15, the estimated Darcy flux is approximately 10 times higher of those in P3 and P4, of the order of $2 \times 10^{-4} \text{ m s}^{-1}$. This seems to indicate a zone of higher hydraulic conductivity in the region of U15.

4.4. Possible limitations of the FVPDM

The two case studies where the FVPDM was applied indicate that it is applicable in a large range of contexts. However, two limitations should be mentioned. Because of the water circulation required in the injection well for the homogenization of the tracer concentration and for sampling, the FVPDM can not be used for profiling groundwater fluxes along well screens, contrary to the PDM. It is also likely that the FVPDM technique would be more difficult to apply in large or very deep wells where the homogenization of concentration would not be evident because the turnover of water in the well bore would be long. However, developments are on the way

to develop the use of the FVPDM in deep wells, as a tracer-based well logging technique, where the water circulation system is progressively moved along the well axis.

5. Conclusions and perspectives

One of the main outcomes of this research is the development of a new tracer technique for the quantification of Darcy fluxes in groundwater. The mathematical framework has been described and discussed in detail and, from a more practical point of view, detailed guidelines are provided in the experimental setup of the technique, derived from the sensitivity analysis of a non-dimensional formulation of the model. This technique can be used as a “stand-alone” single-well tracer experiment or in combination with any other tracer technique, in which case it can provide a control of injection conditions together with complementary information on groundwater flows in the vicinity of the injection well.

The two case studies presented show that the FVPDM technique has a wide range of applications where the quantification of Darcy fluxes is required, for very contrasting objectives and experimental conditions. For the two case studies, the results indicate that the technique is very robust, reliable and sensitive to groundwater flow conditions. The interpretation can take advantage of both the rising and the stabilized part of the concentration evolutions in the injection well.

As a consequence of its high sensitivity to experimental conditions, the FVPDM is also a candidate technique for studying and monitoring changes in Darcy fluxes and groundwater flows in transient conditions, such as changes in hydraulic gradients, with potential applications in monitoring the dynamics of groundwater — surface water interactions in the hyporheic zone. To do so, one needs to continuously inject a tracer at a very low rate and to monitor the temporal changes in concentration in the injection well. The analytical solution could be straightforwardly extended to account for dynamically changing Darcy fluxes and volumes of water in the injection well.

It would also be very interesting to see if the FVPDM interpretation can not be improved by interpreting the long-term behaviour of the tracer concentration evolution in the injection well using asymptotic approaches, such as those proposed by Jaekel et al. (1996), Vasco and Datta-Gupta (1999), Vereecken et al. (1999a,b) or Haggerty et al. (2000). This improvement could provide useful complementary information on the physico-chemical behaviour of the tracer in the aquifer. The FVPDM could also be efficiently combined to passive flux meters (Hatfield et al., 2004) for a better assessment

of cumulated groundwater fluxes at the vicinity of the monitored well.

A Fortran 90 programme was written in order to calculate the concentration evolution in the injection well and the actual tracer input function in the aquifer for arbitrary tracer injection configurations. It is available from the corresponding author upon request.

Notation and units

C_{in}	variable accounting for the concentration in any injected fluid (generic notation) [$M L^{-3}$]	v_{ap}	apparent Darcy flux prevailing in the aquifer, as measured in the injection well [$L T^{-1}$]
C_{inj}	tracer concentration in the injected fluid during tracer injection [$M L^{-3}$]	\underline{v}_D	Darcy flux prevailing in the aquifer without the distorting influence of the injection well [$L T^{-1}$]
C_t	variable accounting for the tracer concentration in the transit flux intercepted by the well screens [$M L^{-3}$]	v_r	radial Darcy flux (in a coordinates system centred on the well) [$L T^{-1}$]
C_w	variable accounting for the tracer concentration in the injection well [$M L^{-3}$]	v_θ	tangential Darcy flux (in a coordinates system centred on the well) [$L T^{-1}$]
$C_{w,0}$	initial concentration of tracer in the injection well [$M L^{-3}$]	V_{in}	variable accounting for any volume of injected fluid (generic notation) [L^3]
$C_{w,einj}$	residual tracer concentration in the injection well at the end of the injection of the tracer fluid [$M L^{-3}$]	V_{inj}	volume of tracer fluid injected in the well [L^3]
$C_{w,en}$	residual tracer concentration in the injection well at the end of the flushing operations [$M L^{-3}$]	V_{fl}	volume of water flush injected in the well after tracer injection [L^3]
$C_{w,stab}$	stabilized concentration in the well [$M L^{-3}$]	V_w	volume of water in the injection well [L^3]
C_{DL}	tracer concentration representing the device detection limit [$M L^{-3}$]	V_w^{mix}	mixing volume of water usually equal to V_w [L^3]
C_{SL}	tracer concentration representing the device saturation limit [$M L^{-3}$]	V_t	volume of water intercepted by the screen of the well during tracer injection [L^3]
e_{scr}	length of the well screens [L]	α_w	distortion coefficient accounting for the discontinuity introduced in the flow field by the injection well bore [–]
h_w	height of the water column in the well bore [L]		
M_{inj}	mass of tracer injected in the well [M]		
Q_{cr}	critical injection flow rate [$L^3 T^{-1}$]		
Q_{in}	variable accounting for the any injection flow rate (generic notation) [$L^3 T^{-1}$]		
Q_{inj}	injection flow rate during tracer injection operations [$L^3 T^{-1}$]		
Q_{fl}	injection flow rate during flushing operations [$L^3 T^{-1}$]		
Q_{out}	flow rate leaving the well through the screens [$L^3 T^{-1}$]		
Q_t^0	transit flow rate across the well screens under natural groundwater flow conditions [$L^3 T^{-1}$]		
Q_t^{in}	variable accounting for the transit flow rate intercepted by the well screens as a function of the injection rate Q_{in} (generic notation) [$L^3 T^{-1}$]		
r_w	radius of the injection well [L]		
T_{inj}	tracer injection duration [T]		
T_{fl}	water flush duration [T]		
T_w	time needed to replace the water in the well at the critical injection flow rate [T]		

Non-dimensional formulations:

$$C^* = \frac{C}{C_{inj}}, Q^* = \frac{Q}{Q_{cr}}, V^* = \frac{V}{V_w}, t^* = \frac{t}{T_w}$$

Acknowledgements

This work was supported by the European Union FP6 Integrated Project AquaTerra (Project no. 505428) under the thematic priority, sustainable development, global change and ecosystems and by Research funds provided by Aquapôle-ULg. Mr. B. Belot, from the Laboratory of water analysis of HGULg performed the analyses of lithium and iodide. Dr. Ph. Meus, from the SME “European Water Tracing Services — EWTS”, assisted in using the field fluorimeter and performed the analyses of the fluorescent tracers. They are gratefully acknowledged for suggestions and comments on the interpretation of the results. Thanks to the BRGM — Water Division, especially C. Mouvet who gave us the opportunity to work on the Brévilles test site and A. Gutierrez who assisted in the field experiments. Thanks to the SPAQuE, especially H. Halen and A. Lox, for access to data and to the brownfield in the alluvial plain of the Meuse River in Belgium. Thanks are also due to P. Theunissen (SPE-TGV) for his gracious contribution on Meuse data time series. Special thanks to René Therrien for his careful review of the manuscript.

References

- Arntzen, E.V., Geist, D.R., Dresel, P.E., 2006. Effects of fluctuating river flow on groundwater/surface water mixing in the hyporheic zone of a regulated, large cobble bed river. *River Res. Applic.* 22 (8), 937–946.
- Australian Government, http://www.connectedwater.gov.au/framework/stream_flow_dilution.php, 2006.
- Barlow, P.M., Moench, A.F., 1998. Analytical solutions and computer programs for hydraulic interactions of stream-aquifer systems. USGS, Marlborough, Massachusetts, USA. 99 pp.
- Barlow, P.M., DeSimone, L.A., Moench, A.F., 2000. Aquifer response to stream-stage and recharge variations. II. Convolution method and applications. *J. Hydrol.* 230, 211–229.
- Battle-Aguilar, J., Brouyère, S., 2005. Documentation of site equipment and description of experiments performed and still planned in the former cokery test site A. Deliverable R3.15, AquaTerra (Integrated Project FP6 no. 505428). 22 pp.
- Battle-Aguilar, J., Brouyère, S., 2006. Update on field experiments and description of the groundwater flow and transport model for the cokery site A., AquaTerra (Integrated Project FP6 no. 505428). 50 pp.
- Bidaux, P., Tsang, C.-F., 1991. Fluid flow patterns around a well bore or an underground drift with complex skin effects. *Water Resour. Res.* 27 (11), 2993–3008.
- Brouyère, S., 2001. Etude et modélisation du transport et du piégeage des solutés en milieu souterrain variablement saturé (Study and modelling of transport and retardation of solutes in variably saturated media). Faculté des Sciences Appliquées. Laboratoire de géologie de l'ingénieur, d'Hydrogéologie et de Prospection géophysique. Université de Liège, Liège, Belgium, p. 640 (In French).
- Brouyère, S., 2003. Modeling tracer injection and well-aquifer interactions: a new mathematical and numerical approach. *Water Resour. Res.* 39 (3). doi:10.1029/2002WR001813.
- Brouyère, S., Carabin, G., Dassargues, A., 2005. Influence of injection conditions on field tracer experiments. *Ground Water* 43, 389–400.
- Brusseau, M.L., 1994. Transport of reactive contaminants in heterogeneous porous media. *Rev. Geophys.* 32 (3), 285–313.
- Devlin, J.F., McElwee, C.D., 2007. Effects of measurement error on horizontal hydraulic gradient estimates. *Ground Water* 45 (1), 62–73.
- Drost, W., Klotz, D., Arnd, K., Heribet, M., Neumaier, F., Rauert, W., 1968. Point dilution methods of investigation ground water flow by means of radioisotopes. *Water Resour. Res.* 4 (1), 125–146.
- Gilman, K., 1977a. Dilution gauging on the recession limb: 1. Constant rate injection method. *Hydrol. Sci. Bull.* 22 (3), 353–369.
- Gilman, K., 1977b. Dilution gauging on the recession limb: 2. The integration method. *Hydrol. Sci. Bull.* 22 (4), 469–481.
- Goderniaux, P., Brouyère, S., 2006. Report on the tracer tests (experimental setup, results and interpretation). Deliverable H2.3, AquaTerra (Integrated Project FP6 no. 505428). 49 pp.
- Haggerty, R., McKenna, S.A., Meigs, L.C., 2000. On the late-time behavior of tracer test breakthrough curves. *Water Resour. Res.* 36 (12), 3467–3479.
- Hall, S.H., 1996. Practical single-well tracer methods for aquifer testing. Tenth National Outdoor Action Conference and Exposition, Columbus, Ohio, USA. Natural Groundwater Association.
- Hatfield, K., Annable, M., Cho, J., Rao, P.S.C., Klammner, H., 2004. A direct passive method for measuring water and contaminant fluxes in porous media. *J. Contam. Hydrol.* 75, 155–181.
- Havely, E., Moser, H., Zellhofer, O., Zuber, E., 1967. Borehole dilution techniques: a critical review. *Isotopes in Hydrology*. I.A.E. A., Vienna, Austria.
- Jaekel, U., Georgescu, A., Vereecken, H., 1996. Asymptotic analysis of nonlinear equilibrium solute transport media. *Water Resour. Res.* 32 (10), 3039–3098.
- Kalbus, E., Reinstorf, F., Schirmer, M., 2006. Measuring methods for groundwater–surface water interactions: a review. *Hydrol. Earth Syst. Sci.* 10, 873–887.
- Klotz, D., Moser, H., Trimborn, P., 1978. Single-borehole techniques; present status and examples of recent applications. Symposium IAEA, Neuherberg, Germany.
- Li, L., Barry, D.A., Culligan-Hensley, P.J., Bajracharya, K., 1994. Mass transfer in soils with local stratification of hydraulic conductivity. *Water Resour. Res.* 30 (11), 2891–2900.
- Morrison, S.J., Metzler, D.R., Dwyer, B.P., 2002. Removal of As, Mn, Mo, Se, U, V and Zn from groundwater by zero-valent iron in a passive treatment cell: reaction progress modeling. *J. Contam. Hydrol.* 56, 99–116.
- Morvan, X., Mouvet, C., Baran, N., Gutierrez, A., 2006. Pesticides in the groundwater of a spring draining a sandy aquifer: temporal variability of concentrations and fluxes. *J. Contam. Hydrol.* 87, 176–190.
- Roulier, S., Baran, N., Mouvet, C., Stenemo, F., Morvan, X., Albrechtsen, H.J., Clausen, L., Jarvis, N., 2006. Controls on atrazine leaching through a soil-unsaturated fractured limestone sequence at Brévilles, France. *J. Contam. Hydrol.* 84, 81–105.
- Ruehl, C., Fisher, A.T., Hatch, C., Los Huertos, M., Stemler, G., Shennan, C., 2006. Differential gauging and tracer tests resolve seepage fluxes in a strongly-losing stream. *J. Hydrol.* 330, 235–248.
- Srivastava, K., Serrano, S.E., Workman, S.R., 2006. Stochastic modeling of transient stream-aquifer interaction with the nonlinear Boussinesq equation. *J. Hydrol.* 328, 538–547.
- Valocchi, A.J., 1985. Validity of the local equilibrium assumption for modelling sorbing solute transport through homogeneous soils. *Water Resour. Res.* 21 (6), 808–820.
- Vasco, D.W., Datta-Gupta, A., 1999. Asymptotic solutions for solute transport: A formalism for tracer tomography. *Water Resour. Res.* 35 (1), 1–16.
- Vereecken, H., Jaekel, U., Esser, O., Nitzsche, O., 1999a. Solute transport analysis of bromide, uranine and LiCl using breakthrough curves from aquifer sediment. *J. Contam. Hydrol.* 39, 7–34.
- Vereecken, H., Jaekel, U., Georgescu, A., 1999b. Asymptotic analysis of solute transport with linear nonequilibrium sorption in porous media. *Transp. Porous Media* 36, 189–210.
- Workman, S.R., Serrano, S.E., Liberty, K., 1997. Development and application of an analytical model of stream/aquifer interaction. *J. Hydrol.* 200, 149–163.
- Wroblicky, G.J., Campana, M.E., Valett, H.M., Dahm, C.N., 1998. Seasonal variation in surface–subsurface water exchange and lateral hyporheic area of two stream-aquifer systems. *Water Resour. Res.* 34 (3), 317–328.



Contribution of the finite volume point dilution method for measurement of groundwater fluxes in a fractured aquifer



P. Jamin^a, P. Goderniaux^{b,c}, O. Bour^b, T. Le Borgne^b, A. Englert^d, L. Longuevergne^b, S. Brouyère^{a,*}

^a University of Liège, Fac. Applied Sciences, Dpt ArGenCo, Geo³-Hydrogeology and Environmental Geology, Building B52, 4000 Sart Tilman, Belgium

^b Géosciences Rennes (UMR CNRS 6118)-OSUR, University of Rennes 1, Rennes, France

^c University of Mons, Department of Geology and Applied Geology, Mons, Belgium

^d Ruhr-Universität Bochum, Geology, Mineralogy and Geophysics, Bochum, Germany

ARTICLE INFO

Article history:

Received 22 April 2015

Received in revised form 25 August 2015

Accepted 3 September 2015

Available online 8 September 2015

Keywords:

Finite volume point dilution method

Groundwater flux

Uncertainty analysis

Double packer

Single-well tracer test

Fractured aquifer

ABSTRACT

Measurement of groundwater fluxes is the basis of all hydrogeological study, from hydraulic characterization to the most advanced reactive transport modeling. Usual groundwater flux estimation with Darcy's law may lead to cumulated errors on spatial variability, especially in fractured aquifers where local direct measurement of groundwater fluxes becomes necessary.

In the present study, both classical point dilution method (PDM) and finite volume point dilution method (FVPDM) are compared on the fractured crystalline aquifer of Ploemeur, France. The manipulation includes the first use of the FVPDM in a fractured aquifer using a double packer. This configuration limits the vertical extent of the tested zone to target a precise fracture zone of the aquifer. The result of this experiment is a continuous monitoring of groundwater fluxes that lasted for more than 4 days.

Measurements of groundwater flow rate in the fracture (Q_f) by PDM provide good estimates only if the mixing volume (V_w) (volume of water in which the tracer is mixed) is precisely known. Conversely, the FVPDM allows for an independent estimation of V_w and Q_f , leading to better precision in case of complex experimental setup such as the one used. The precision of a PDM does not rely on the duration of the experiment while a FVPDM may require long experimental duration to guarantee a good precision.

Classical PDM should then be used for rapid estimation of groundwater flux using simple experimental setup. On the other hand, the FVPDM is a more precise method that has a great potential for development but may require longer duration experiment to achieve a good precision if the groundwater fluxes investigated are low and/or the mixing volume is large.

© 2015 Elsevier B.V. All rights reserved.

1. Introduction

Estimation of groundwater fluxes remains the basis of all hydrogeological study, from hydraulic characterization to the most advanced reactive transport modeling. Investigations on contaminant behavior, design of remediation systems, groundwater–surface water interactions or geothermal applications, all would benefit from a precise quantification of

groundwater fluxes and their temporal and spatial variability. Groundwater fluxes are usually indirectly calculated with Darcy's law from piezometric gradient measurements and the estimation of hydraulic conductivity with pumping/slug tests. This simple method may be adequate for the estimation of general groundwater fluxes in homogeneous media but the resolution is generally low, leading to cumulated errors on spatial variability in heterogeneous context (Bright et al., 2002; Devlin and McElwee, 2007).

Estimation of groundwater fluxes in fractured aquifer is a challenge given the heterogeneity that is induced by discrete

* Corresponding author.

E-mail address: Serge.Brouyere@ulg.ac.be (S. Brouyère).

fractures (Novakowski, 2006). The characterization of fracture flow based on hydraulic pressure measurements can actually lead to misinterpretation about the role of the fracture in terms of flow path and solute transport. For example, a dead-end fracture subjected to pumping will respond in terms of hydraulic pressure variations even if no groundwater flow is occurring. Zha et al. (2014) recently emphasized that flux data used in hydraulic characterization of fractured media improve estimation of fracture patterns and hydraulic conductivity fields.

Therefore, tracer tests become essential tools because they allow studying the actual displacement of water. Classical tracer tests provide averaged information between two injection and recovery points. Alternative methods, such as point dilution tracer tests are promising to obtain a direct measurement of local groundwater fluxes or Darcy fluxes (q_D) (Halevy et al., 1967; Klotz et al., 1979; Zlotnik and Zurbuchen, 2003; Brainerd and Robbins, 2004; Hatfield et al., 2004; Huang and Goltz, 2005; Pitrak et al., 2007; West and Odling, 2007; Sale et al., 2007). Novakowski et al. (1995 and 2006) performed classical dilution tests between packers and pointed out two major issues. The first issue is related to the estimation of the actual mixing volume (V_w), which has to be accurately known to interpret the dilution test. This mixing volume is difficult to calculate in the case of dilution test performed between the packers because the test space is full of equipment (hoses, probes, mixing propellers ...) and may include zone of immobile water. Furthermore, the geometry of the borehole in front of the tested zone may not be perfectly cylindrical and part of the adjacent fractured medium may also be involved in the mixing processes. The second issue is that groundwater velocity changed during their experiments and disturbed the recording. The point dilution method (PDM) is actually a short time experiment that is constrained by both the maximum concentration that can be injected and the minimum concentration that can be measured in the well. The experiment stops when the entire amount of tracer has been eluted from the well, precluding continuous monitoring of groundwater fluxes.

The finite volume point dilution method (FVPDM) (Brouyère, 2003; Brouyère et al., 2005; Brouyère et al., 2008) allows overcoming those two issues and provides a quantification by a simultaneous and independent estimation of the mixing volume (V_w) and Darcy's flux (q_D) on experimental data. The duration of the test is not limited and can last as long as the experiment is maintained active by injecting tracer and monitoring its concentrations in the mixed water volume. Measurements of groundwater flux at a local scale, as achieved with this method, are complementary with more regional and indirect estimations from Darcy's law. The method was tested successfully in porous media (Brouyère et al., 2008; Goderniaux et al., 2010), but has never been experienced in fractured aquifers.

In this context, the objectives of this paper are twofold: (1) test the method in a fractured geological context; and (2) compare the FVPDM with classical PDM on the same experimental site, hydraulic conditions, and experimental setup. The comparison investigates the relative precision of the two techniques on the measurement of groundwater fluxes and it provides guidelines for dilution experiments in fractured media. The contribution of the FVPDM for groundwater flux measurement in fractured aquifer is also discussed in terms of experimental setup.

A series of tracer dilution experiments were performed in the Ploemeur test site (Britany, France) on several fractured zones of an open well. For the first time, the FVPDM was used between a double-packer system to investigate localized groundwater flows in discrete fractures. Successive experiments were carried out with different pumping rates applied at a nearby well, to investigate the largest range of possible groundwater flux measurements, and to study the consistency of results over this range. Classical PDM was also performed following each FVPDM experiment to compare the sensitivity and uncertainties of both methods. After a description of the methodology and the experimental setup, the results of the groundwater flux measurements are discussed along with uncertainties on the interpretation of the FVPDM and PDM.

2. Methodology

2.1. Point dilution techniques

The aim of a single borehole dilution test is to perform a direct measurement of groundwater fluxes. Point dilution methods relate the concentration evolution of a tracer previously injected in a borehole as a function of the intensity of groundwater flow through the screen of the borehole. The result of such test is a groundwater flux, which depends on the hydraulic conditions within the geological formation and in the vicinity of the tested borehole (Drost et al., 1968; Hall, 1996). Since the first use of PDM in 1916 reported by Halevy et al. (1967), many PDM configurations have been tested, including the experiments by Kaufmann and Todd (1962) and Novakowski et al. (1998, 2006), using inflatable packers to limit the vertical extension of the investigated zone. The tracer can be salt species, fluorescent dyes or radio isotopes (Klotz et al., 1979).

The finite volume point dilution method (FVPDM) generalizes the PDM to more advanced tracer injection scenarios. The FVPDM is performed by continuously injecting a tracer fluid into a well and monitoring the evolution of the tracer concentration into the same well. During all the experiment, the water column within this well is mixed to ensure a homogeneous repartition of the tracer mass. This method is originally based on a mathematical and a numerical model of tracer injection into a well, considered as a mass balance of the injection of tracer fluid and transit groundwater flow passing through the well screen (Brouyère, 2003). An analytical solution obtained from this model (Eq. (1)) was further applied as a single well tracer technique, enabling an accurate estimation of Darcy fluxes (Brouyère et al., 2008).

$$C_w(t) = \frac{Q_{in} \times C_{in} - (Q_{in} \times C_{in} - Q_{out} \times C_{w,0}) \times e^{-\frac{Q_{out}}{V_w} \times (t-t_0)}}{Q_{out}} \quad \text{with} \\ Q_{out} = Q_{in} + Q_t^{in} \quad (1)$$

The tracer concentration within the well $C_w(t)$ [$M L^{-3}$] can be calculated at each time t [T] using the parameters defined by the experimental setup C_{in} [$M L^{-3}$] the tracer concentration in the injection solution, $C_{w,0}$ [$M L^{-3}$] the tracer concentration within the well at initial time t_0 [T], Q_{in} [$L^3 T^{-1}$] the tracer fluid injection flow rate and V_w [L^3] the volume of water in the

injection well, assumed to be constant. Q_{out} [$L^3 T^{-1}$], the flow rate leaving the well through the screen, carrying tracer at concentration C_w and representing the sum of Q_{in} and Q_t^{in} [$L^3 T^{-1}$] the transit flow rate intercepted by the well screen during tracer fluid injection at a rate Q_{in} . When $Q_{in} = 0$, $Q_t^{in} = Q_{out}$ and can be defined as Q_t , the transit flow rate under ambient conditions. Q_t is directly related to the Darcy's flux v [$L T^{-1}$] by the flow section A [L^2] perpendicular to the groundwater flow. This area corresponds for fractured aquifer to the aperture of the fractures multiplied by the diameter of the borehole. Q_t^{in} , Q_t and v is related by the Eqs. (9) and (13) described in details in Brouyère et al., 2008.

Note that the dimensioning of a FVPDM experiment required an a priori estimation of a critical injection rate Q_{cr} [$L^3 T^{-1}$] (Eq. (2)). If the tracer injection flow rate Q_{in} exceeds Q_{cr} , it induces a hydraulic loading of the well, which completely cancels the transit flow rate, making the experiment invalid.

$$Q_{cr} = \pi Q_t \quad (2)$$

During the experiment, the tracer concentration first increases in the injection well, until reaching a plateau when steady state conditions are observed between the rate of tracer injection and the rate of tracer that is carried out of the well by the groundwater flow. The experiment can thus be divided into three phases (Fig. 1). The first phase corresponds to transient concentrations and its duration is a function of the mixing volume V_w and the transit flow rate Q_t . The steady state conditions are reached faster if the mixing volume is small and the transit flow rate is high. The second phase begins when the concentration C_w in the well has stabilized, corresponding to steady state conditions. At this moment, C_w only depends on the tracer injection flow rate and on the transit flow rate (see Brouyère et al., 2008 Eq. 16 for more details). As a consequence, the interpretation of a FVPDM test consists in (1) calculating the transit flow rate from the steady state C_w and (2) in adjusting the mixing volume (V_w) to fit the transient phase of the experiment. Allowing the system to reach this steady state strongly increases the precision of the FVPDM interpretation because the two unknown parameters of the FVPDM equation

(V_w and Q_t) can be determined independently on different parts of the experimental curve. At the end of the experiment, the injection of tracer is stopped and this last phase corresponds to a classical dilution.

Considering Eq. (1), the classical PDM (Eq. (3)) is only a specific case of the FVPDM, for $Q_{in} = 0$ and $C_{w,0} > 0$. C_w is related to the ratio of the transit flow rate on the mixing volume, in an exponential decay relation. This implies that the precision of the calculation of the transit flow rate (Q_t) fully relies on an accurate external estimation of the mixing volume (V_w). The transit flow rate could then be converted into a Darcy's flux v [$L T^{-1}$] by the flow section A [L^2] perpendicular to the undisturbed groundwater flow.

$$C_w(t) = C_{w,0} \times e^{-\frac{Q_t}{V_w}(t-t_0)} \quad (3)$$

Considering the assumptions that are inherent to the classical PDM and FVPDM, both methods are affected by a priori limits. Classical PDM requires (1) steady state of the aquifer groundwater flow during a time sufficient for estimating Q_t , (2) an homogeneous mixing of a large amount of the tracer in the water column instantaneous at the beginning and continuously during the experiment and (3) the accurate and precise knowledge of the mixing volume. The quality of FVPDM relies on the duration of the experiment. In the case of large mixing volume and/or limited groundwater flux, the FVPDM may require a long time to reach the steady state phase.

2.2. Experimental test site

The Stang Er Brune experimental test site is located at Ploemeur on the south coast of Brittany (France), in a crystalline rock aquifer constituted of micashists and granites (Fig. 2a). This site belongs to the H+ observatory (<http://hplus.ore.fr/en/>) which is a national network of highly instrumented research sites in subsurface hydrology. The site is equipped with three uncased, 0.12 m diameter wells of 80 to 100 m depth (B1, B2 and B3) and separated by less than 10 m and arranged in a triangular shape (Fig. 2b). At this location the contact between the micashists and the underlying granite is observed at about

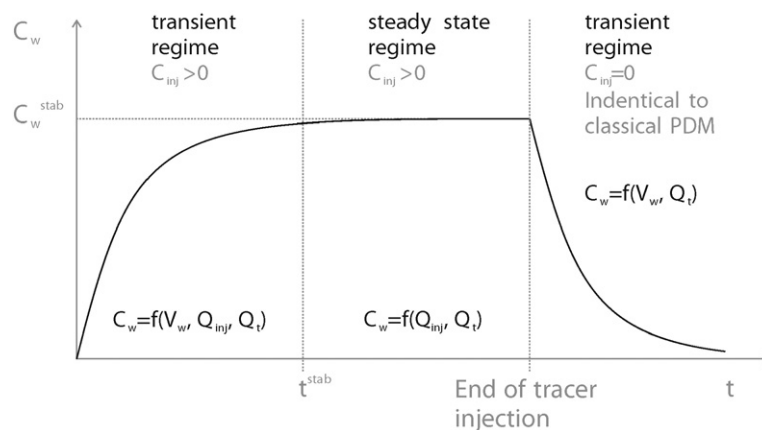


Fig. 1. Evolution of tracer concentrations (C_w) in a well where a FVPDM is performed. The steady state regime is reached when the mass flux of tracer injected in the well equilibrate with the mass flux of tracer flushed out of the well by the groundwater flow that transit by the well screen. The experiment ends as a classical PDM when the injection of tracer is stopped.

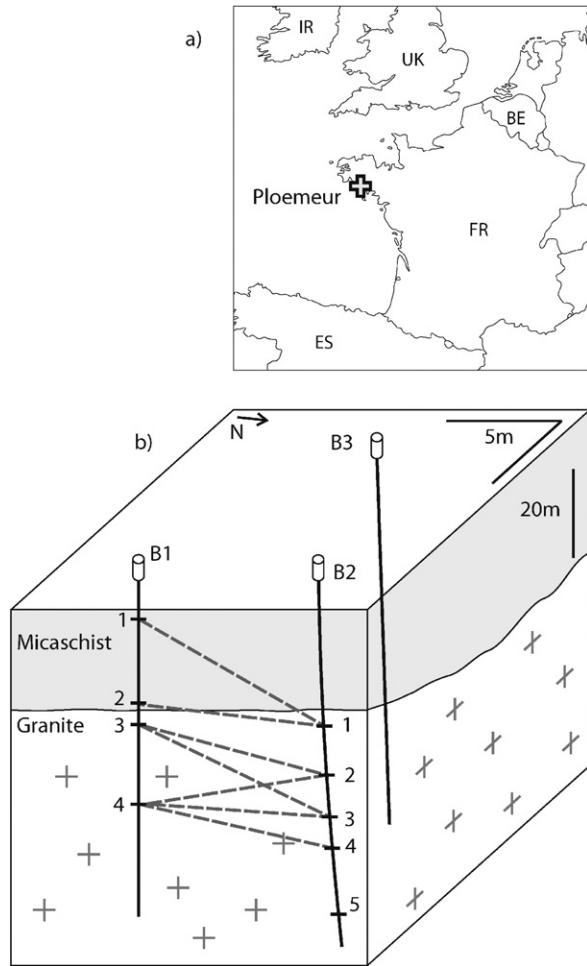


Fig. 2. a) Location of the Ploemeur test site. b) Configuration of the three 90 m deep wells (B1, B2, B3), and the fracture network. Dashed lines represent the hydraulic connections by group of fractures between B1 and B2 identified by tracer tests (Le Borgne et al., 2007; Dorn et al., 2012).

40 m below ground surface. The mean transmissivity obtained by various hydraulic tests in all the wells is around $10^{-3} \text{ m}^2/\text{s}$ (Le Borgne et al., 2006 and b). For the experiments described in this paper, two of the open boreholes (B1 and B2) were used. Wells B1 and B2 are intersected by 4 and 5 fracture zones, respectively, which are designated B1-1 to B1-4 and B2-1 to B2-5 (Fig. 2b).

This site offers several advantages. (1) The fractured aquifer has already been characterized by geophysical, thermal, hydraulic and tracer tests (Le Borgne et al., 2007; Dorn et al., 2012; Read et al., 2013). (2) Open boreholes without any casing are suitable for instrumentation with packers. (3) The small distances between the wells ensure a hydraulic connection that can be exploited for the purposes of the FVPDM experiments, i.e., to modify the transit flow rate Q_t in a given fracture set in the test well by pumping one of the other wells.

2.3. Double packer experimental setup

The experiments were performed in the deepest fracture zone identified in the well B1 (B1-4), where optical imagery

showed two open fractures of 3 cm aperture in total at 78.7 m below the surface. The transmissivity of this fracture zone was estimated at $1.6 \times 10^{-4} \text{ m}^2/\text{s}$ (Klepikova et al., 2014). The flow section $A [L^2]$ perpendicular to the direction of the groundwater flow is then 0.0036 m^2 .

The experimental setup is designed to support FVPDM testing between a double packer system, which isolates the fracture zone (Fig. 3). Vertical borehole flows are prevented and the dilution experiment is carried out within the delineated space. The length of the test chamber between the upper and lower inflatable packer was 1.2 m. Pressure sensors were used to monitor piezometric head below, between and above the double packer in order to detect any leaky seals. A submersible pump was connected above the upper packer and linked to the test chamber to create a water circulation loop between the packers and the ground surface, where the loop was connected to a field fluorimeter, a pressure gauge, a water meter (to monitor flow rate of circulated water) and an electromagnetic pump for the low flow rate tracer injection. From the surface, the loop was completed at a connection allowing tracer injection at the bottom of the double packer test chamber (Fig. 3). The B2 well, located 6 m away from B1, was equipped with a submersible pump to impose the groundwater fluxes around B2 and in all the surrounding fractures, including the fractured zone identified in B1-4. The FVPDM-PDM experiments were performed for different pumping rates in well B2 in order to investigate the ability and limitations of the two dilution methods to measure different groundwater fluxes. B2 pumping rates ranged from 0 and $2.4 \times 10^{-3} \text{ m}^3/\text{s}$ (0 to 144 L/min). Groundwater levels are also monitored in B2 and B3 wells using STS pressure sensors.

FVPDM experiments were performed under specified pumping flow rates in well B2. When the conditions have stabilized in the vicinity of wells (no pressure variations greater than 1 cm in 5 min), the tracer injection was started and the tracer concentration was monitored in the test chamber (thanks to the circulation loop). The circulation flow rate was precisely maintained at $4.2 \times 10^{-5} \text{ m}^3/\text{s}$ (2.52 L/min) and the tracer injection at $3.5 \times 10^{-7} \text{ m}^3/\text{s}$ (0.02 L/min) with a concentration of 207 ppb of fluoresceine (CAS no. 518-47-8). In total, a succession of 10 FVPDM (F1 to F10) and 8 classical PDM (P1 to P8) experiments was performed iteratively (Table 1). Mixing volume V_w and transit flow rate Q_t were then adjusted on the experimental data for each test separately. For the PDM experiments, an external estimations of V_w was used (i.e., independent of the interpretation of the exponential decay of tracer concentration observed during the PDM experiment). Uncertainties around adjusted values were estimated, and the results obtained for PDM and FVPDM compared and discussed.

2.4. Uncertainty estimation using a Bayesian approach

An adequate management of uncertainties is a critical issue in experimentation, and more generally in model calibration. Various sources of uncertainties co-exist (observations, experiment set up, simplified interpretation model) and might affect the parameter inference process. The Bayesian approach is a preferred method to perform inversion of nonlinear problems, and has been widely used to invert geophysical or hydrogeological data (e.g., Tarantola and Valette, 1982; Ghorbani

et al., 2007; Fasbender et al., 2008). This approach consists in propagating the knowledge provided by measurements m through a known and supposed to be exact forward model G (here the dilution Eqs. (1) and (3)), and to combine with an a-priori knowledge of model parameters (here, mixing volume V_w and transit flow rate Q_t). Here, we will use a simplified definition of the posterior density function $p(\theta)$ for the parameter vector θ (Tarantola and Valette, 1982). It can be calculated from the a-priori probability density function $\mu(\theta)$

(here taken as uniform), the sum of squared residuals (SSR) between the model with parameter θ and observations m , as $SSR = \sum (m - G(\theta))^2$ and the standard deviation of measured data σ as

$$p(\theta) = \mu(\theta) \times e^{-\left(\frac{\sqrt{SSR(\theta)}}{2\sigma}\right)^2}. \quad (4)$$

Parameter uncertainties are finally computed as marginal probability density function.

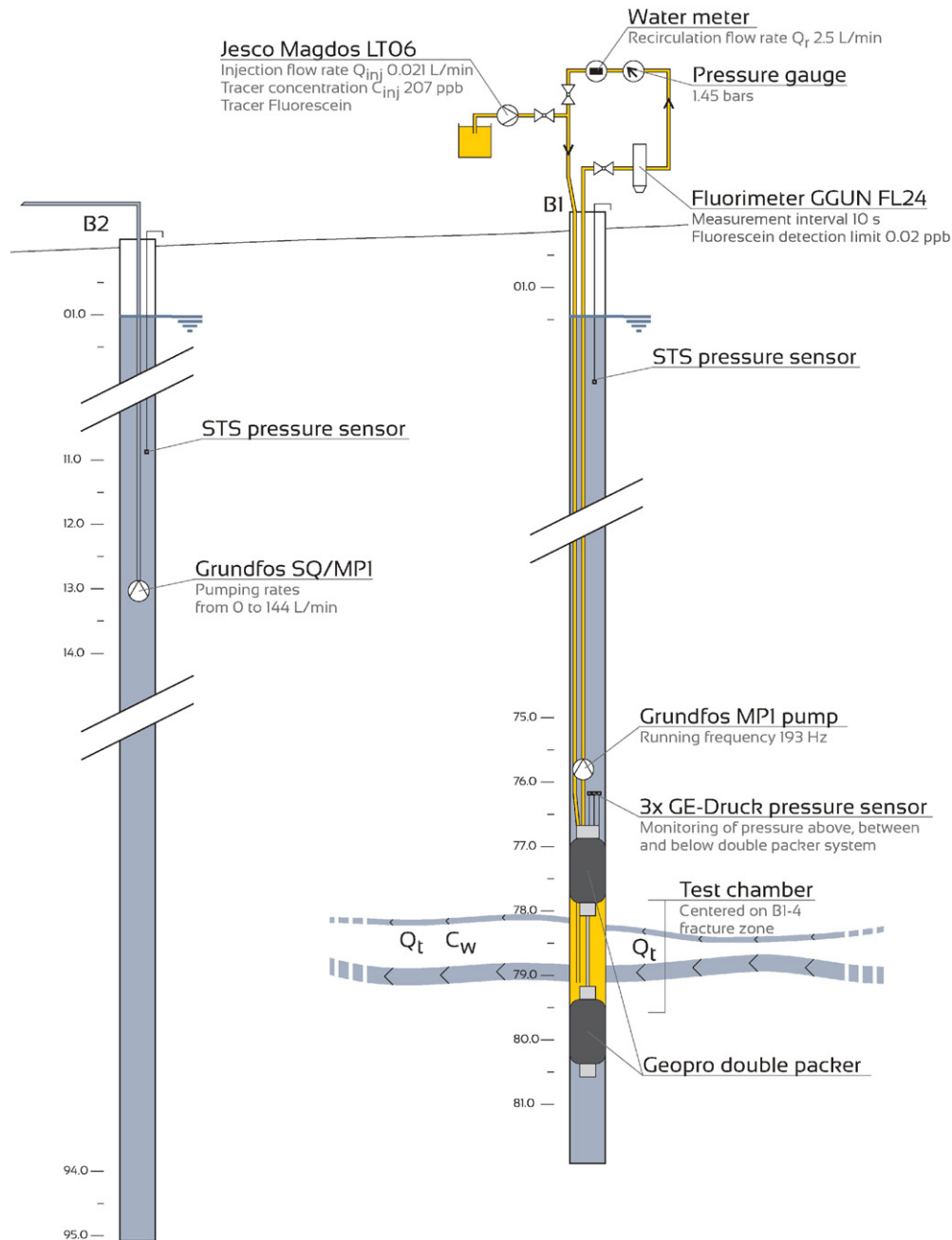


Fig. 3. Experimental setup limiting vertically the investigated fracture zone with double packers. The dilution tests are performed within this 1.2 m delineated test chamber. The corresponding volume of groundwater is mixed using a pump and circulated to the surface, where tracer is injected using a dosing pump. Concentration of tracer in the loop is monitored using a field fluorimeter placed in line. An immersed pump placed in the nearby well B2 allows the modification of the groundwater fluxes in the fracture B1-4. The aperture of the fractures is not at scale.

3. Results

Fig. 4 shows the experimental data of the succession of FVPDM–PDM tests conducted within the fracture B1–4 under different pumping rates in the nearby well B2. PDM experiments correspond to the periods when the tracer injection flow rate is null (Fig. 4b). The cumulated measurement time exceeds 100 h. As explained in previous sections, it is observed that the time to reach the steady state regime of FVPDM is longer when the pumping rate in B2, and thus the transit flow rates in fractures, decreases. The steady state concentration C_w^{stab} is also higher in this case, due to less important dilution effects.

Each phase of the experiment, corresponding to a specific pumping rate in the well B2 and to the PDM or FVPDM configuration, was interpreted separately. The adjustment of V_w and Q_t was performed by evaluating the RMS error between the experimental C_w values and the C_w values simulated using the analytical solutions of the PDM (Eq. (2)) and FVPDM (Eq. (1)).

3.1. Interpretation of a selected FVPDM and PDM experiment

Fig. 5 shows the results for the FVPDM and PDM experiment no. 3 (FVPDM 3 and PDM 3, see Table 1 for experimental setup parameters) for a specific pumping rate (Q_{pump}) of $1.5 \times 10^{-3} \text{ m}^3/\text{s}$ (90 L/min) in well B2. Fig. 5a shows the FVPDM experimental and simulated curves, which present the typical evolution of the tracer concentration with a transient phase at the beginning of the experiment and a steady state at the end of the test when the system has reached equilibrium. Fig. 5c is the RMS error plot between experimental data (FVPDM 3) and the simulated curves, obtained for different values of V_w and Q_t . The graph shows that a minimum RMS value is relatively well identified, corresponding to a unique (V_w, Q_t) pair that best fits the experimental data (Fig. 5a). These values are V_w equal to 35.6 L and Q_t equal to $7.43 \times 10^{-6} \text{ m}^3/\text{s}$.

Fig. 5b and d is similar but corresponds to the PDM experiment no. 3. The experimental curve (Fig. 5b) shows the expected exponential decrease of the concentrations with time. However, with this method, it is rather difficult to adjust V_w and

Q_t independently. A ratio Q_t/V_w of $2.12 \times 10^{-4} \text{ s}^{-1}$ can be fitted on experimental results and, theoretically, a large range of couples (V_w, Q_t) are possible. Accordingly, the RMS error obtained for the adjustment of V_w and Q_t (Fig. 5d) shows that a minimum RMS value cannot be identified and that the solution is not unique. Consequently, the mixing volume has to be precisely known to constrain the PDM model and to estimate the transit flow rate correctly.

Note that the values in the RMS plots depend on the data and duration of the experiments, but the shape of these plots will generally remain similar for longer experimental time.

3.2. External estimations of V_w for PDM interpretation

Estimating the actual mixing volume based on the characteristics of the experimental setup is difficult, mainly because of the geometry of the well, the use of the double packer system, the presence of equipment in the test chamber, and the use of circulation loop. It has been estimated to approximately 29 L, but the uncertainty on this value is unknown because the estimation was only based on the length and radius of the circulation pipes and on the dimension of the test chamber (radius of the well and distance between upper and lower packer when they are inflated) without taking into account the various equipment present within this delineated space. In this study, the actual mixing volume has been estimated using an alternative method based on an experimental artifact. At Fig. 5, PDM and FVPDM curves show oscillations (sequential plateaus) at the beginning of the experiment that attenuate with time. This artifact is due to a non-instantaneous mixing of tracer in the whole recirculated water volume. At the beginning or stopping of the tracer injection, a front of high or low concentration develops when the tracer injection is started or stopped. The mean wavelength of these oscillations has been estimated using Fourier transformations for all the dilution experiments and is equal to $762 \text{ s} \pm 119 \text{ s}$ (95% confidence interval). It actually corresponds to the time necessary for the water to travel the entire water circulation loop. Considering a circulation flow rate (Q_r) of 0.042 L/s, V_w equals $32 \pm 5 \text{ L}$.

Table 1

Characteristics and sequence of tracer injections for FVPDM and PDM experiments on well B1–4. $C_{w,0}$ is the initial tracer concentration in well B1–4 at the beginning of the experiment. Q_{pump} corresponds to the pumping rate at well B2 and Q_{inj} to the tracer injection flow rate at a concentration C_{in} of 207 ppb.

Id	Duration [h]	$C_{w,0}$ in B1-4 [ppb]	Q_{in} in B1-4 [$\times 10^{-7} \text{ m}^3/\text{s}$]	Q_{pump} in B2 [$\times 10^{-3} \text{ m}^3/\text{s}$]
FVPDM 1	4.02	0	3.5	2.39
PDM 1	0.88	5	0	2.39
FVPDM 2	2.35	0.2	3.5	1.86
PDM 2	2.28	6.1	0	1.86
FVPDM 3	6.70	0.3	3.5	1.46
PDM 3	1.67	9.2	0	1.46
FVPDM 4	3.39	1.4	3.5	1.00
FVPDM 5	2.83	12.5	3.5	0
PDM 4	1.88	31.4	0	0
PDM 5	2.24	30.3	0	1.00
FVPDM 6	3.15	10.2	3.5	1.00
FVPDM 7	8.67	14.1	3.5	0.63
FVPDM 8	7.84	23.2	3.5	0
PDM 6	5.93	68.0	0	0
PDM 7	2.45	64.9	0	0.63
FVPDM 9	28.01	2.4	3.5	0.31
FVPDM 10	8.72	45.1	3.5	0.62
PDM 8	2.10	23.5	0	0.29

Using this value, the transit flow Q_t rate can be calculated from PDM experiments. For PDM no. 3 experiment, it is equal to $6.82 \times 10^{-6} \text{ m}^3/\text{s}$. Both values for V_w (32 L) and Q_t ($6.82 \times 10^{-6} \text{ m}^3/\text{s}$) agree with FVPDM estimates ($V_w = 35.6 \text{ L}$ and $Q_t = 7.43 \times 10^{-6} \text{ m}^3/\text{s}$) within 10% of error.

3.3. Evaluation of uncertainties on the adjustment of V_w and Q_t for a selected FVPDM and PDM test

Both FVPDM and PDM can be used to estimate groundwater fluxes within the B1–4 fracture zone. However, the two methods are different and the confidence to be attributed to the results has to be determined. The uncertainties on calculated fluxes are related to the adjustment of the analytical solutions on experimental data and to the confidence on the V_w value, in the case of the PDM. The analysis of uncertainties is based on the exploration of Q_t and V_w values between specified intervals, using Eqs. (1) and (2). The RMS errors between the experimental and simulated C_w values have been converted into probabilities according to Eq. (4) (see Section 2.4).

The probabilities are calculated for the FVPDM and PDM experiment no. 3. They are multiplied with the normal distribution related to the estimation of V_w , equal to $32 \text{ L} \pm 5 \text{ L}$, to draw the probability plots presented in Fig. 6. These plots are further used to calculate the most probable value for V_w and Q_t and the 95% confidence intervals (Table 2), for both PDM and FVPDM. Considering the results related to the experiment no. 3, the 95% confidence interval on the calculated transit flow rate is more than five times smaller for the FVPDM than for the PDM. These methodology and results are also dependent on the respective durations of the experiments, which are not equivalent in this case. To conclude about the general performances of both methods, the issues related to the duration

of the different experiments are further discussed in the next section.

3.4. Influence of the duration of the experiment

The accuracy of the adjusted values for the PDM and FVPDM increases with the duration of the experiment. Concerning the FVPDM, this accuracy reaches a maximum value when the tracer concentration has stabilized in the injection well. The time to reach this steady state increases as the mixing volume increases and the transit flow rate decreases. To compare the FVPDM and PDM including the ‘time’ issue, uncertainties on the adjusted Q_t are investigated as a function of a normalized experiment duration. A normalized time t^* independent of V_w and Q_t is used and is obtained by dividing the mixing volume V_w by the critical injection flow rate Q_{cr} (see Section 2.1).

$$t^* = \frac{V_w}{Q_{cr}} = \frac{V_w}{\pi \times Q_t} \quad (5)$$

The uncertainty around Q_t^0 has been calculated for the FVPDM and PDM experiment no. 3, but by artificially considering on specific fractions of the available experimental data, corresponding to specific numbers of t^* (Fig. 7). Considering Eq. (1), the critical time t_c , necessary to reach 99% of the steady state concentration, is reached after $13.9 t^*$. If Q_{in} is small enough and neglected in comparison to Q_t , this critical time tends to $14.5 t^*$. This is in accordance with the results shown in Fig. 7. The total duration of the FVPDM no. 3 is $16.8 t^*$. The corresponding non-dimensional time for the PDM no. 3 allowed only a duration of $4.5 t^*$.

The uncertainty (P05–P95) around the calculated transit flow rate Q_t decreases significantly with time for the FVPDM. The FVPDM is less precise for the determination of Q_t for short

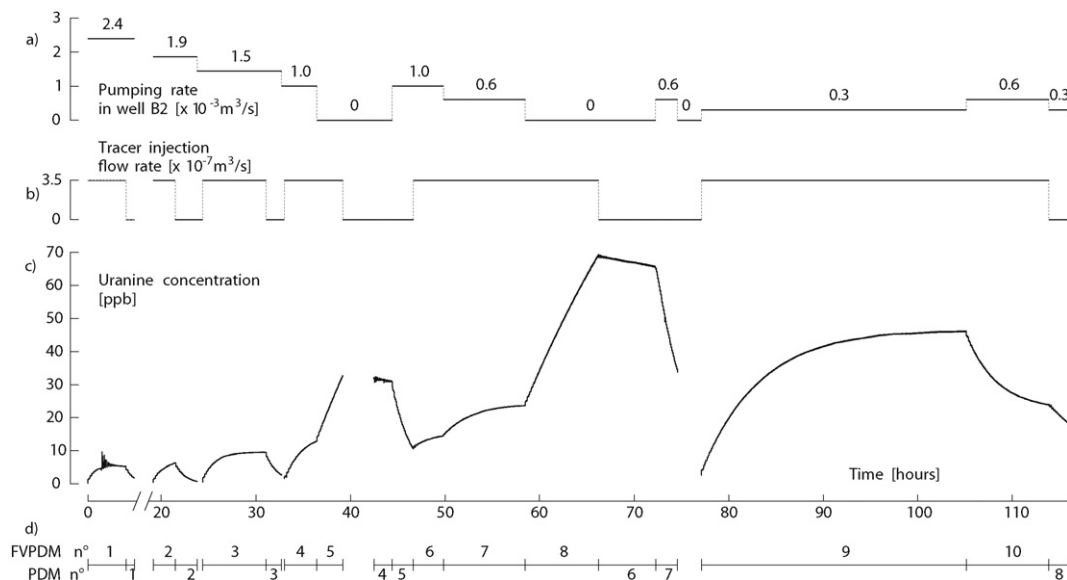


Fig. 4. Evolution of tracer concentration (c) during the measurement of groundwater flow by FVPDM and PDM in the B1–4 fracture. The distinction between natural and forced hydraulic conditions is represented by the pumping rate applied in the well B2 (a). The distinction between FVPDM and PDM experiments is figured by the tracer injection flow rate (b), PDM being performed when Q_{in} is null. Discontinuity in the measurement of tracer concentration is due to stops of the fluorimeter during equipment manipulations. Spike of tracer concentration during FVPDM no. 1 is due to a technical problem but does not prevent the interpretation of the test. The identification numbers of the FVPDM and PDM successive experiments are named in Fig. 4d.

experiment durations (t lower than approximately $4 t^*$ or $0.29 t_c$) and clearly overestimates the value of Q_t . In this field campaign, this is partly explained by the non-uniform mixing of tracer in the circulated volume, which disturbed the increase of tracer concentration at the beginning of the experiment. It also comes from the time required for a good estimate. But for long experiment, the accuracy of measurements becomes very good, with an uncertainty less than 10% of Q_t , for duration higher than $10 t^*$ or $0.72 t_c$. Concerning the classical PDM, the uncertainty also decreases with time due to the attenuation of oscillations in tracer concentration at the beginning of the dilution and but seems to stay relatively high, around 25% of Q_t . But this uncertainty is only dependent on the precision of the externally estimated V_w (see previous sections). Although the uncertainty is relatively high, the mean estimates are acceptable for all times including short times.

Whatever the duration of the PDM test, a complete FVPDM (i.e., a FVPDM that reaches the steady state) is more precise. The ‘threshold time’, when the FVPDM becomes more precise

than the PDM is in this case equal to $0.29 t_c$, but it depends on the precision of the externally estimated V_w used in the PDM experiments, and increases as V_w is more accurately estimated.

3.5. Comparison of results for different fracture flow rates

All the dilution experiments have been interpreted separately, considering an a priori estimated mixing volume of 32 ± 5 L and an unknown transit flow rate. Results are presented in Table 3 and in Fig. 8. The critical time t_c corresponds to the time necessary to reach 99% of the FVPDM steady state tracer concentration. It is estimated from Eq. (1) considering that the initial tracer concentration is zero. This critical time can be compared to the actual duration of each experiment to estimate if steady state has been reached.

The relationship between the transit flow rate in the fracture B1-4 determined by both FVPDM and PDM and the pumping rate applied in B2 (Fig. 8) appears to be linear. A slight deviation may be observed for the highest pumping rates, but

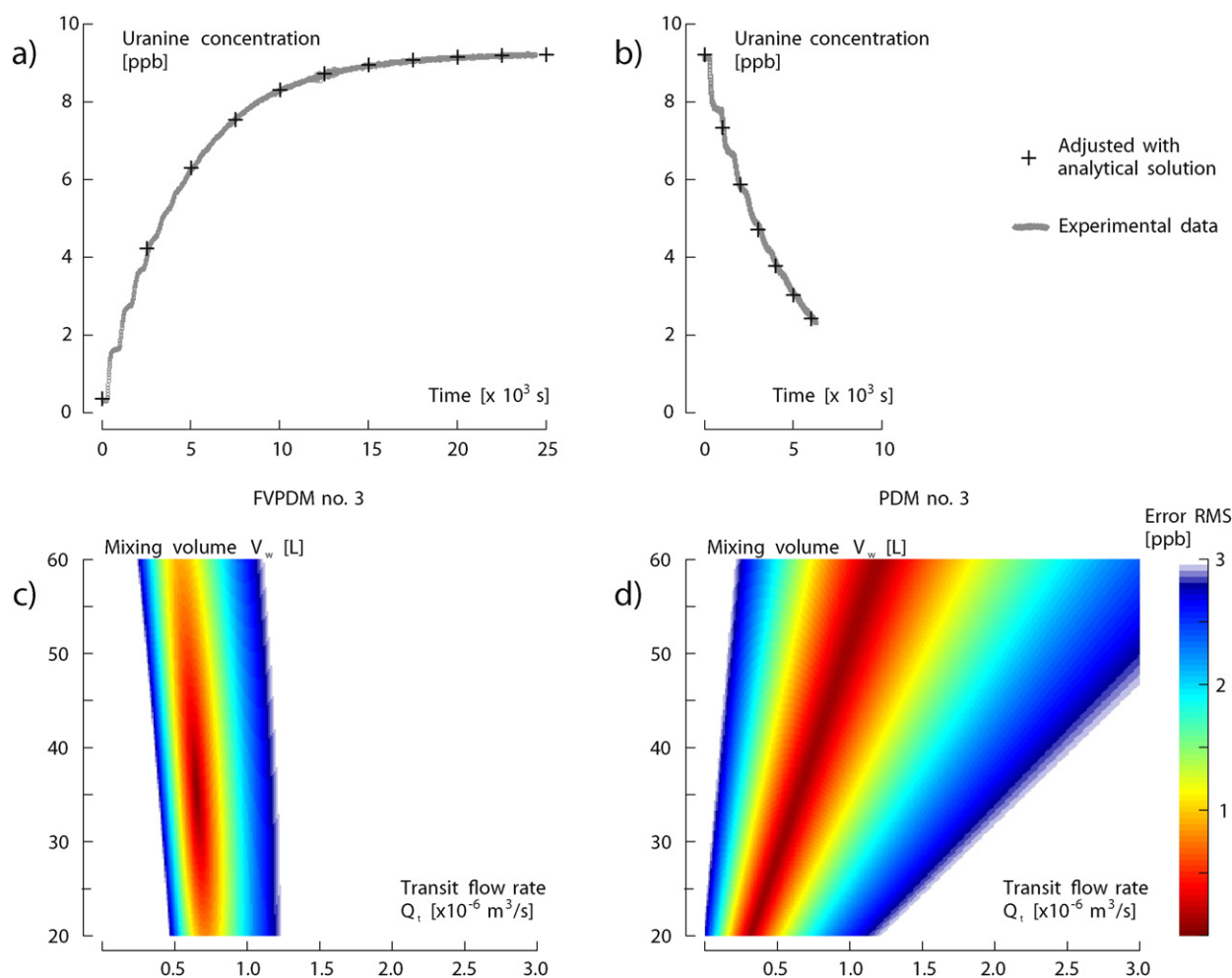


Fig. 5. Experimental data (gray points) and adjusted analytical solutions (black crosses) of FVPDM no. 3 (a) and PDM no. 3 (b) experiments corresponding to a pumping rate of 1.5×10^{-3} m³/s (90 L/min) in the B2 well. (c) and (d) are the RMS error plot for the FVPDM and PDM experiments for the adjustment of the mixing volume and the groundwater transit flow rate. A unique pair of Q_t/V_w value fits the FVPDM equation ($V_w = 35.6$ L, $Q_t = 7.43 \times 10^{-6}$ m³/s). On the contrary, a wide range of Q_t/V_w pairs that satisfies the PDM equation without being able to determine a most probable one ($Q_t/V_w = 2.12 \times 10^{-4}$ s⁻¹). Note the oscillations of tracer concentration in the well (sequential plateaus) at the beginning of FVPDM and PDM experiment.

this is difficult to confirm, given the calculated uncertainties (see discussion below). However, the relationship between the drawdown and the pumping rate in B2 (data Table 3) also presents a slight deviation from the linear behavior, suggesting that flow in the system may not be fully Darcyan.

The adjusted transit flow rates for all the dilution experiments are always higher for the FVPDM (hollow circles) than for the PDM (gray squares), but the confidence intervals are intersecting. Concerning the PDM, the information on the mixing volume is only provided externally (in this case, thanks to the oscillations artifacts), and it impacts the estimation of the transit flow rate. The bias between FVPDM and PDM results (Fig. 8 and Table 3) can be explained by underestimation of this mixing volume. This volume was estimated to 29 L based on geometric characteristics, to 32 ± 5 L based the oscillations in the experimental curves (Section 3.2), and a bit higher for the most accurate FVPDM experiments (FVPDM 3 and FVPDM 9 in Table 3). If the PDM is interpreted using a higher value for V_w , as suggested by the most accurate FVPDM tests, the adjusted Q_t converge for the FVPDM and PDM tests. This is indeed logical since the PDM is only the last part of a full FVPDM experiment. This also illustrates the need for precise external estimation of V_w , if using PDM experiments only. This level of precision is however not always possible.

The FVPDM generally presents a better precision with smaller confidence intervals, which increase with the calculated transit flow rate and pumping flow rate in well B2 (Fig. 8). The differences are due to a higher sensitivity of the FVPDM to the experimental data, and because the FVPDM is also able to provide an independent information on both transit flow rate and mixing volume. In this case, the results of Table 3 show that the adjusted V_w varies for the different FVPDM experiments. These variations of adjusted V_w can be due to the oscillations of tracer concentrations that disturb the rising part of the FVPDM curve and observation errors. This is precisely the part of the curve which is used to adjust the value of the mixing volume. This is particularly the case when the duration of the FVPDM experiment that has not last enough to reach the steady state and therefore limit the precision of the adjustments of V_w and Q_t , as explained in previous sections.

The transit flow rate estimated for the FVPDM no. 2 carried out with a pumping rate of 1.86×10^{-3} m³/s at well B2 presents a more important uncertainty and appears to deviate, compared to the other FVPDM experiments. This can be explained by a short experiment duration (see Section 3.4 and Table 3) of only $0.64 t_c$, leading to more uncertainty and potential errors. Note that the results of FVPDM no. 1 are also affected by some ‘noise’ in the experimental data (see Fig. 4), due to a technical problem, leading to more uncertainty.

No transit flow rate could be calculated for the FVPDM no. 5 and no. 8 performed with no pumping at the well B2 (i.e., under natural ambient groundwater flow in the aquifer). Under these slow groundwater flow conditions, the critical flow rate determined by the PDM nos. 4 and 6 is around 2×10^{-7} m³/s. The injection of tracer at a rate of 3.5×10^{-7} m³/s (the lowest that can be achieved with the available equipment) exceeds thus the critical injection rate Q_{cr} making the experiment invalid as explained in Section 2.1. With the available acer injection pump and an injection flow rate Q_{in} of 6×10^{-8} m³/s, t_c would have been around 10 days.

4. Discussion

A comparison of the present results with the experiments of Novakowski (2006) that performed PDM between packer shows that the FVPDM experimental setup used during this field campaign can investigate a range of Darcy's flux transit flow rate higher than Novakowski's PDM. Nevertheless the FVPDM offers a distinct estimation of V_w that is unavailable with the PDM. The measurement of fracture flow velocities of Novakowski ranges from 1.2×10^{-5} to 4.5×10^{-3} m/s, the present FVPDM performed at Ploemeur measured fractures flow from 3.1×10^{-3} to 3.8×10^{-2} m/s.

Considering these experimental data for dilution experiment no. 3, the FVPDM becomes more precise than the PDM from a time corresponding to approximately $4 t^*$ or $0.29 t_c$. This result is consistent with the initial recommendation of Brouyère et al. (2008) that recommended an experiment duration of 5 to 7 times t^* , to ensure reaching the steady state of the FVPDM. The same calculation has been carried out for all

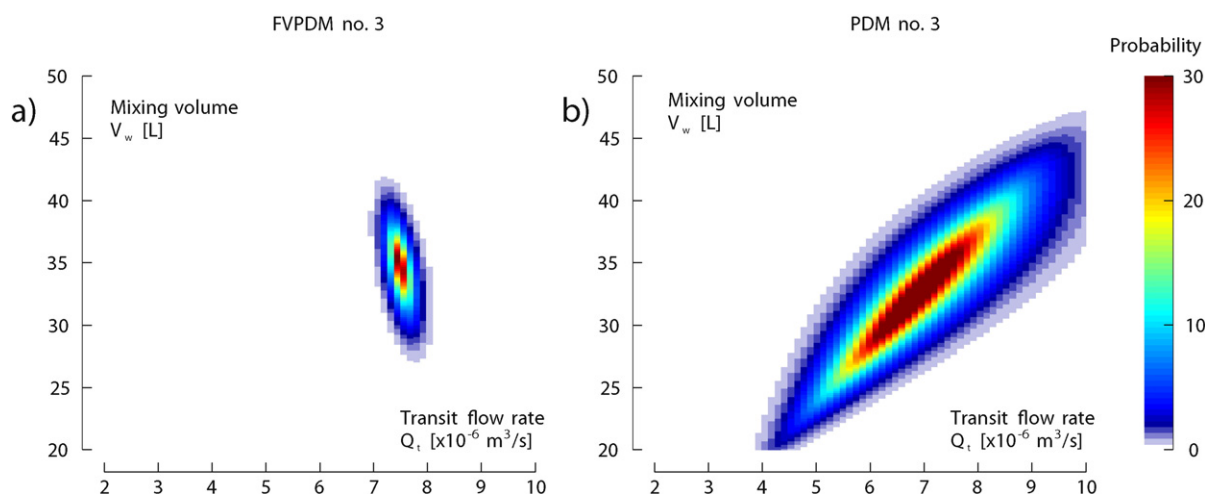


Fig. 6. Adjustment of V_w and Q_t for the experiment no. 3 (with pumping at 1.5×10^{-3} m³/h in B2) considering an a priori known V_w of 32 ± 5 L.

Table 2Results of the adjustment of the parameters Q_t and V_w considering a probability density function on V_w of 32 ± 5 L for PDM and FVPDM experiment no. 3.

	Q_t [$\times 10^{-6}$ m ³ /s]				V_w [L]			
	Adjusted	P05	P95	P95–P05	Adjusted	P05	P95	P95–P05
FVPDM 3	7.55	7.19	7.89	0.70	34.0	29.2	38.0	8.8
PDM 3	6.82	5.11	9.12	4.01	32.2	25.3	41.2	15.9

the dilution tests and shows identical trends with the precision on the adjusted Q_t increasing with time for FVPDM. This precision remains high for PDM, whatever the duration of the experiment, but mainly depends on the accuracy of the external estimation of V_w . As a conclusion, classical PDM seems to be a technique suitable for rapid results, including a large range of groundwater fluxes. However, this study has highlighted the crucial need for accuracy regarding the a priori knowledge of V_w when accuracy using PDM experiments. This accuracy actually directly affects the performance and possible bias of PDM results. At the contrary, the FVPDM is more precise, even without estimation of V_w , but may require long experiment durations under specific conditions. In case of very slow groundwater flow and large mixing volume, the time required to reach steady state may actually become very long and unmanageable. For example, if the transit flow rate Q_t is lower than 10^{-7} m³/s and the mixing volume is higher than 10 L simultaneously, the time to reach the critical time t_c (or $5 t^*$) exceeds 48 h. Furthermore, the estimation of the mixing volume V_w by the FVPDM is more robust than simply by using the geometry of the well. V_w determined by FVPDM is an apparent value that takes into account all the water that participates to the mixing of tracer. For example it can integrate an unknown dead-end fracture that would not be considered with a classic PDM and bias the result of the transit flow rate.

Considering the results of Table 3, the ratio between the transit flow rate calculated with FVPDM and the pumping flow rate in B2, ranges between 170 and 230, approximately. If the fluxes are assumed uniformly distributed around B2, this ratio should be equal to 754. This last value is obtained by considering the following values. The distance between B1 and B2 is equal to 6 m. Calculated flow rates correspond to a 0.1 m section (the diameter of B1) of the circle

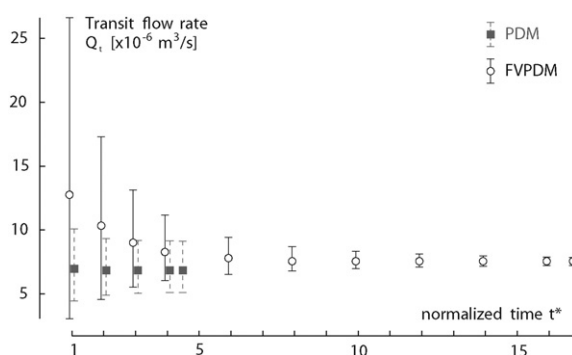


Fig. 7. Evolution of the calculated Q_t and the 95% confidence intervals, as a function of the duration of the experiment for FVPDM no. 3 (hollow circles) and PDM no. 3 (gray squares) (pumping rate of 1.5×10^{-3} m³/s in B2). t^* corresponds to a normalized time allowing the comparison between dilution experiments with different transit flow rates.

intercepting B1, and having B2 as a center. Finally, only 50% the total pumping flow rate in B2 is coming from the B1–4 fracture. This was evidenced by Read et al. (2013) using heat tracer tests. The lower experimental ratio, compared to the theoretical ratio, highlights the fact that fluxes are more probably non-uniform within the fractures, for example with some possible channelization.

From a practical point of view, an improvement of the experimental setup could be to get rid of the circulation loop by placing all the surface equipment (tracer injection pump, fluorimeter and mixing propeller) into the test chamber. In this case, the water present in the loop represents 25% of the total mixing volume. Such a reduction of V_w would significantly decrease the time to reach a steady state for the FVPDM and avoid the oscillatory effect of the circulation of tracer along the loop. The use of a dosing pump with smaller minimum tracer injection rate would also allowed for determination of smaller transit flow rate such as in natural flow conditions. Moreover, an inflatable double packer of this size (more than 4 m) is not easy to use in the field and requires heavy equipment to be installed in the well. The development of a specific probe gathering all the required equipment into a compact size device will also improve the practicality of the method.

The FVPDM nos. 4 and 5; 6, 7 and 8; and 9 and 10 were performed consecutively by maintaining the injection of tracer and changing the pumping rate at the nearby well. The changes in the groundwater flow velocity were recorded by those continuous FVPDM experiments. This highlights that the FVPDM is capable of monitoring temporal changes of groundwater flow. On the contrary, a variable groundwater flux precludes the interpretation of classical PDM because this method is based on the hypothesis that the groundwater flux is constant. Development of the FVPDM for long term monitoring of transient groundwater flow constitutes the most interesting perspective. For that, the experimental setup has to be optimized by reducing the tracer injection flow rate to avoid frequent refill of the tracer solution tank. And finally a mathematical model has to be developed to interpret the FVPDM experiment in case of transient groundwater flow.

5. Conclusions

The finite volume point dilution method has been applied to measure groundwater fluxes within a local fracture zone of the crystalline aquifer of Ploemeur, France. This manipulation is the first successful application of the FVPDM technique in a fractured aquifer and using a double packer system. Experiments have been carried out for variable groundwater flow, induced by pumping in a well located close to the tested well. In total, 10 FVPDM and 8 classical PDM were performed to compare the two methods.

Measurements of groundwater fluxes by classical PDM provide good estimates, even for short times experiments, if V_w

Table 3

Result of the dilution experiments carried out on B1–4. Uncertainties on V_w and Q_t correspond to the calculated confidence interval at 95%. t_c is the critical time necessary to reach 99% of the steady state concentration (* not interpretable).

Id	Data					Results		
	Duration [h]	Q_{pump} in B2 [$\times 10^{-3}$ m ³ /s]	Drawdown B2 [m]	Drawdown B1 [m]	Duration/ t_c [–]	Q_t [$\times 10^{-6}$ m ³ /s]	V_w [L]	ν [$\times 10^{-3}$ m/s]
FVPDM 1	4.02	2.39	1.89	0.88	1.35	13.80 \pm 1.21	32.9 \pm 5.5	38.33 \pm 3.36
PDM 1	0.88	2.39	1.89	0.88		10.69 \pm 3.66	32.5 \pm 7.9	29.69 \pm 10.17
FVPDM 2	2.35	1.86	1.30	0.60	0.64	11.6 \pm 1.80	34.5 \pm 6.5	32.22 \pm 5
PDM 2	2.28	1.86	1.30	0.60		8.56 \pm 2.63	32.4 \pm 7.9	23.78 \pm 7.31
FVPDM 3	6.7	1.46	0.98	0.44	1.22	7.55 \pm 0.35	34.0 \pm 4.4	20.97 \pm 0.97
PDM 3	1.67	1.46	0.98	0.44		6.82 \pm 2.00	32.2 \pm 7.9	18.94 \pm 5.56
FVPDM 4	3.39	1.00	0.62	0.31	0.48	4.83 \pm 0.83	28.8 \pm 5.4	13.42 \pm 2.31
PDM 5	2.24	1.00	0.68	0.37		4.25 \pm 1.16	32.4 \pm 7.9	11.81 \pm 3.22
FVPDM 6	3.15	1.00	0.68	0.37	0.43	4.60 \pm 0.23	28.2 \pm 6.4	12.78 \pm 0.64
FVPDM 7	8.67	0.63	0.36	0.17	0.67	2.78 \pm 0.08	31.7 \pm 4.4	7.72 \pm 0.22
PDM 7	2.45	0.63	0.41	0.21		2.33 \pm 0.66	32.5 \pm 7.9	6.47 \pm 1.83
FVPDM 10	8.72	0.62	0.38	0.17	0.64	2.93 \pm 0.17	34.8 \pm 6.0	8.14 \pm 0.47
FVPDM 9	28.01	0.31	0.13	0.03	1.09	1.32 \pm 0.04	33.5 \pm 2.5	3.67 \pm 0.11
PDM 8	2.1	0.29	0.17	0.06		1.20 \pm 0.32	32.7 \pm 7.9	3.33 \pm 0.89
FVPDM 5	2.83	0	0.04	0.02	0.03	*	27.0	*
PDM 4	1.88	0	0.04	0.02		0.22 \pm 0.09	32.5 \pm 10.2	0.61 \pm 0.25
FVPDM 8	7.84	0	0.06	0.02	0.07	*	32.0	*
PDM 6	5.93	0	0.06	0.02		0.07 \pm 0.02	32.7 \pm 7.9	0.19 \pm 0.06

can be precisely estimated. With this method, the precision on the calculated groundwater flux fully depends on the precision of the estimation of the water circulation volume. On the contrary, the FVPDM allows for an independent estimation of both groundwater flow rate Q_t and water mixing volume V_w . The best precision is obtained when steady state conditions are reached for tracer concentration in the tested well, which may require long experimental durations. Classical PDM seems to be more accurate than FVPDM for short experiments provided the mixing volume is accurately known. FVPDM generally provides a better accuracy but requires longer experiment durations.

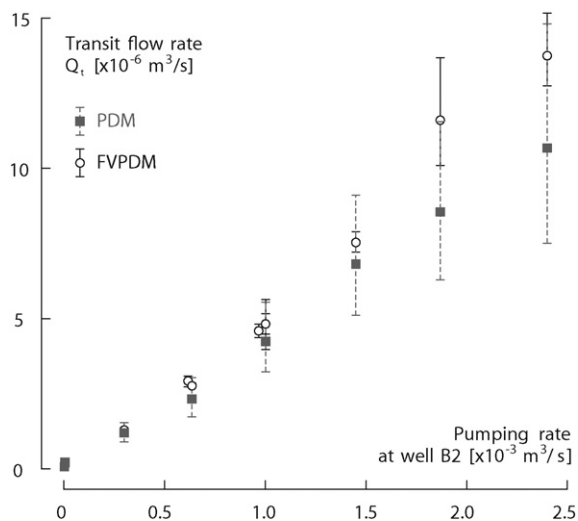


Fig. 8. A linear relation is observed between the pumping rate applied in the well B2 and the groundwater flow rate observed in the fracture B1–4. The transit flow rate (Q_t) adjusted for all the dilution experiments are always higher for the FVPDM (hollow circles) than for the PDM (gray squares) due to difference of adjusted V_w and 95% confidence intervals are always shorter for FVPDM than PDM.

The ‘threshold’ after which FVPDM becomes more accurate than PDM depends on the precision reached in the external estimation of the mixing volume.

The present experiments also highlight the ability of the FVPDM to continuously monitor continuous transient groundwater fluxes. Two short term perspectives could be (1) to develop a mathematical model to interpret a fully transient FVPDM test and (2) to follow a multiple stages pumping test performed at a well with FVPDM monitoring at some nearby piezometer to investigate the benefits of groundwater fluxes information in the interpretation of pumping tests.

In conclusion, both methods are complementary and can investigate the same range of groundwater fluxes. The classical PDM should be used for rapid estimation of steady state groundwater flux. The FVPDM is a more precise method but requires longer duration experiment to achieve a good precision if the investigated groundwater fluxes are low and/or if the mixing volume is large, and has a strong development potential for monitoring of transient groundwater fluxes.

Acknowledgments

This work has been supported by research grants from the University of Liège no. FSRC-12/81 and FNRS Belgium no. 1.5060.12, by the CLIMAWAT project (Adapting to the Impacts of Climate Change on Groundwater Quantity and Quality – EU-RDF INTERREG IVA (Channel) France–England Program), and by the National Network of Hydrogeological Sites H+ and the ANR project CRITEX ANR-11-EQPX-0011.

References

- Brainerd, R.J., Robbins, G.A., 2004. A tracer dilution method for fracture characterization in bedrock wells. *Ground Water* 42 (5), 774–780.
- Bright, J., Wang, F., Close, M., 2002. Influence of the amount of available K data on uncertainty about contaminant transport prediction. *Ground Water* 40 (5), 529–534.

- Brouyère, S., 2003. Modeling tracer injection and well–aquifer interactions: a new mathematical and numerical approach. *Water Resour. Res.* 39 (3), 1070–1075.
- Brouyère, S., Carabin, G., Dassargues, A., 2005. Influence of injection conditions on field tracer experiments. *Ground Water* 43 (3), 389–400.
- Brouyère, S., Battle-Aguilar, J., Goderniaux, P., Dassargues, A., 2008. A new tracer technique for monitoring groundwater fluxes: the finite volume point dilution method. *J. Contam. Hydrol.* 95 (3–4), 121–140.
- Devlin, J.F., McElwee, C.D., 2007. Effects of measurement error on horizontal hydraulic gradient estimates. *Ground Water* 45 (1), 62–73.
- Dorn, C., Linde, N., Le Borgne, T., Bour, O., Klepikova, M., 2012. Inferring transport characteristics in a fractured rock aquifer by combining single-hole ground-penetrating radar reflection monitoring and tracer test data. *Water Resour. Res.* 48 (11), W11521. <http://dx.doi.org/10.1029/2011WR011739>.
- Drost, W., Klotz, D., Koch, A., Moser, H., Neumaier, F., Rauert, W., 1968. Point dilution methods of investigating ground water flow by means of radioisotopes. *Water Resour. Res.* 4 (1), 125–146.
- Fasbender, D., Peeters, L., Bogaert, P., Dassargues, A., 2008. Bayesian data fusion applied to water table spatial mapping. *Water Resour. Res.* 44 (12), W12422. <http://dx.doi.org/10.1029/2008WR006921>.
- Ghorbani, A., Camerlynck, C., Florsch, N., Cosenza, P., Revil, A., 2007. Bayesian inference of the Cole–Cole parameters from time- and frequency-domain induced polarization. *Geophys. Prospect.* 55, 589–605. <http://dx.doi.org/10.1111/j.1365-2478.2007.00627.x>.
- Goderniaux, P., Brouyère, S., Gutierrez, A., Baran, N., 2010. Multi-tracer tests to evaluate the hydraulic setting of a complex aquifer system (Brévilles Spring Catchment, France). *Hydrogeol. J.* 18 (7), 1729–1740.
- Hall, S.H., 1996. Practical single-well tracer methods for aquifer testing. *Workshop Netbook, Tenth National Outdoor Action Conference and Exposition* (11 pp.).
- Hatfield, K., Annable, M.D., Cho, J., Rao, P.S.C., Klammler, H., 2004. A direct passive method for measuring water and contaminant fluxes in porous media. *J. Contam. Hydrol.* 75 (3–4), 155–181.
- Halevy, E., Moser, H., Zellhofer, O., Zuber, A., 1967. Borehole dilution techniques a critical review. *Isotope in Hydrology. I.A.E.A., Vienna*, pp. 531–564.
- Huang, J., Goltz, M.N., 2005. A three-dimensional analytical model to simulate groundwater flow during operation of recirculating wells. *J. Hydrol.* 314, 67–77.
- Kaufman, W.J., Todd, D.K., 1962. Application of tritium tracer to canal seepage measurements. *International Atomic Energy Agency, Tritium in the Physical and Biological Sciences* 1 pp. 83–94.
- Klepikova, M.V., Le Borgne, T., Bour, O., Gallagher, K., Hochreutener, R., Lavenant, N., 2014. Passive temperature tomography experiments in fractured media. *J. Hydrol.* 512, 549–562. <http://dx.doi.org/10.1016/j.jhydrol.2014.03.018>.
- Klotz, D., Moser, H., Trimbom, P., 1979. Single borehole techniques present status and examples of recent applications. *Isotope in Hydrology. I.A.E.A., Neuherberg*, pp. 150–179.
- Le Borgne, T., Bour, O., Paillet, F., Caudal, J.P., 2006. Assessment of preferential flow path connectivity and hydraulic properties at single-borehole and cross-borehole scales in a fractured aquifer. *J. Hydrol.* 328 (1–2), 347–359. <http://dx.doi.org/10.1016/j.jhydrol.2005.12.029>.
- Le Borgne, T., Bour, O., Riley, M.S., Gouze, P., Pezard, P.A., Belghoul, A., Lods, G., et al., 2007. Comparison of alternative methodologies for identifying and characterizing preferential flow paths in heterogeneous aquifers. *J. Hydrol.* 345 (3–4), 134–148. <http://dx.doi.org/10.1016/j.jhydrol.2007.07.007>.
- Novakowski, K.S., Lapcevic, P., Voralek, J., Bickerton, G., 1995. Preliminary interpretation of tracer experiments conducted in a discrete rock fracture under conditions of natural flow. *Geophys. Res. Lett.* 22 (11), 1417–1420.
- Novakowski, K., Lapcevic, P., Voralek, J., Sudicky, E., 1998. A note on a method for measuring the transport properties of a formation using a single well. *Water Resour. Res.* 34 (5), 1351–1356. <http://dx.doi.org/10.1029/98WR00292>.
- Novakowski, K.S., Bickerton, G., Lapcevic, P., Voralek, J., Ross, N., 2006. Measurements of groundwater velocity in discrete rock fractures. *J. Contam. Hydrol.* 82 (1–2), 44–60. <http://dx.doi.org/10.1016/j.jconhyd.2005.09.001>.
- Pittrak, M., Mares, S., Kobr, M., 2007. A simple borehole dilution technique in measuring horizontal ground water flow. *Ground Water* 45 (1), 89–92.
- Read, T., Bour, O., Bense, V., Le Borgne, T., Goderniaux, P., Klepikova, M.V., Hochreutener, R., Lavenant, N., Boschero, V., 2013. Characterizing groundwater flow and heat transport in fractured rock using fiber-optic distributed temperature sensing. *Geophys. Res. Lett.* 40 (10), 2055–2059.
- Sale, T., Taylor, G.R., Iltis, G., Lyverse, M., 2007. Measurement of LNAPL flow using single-well tracer dilution techniques. *Ground Water* 45 (5), 569–578. <http://dx.doi.org/10.1111/j.1745-6584.2007.00337.x>.
- Tarantola, A., Valette, B., 1982. Inverse problems = quest for information. *J. Geophys.* 50, 159–170.
- West, L.J., Odling, N.E., 2007. Characterization of a multilayer aquifer using open well dilution tests. *Ground Water* 45 (1), 74–84. <http://dx.doi.org/10.1111/j.1745-6584.2006.00262.x>.
- Zha, Y., Yeh, T.-C.J., Mao, D., Yang, J., Lu, W., 2014. Usefulness of flux measurements during hydraulic tomographic survey for mapping hydraulic conductivity distribution in a fractured medium. *Adv. Water Resour.* 71, 162–176.
- Zlotnik, V.A., Zurbuchen, B.R., 2003. Field study of hydraulic conductivity in a heterogeneous aquifer: comparison of single-borehole measurements using different instruments. *Water Resour. Res.* 39 (4), WR001415 (12 pp.).



Coupling heat and chemical tracer experiments for estimating heat transfer parameters in shallow alluvial aquifers

S. Wildemeersch^a, P. Jamin^{a,*}, P. Orban^a, T. Hermans^{b,1}, M. Klepikova^a, F. Nguyen^b, S. Brouyère^a, A. Dassargues^a

^a University of Liege, ArGenCo, GEO³, Hydrogeology and Environmental Geology, Aquapôle, B52/3 Sart-Tilman, 4000 Liege, Belgium

^b University of Liege, ArGenCo, GEO³, Applied Geophysics, B52/3 Sart-Tilman, 4000 Liege, Belgium

ARTICLE INFO

Article history:

Received 22 November 2013
Received in revised form 25 July 2014
Accepted 5 August 2014
Available online 12 August 2014

Keywords:

Heat tracer test
Shallow geothermal energy
Very low temperature geothermy
Aquifer thermal energy storage
Heat transfer
Solute transport

ABSTRACT

Geothermal energy systems, closed or open, are increasingly considered for heating and/or cooling buildings. The efficiency of such systems depends on the thermal properties of the subsurface. Therefore, feasibility and impact studies performed prior to their installation should include a field characterization of thermal properties and a heat transfer model using parameter values measured in situ. However, there is a lack of in situ experiments and methodology for performing such a field characterization, especially for open systems. This study presents an in situ experiment designed for estimating heat transfer parameters in shallow alluvial aquifers with focus on the specific heat capacity. This experiment consists in simultaneously injecting hot water and a chemical tracer into the aquifer and monitoring the evolution of groundwater temperature and concentration in the recovery well (and possibly in other piezometers located down gradient). Temperature and concentrations are then used for estimating the specific heat capacity. The first method for estimating this parameter is based on a modeling in series of the chemical tracer and temperature breakthrough curves at the recovery well. The second method is based on an energy balance. The values of specific heat capacity estimated for both methods (2.30 and 2.54 MJ/m³/K) for the experimental site in the alluvial aquifer of the Meuse River (Belgium) are almost identical and consistent with values found in the literature. Temperature breakthrough curves in other piezometers are not required for estimating the specific heat capacity. However, they highlight that heat transfer in the alluvial aquifer of the Meuse River is complex and contrasted with different dominant process depending on the depth leading to significant vertical heat exchange between upper and lower part of the aquifer. Furthermore, these temperature breakthrough curves could be included in the calibration of a complex heat transfer model for estimating the entire set of heat transfer parameters and their spatial distribution by inverse modeling.

© 2014 Elsevier B.V. All rights reserved.

1. Introduction

Geothermal energy is a renewable and sustainable energy source particularly attractive in the current context of environmental protection and fighting against climate change.

Consequently, shallow geothermal energy systems are increasingly considered for heating and/or cooling buildings (Lund et al., 2011). The main techniques for exploiting shallow geothermal energy are ground source heat pumps (GSHP), which are closed systems with a horizontal or a vertical heat exchanger, and groundwater heat pumps (GWHP), which are open systems requiring a pair of injection and withdrawal wells or a withdrawal well and a discharge through surface water.

* Corresponding author. Tel.: +32 43662035; fax: +32 43669520.

E-mail address: pierre.jamin@ulg.ac.be (P. Jamin).

¹ F.R.S.-FNRS, Research Fellow, Brussels, Belgium.

The efficiency of heating systems depends on the hydraulic properties (hydraulic conductivity, porosity, specific yield) and the thermal properties (specific heat capacity, thermal conductivity, and thermal dispersivity) that govern heat transfer in the subsurface. Therefore, prior to their implementation, a feasibility study is recommended. An impact study is also required in some countries to prove compliance of the system with the ongoing regulations (Haehlein et al., 2010). This impact study is important since such systems induce thermal anomalies in the form of cold or heat plumes in groundwater (Molson et al., 1992; Palmer et al., 1992; Warner and Algan, 1984) which may influence groundwater chemistry (e.g. Jesubek et al., 2013) and microbiology (e.g. Brielmann et al., 2009). This impact study is also important for evaluating the long-term efficiency of the system. These feasibility and impact studies should ideally include a field characterization of the thermal properties of the subsurface and a heat transfer model of the heating system using heat transfer parameter values measured in situ. However, field characterization is often limited and the dimensioning of heating systems is generally based on parameter values found in the literature or on default values of software (e.g. de Paly et al., 2012; Freedman et al., 2012; Lo Russo and Civita, 2009; Lo Russo et al., 2012). This is related to the lack of in situ experiments and methodology available for estimating heat transfer parameters in the subsurface. The thermal response test (TRT) has become very popular for designing closed systems. This test provides an estimation of the effective ground thermal conductivity, including the effects of groundwater flow and natural convection (Gehlin, 2002; Sanner et al., 2005, 2013). The effective ground thermal conductivity is representative for closed systems but not for open systems because the TRT does not take into account the significant influence of withdrawal wells on groundwater flow. Furthermore, the TRT does not provide any estimation of specific heat capacity and thermal dispersivity. Therefore, there is a need for other in situ experiments capable of estimating these parameters. This is particularly important for open systems since heat exchange between the groundwater and the aquifer solids is proportional to the specific heat capacity of the saturated porous medium and it modifies the temperature of the pumped groundwater.

The methodology we propose couples heat and chemical tracer experiments. The originality is to simultaneously inject hot water and a chemical tracer into the aquifer and to monitor the evolution of groundwater temperature and tracer concentration in different piezometers located down gradient (including the recovery well). The coupling with a chemical

tracer experiment is performed for taking advantage of the similarities between heat transfer and solute transport in porous media in order to facilitate the separation of heat transfer processes and identify related parameters with focus on specific heat capacity. The effective porosity, in particular, simultaneously governs heat transfer by convection and solute transport by advection. Therefore, this parameter is estimated by fitting the chemical tracer breakthrough curve. Given that the effective porosity is known, the temperature breakthrough curve is used for estimating the thermal retardation factor which is proportional to the specific heat capacity of the saturated porous medium, key parameter governing heat exchange between groundwater and aquifer solids.

The use of heat as a groundwater tracer for estimating hydraulic parameters such as hydraulic conductivity is quite usual (Anderson, 2005). However, only a few studies focus on the use of groundwater temperature for estimating heat transfer parameters (Giambastiani et al., 2013; Vandenbohede et al., 2009, 2011). These studies are interesting since they show the capabilities and the limitations of such experiments. However, they mainly consist in laboratory experiments in a tank (Giambastiani et al., 2013) or in situ experiments with injection of only a small volume of hot water (5.8 m³) (Vandenbohede et al., 2011). Here, we focus on in situ heat tracer experiments with injection of a significant volume of hot water (72 m³) and with a monitoring of the temperature both in the upper and lower parts of the aquifer thanks to a network of double screened piezometers.

A short presentation of the experimental site is followed by a description of the experimental setup and the methodology. The measured breakthrough curves for the temperature and the chemical tracer are then presented, interpreted, and discussed. The paper ends with the conclusions and the perspectives.

2. Field site

The experimental site is located in the village of Hermalle-sous-Argenteau, 13 km north-east of the city of Liège in Belgium. The site consists in a vast meadow lying on the alluvial plain of the Meuse River (Fig. 1). The alluvial deposits can be divided into four different units. The upper layer is 1 to 1.5 m thick and is composed of loam with clay lenses. The second unit consists of sandy loam with millimetric gravels which proportion increases with depth down to 3 m depth. From 3 to 10 m below ground surface, the third layer is mainly made of alluvial sand and gravels. The gravels to sand ratio increases progressively with

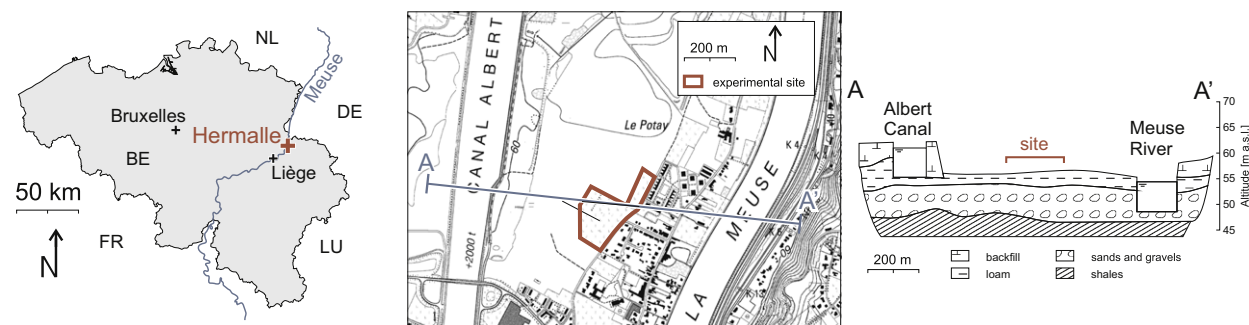


Fig. 1. The test site is located 13 km north east of Liège, Belgium, Western Europe, on the alluvial plain of the River Meuse.

depth to reach at the bottom a zone of clean pebbles frequently more than 0.2 m in diameter. This third layer contains the main mostly unconfined alluvial aquifer. The groundwater table is located approximately 3.2 m below land surface when not artificially disturbed. The annual fluctuation of the water level in the aquifer is approximately 0.5 m with the highest levels observed during the month of January. Below the alluvial deposits, low permeability carboniferous shale and sandstone formations are considered as the basement of the alluvial aquifer (Fig. 1).

The test site is located between the Albert Canal and the Meuse River. The alluvial aquifer is recharged with water by direct infiltration of rainfall but also from the Albert Canal which basement is not perfectly impervious. The Meuse River imposes the base hydraulic head and constitutes the outflow for the alluvial aquifer. The topography of the site is almost flat and the natural hydraulic gradient in the alluvial aquifer is on the order of 0.06% directed toward the north-east. Pumping and tracer tests performed in 1999 (Brouyère, 2001, 2003) showed a mean hydraulic conductivity for the alluvial aquifer ranging from 2×10^{-2} m/s to 7×10^{-2} m/s, a longitudinal dispersivity ranging between 0.5 and 5 m and an effective porosity from 4 to 8%.

The experimental site includes 1 pumping well and 18 piezometers in total. The pumping well is 0.152 m of internal diameter and is screened from 3 to 9.5 m depth. Six piezometers were installed during the 1980s. They are equipped with PVC tubes of 0.05 m in diameter and screened within the alluvial gravels. More recently (June 2012), twelve new piezometers were specifically drilled for the purpose of this research. They

are located upgradient from the pumping well and organized as three transverse control planes across the main groundwater flow direction, at respective distances of 17, 12 and 5 m from the pumping well. Laterally, the piezometers are separated of approximately 1 m. An injection piezometer is also implanted 20 m upgradient the pumping well. Nine of the new piezometers are double-screened with a 2 m lower screen level set at the bottom of the aquifer between 8 and 10 m depth and an upper screen level placed between 5 and 6 m depth. The most upgradient injection piezometer and two lateral piezometers from the second (central) transverse control plane are fully screened from 3 to 10 m depth. Fully screened piezometers were used to monitor the experiment with cross borehole electrical resistivity tomography (Hermans et al., 2015). This technique has recently proved its efficiency to monitor heat injection and storage experiments (Hermans et al., 2012). The detailed setup is presented in Fig. 2.

Temperature and hydraulic head surveys were performed during 2011 and 2012 in several piezometers of the site. A continuous monitoring showed a maximum temperature of the groundwater of 13.34 °C in December and a minimum temperature of 11.91 °C in June. This variation is indeed in opposition with the annual variation of mean atmospheric temperatures which shows monthly average temperature with a maximum of 18.4 °C in July and a minimum of 3.3 °C in January (IRM, 2013).

The only data available on the geothermal properties of the alluvial aquifer in the vicinity of the experimental site come from the ThermoMap project (Bertermann et al., 2013 – <http://www.thermomap-project.eu/>). The objective of this project is

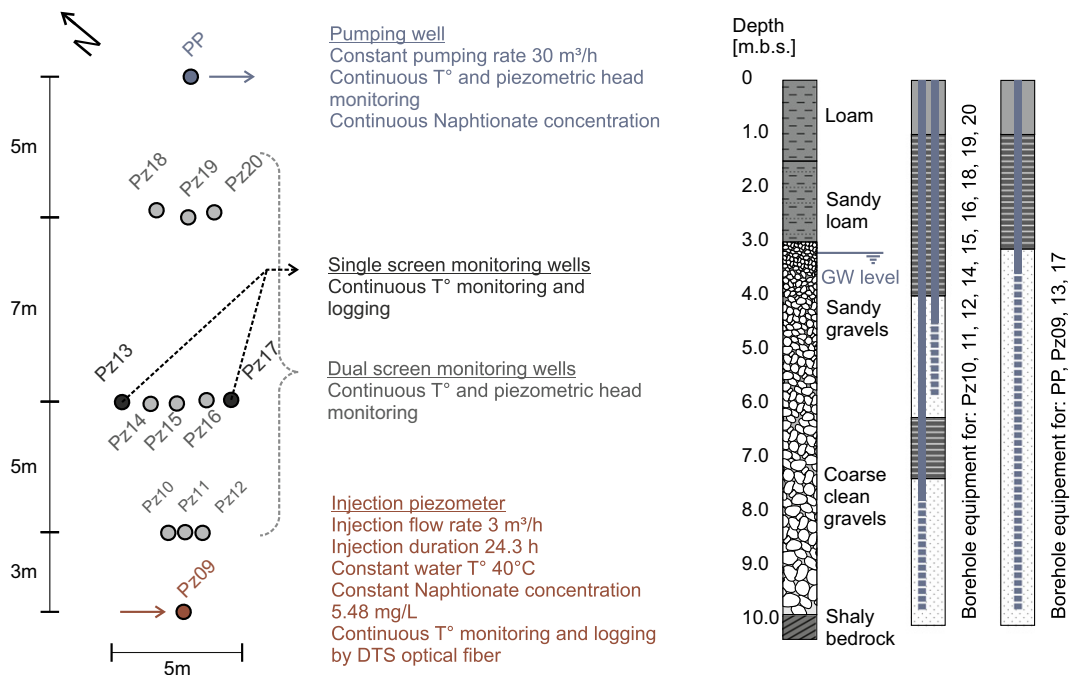


Fig. 2. The experimental setup consists in simultaneous injection of heat and chemical dye (naphtionate) tracer from Pz09 and monitoring of their breakthrough at the recovery pumping well (PP). Temperature is continuously monitored at piezometer Pz10 to Pz20. These piezometers are either single-screened in the whole alluvial aquifer made of sandy gravels, or double-screened with an upper screen in the finest part of the aquifer at its top, and a lower screen within the coarse gravels at the bottom of the aquifer.

to map the superficial geothermic resources of Europe by soil and groundwater data. The mapping is performed using empirical laws (Dehner, 2007; Kersten, 1949) for calculating the thermal conductivity and the volumetric heat capacity of the subsurface using soil and groundwater fundamental properties such as bulk density, texture, and water content These empirical estimations of heat transfer parameters are performed for three horizons: 0 to 3 m, 3 to 6 m, and 6 to 10 m. Results are shown in Table 1.

3. Experimental setup and methodology

The tracer experiment was performed under radially converging flow conditions, by pumping at a constant rate of 30 m³/h at the recovery well with a Grundfos SP30-3 submersible pump. Drawdown induced by pumping in this very conductive unconfined aquifer was 0.05 m in the recovery well and 0.04 m at Pz19 located 5 m upgradient. 90% of abstracted groundwater was discharged in a nearby sewage system, outside the study area. The remaining 10%, corresponding to 3 m³/h, was heated in a fuel boiler (Swingtec Aquamobile DH6) and reinjected as heat tracer together with the chemical tracer at piezometer Pz09. The boiler was theoretically capable of producing a maximum differential of temperature of 30 °C at a maximum flow rate of 3 m³/h. During the field experiment, the boiler actually allowed injecting water at a constant temperature of 40 °C into a groundwater at a natural temperature of 13.33 °C.

Sodium naphthionate (4-Amino-1-naphthalenesulfonic acid sodium salt, CAS no. 130-13-2) was used as a chemical tracer because its specific behavior in the alluvial aquifer of this particular site was well established from previous experiments (Brouyère, 2001), with no sorption but significant first-order degradation of $5.5 \cdot 10^{-6} \text{ s}^{-1}$. Sodium naphthionate is a fluorescent dye tracer with absorption and emission wavelengths of 325 nm and 420 nm respectively. A quantity of 0.4 kg of naphthionate was used, diluted into 0.1 m³ of water coming from the aquifer, resulting in a concentration of 4000 ppm of naphthionate injected in Pz09 at a rate of 3.9 L/h using a Jesco Magdos LT17 electromagnetic dosing pump in addition to the 3 m³/h of heated water.

For heat tracer monitoring, the 18 screens of the 9 piezometers located in the control planes (Pz10 to Pz12, Pz14 to Pz16 and Pz18 to Pz20) were equipped either with SWS MiniDiver or In-Situ Level Troll automated temperature and pressure probes which allowed monitoring hydraulic head and temperatures during all the experiment duration, with a measurement time step of 10 min. The injection piezometers Pz09, Pz13 and Pz17, both located at the extremity of the central control plane were all equipped with DTS optical fiber (AP-Sensing Linear Pro Series) for

temperature logging measurements along the vertical axis of the piezometer. The recovery well was also equipped with an In-Situ Level Troll probe to monitor the heat tracer breakthrough. Naphtionate was monitored at the recovery well using a GGUN-FL30 field fluorimeter connected in parallel on groundwater discharge with a measurement every 2 min. Available equipment did not allow for monitoring of naphthionate concentrations at the piezometers during the tracer test.

The combined heat–naphthionate tracer injection was performed in Pz09 on October 30th 2012 and lasted for 24 h 20 min. Monitoring of temperature in the piezometers and at the well was maintained for 14 days.

Pumping at the recovery well was maintained for several weeks after the tracer test. During this time groundwater fluxes were measured using the Finite Volume Point Dilution Method (FVPDM) (Brouyère et al., 2008). This single well dilution method allows a direct measurement of the Darcy's fluxes at each screen of every piezometers at the site.

4. Results and discussion

4.1. Analysis of the breakthrough curves

The evolution of the temperature measured in each piezometer is presented in Fig. 3. The breakthrough curves in blue and in red correspond to the temperatures measured in the lower and in the upper parts of the aquifer, respectively. The green breakthrough curve represents the mean temperature recorded along the thickness of the aquifer by DTS.

The comparison between temperature breakthrough curves in the lower and the upper parts of the aquifer clearly shows that heat pulse travels faster in the lower part of the aquifer. The breakthrough curves in the upper part of the aquifer are also characterized by longer tailings. A maximum temperature change of 14.98 °C was observed at control plane 1 in the upper part of the aquifer 26 h after the beginning of the injection. This observation was made in the central piezometer Pz11 located 3 m down gradient of the injection well. The maximum temperature change in the lower part of the aquifer was only 4.17 °C. This observation was made 27 h after the beginning of the injection and in the piezometer Pz14 located 8 m down gradient of the injection well and to the left part of this control plane. At the end of the second control plane, a mean (across the entire screen length) maximum temperature of 5.41 °C was recorder 1.02 days after the beginning of the injection at the fully screened piezometer Pz13. Except at the first control plane, the highest changes in temperatures are always observed in the lower part of the aquifer. In the upper part, a quick decrease of the temperature change is observed from one plane to the next. On the contrary, in the lower part of the aquifer, the temperature change tends to be slightly higher with the distance from the injection piezometer.

Fig. 4 shows the temperature monitoring and logging at the injection well Pz09 using the DTS. The temperature stratification is obvious with a maximum injection temperature of 40 °C at the lower part of the piezometer and 34 °C at the upper part. At the end of the heat tracer injection, the temperature decreases rapidly in the lower part of the piezometer while a significant amount of heat remains in the upper part. This is due to a vertical heterogeneity of the groundwater flux in the

Table 1

Thermal conductivity and volumetric heat capacity values estimated in the zone of the experimental site in the framework of the ThermoMap project (Bertermann et al., 2013).

Depth of layer [m]	Thermal conductivity [W/m/K]	Volumetric heat capacity [MJ/m ³ /K]
0–3	1.17 ± 0.30	2.24
3–6	1.37 ± 0.35	2.22
6–10	1.86 ± 0.52	2.34

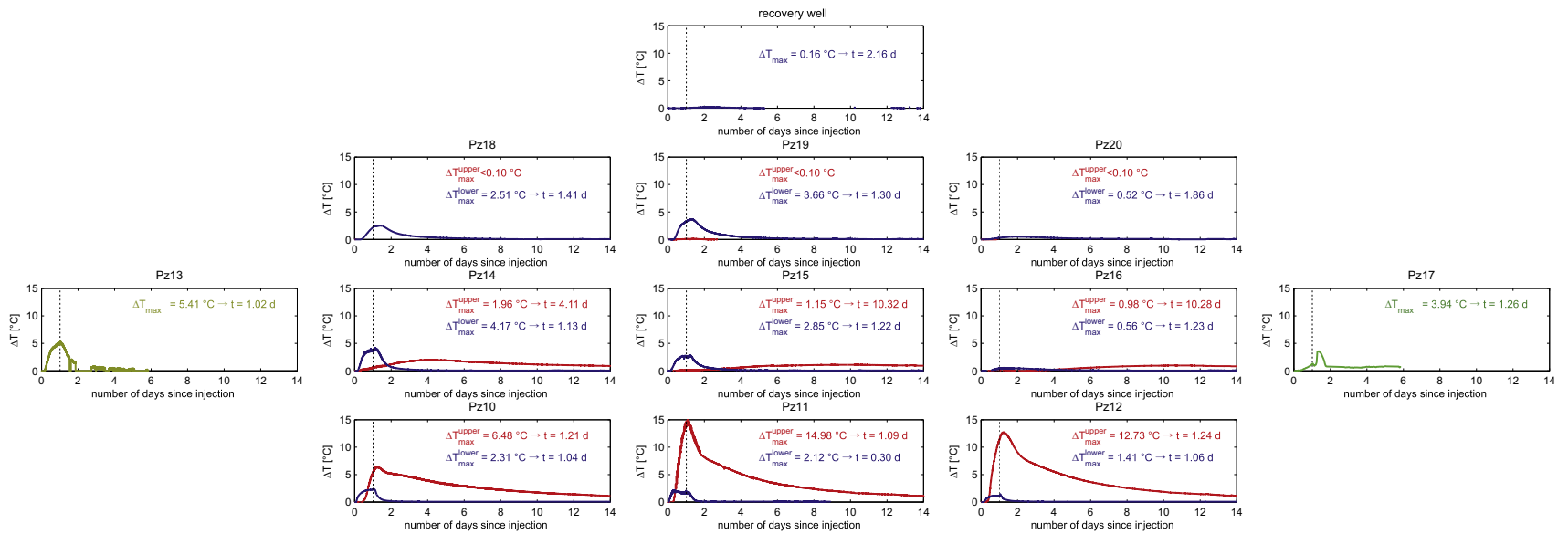


Fig. 3. Temperature breakthrough curves measured in each piezometer. The blue curves correspond to the lower part of the aquifer. The red curves correspond to the upper part of the aquifer. The green curves correspond to the mean temperature along the whole thickness of the aquifer.

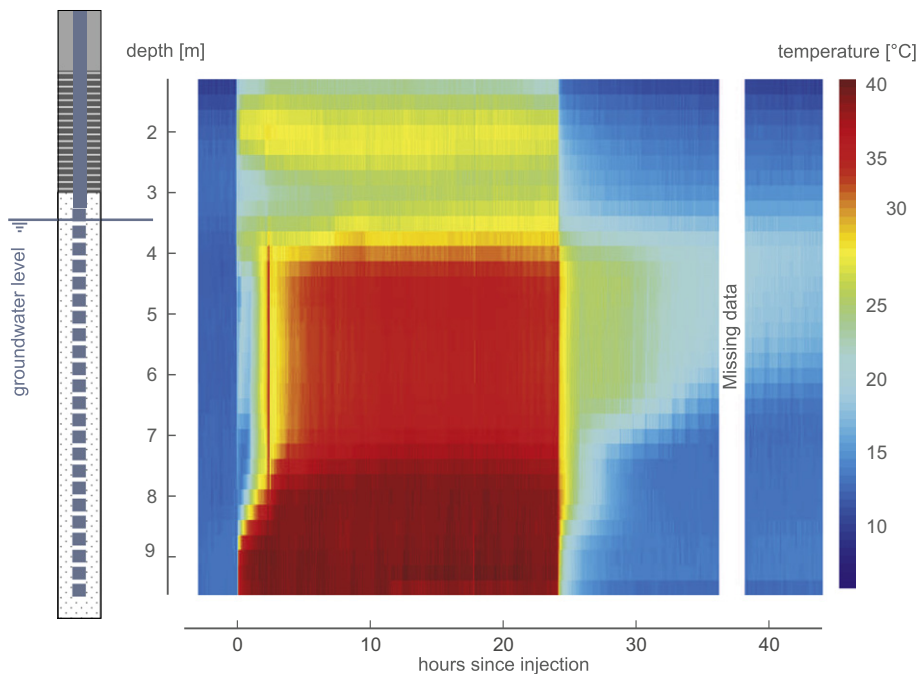


Fig. 4. Vertical temperature profiles monitored by DTS at the injection piezometer Pz09. After the injection stops, the heat is rapidly flushed out of the lower part of the piezometer although the temperature remains high at the top of the piezometer due to slower groundwater flow in the upper part of the aquifer.

aquifer that is faster in the lower part of the aquifer leading to a fast flushing of the heat out of the injection piezometer. This is consistent with the lithological observation during the drilling of the piezometer with coarser gravels found at the bottom of the aquifer.

In order to quantify the vertical heterogeneity of the groundwater velocities, Darcy's fluxes have been measured at each screen of every piezometer on the site using the FVPDM technique. Results of the Darcy's flux measurements indicate a much faster groundwater flow in the lower part of the aquifer of an order of magnitude (Table 2). The mean Darcy's flux for the upper screens was $2.8 \cdot 10^{-4}$ m/s and $3.3 \cdot 10^{-3}$ m/s for the lower screens, corresponding to the lower part of the aquifer.

The complex evolution of temperature, suggesting that heat transfer is highly sensitive to local heterogeneities of the alluvial aquifer, can be described and interpreted as follows. The temperature breakthrough curves indicate that heat transfer is mainly convective in the lower part of the aquifer and mainly conductive/dispersive in the upper part. As the proportion of gravels in the aquifer progressively increases with depth, the hydraulic conductivity is most probably higher in the lower part of the aquifer. Therefore, the transition from a conductive/dispersive-dominated heat transfer in the upper part to a convection-dominated heat transfer in the lower part is consistent with the geology of the alluvial aquifer. At the same

time, the fast convective heat transfer in the lower part and the slow conductive/dispersive heat transfer in the upper part quickly produce a vertical temperature gradient. This vertical temperature gradient leads to heat exchange by conduction from the upper part to the lower part of the aquifer. This represents the first explanation for the progressive temperature increase downgradient in the lower part of the alluvial aquifer. As the vertical temperature gradient progressively decreases with the distance from the injection piezometer, the heat exchange also decreases. Furthermore, due to the pumping, convection is also higher close to the recovery well. The second explanation is that the heterogeneity of the alluvial deposit induce preferential flow path that can be deviated from a straight line between injection and recovery well. If the main flow path is considered following as the maximum temperatures reached in the lower part of the aquifer, the flow line should describe a curve through the north-west passing by Pz10, Pz13 or Pz14, and Pz19. This paths correspond, by control planes, to the piezometers showing the highest Darcy's flux measured by the FVPDM technique in their lower screens. This path may correspond to a former curved alluvial channel.

The comparison between the temperature and the naphionate breakthrough curves in the recovery well clearly shows that heat transfer is delayed and retarded as compared to solute transport (Fig. 5). First arrival times are separated by 14 h and modal times are separated by 25 h. This suggests that heat

Table 2

Darcy's fluxes (10^{-4} m/s) measured by the FVPDM are ten times higher in the lower part of the aquifer than in the upper part.

Piezometer	10	11	12	13	14	15	16	17	18	19	20	Mean
Upper screen	3.50	6.56	3.37	10.18	3.50	2.27	1.75	8.08	1.22	0.87	1.97	2.78
Lower screen	59.93	19.03	22.31	31.63	9.95	9.89			26.68	46.37	74.37	33.35

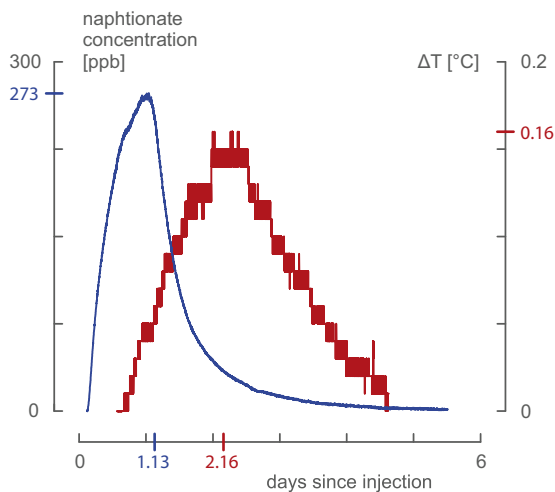


Fig. 5. Temperature and naphthionate breakthrough curves measured in the recovery well.

transfer is slower than solute transport. This can be explained by heat exchange between groundwater and aquifer solids leading to thermal retardation. The comparison also shows that the temperature breakthrough curve seems more dispersed than the naphthionate breakthrough curve. The dispersion of the temperature and naphthionate breakthrough curves is related, respectively, to heat transfer by conduction and by thermal dispersion and to solute transport by molecular diffusion and mechanical dispersion. These heat transfer and solute transport processes can be compared in pairs. This is possible because of the analogy between heat transfer and solute transport equations in porous media. The three-dimensional heat transfer equation in homogeneous porous media that is expressed as (Domenico and Schwartz, 1998):

$$\frac{\kappa_e}{\rho_m c_m} \nabla^2 T - \frac{\rho_w c_w}{\rho_m c_m} \nabla \cdot (T q) = \frac{\partial T}{\partial t} \quad (1)$$

where T is the temperature [K], t is time [s], ρ_w is the density of the water [kg/m^3], c_w is the specific heat capacity of the water [$\text{J}/\text{kg}/\text{K}$], ρ_m is the density of the saturated porous medium [kg/m^3], c_m is the specific heat capacity of the saturated porous medium [$\text{J}/\text{kg}/\text{K}$], κ_e is the effective thermal conductivity of the saturated porous medium [$\text{W}/\text{m}/\text{K}$] and q is the effective velocity [m/s]. As explained by Anderson (2005), among others, the first term in Eq. (1) represents heat transfer by conduction, analogous to solute transport by molecular diffusion, as well as heat transfer by thermal dispersion, analogous to hydrodynamic dispersion in solute transport. The term $\frac{\rho_w c_w}{\rho_m c_m}$, including the effects of conduction through the porous medium as well as the effects of thermal dispersion, can be written in an extended form:

$$\frac{\rho_w c_w}{\rho_m c_m} = \frac{n \kappa_w + (1-n) \kappa_s}{n \rho_w c_w + (1-n) \rho_s c_s} + \alpha^* |q| = \frac{\kappa_0}{\rho_m c_m} + \alpha^* |q| \quad (2)$$

where $\rho_m \times c_m$ is the volumetric heat capacity of the saturated porous medium [$\text{J}/\text{m}^3/\text{K}$], n is the total porosity [–], κ_w is the

thermal conductivity of the water [$\text{W}/\text{m}/\text{K}$], κ_s is the thermal conductivity of the aquifer solids [$\text{W}/\text{m}/\text{K}$], $\rho_w \times c_w$ is the volumetric heat capacity of the water [$\text{J}/\text{m}^3/\text{K}$], $\rho_s \times c_s$ is the volumetric heat capacity of the aquifer solids [$\text{J}/\text{m}^3/\text{K}$], α^* is the thermal dispersivity [m], $|q|$ is the effective velocity norm [m/s], and κ_0 is the effective thermal conductivity of the saturated porous medium [$\text{W}/\text{m}/\text{K}$]. The term $\frac{\kappa_0}{\rho_m c_m}$, referred as the thermal diffusivity and representing the thermal conduction in the porous medium, is analogous to the molecular diffusion coefficient D_m in the solute advection–diffusion equation (Anderson, 2005). When comparing, in porous medium, the orders of magnitude of this thermal diffusivity (10^{-6} to $10^{-7} \text{ m}^2/\text{s}$) (Domenico and Schwartz, 1998, p. 196) and the order of magnitude of molecular diffusion ($10^{-10} \text{ m}^2/\text{s}$), it is clear that thermal conduction in heat transfer is far more important than molecular diffusion in solute transport. The term α^* is analogous to the dispersivity coefficient α in the solute advection–diffusion equation. However, there is conflicting points of view in the literature on their respective values. For de Marsily (1986), thermal and solute dispersivity are on the same order of magnitude. For Bear (1972), Ingebritsen and Sanford (1998), Hopmans et al. (2002), among others, the effects of thermal dispersivity are negligible with respect to heat transfer by conduction and convection and should be set equal to zero. For Vandenbohede et al. (2009), thermal dispersivity is smaller than solute dispersivity. Therefore, the comparison between thermal and solute dispersion is not as easy as between thermal diffusivity and molecular diffusion.

The temperature breakthrough curve recorded at the recovery well can be converted into a recovered heat breakthrough to calculate that the recovered heat only represents 1% of injected heat. This indicates that a significant portion of injected heat is lost, most probably by heat exchange and storage in the porous medium. The lost can occur through the vadose zone, to the shaly bedrock or even laterally if the injection is not performed in a perfectly radial converging regime. This heat exchange must be especially significant in the vicinity of the injection well where the temperature contrast is very high (up to 25 °C). As the drawdown induced by the pumping is limited, it is also likely that a portion of heated groundwater simply does not reach the recovery well. Furthermore, due to the precision of the temperature probes, the heat breakthrough curve cannot be recorder at the pumping well after 5 days following injection. Nevertheless, a substantial amount of heat remains in the upper part of the aquifer 5 days after the injection. This can be seen e.g. at the upper screen of Pz11 (Fig. 3) where the elevation of temperature is still more than 4 °C after 5 days. This remaining amount of thermal energy is too diluted when it reaches the recover well to induce a significant temperature difference captured by the temperature probe.

The normalized cumulative breakthrough curve for the naphthionate indicates that 67% of the injected mass is recovered. The remaining 33% are most probably degraded since naphthionate degradation processes have already been observed on the experimental site. Brouyère (2001) obtained mean recovery ratios of 70% from pulse injections performed 25 m upgradient the recovery well, where the pumping rate was 52.6 m^3/h inducing faster groundwater fluxes and therefore less time for degradation to occur.

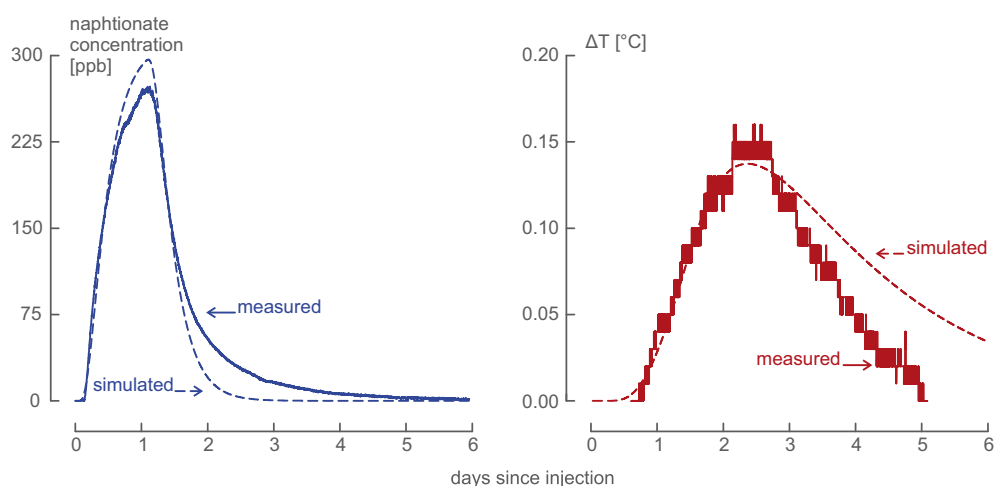


Fig. 6. Fitted and measured breakthrough curves for the naphionate and temperature. The fit has been focused on first arrival, modal time and rising part of the curve. Imperfect tailings fit is due to (1) a vertical integration on the whole aquifer thickness at the recovery well although the lower part responsible for shape of the curve in transport of solute and heat transfer, (2) no mobile/immobile water effect has been considered and (3) heat diffusion is not considered explicitly in the semi analytical solution used to interpret the curves.

4.2. Temperature and solute breakthrough curve modeling using a semi-analytical transport model

Temperature and naphionate breakthrough curves were also interpreted using the TRAC software developed by BRGM (Gutierrez et al., 2012b), using the semi-analytical solution for tracer experiments in a radially converging flow field considering advection, dispersion, retardation and degradation, and a continuous injection of tracer or heat (Gutierrez et al., 2012a).

The naphionate breakthrough curve is used to estimate the effective (transport) porosity n_e and the longitudinal dispersivity α by fitting the model with focus on reproducing the first arrival and modal times. The 1st order degradation coefficient λ is also included in the fitting process as degradation of the naphionate in the experimental site was highlighted by Brouyère (2001). Fitted and measured breakthrough curves are presented in Fig. 6. The fit focused on the first arrival, the rising and the modal time of the breakthrough curve. The tailings of the simulated curves do not perfectly match with the field data for three major reasons. The first one is that the well is screened across the entire thickness of the aquifer. This does not allow for a separate interpretation of heat transfer within the upper and the lower zone although it has been proved that groundwater flows heterogeneously in the aquifer. The second reason is that no immobile/mobile water transfer is used although it is likely to happen in this aquifer. And finally, the heat diffusion (conduction), whereas it is likely to play a more important role than in solute transport, is not taken into account explicitly within the analytical solution, it is rather gathered with the dispersivity in a dispersion factor. The values obtained for the parameters after the fitting process are given in Table 3. The fitted effective porosity (0.04) is in good agreement with Brouyère (2001) who obtain an effective porosity ranging from 0.037 to 0.055 based on 6 tracer tests performed around the pumping well at the same experimental site.

The temperature breakthrough curve was used in a second step for estimating the thermal retardation factor R reflecting heat exchange between the groundwater and the aquifer solids.

For heat transport, the 1st order degradation coefficient λ is set equal to 0. The fitted and measured temperature breakthrough curves are presented in Fig. 6 and the corresponding adjusted parameter values are summarized in Table 3.

The thermal retardation factor is given by the following equation (Hecht-Méndez et al., 2010):

$$R = \frac{\rho_m c_m}{n \rho_w c_w} = \frac{C_m}{n C_w} \quad (3)$$

where C_m is the volumetric heat capacity of the saturated porous medium (total phase) [J/m³/K], n is the total porosity [–], and C_w is the volumetric heat capacity of the water [J/m³/K].

With a total porosity of 0.11 for the experimental site (Brouyère, 2001), it is possible to estimate the volumetric heat capacity of the saturated porous medium C_m . The value obtained is equal to 2.30 MJ/m³/K. This value, slightly lower than the value obtained with the energy balance, is consistent with the range of values found in the literature that ranges from 2 to 3.1 MJ/m³/K (Palmer et al., 1992; Wagner et al., 2013). Since the solute and heat breakthrough curve recorded at the recovery well is mainly due to fast groundwater flow in the lower part of the aquifer, the volumetric heat capacity determined on the breakthrough curve is mainly representative for the lower part of the aquifer.

Table 3

Parameter values obtained after the fitting process for the naphionate and temperature breakthrough curves.

	Naphionate	Temperature
Effective porosity n_e [–]		0.04
Longitudinal dispersivity α [m]		3
1st order degradation coefficient λ [s ⁻¹]	$1.5 \cdot 10^{-5}$	0
Retardation factor R [–]	1	5

4.3. Energy balance of the heat tracer experiment

The energy balance equation on a volume of porous medium corresponding to the portion of the aquifer investigated by the heat tracer experiment can be written as follows:

$$\begin{aligned} \dot{M}_{inj} c_w T_{inj} + (\dot{M}_{ext} - \dot{M}_{inj}) c_w T_0 - \dot{M}_{ext} c_w T_{ext} - \dot{Q}_{lost} \\ = M_m c_m \frac{dT_{ext}}{dt} \end{aligned} \quad (4)$$

with \dot{M}_{inj} is the mass rate of water injected into the aquifer [kg/s], c_w is the specific heat capacity of water [4181.3 J/kg/K], T_{inj} is the temperature of injected water [K], \dot{M}_{ext} is the mass rate of water abstracted from the aquifer [kg/s], T_0 is the initial temperature of groundwater [K], T_{ext} is the temperature of abstracted groundwater, representative of the saturated porous medium [K], \dot{Q}_{lost} is the lost energy flux [J/s], M_m is the mass of saturated porous medium [kg], and c_m is the specific heat capacity of the saturated porous medium [J/kg/K].

The left side terms correspond respectively to the energy fluxes related to (1) the injection of hot water into the aquifer at mass flow rate \dot{M}_{inj} (0.83 kg/s) at temperature T_{inj} (in the injection well equal to 40 °C), (2) groundwater in motion at the initial temperature of the aquifer T_0 (13.33 °C), (3) groundwater withdrawal from the aquifer at temperature T_{ext} (at the recovery well) and a mass flow rate \dot{M}_{ext} (8.33 kg/s), and (4) \dot{Q}_{lost} the lost energy toward the unsaturated zones and the shaly bedrock. The right side term corresponds to storage of energy in the saturated porous medium. The unknowns of this the energy balance equation are the lost energy flux \dot{Q}_{lost} , the mass of the saturated porous medium M_m , and the specific heat capacity of the saturated porous medium c_m . The other variables correspond to data measured on the field (mass rates \dot{M} and temperature T) or easily found in the literature (specific heat capacity of the water c_w).

The lost energy flux \dot{Q}_{lost} can be estimated as follows. If the temperature of the saturated porous medium T_m is constant for a certain period, the storage term (time derivative) vanishes and Eq. (4) can be formulated as follows:

$$\dot{Q}_{lost} = \dot{M}_{inj} c_w T_{inj} + (\dot{M}_{ext} - \dot{M}_{inj}) c_w T_0 - \dot{M}_{ext} c_w T_{ext} \quad (5)$$

The heat injection, as performed during this 24 h test, did not last enough to create a steady state for the heat transfer within the aquifer. Therefore, the heat transfer parameters adjusted on the heat breakthrough curve (Table 3) have been used to simulate an extrapolated temperature breakthrough curve for a continuous heat injection scenario. The maximum temperature at the recovery well reaches 13.83 °C after 17 days. This value is used as T_{ext} in the Eq. (5) to calculate the lost energy flux \dot{Q}_{lost} at $7.54 \cdot 10^{-2}$ MJ/s.

Given that the lost energy flux \dot{Q}_{lost} is known, it is now possible to calculate the volumetric heat capacity of the saturated porous medium C_m by dividing the heat capacity of the saturated porous medium $M_m c_m$ by its volume V_m :

$$C_m = \frac{M_m c_m}{V_m} \quad (6)$$

Steady state simulations using a numerical model allowed an estimation of the volume of aquifer interrogated by the heat

tracer test. With a temperature cut-off value set at 0.01 °C, the heat spreads laterally up to 25 m (so way further Pz13 and Pz17) and stretches 3 m upgradient the injection well. The volume V_m is then 4025 m³ for this 7 m thick aquifer.

Using Eq. (3) under transient conditions and considering the rising part of the heat breakthrough curve recorded at the recovery well (between 1 and 3 days after the start of the tracer injection) with a slope $\frac{dT_m}{dt}$ of $1.5 \cdot 10^{-6}$ K/s, C_m is estimated at 2.54 MJ/m³/K. The value estimated with the energy balance for this parameter is consistent with the range of values found in the literature that ranges from 2 to 3.1 MJ/m³/K (Palmer et al., 1992; Wagner et al., 2013).

5. Conclusions

The coupled heat and chemical tracer experiment we present in this paper provides an efficient way of estimating this parameter in the field using temperature and concentration measurements in the recovery well. At this first step of the modeling approach, temperature measured in the other piezometers was not explicitly used. However, these temperature measurements were very useful for improving our understanding of heat transfer in a highly heterogeneous and relatively stratified shallow alluvial aquifer. As the proportion of gravels progressively increases with depth, the hydraulic conductivity is higher in the lower part of the aquifer than in the upper part. Therefore, heat transfer is conduction/dispersion-dominated in the upper part of the aquifer and convection-dominated in the lower part. This creates a vertical temperature gradient leading to heat exchange from the upper part to the lower part of the aquifer. As this vertical temperature gradient progressively decreases with the distance from the injection piezometer, the related heat exchange also decreases.

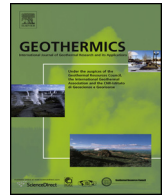
The comparison between temperature and naphthionate breakthrough curves shows that heat transfer in the alluvial aquifer is slower and more dispersive than solute transport. This is mainly related to heat exchange between groundwater and aquifer solids. This process is proportional to the specific heat capacity of the porous medium which proves that in situ estimation of this parameter is particularly useful. The values of specific heat capacity estimated with the energy balance approach (2.54 MJ/m³/K) and with the modeling of the temperature breakthrough curve at the recovery well (2.30 MJ/m³/K) are close and consistent with the range of values found in the literature. Therefore, unlike the TRT, temperature and concentration measurements performed during such a coupled experiment allow estimating the specific heat capacity of the porous medium. Additionally, the data gathered potentially contain enough information for deducing the entire set of heat transfer parameters as well as their spatial distribution. However, this will require developing a complex numerical model of the experiment for estimating these parameters by calibration with inverse modeling. Chemical tracer data are optional for estimating heat transfer parameters. However, prior to the inverse modeling, they can be used for estimating common parameters in heat transfer and solute transport such as effective porosity or they can advantageously be included in the inverse modeling for better constraining the problem.

Acknowledgments

This work was supported by research grants provided by the University of Liège Research Council project no. C-11/33. Thanks are due to two anonymous reviewers for providing useful review feedback.

References

- Anderson, M.P., 2005. Heat as a ground water tracer. *Ground Water* 43 (6), 951–968.
- Bear, J., 1972. *Dynamics of Fluids in Porous Media*. American Elsevier Publishing Company Inc., New York.
- Bertermann, D., Bialas, C., Rohn, J., 2013. ThermoMap – area mapping of superficial geothermic resources by soil and groundwater data. Available at <http://www.thermomap-project.eu/wp-content/uploads/2012/04/Poster-ThermoMap-English-2012.pdf>.
- Brielmann, H., Griebler, C., Schmidt, S.I., Michel, R., Lueders, T., 2009. Effects of thermal energy discharge on shallow groundwater ecosystems. *FEMS Microbiol. Ecol.* 68, 273–286.
- Brouyère, S., 2001. *Etude et modélisation du transport et du piégeage de solutes en milieu variablement saturé*. (PhD thesis) University of Liege, Belgium, (in French).
- Brouyère, S., 2003. Modeling tracer injection and well-aquifer interactions: a new mathematical and numerical approach. *Water Resour. Res.* 39 (3).
- Brouyère, S., Batlle-Aguilar, J., Goderniaux, P., Dassargues, A., 2008. A new tracer technique for monitoring groundwater fluxes: the finite volume point dilution method. *J. Contam. Hydrol.* 95, 121–140.
- de Marsily, G., 1986. *Quantitative Hydrogeology*. Academic Press, San Diego.
- de Paly, M., Hecht-Méndez, J., Beck, M., Blum, P., Zell, A., Bayer, P., 2012. Optimization of energy extraction for closed shallow geothermal systems using linear programming. *Geothermics* 43, 57–65.
- Dehner, U., 2007. *Bestimmung der thermischen Eigenschaften von Böden als Grundlage für die Erdwärmennutzung*. Mainzer geowissenschaftliche Mitteilungen. 35, pp. 159–186 (Mainz, (in German)).
- Domenico, P.A., Schwartz, F.W., 1998. *Physical and Chemical Hydrogeology*. John Wiley & Sons Inc., New York.
- Freedman, V.L., Waichler, S.R., Mackley, R.D., Horner, J.A., 2012. Assessing the thermal environmental impacts of an groundwater heat pump in southeastern Washington State. *Geothermics* 42, 65–77.
- Gehlin, S., 2002. *Thermal Response Test. Method Development and Evaluation*. (PhD thesis) Luleå University of Technology, Sweden.
- Giambastiani, B.M.S., Colombani, N., Mastrociccio, M., 2013. Limitation of using heat as a groundwater tracer to define aquifer properties: experiment in a large tank model. *Environ. Earth Sci.* 70, 719–728.
- Gutierrez, A., Klinka, T., Thiéry, D., 2012a. Manuel d'utilisation de TRAC: Aide à l'interprétation de traçages en milieux poreux. Final report BRGM/RP-60660-FR (116 pp., Retrieved from <http://trac.brgm.fr/spip.php?article24> (In French)).
- Gutierrez, A., Klinka, T., Thiéry, D., 2012b. Validation du logiciel TRAC: Aide à l'interprétation de traçages en milieu poreux. Rapport BRGM/RP-59425-FR (58 pp., 43 fig., 1 ann. (in French)).
- Haehlein, S., Bayer, P., Blum, P., 2010. International legal status of the use of shallow geothermal energy. *Renew. Sust. Energ. Rev.* 14 (9), 2611–2625.
- Hecht-Méndez, J., Molina-Giraldo, N., Blum, P., Bayer, P., 2010. Evaluating MT3DMS for heat transport simulation of closed geothermal systems. *Ground Water* 48 (5), 741–756.
- Hermans, T., Vandenbohede, A., Lebbe, L., Nguyen, F., 2012. A shallow geothermal experiment monitored with electric resistivity tomography. *Geophysics* 77 (1), B11–B21.
- Hermans, T., Wildemeersch, S., Jamin, P., Orban, P., Brouyère, S., Dassargues, A., Nguyen, F., 2015. Quantitative temperature monitoring of a heat tracing experiment using cross-borehole ERT. *Geothermics* 53, 14–26. <http://dx.doi.org/10.1016/j.geothermics.2014.03.013>.
- Hopmans, J.W., Simunek, J., Bristow, K.L., 2002. Indirect estimation of soil thermal properties and water flux using heat pulse probe measurements: geometry and dispersion effects. *Water Resour. Res.* 38 (1), 7-1–7-14.
- Ingebritsen, S.E., Sanford, W.E., 1998. *Groundwater in Geologic Processes*. Cambridge University Press, Cambridge, UK.
- IRM Institut Royal Meteorologique de Belgique, 2013. Rapport annuel 2012. Available at <http://www.meteo.be/meteo/view/fr/103541-Publications.html>.
- Jesušek, A., Grandel, S., Dahmke, A., 2013. Impacts of subsurface heat storage on aquifer hydrogeochemistry. *Environ. Earth Sci.* 69 (6), 1999–2012.
- Kersten, M.S., 1949. *Thermal properties of soils*. Bulletin. 28. Engineering Experiment Station, University of Minnesota, Minneapolis.
- Lo Russo, S., Civita, M.V., 2009. Open-loop groundwater heat pumps development for large buildings: a case study. *Geothermics* 38, 335–345.
- Lo Russo, S., Taddia, G., Verda, V., 2012. Development of the thermally affected zone (TAZ) around a groundwater heat pump (GWHP) system: a sensitivity analysis. *Geothermics* 43, 66–74.
- Lund, J.W., Freeston, D.H., Boyd, T.L., 2011. Direct utilization of geothermal energy 2010 worldwide review. *Geothermics* 40 (3), 159–180.
- Molson, J.W., Frind, E.O., Palmer, C.D., 1992. Thermal energy storage in an unconfined aquifer 2. Model development, validation and application. *Water Resour. Res.* 28, 2857–2867.
- Palmer, C.D., Blowes, D.W., Frind, E.O., Molson, J.W., 1992. Thermal energy storage in an unconfined aquifer 1. Field injection experiment. *Water Resour. Res.* 28, 2845–2866.
- Sanner, B., Hellström, G., Spitler, J., Gehlin, S., 2005. Thermal response test – current status and world-wide application. Proc World Geothermal Congress 2005, Antalya, Turkey (24th–29th April).
- Sanner, B., Hellström, G., Spitler, J., Gehlin, S., 2013. More than 15 years of mobile thermal response test – a summary of experiences and prospects. Proc European Geothermal Congress, Pisa, Italy (3rd–7th June).
- Vandenbohede, A., Louwyck, A., Lebbe, L., 2009. Conservative solute versus heat transport in porous media during push–pull tests. *Transp. Porous Media* 76, 265–287.
- Vandenbohede, A., Hermans, T., Nguyen, F., Lebbe, L., 2011. Shallow heat injection and storage experiment: heat transport simulation and sensitivity analysis. *J. Hydrol.* 409, 262–272.
- Wagner, V., Li, T., Bayer, P., Leven, C., Dietrich, P., Blum, P., 2013. Thermal tracer testing in a sedimentary aquifer: field experiment (Lauswiesen, Germany) and numerical simulation. *Hydrogeol. J.* 22 (1), 175–187.
- Warner, D.L., Algan, U., 1984. Thermal impact of residential ground-water heat pumps. *Ground Water* 22, 6–12.



Quantitative temperature monitoring of a heat tracing experiment using cross-borehole ERT



Thomas Hermans^{a,c,*}, Samuel Wildemeersch^b, Pierre Jamin^b, Philippe Orban^b, Serge Brouyère^b, Alain Dassargues^b, Frédéric Nguyen^a

^a University of Liege, Applied Geophysics, Department ArGenCo, Engineering Faculty, B52, 4000 Liege, Belgium

^b University of Liege, Hydrogeology and Environmental Geology, Aquapole, Departement ArGenCo, Engineering Faculty, B52, 4000 Liege, Belgium

^c F.R.S.-FNRS Research Fellow, Brussels, Belgium

ARTICLE INFO

Article history:

Received 13 September 2013

Accepted 29 March 2014

Available online 8 May 2014

Keywords:

Heat tracing

Geothermal system

Time-lapse

Cross-borehole electrical resistivity tomography

Temperature monitoring

ABSTRACT

The growing demand for renewable energy leads to an increase in the development of geothermal energy projects and heat has become a common tracer in hydrology and hydrogeology. Designing geothermal systems requires a multidisciplinary approach including geological and hydrogeological aspects. In this context, electrical resistivity tomography (ERT) can bring relevant, qualitative and quantitative information on the temperature distribution in operating shallow geothermal systems or during heat tracing experiments. We followed a heat tracing experiment in an alluvial aquifer using cross-borehole time-lapse ERT. Heated water was injected in a well while water of the aquifer was extracted at another well. An ERT section was set up across the main flow direction. The results of ERT were transformed into temperature using calibrated petrophysical relationships. These ERT-derived temperatures were then compared to direct temperature measurements in control piezometers collected with distributed temperature sensing (DTS) and groundwater temperature loggers. Spatially, it enabled to map the horizontal and vertical extent of the heated water plume, as well as the zones where maximum temperatures occurred. Quantitatively, the temperatures and breakthrough curves estimated from ERT were in good agreement with the ones observed directly during the rise and maximum of the curve. An overestimation, likely related to 3D effects, was observed for the tail of the heat breakthrough curve. The error made on temperature can be estimated to be between 10 and 20%, which is a fair value for indirect measurements. From our data, we estimated a quantification threshold for temperature variation of 1.2 °C. These results suggest that ERT should be considered when designing heat tracing experiments or geothermal systems. It could help also to assess the geometrical complexity of the concerned reservoirs. It also appears that ERT could be a useful tool to monitor and control geothermal systems once they are in operation.

© 2014 Elsevier Ltd. All rights reserved.

1. Introduction

Shallow alluvial aquifers constitute potential shallow geothermal energy reservoirs, relatively abundant and easily accessible. In these low temperature systems, groundwater has an average temperature ranging from 5 to 30 °C and may be used for domestic or industrial cooling and heating (Allen and Milenic, 2003; Haehnlein et al., 2010).

The two main techniques to exploit shallow geothermal energy systems are ground source heat pump (GSHP), which are closed

systems with a vertical or horizontal heat exchanger, and groundwater heat pump (GWHP), which are open systems circulating groundwater between production and injection wells. Designing such systems requires a multidisciplinary approach including geological and hydrogeological aspects. The most common approach is to model the system using a coupled groundwater and heat flow simulator. However, such models require estimating parameters governing heat transport such as heat capacity, thermal conductivity and density. Due to a lack of data, authors often have to rely on standard calculation charts, values found in the literature or default values implemented in softwares (e.g. Busby et al., 2009; Lo Russo and Civita, 2009; Liang et al., 2011; de Paly et al., 2012). In situ tests, such as thermal response tests (Raymond et al., 2011; Mattsson et al., 2008), or laboratory measurements (e.g. Haffen et al., 2013) are sometimes possible but the deduced values may deliver only well-centered information or may not always be representative of in situ conditions.

* Corresponding author at: University of Liege, Applied Geophysics, Department ArGenCo, Engineering Faculty, B52, Chemin des Chevreuils 1, 4000 Liege, Belgium. Tel.: +32 43669263; fax: +32 43669520.

E-mail address: thomas.hermans@ulg.ac.be (T. Hermans).

Thermal tracing experiments are performed for decades in hydrogeology (Anderson, 2005; Saar, 2011). Such experiments are used to improve the characterization of hydrogeological parameters (e.g. hydraulic conductivity or dispersivity), but the same methodologies may be used to study the thermal properties of shallow geothermal systems (e.g. Vandenbohede et al., 2009, 2011; Giambastiani et al., 2012). However, the heterogeneity of geothermal and hydrogeological systems may be too complex to be fully caught by thermal or solute tracer experiments alone (e.g. Brouyère, 2001).

In this context, electrical resistivity tomography (ERT) can bring relevant and spatially distributed information both on the heterogeneity of aquifers and on the temporal behavior of tracers. Indeed, ERT has proven its efficiency to image and/or monitor spatial phenomena (Vereecken et al., 2006) such as salt water intrusions (Nguyen et al., 2009; Hermans et al., 2012c), variations in moisture content (Binley et al., 2002), biodegradation of hydrocarbons (Atekwana et al., 2000), salt tracer experiments (Kemna et al., 2002; Robert et al., 2012) and heat injection experiments (Hermans et al., 2012b). It was also used in the characterization of geological structures, for example in the exploration of geothermal systems, where hydrothermal fluids may generate high contrasts of resistivity (Pérez Flores and Gomez Trevino, 1997; Bruno et al., 2000; Garg et al., 2007; Arango-Galván et al., 2011).

Besides the characterization of shallow geothermal systems themselves, their impact on the groundwater temperatures in the aquifer may be important since their exploitation yields cold and heat plumes (Molson et al., 1992; Palmer et al., 1992; Warner and Algan, 1984) which may influence aquifer properties and groundwater chemistry (e.g. Jesužek et al., 2013) and microbiology (Briemann et al., 2009). Haehnlein et al. (2010) pointed out that, if laws and rules exist in some countries to limit the temperature difference caused by the use of geothermal systems, the development of anomalies is rarely monitored. With the growth of the demand for renewable energy, we can expect that regulations will become stricter and controls of installations more common. New monitoring technologies will be needed and ERT may play an important role to monitor spatially, i.e. not only in wells, the variations of temperature in the aquifer. For example, the temperature changes observed on operating GWHP systems (e.g. Vanhoudt et al., 2011) are typically in the range of temperature that could be detected by ERT.

ERT aims at imaging the electrical resistivity distribution of the subsurface. Using petrophysical relationships such as Archie's law, one may recover indirect parameters such as saturation, water electrical conductivity or total dissolved solid content. Bulk electrical resistivity also decreases with temperature (e.g. Revil et al., 1998). In most studies, temperature effects are undesirable and may create artifacts in the interpretation, a correction term is applied to remove the influence of temperature variations (Hayley et al., 2007; Sherrod et al., 2012). Few studies used time-lapse ERT to monitor directly temperature changes (Ramirez et al., 1993; LaBrecque et al., 1996b), generally in a context quite different from GWHP or GSHP systems.

Hermans et al. (2012b) monitored with time-lapse surface ERT a heat injection experiment at a relatively small scale (45 m) and at shallow depth (2–4.5 m). Their results show that ERT is a reliable tool to monitor temperature changes and may be a method of choice for the design and the monitoring of geothermal systems. However, the results need to be extended to deeper and more complex, heterogeneous reservoirs, as it will be considered in this paper. ERT-derived temperatures were very close to temperatures modeled using a calibrated coupled groundwater and heat flow and transport model bringing additional constraints on the thermal properties of the aquifer.

For deeper reservoirs, the rapid decrease in resolution and sensitivity of surface ERT becomes a major drawback (Caterina et al.,

2013). It is then necessary to consider borehole ERT to improve resolution (Perri et al., 2012). For example, Prevedel et al. (2009) installed deep (600–750 m) borehole electrodes to monitor the migration of CO₂ within a storage reservoir (Bergmann et al., 2012). For cross-hole ERT, the results obtained for a specific study are more easily extendable than for surface ERT because resolution patterns are not depth dependent.

In borehole ERT, electrodes are located under the ground surface, either fixed at the outer-edge of the casing or mounted on cables with the borehole fluid ensuring the electrical contact with the surrounding rock. In the latter case, borehole fluid is generally more conductive than the rock and may influence resistance measurements (Doetsch et al., 2010). Using time-lapse ERT, the relative fluid effect will be almost similar at each time-step and should be insignificant in inversion results (Nimmer et al., 2008).

In this paper, we study the ability of ERT to monitor temperature changes in a heterogeneous aquifer and follow thermal tracing experiments. We pumped water from a gravel aquifer, heated it and reinjected it in a second well, similar to a GWHP system operation.

The paper is organized as follows: first, the field site is described; second, the methodology is presented; then, the results of the ERT monitoring are compared with direct measurements in wells; finally, conclusions are presented.

2. Field site

The study site is located in Hermalle-sous-Argenteau in Belgium near the Belgian-Dutch border (Fig. 1). It lies on the alluvial aquifer of the Meuse River. A pumping well and 8 piezometers were already present on the site since the 1980s and 11 new piezometers were drilled in June 2012 together with an injection well. They were arranged in three different panels crossing the main flow direction between the injection well and the pumping well in order to study the spatial variability during tracing experiments (Pz10–20, Fig. 2).

Borehole logs enabled to divide the deposits in four different units. The first layer consists of loam and clay with a thickness between 1 and 1.5 m. The second layer is composed of gravel in a clayey matrix. The bottom of this layer is found at depth between 2 and 3.2 m. These two first layers have little importance in this study because they are located in the unsaturated zone. The water table lies at approximately 3.2 m depth, with a very small gradient toward the northeast which is the main direction of flow (Fig. 2). The third unit is composed of gravel and pebbles in a sandy matrix. The quantity of sand decreases with depth, whereas the size of the pebbles increases with depth, a vertical variability is thus present. Lateral variability in the grain size distribution of the deposits is also expected in this heterogeneous aquifer, leading to variable hydrogeological parameters. Between 9.7 and 10.1 m, the Carboniferous bedrock composed of folded shales and sandstones is found.

In the middle panel, the outer piezometers are screened on the whole thickness of the alluvial aquifer. This is also the case for the injection and pumping wells. Except for the latter, they were equipped with a distributed temperature sensing (DTS) system to monitor the temperature during the experiment (Leaf et al., 2012 and references therein) with a spatial resolution of 0.5 m. Pz14 and Pz16 were screened at two different levels, with a 2 m long screen between 4 and 6 m depth and 1 m screen between 8.5 and 9.5 m. All other piezometers were screened at two different levels, with a 1 m screen between 4.5 and 5.5 m depth and a 2 m screen between 8 and 10 m depth. In the middle of each screened zone, a groundwater temperature logger was placed to monitor the temperature and the pressure during all the experiment.

Previous studies have shown that the gravel aquifer is very permeable. Calibrated hydraulic conductivity values were found

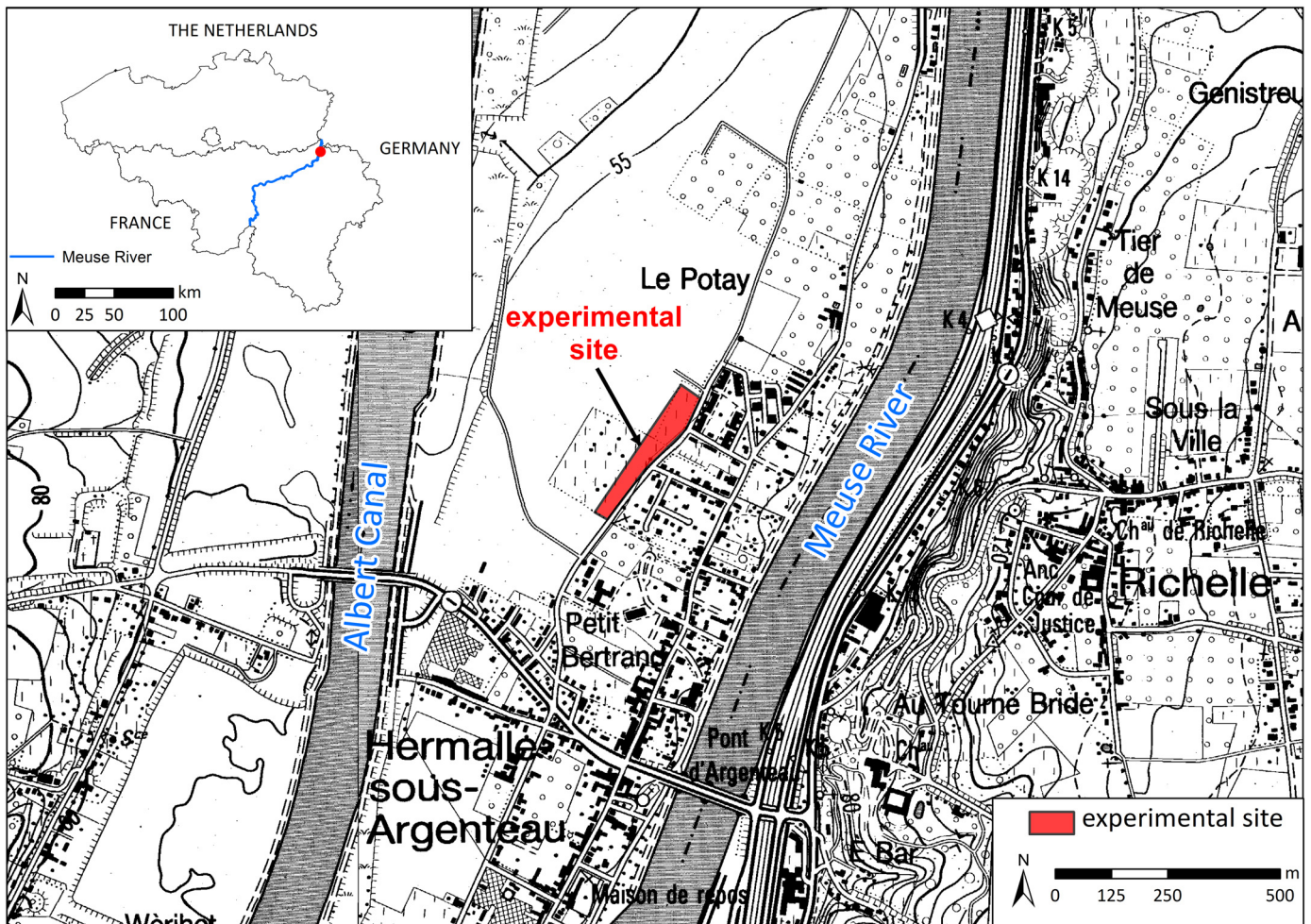


Fig. 1. The site of Hermalle-sous-Argenteau is located at the northern part of the Meuse River in Belgium (Wallonia) near the Dutch border. It is located almost at mid-distance between the Meuse River and the Albert Canal.

previously between 1.2×10^{-1} and 2×10^{-3} m/s (Dassargues, 1997; Derouane and Dassargues, 1998; Brouyère, 2001). With such values, it is possible to inject at a rate much higher than Hermans et al. (2012b) who were limited by the low hydraulic conductivity of fine sands and the small thickness of the aquifer.

3. Methodology

3.1. Heating and injection procedure

The experiment consists of an injection and pumping test. The groundwater is pumped from the pumping well, located in the northeastern part of the site, downstream from the injection well. We used a pumping rate of $30 \text{ m}^3/\text{h}$. Given the high hydraulic conductivity values of the aquifer, the corresponding drawdown is only 5 cm in the pumping well and 4 cm in Pz19 (5 m upgradient from the well). The pumping process ensures that the main direction of flow will cross the three intermediate panels. Pumping was started one day before the beginning of the injection of heated water, far early enough to reach a steady-state flow, and continued after the end of injection.

We used a mobile water heater (AQUAMOBIL DH6 system) to heat the water injected in the aquifer. It can work at a maximum rate of $3 \text{ m}^3/\text{h}$ with a difference in temperature of about 30°C . Given the high hydraulic conductivity of the aquifer, we decided to inject at this maximal rate. During the injection phase, $3 \text{ m}^3/\text{h}$ of

the pumped water were derived in a stocking tank, passed through the water heater and injected in the injection well. The mean temperature of the extracted water at the time of the experiment (October–November 2012) was 13°C . With the maximum injection rate, the temperature of the injected water reached a stabilized mean value of 38°C .

Injection started on October 30th and lasted for 1 day, resulting in the injection of 72 m^3 of heated water. Using groundwater also for injection, the transformation of ERT results into temperatures will be direct and only require a unique petrophysical relationship. However, the heterogeneity of the aquifer and the advection component make the experimental set-up quite complex.

3.2. Petrophysical relationship linking temperature and conductivity

The aim of the petrophysical relationships is to quantify the link between bulk electrical conductivity and temperature. Bulk electrical conductivity is generally expressed as a function of porosity, grain size and tortuosity (often joined in a term called formation factor), saturation, fluid electrical conductivity and surface conductivity. In this case, we are interested in the saturated zone (saturation = 1) where the grain size distribution is dominated by gravel with very few fine elements. We can thus neglect the surface conductivity which is very low for coarse grains (Revil and

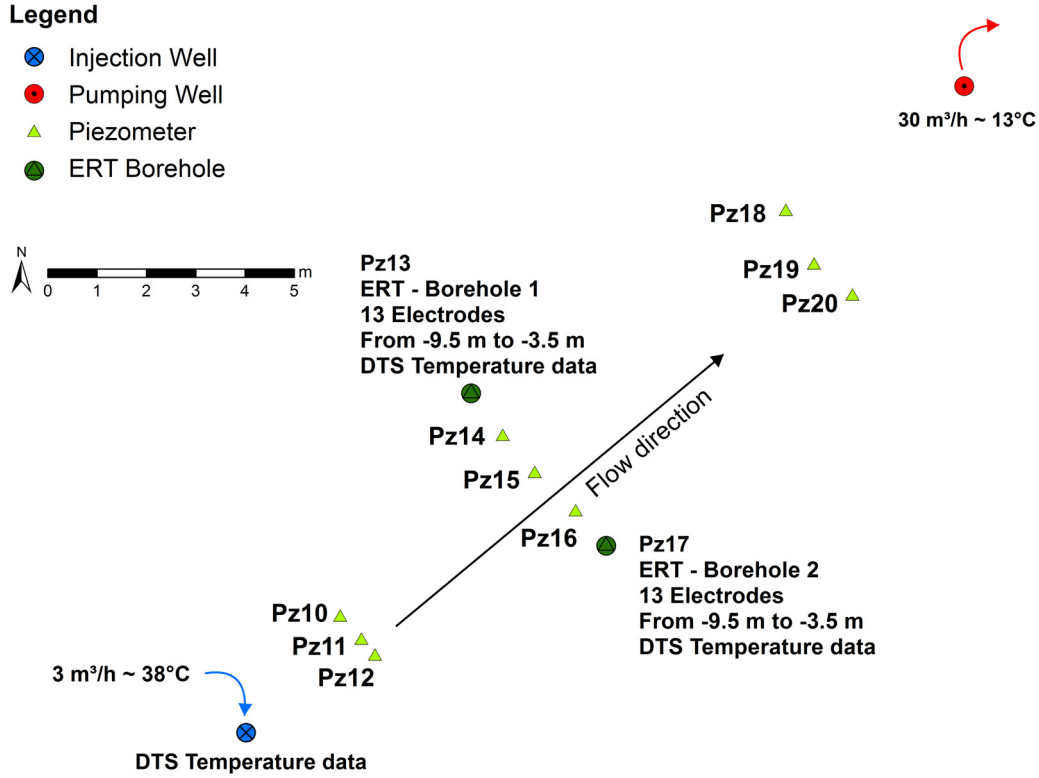


Fig. 2. The new piezometers are arranged in three different panels crossing the expected flow direction between an injection and a pumping well. Pz 10–12, Pz 14–16 and Pz 18–20 are equipped with groundwater temperature loggers at two different levels. On the middle panel, the outer piezometers were equipped with a DTS system and with electrodes.

Linde, 2006). With this assumption, the link between bulk electrical conductivity σ_b and fluid electrical conductivity σ_f is

$$\sigma_b = \frac{\sigma_f}{F} \tag{1}$$

where F is the formation factor (Archie, 1942). The latter is variable spatially, depending on the lithology. In the case of a monitoring study, we measure bulk electrical resistivity at different time steps and compare it to a reference state, called the background. If we take the ratio of Eq. (1) between a specific time-step, representing state 2, and the reference background, representing state 1, we have

$$\frac{\sigma_{b2}}{\sigma_{b1}} = \frac{\sigma_{f2}}{\sigma_{f1}} \tag{2}$$

and the relation is not dependent on the formation factor anymore. In Eq. (2), σ_{b1} and σ_{b2} are determined with ERT after inversion of resistance data and σ_{f1} is either measured on the field directly or deduced from the temperature of the formation water in the aquifer. The only unknown in Eq. (2) is the fluid electrical conductivity at state 2, which can be expressed as

$$\sigma_{f2} = \frac{\sigma_{b2}}{\sigma_{b1}} \sigma_{f1} \tag{3}$$

Through Eqs. (1)–(3), we see that the variation in bulk electrical conductivity in the saturated zone is related to a variation of the fluid electrical conductivity only. The latter can be caused by a change in fluid salinity or by a change in temperature. If we assume that the salinity of the fluid remains constant during the experiment, the water electrical conductivity depends only on temperature.

Hermans et al. (2012a) have shown that for long term experiments (storage phase) at relatively high temperature, the link between temperature and electrical resistivity may be more complex, due to precipitation/dissolution effects related to temperature

changes, as shown by Robert et al. (2013). However, in this case, the temperature difference is about 25 °C and should rapidly decrease due to dispersion effects. The variation of salinity with changing chemical equilibrium should be relatively small. If this effect is not negligible, an additional term in Eq. (5) should be added and calibrated to derive temperatures.

In the temperature interval considered in this experiment (10–40 °C globally, and 10–20 °C for the panel monitored with ERT), a linear dependence can be assumed between temperature and fluid electrical conductivity (e.g. Sen and Goode, 1992 and Hayley et al., 2007 or Hermans et al., 2012b for applications). This relation can be expressed as

$$\frac{\sigma_{f,T}}{\sigma_{f,25}} = m_f(T - 25) + 1 \tag{4}$$

where $\sigma_{f,T}$ is water electrical conductivity at temperature T in °C, $\sigma_{f,25}$ is the conductivity at 25 °C, considered as the reference temperature (another reference could be chosen as well) and m_f is the fractional change in electrical conductivity per degree Celsius at the reference temperature.

A water sample was taken on the site and relation (4) was verified experimentally in the laboratory (Fig. 3). Fig. 3 shows the results up to 20 °C (temperature encountered in the middle panel), but the trends remains the same until 40 °C. Fitting a linear curve to the experimental points, we found m_f equal to 0.0194 and the conductivity at the reference temperature (25 °C) is equal to 0.0791 S/m. The value for the fractional change per degree Celsius is in the same range as observed by Hayley et al. (2007) and Hermans et al. (2012b).

Introducing Eq. (4) into Eq. (3), we can express the temperature T (in °C) according to bulk electrical conductivity, water electrical

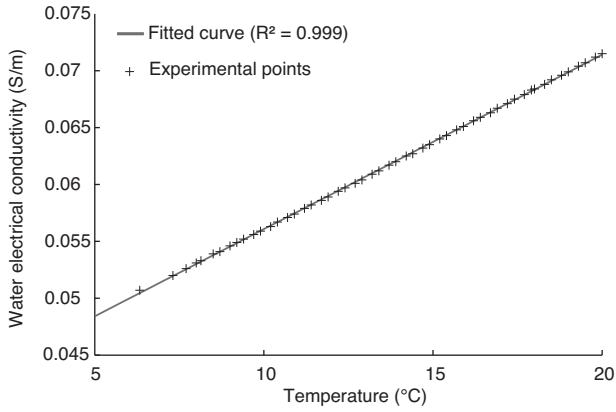


Fig. 3. The water electrical conductivity of formation water increases linearly with temperature (points). Parameters of Eq. (4) were fitted with a fractional change per degree Celsius, m_f , equal to $0.0194\text{ }^\circ\text{C}^{-1}$ and the electrical conductivity at $25\text{ }^\circ\text{C}$ is 0.0791 S/m .

conductivity at the temperature of reference and at the temperature of the background and the fractional change per degree Celsius

$$T = \frac{1}{m_f} \left[\frac{\sigma_{b2,T}}{\sigma_{b1}} \frac{\sigma_{f1}}{\sigma_{f,25}} - 1 \right] + 25 \quad (5)$$

where $\sigma_{b2,T}$ represents the bulk electrical conductivity at the time-step for which we try to determine the temperature.

3.3. Electrical resistivity measurements

The two outer piezometers of the middle panel (Pz13 and Pz17 on Fig. 2) were equipped with borehole electrode cables with 0.5 m spacing. Each borehole has thus 13 electrodes made of stainless steel located from 3.5 to 9.5 m depth. The first electrode is located just below the water table whereas the last electrode is located just above the bedrock.

The two boreholes are separated horizontally by 4.5 m. The thickness covered by the electrodes is 6 m. The aspect ratio, i.e. the ratio of the separation between boreholes and the length of the equipped borehole is thus equal to 0.75. This value is often considered as the maximum acceptable value to obtain a sufficient resolution. Optimal resolution is generally achieved with an aspect ratio of 0.5 (LaBrecque et al., 1996b).

We used a combination of bipole–bipole (also called AM–BN) and dipole–dipole (AB–MN) configurations as measuring sequence. The first one has a better signal-to-noise, but a lower resolution (Zhou and Greenhalgh, 2000). For bipole–bipole measurements, we measured every possible configuration. For the dipole–dipole, we kept only the cross-borehole measurements, using a dipole spacing ranging from 0.5 to 5 m and measuring dipoles sharing one electrode. The complete data set contains 969 possible measurements.

We used an ABEM Terrameter LS to acquire the data with an acquisition delay of 0.5 s and an acquisition time of 1 s. We used a standard deviation limit of 1% on the repeatability error after 3 stacks to filter the data. For almost each time step, we collected both normal and reciprocal measurements to assess the error level on the data. The latter are obtained by swapping current and potential electrodes (LaBrecque et al., 1996a). Acquiring a complete data set took about 45 min (normal and reciprocal measurements).

The error level was estimated using both the methods of Slater et al. (2000) and Koestel et al. (2008). They both used the reciprocal error to derive a linear relationship between the mean measured resistance R_m (mean between normal and reciprocal resistance, in

Ω) and error e (in Ω) defined as the difference between normal and reciprocal measurements

$$|e| = a + bR_m \quad (6)$$

where a is an absolute error (Ω) and b is a relative error. Slater et al. (2000) considered the envelope curve as error model, which can be considered as conservative, since the mean error is overestimated. Koestel et al. (2008) worked with standard deviation of logarithmic bins to determine the coefficients. This method may result in a mean error model, less conservative.

Nguyen et al. (2011) have shown that the noise level characterization is of great importance in time-lapse studies and should always be investigated carefully. If the noise levels are too different between time-steps, it may prevent a quantitative interpretation of monitoring data. If noise levels are almost similar, one should choose a common error model to invert all data sets. We calculated error models for both methods and each time-step. We chose a common error model with an absolute error of $0.002\ \Omega$ and a relative error of 0.5%. We tested different error level around these values, with few differences in the final images, both qualitatively and quantitatively.

The aim of cross-hole electrical resistivity was to detect the first arrival of the tracer, the maximum temperature reached in the middle panel and, to image vertical and lateral variations in the temperature distribution. Data sets were collected about every 6 h during the injection and the day after. For the next days, we increased the time-steps to about 18 h, with one or two sections per day. The total monitoring time was 6 days, time at which the resistivity distribution had almost returned to the background distribution. For comparison, a DTS system was set in both boreholes to control the temperature directly and assess the ability of ERT to derive reliable temperatures.

3.4. Inversion procedure

In electrical resistivity tomography, the solution of the inverse problem is non-unique. A common way to solve such inverse problems is to add a regularization constraint to the least-square problem (Tikhonov and Arsenin, 1977). The problem is then to minimize, through an iterative process an objective function of the form

$$\psi(\mathbf{m}) = \|\mathbf{W}_d(\mathbf{d} - f(\mathbf{m}))\|^2 + \lambda \|\mathbf{W}_m \mathbf{m}\|^2 \quad (7)$$

where λ balances between the data misfit (first term of the right hand side of Eq. (7)) and the model a priori characteristic (second term), \mathbf{d} represents the vector containing the data, expressed as the logarithm of measured impedance, \mathbf{m} is the model of the logarithm of subsurface electrical conductivity, $f(\mathbf{m})$ is the forward operator, \mathbf{W}_d is the data weighting matrix using the reciprocal error as estimate (Eq. (6)) and \mathbf{W}_m is a matrix describing an a priori characteristic of the conductivity model. Several forms are possible for \mathbf{W}_m , for example to include prior information (e.g. Hermans et al., 2014). The most common method, used in this study, is to penalize roughness to describe smooth model variations (de Groot-Hedlin and Constable, 1990).

With time-lapse data sets, we are more interested in the change in electrical conductivity than in the absolute value of conductivity. Generally, the process of inversion is adapted in order to improve inversion results. In this paper, we do not consider coupled inversion of time-lapse ERT data and hydrogeological models (e.g. Irving and Singha, 2010). Three main procedures, with several variants, exist to invert for time-lapse ERT data (e.g. Miller et al., 2008), namely independent inversion, time-constrained or reference model inversion and difference inversion. In the first one, inversion results obtained separately are simply subtracted, which should eliminate systematic errors but amplify uncertainties

in the data. For temporally constrained schemes, a regularization operator is added in the time dimension in addition to the space dimensions, to minimize changes between successive sections (e.g. Karaoulis et al., 2011, 2014). This enables 4D inversions of ERT time-lapse data sets and has already shown to be efficient in tracer tests (Revil et al., 2013). In this study, we used the difference inversion scheme (Kemna et al., 2002) where the problem is formulated in terms of variations for both data and model. Eq. (7) becomes

$$\psi(\mathbf{m}) = \left\| \mathbf{W}_d(\mathbf{d} - \mathbf{d}_0 + f(\mathbf{m}_0) - f(\mathbf{m})) \right\|^2 + \lambda \left\| \mathbf{W}_m(\mathbf{m} - \mathbf{m}_0) \right\|^2 \quad (8)$$

where \mathbf{d}_0 and \mathbf{m}_0 are respectively the data set and the model corresponding to the background state. The results obtained for the background are thus used as reference for subsequent inversions. This method should reduce the systematic error and provide a faster convergence (LaBrecque and Yang, 2000).

To compare the successive models in the monitoring study, it is important that all data sets are inverted with the same level of data misfit corresponding to the expected noise level. Indeed, over-fitting the data may create artifacts of inversion in the corresponding image, whereas the contrary would result in an over-smoothed inverted section (LaBrecque et al., 1996a). To achieve this, the iteration process is stopped when the root-mean-square (RMS) value of error-weighted data misfit

$$\varepsilon_{RMS} = \sqrt{\frac{\left\| \mathbf{W}_d(\mathbf{d} - f(\mathbf{m})) \right\|^2}{N}} \quad (9)$$

with N representing the number of data, reaches the value 1 for a maximum possible value of λ , corresponding to data fitted to its error level. At each iteration, λ is optimized to obtain the minimum value of ε_{RMS} . When, ε_{RMS} is inferior to 1, we looked for the unique value of λ that satisfies the data misfit criterion ($\varepsilon_{RMS} = 1$).

We used the code CRTomo (Kemna, 2000) to invert our data. This code is a 2.5D inversion code; it means that the electrical conductivity distribution is assumed to be constant in the direction perpendicular to the section and that the effect of boreholes themselves cannot be taken into account (Nimmer et al., 2008; Doetsch et al., 2010). Effects caused by boreholes are of more concern when the investigated site is located in high resistive rocks. They may also be, at least partly, avoided with time-lapse inversion. Indeed, we can expect that, if present, 3D artifacts will be compensated because present in both background and monitoring states (Nimmer et al., 2008). However, a possible 3D effect when imaging a contrasting plume, also called shadow effect, is that the plume is imaged even if it is outside the image plane, because the 3D heterogeneity caused by the moving tracer is not taken into account in the 2.5D inversion scheme (Nimmer et al., 2008). This may result in bias in the breakthrough curve, leading to an apparent more diffuse behavior of tracers (Vandenborgh et al., 2005).

We used a grid with square elements of $0.25 \text{ m} \times 0.25 \text{ m}$, to have two elements between electrodes, extended laterally and in depth for inversion. ERT-borehole 1 is located at abscissa 1 m and ERT-borehole 2 at abscissa 5.5 m on the grid.

To assess the quality of the ERT image, we used the error weighted cumulative sensitivity matrix (Kemna, 2000; Caterina et al., 2013). The cumulative sensitivity \mathbf{S} is defined as

$$\mathbf{S} = \text{diag}(\mathbf{J}^T \mathbf{W}_d^T \mathbf{W}_d \mathbf{J}) \quad (10)$$

where \mathbf{J} is the Jacobian matrix and T denotes the transpose operator. \mathbf{S} depends on both the distribution of resistivity in the model parameters and the data weighting matrix which depends on the error assessment. A high value of sensitivity for a parameter signifies that a change of its resistivity would strongly influence the data. In contrast, a low value of sensitivity is characteristic of a parameter having less influence on the predicted data. Such a low

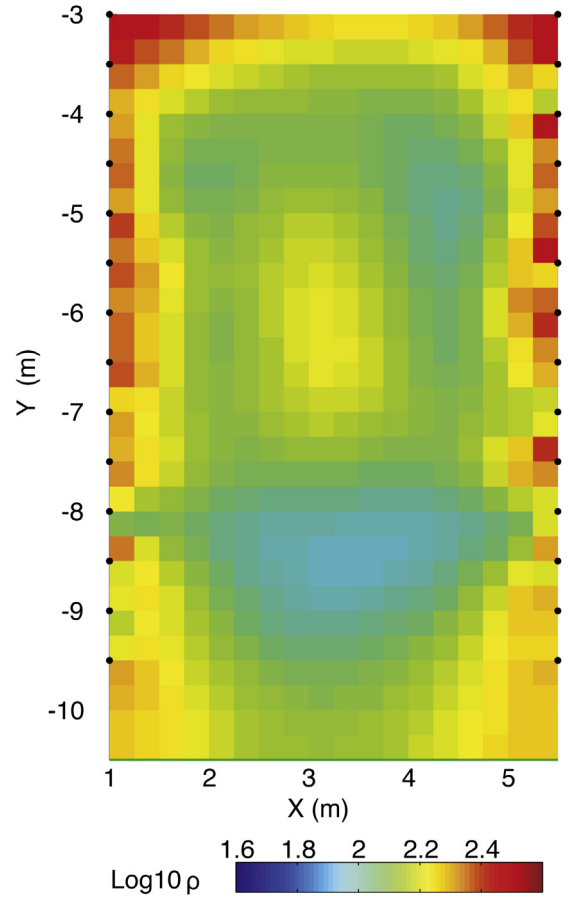


Fig. 4. The background inverted section shows resistivity values ($\Omega \text{ m}$) varying between 100 and 200 $\Omega \text{ m}$. The section seems slightly heterogeneous.

sensitivity zone will most likely be badly resolved in the inverted section. However, it has to be noted that high sensitivity does not necessarily mean high resolution.

4. Results and discussion

4.1. Cross-borehole ERT background

The background image was obtained using Eq. (7), corresponding to the smoothness-constrained solution (Fig. 4). In the zone between the boreholes, we see that the resistivity lies between 100 and 200 $\Omega \text{ m}$, with lower resistivities at the bottom of the section. These resistivity values are characteristic of saturated sand and gravel. The lower resistivity observed at the bottom of the aquifer corresponds with coarser gravel and a lower sand content.

The resistivity tends to increase toward the unsaturated zone (above -3.5 m), but there was no electrode in this part of the section (the electrode at -3 m was modeled but not used for any configuration). However, we do not expect these absolute values to be accurate due to borehole and 3D effects in the inversion (Nimmer et al., 2008).

The sensitivity pattern is typical of cross-borehole measurements (Fig. 5). The sensitivity is high in the neighborhood of the boreholes and decreases toward the middle part of the section. The sensitivity is lower in two opposite triangles in the upper and bottom part of the saturated zone, due to a smaller coverage of data points in this zone. The lowest sensitivity values are found in the unsaturated zone. The electrical contact through borehole electrodes was not possible because the borehole is not filled with water in this part; no surface electrodes were used to improve the

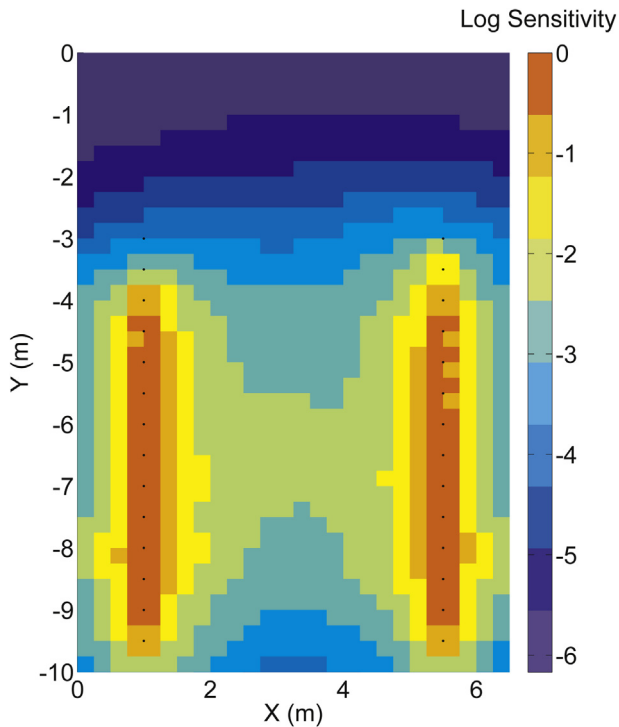


Fig. 5. The relative sensitivity pattern is typical of cross-borehole measurements, with smaller sensitivity values in the middle part of the section, especially at the position of top and bottom electrodes.

resolution, because the aim is to image temperature changes in the saturated zone. Given the sensitivity values and the aspect ratio, we assume that the chosen configuration is sufficient to monitor temperature changes within the section.

4.2. Cross-borehole ERT monitoring results

Before looking at inverted data, it is important to qualitatively check if the acquired data contains some information about the monitored process. We calculated the mean resistance of each data set after removing data with repeatability error higher than 1% (870 points remaining). The mean resistance for the background data set is 14.31 Ω . The first monitoring set was taken after 7 h of injection, the mean resistance slightly increases, but not significantly (Fig. 6). This is likely an effect of noise on the data. We can state that temperature changes are too small to influence the measured resistance. The same effect can be observed on individual

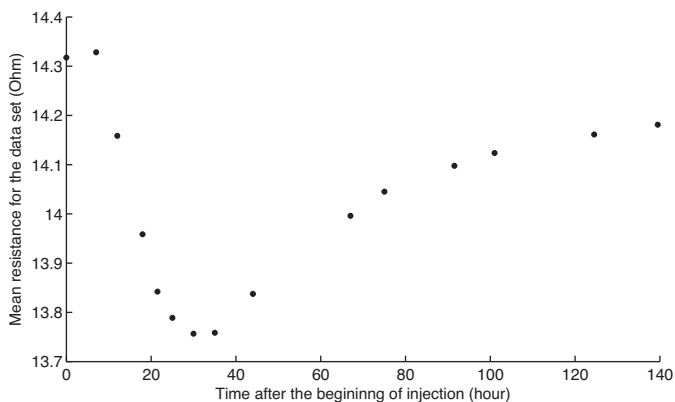


Fig. 6. The mean resistance (in Ω) of the global data set first decreases with depth as the plume of heated water approaches, it reaches a minimum after 30–35 h and then starts to increase slightly.

measurements. The mean resistance then decreases with time to reach a minimum value of 13.76 Ω after 30–35 h after the beginning of injection, which corresponds to 6–11 h after the end of injection. After the minimum, the mean resistance starts to increase and slightly tends to its initial state, even if it is not totally reached at the end of the monitoring process.

Fig. 6 can be seen as a qualitative mean breakthrough curve of the heat tracing experiment. It enables to derive two important parameters: the first detected arrival of heat, which occurs between 7 and 12 h, and the maximum changes, which occurs between 30 and 35 h.

The time-lapse data sets were inverted using Eq. (8), i.e. the results of Fig. 4 are used as a reference and we inverted data differences to derive model perturbations. We kept the same error model for all inversions and we reached a value of ε_{RMS} equal to 1 for all inversions, ensuring that all models are fitted to the same level of noise. The results are presented as percentage change of resistivity

$$\Delta\rho = \frac{\rho_i - \rho_{BG}}{\rho_{BG}} \times 100 \quad (11)$$

where ρ_i is the resistivity of the time-lapse section and ρ_{BG} is the resistivity of the background section. A negative value corresponds to a decrease in resistivity (or increase of conductivity) and a positive value corresponds to an increase in resistivity.

Given the process that is monitored, only negative changes related to an increase in temperature are expected. However, in the inverted time-lapse sections (Fig. 7) positive changes of resistivity appear. They are limited in absolute value to +5% in the unsaturated zone which suffers from a very poor resolution, and +3% in the saturated zone. We relate these positive changes to the propagation of data noise in the inversion process (Robert et al., 2012). Consequently, we consider that variations in the range -3% to $+3\%$ cannot be directly related to temperature variations. They are whitened in the figure. If -3% is the minimum change in resistivity that can be correctly imaged, the limit of detection of ERT for temperature around 13 $^{\circ}\text{C}$ is about 1.2 $^{\circ}\text{C}$ (Eq. (5)).

The inverted time-lapse sections (Fig. 7) show a general behavior of the plume similar to the one observed from the mean resistance. After 7 h (not shown), changes in resistance are low and under the level of noise, yielding a section with no changes, i.e. the background model is sufficient to explain the data. After 12 h, changes of resistivity about -5% appear. Then, the decrease in resistivity becomes stronger and reaches a maximum between 25 and 35 h. Afterwards, the contrast becomes less strong and after 90 h, almost all changes are below 5%. It signifies that their level becomes low to be interpreted quantitatively (close to the limit of detection). However, their spatial distribution is coherent with previous time steps, so it means that the aquifer has not returned to its initial state yet, which is confirmed by the mean resistance.

The apparent decrease in resistivity observed in the 101 h section is likely due to an artifact of inversion since it is not physically plausible and does not appear in any other sections. The fact that all other anomalies observed in the sections are recurrent for all time steps and that their amplitude variation follows the trend of classical breakthrough curves validate qualitatively the results of inversion. If some anomalies were related to artifacts of inversion, they would be more randomly distributed for the different time-steps.

The advantage of crosshole ERT compared to direct measurements is to provide a spatial distribution of the changes occurring in the aquifer. Fig. 7 clearly shows that the changes in resistivity are not homogeneously distributed in the aquifer. Most important changes are observed below -7.5 m depth. This part of the alluvial aquifer is dominated by very coarse gravel with pebbles and a limited amount of sandy matrix, as was observed during drilling. The hydraulic conductivity of the bottom part is higher and the

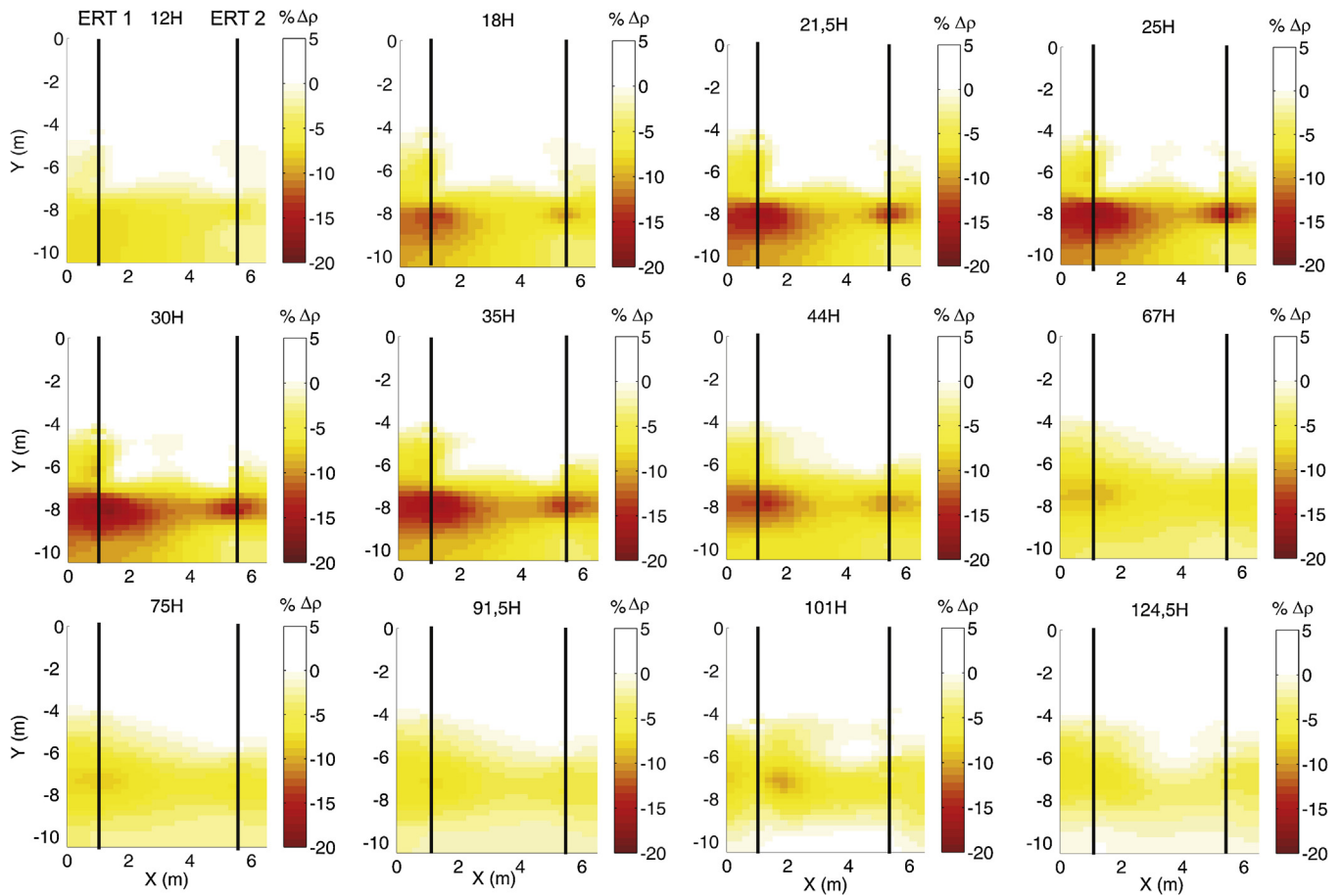


Fig. 7. The inverted sections (% change in resistivity) evolve in time with the arrival of the plume. Maximum changes are observed between 30 and 35 h in the surrounding of ERT borehole 1. These sections highlight the spatial heterogeneity of the aquifer. Time is given from the beginning of injection.

flux is greater, so a major part of heat is flowing in this zone of the aquifer. In the upper part, the convection velocity is slow and the maximum change in temperature is much lower, below the minimum change that ERT can detect. Laterally, we also see variations. The maximum change does not occur in the middle of the section, along the supposed main flow direction. It is located closer to ERT-borehole 1. The resistivity changes are smaller in the middle part, whereas there are a little bit higher in the neighborhood of ERT-borehole 2. Since sensitivity is smaller in the middle section, there is more uncertainty related to those parameters. However, this trend will be confirmed by direct measurements in boreholes (Section 4.4).

The lateral variations observed in the ERT sections suggest a degree of heterogeneity that was not clearly distinguishable on borehole logs. Zones of preferential flows modify the expected flow direction and result in sections showing a complex spatial behavior. We will see later that these observations are confirmed by direct measurements in borehole.

4.3. ERT-derived temperatures

For simplicity, we decided to use a constant value of σ_{f1} (Eq. (5)) to transform the ERT images into temperature sections.

Eq. (4) proposes a linear relationship between water electrical conductivity and temperature. We thus deduce σ_{f1} based on our direct measurements of temperature. They show that the temperature profile is not constant everywhere in the aquifer and in the ERT section (Fig. 8). In ERT-borehole 1, a maximum temperature difference of 1.3 °C is observed between the top and the bottom of

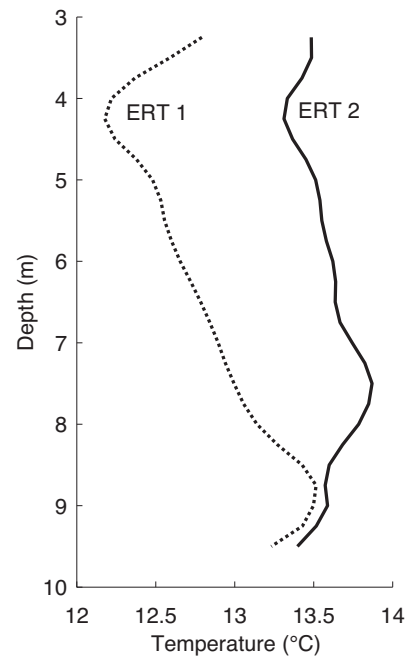


Fig. 8. DTS temperature profiles in the two ERT boreholes before the test are not similar. The temperature varies with depth and the mean temperature is different in the two boreholes: 12.8 °C in ERT-borehole 1 and 13.6 °C in ERT borehole-2.

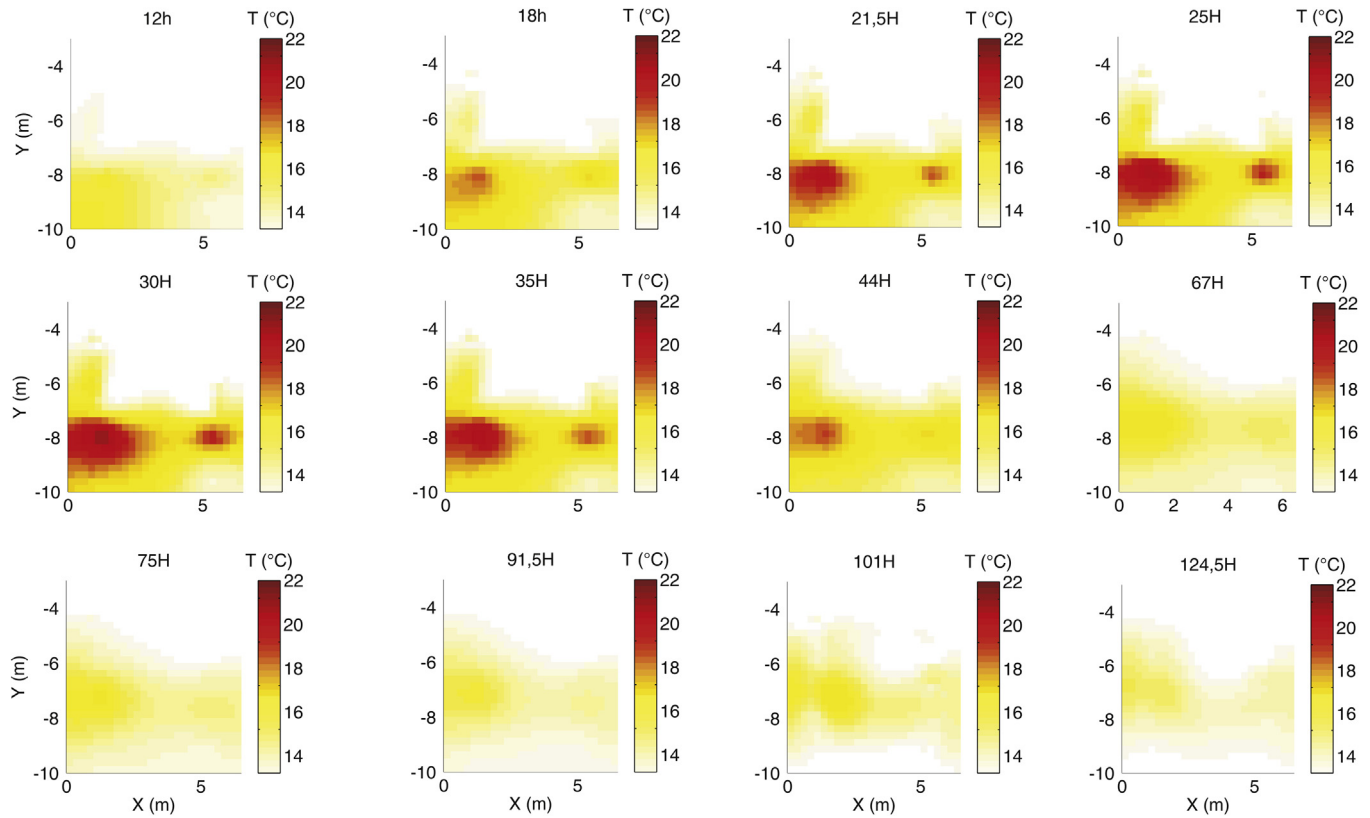


Fig. 9. The ERT-derived temperature sections show that the maximum temperature reached is around 21 °C in the neighborhood of ERT-borehole 1. The sections are limited to the saturated zone, because Eq. (5) is not valid in the unsaturated zone.

the aquifer. It is slightly less in ERT-borehole 2. The mean temperature in the two boreholes is also different: 12.8 °C in ERT-borehole 1 (Pz13) and 13.6 °C in ERT-borehole 2 (Pz17). We took the mean temperature of both ERT-boreholes (13.2 °C) and derived with Eq. (4) a water electrical conductivity of 0.061 S/m. Another solution would have been to interpolate temperatures between boreholes, but it would have made the process more complex without ensuring an improvement of the results.

This process has two additional assumptions. First, the specific electrical conductivity of water is constant with time. This was controlled using water samples collected in Pz15 during the test. The changes in the specific conductivity of water are smaller than 1%. The increase in temperature does not seem to favor precipitation or dissolution of minerals. The second assumption is that, at a given temperature, the ratio $\sigma_{f1}/\sigma_{f,25}$ (Eq. (5)) is constant in space, or similarly that m_f is constant in the whole section. Indeed, if the specific conductivity of water varies in the section, the conductivity at a given temperature varies in the same proportion and the influence on the calculation of temperature is limited. Given the values generally observed in the literature, this assumption is not too severe.

The spatial distribution of temperature (Fig. 9) is similar to electrical resistivity changes (Fig. 7). Maximum changes of temperature are observed in the neighborhood of ERT-borehole 1, with a maximum temperature of 21 °C, which corresponds to an increase around 8 °C. However, we know that the background temperature in ERT-borehole 1 is slightly below the mean value chosen to draw these sections. Considering the limit of detection of 1.2 °C at 13 °C, temperatures in the range 13.2–14.4 °C are only indicative of a small raise in temperature, but the exact value cannot be derived. In addition, we have an error related to the mean water electrical conductivity used in Eq. (5).

4.4. Comparison with direct measurements

The layout of the study site enabled to make a lot of direct measurements in piezometers, at different levels in the aquifer. To compare with ERT results, we have DTS measurements in ERT-boreholes 1 and 2, and groundwater temperature loggers at two levels in the three intermediate piezometers Pz14–Pz16.

The quicker arrival of heat in the bottom part of the aquifer (Figs. 7 and 9) is confirmed in intermediate piezometers (Fig. 10 for Pz15). In the upper part, the arrival is very slow and a clear increase in temperature is only visible after 2 days. The oscillations in the signal are disturbances due to sampling of water by pumping from the piezometer. The amplitude of the signal remains very small,

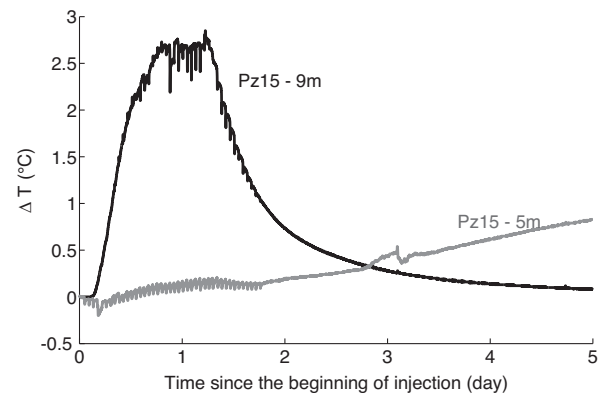


Fig. 10. The temperature monitored at two different levels in Pz15 shows that the arrival of the tracers is much quicker and with much higher amplitude in the bottom part of the aquifer than in the upper part.

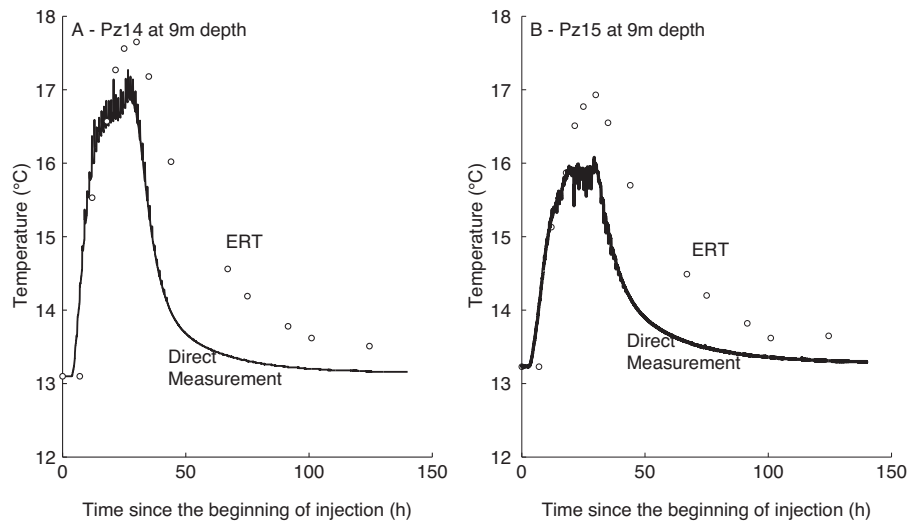


Fig. 11. Breakthrough curves for ERT-derived temperatures and direct measurements in Pz14 (A) and Pz15 (B) show a good temporal agreement, but temperature are overestimated for the maximum and the tail of the curve.

below 1 °C at the end of the test. Actually, the peak would only be observed after 10 days with an amplitude of about 1.15 °C. The same is observed in Pz16 (1 °C after 10 days). In Pz14, the change is slightly higher (2 °C after 4 days). In the bottom part, the arrival of heat is quicker, after a few hours, with a range of temperature slightly above the limit of detection of ERT. This is totally in agreement with the ERT sections. Spatially, the temperatures observed with ERT are also coherent with direct measurements. The temperatures observed in the bottom part of Pz14 to 16 have a decreasing trend from Pz14 to Pz16, which is also evident from ERT sections where the zone near ERT-borehole 1 is hotter than the middle of the section. As an example, the maximum ΔT in Pz14 is 4.2 °C, whereas it is only 2.9 °C in Pz15. We can conclude that the qualitative observations on the spatial and temporal distribution of temperature are confirmed by direct measurements.

To verify the ability of ERT measurements to quantify temperature, we rely on two different indicators. First, we can draw breakthrough curves at the locations of groundwater temperature loggers to compare the direct measured curve with the ERT-derived curve. This will give insights on the ability to quantify temporally temperature changes. Secondly, we may compare temperature logs at ERT-borehole 1 and 2, to investigate quantitatively the spatial distribution of temperature.

Fig. 11 shows the breakthrough curves in the bottom part of Pz14 (A) and Pz15 (B) for both direct measurements and ERT. We used the temperatures measured in the corresponding boreholes to determine σ_{f1} in Eq. (5). For both piezometers, ERT does not detect directly that heat is arrived, because the changes are small, below the sensitivity of the method. However, the rising part of the curve is well resolved with an ERT-derived temperature almost exactly the same as measured directly. The maximum is overestimated, with an error of about 0.5 °C in Pz14. The maximum change being 4 °C, it represents an error of about 12.5%. In Pz15, the fit is less good, but the maximum change is lower and the spatial smoothing of the inversion process may yield an overestimation of the temperature. For both cases, the tail of the curve is overestimated by ERT-derived temperatures. This effect would lead to an overestimation of the thermal dispersivity of the aquifer if ERT results were used alone. This could be related to a 3D effect (shadow effect), because the maximum of the plume, even if not in the section anymore, is still influencing measurements.

It must also be kept in mind that the volume investigated by ERT and direct measurements is not the same. Groundwater temperature loggers give a very local measurement inside the piezometer

which is itself a singularity inside the aquifer. ERT inversion results give a mean resistivity over the surface of the corresponding cell (here 0.25 m \times 0.25 m). Another possibility would be an increase of the specific conductivity of formation water due to dissolution of minerals related to the increase of temperature. However, given the quick decrease of temperature when we move away from the injection well, this effect is negligible. This is confirmed by the samples collected in Pz15 which show an almost constant specific conductivity.

Temporally, the results are very satisfactory because the raising part, the maximum and the tailing of the curve are imaged at correct times. In this specific case, the time resolution of ERT is only of a few hours. It signifies that we cannot expect to detect the first arrival with precision. Given the material used, we could achieve a time resolution of half an hour, by reducing acquisition time and acquisition delay which were chosen conservative.

The comparison of ERT-derived temperatures with DTS measurement in the two ERT-boreholes yields contrasted results and conclusions (Fig. 12). In contrast with Fig. 9, where we used a constant value of σ_{f1} , the temperatures measured with the DTS for the background profile were here used to derive a specific value of σ_{f1} for each depth level. In addition, DTS measurements were averaged on the time interval corresponding to the duration of a complete ERT data acquisition. Consequently, the match would be perfect if we would derive temperatures for the background ERT profile using Eq. (5).

In ERT-borehole 1 (Fig. 12A), ERT results show the same behavior as observed in Fig. 7, with higher temperatures in the bottom part of the aquifer, and smaller in the upper part. In contrast, DTS measurements yield an almost constant temperature on the whole thickness of the aquifer. This is a quite surprising observation, because all direct measurements made on the site have shown a clear contrast in temperature distribution between the bottom and upper parts of the aquifer. We think that DTS measurements are influenced by specific borehole conditions and do not reflect the true formation temperature. A possible explanation is that the water suffers from some mixing in and around the well. ERT measurements, even if influenced by the borehole fluid, are sensitive to the variations outside the borehole itself. This effect may also explain why temperature near ERT-borehole 1 seems to be higher in Fig. 9 in the upper part of the aquifer whereas it is not the case in the middle part of the section.

In ERT-borehole 2 (Fig. 12B–D), the agreement between ERT-derived temperatures and DTS logs is better. It confirms that the

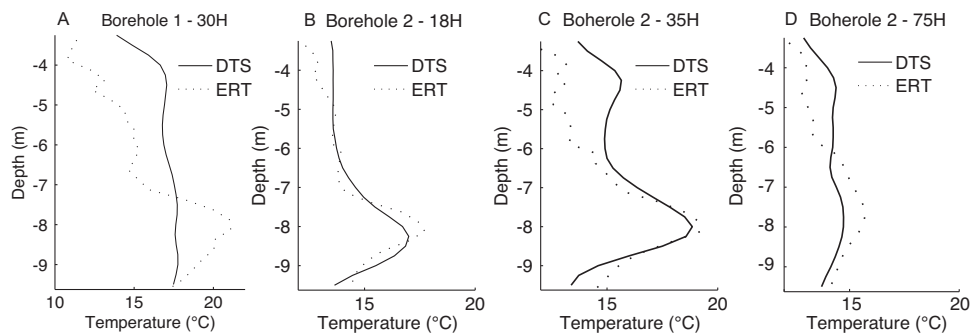


Fig. 12. ERT-derived temperature profiles are not consistent with DTS measurements in ERT-borehole 1 (A), but show a very good agreement in ERT-borehole 2 (B, C and D). The almost constant temperature observed with DTS in ERT-borehole 1 may be due to some mixing of water in and around the well.

hot spot observed near this borehole in Fig. 9 is not an artifact of inversion but is related to an increase in temperature. Globally, DTS measurements show slightly less contrast than ERT, maybe also due to borehole conditions as observed in ERT-borehole 1. Quantitatively, ERT-derived temperatures are close to DTS temperatures for the rising and maximum part of the breakthrough curve (Fig. 12 B and C), but suffer from an overestimation for the tail (Fig. 12 D), as it was observed in Fig. 11. Such an effect would be reduced in a storage experiment with conditions of no flow.

The comparison of ERT results with direct measurements and their good agreement confirm that the alluvial aquifer is heterogeneous and complex. Instead of a unique heat plume in the middle part of the section, we observed two separated arrivals with a minimum temperature observed in the middle.

5. Conclusion

The growing demand for renewable energy leads to an increase in the development of geothermal energy projects. Heat storage has become a common energy storage technology and heat is a common tracer in hydrology and hydrogeology. The variation of electrical resistivity/conductivity of water, soils and rocks is a well-known phenomenon and has been studied for several decades. However, the potential of ERT, a method mapping the electrical resistivity of the subsurface, to monitor and quantify temperature was barely approached in the literature.

In this paper, we investigated the ability of crosshole ERT to monitor a heat tracing experiment in a complex heterogeneous alluvial aquifer. The studied section was located perpendicular to the main direction of flow to cross the plume of heated water. The results, corroborated by direct measurements in several control piezometers, highlight the ability of ERT to qualitatively monitor the variations of temperature in the aquifer. Spatially, it enabled to map the horizontal and vertical extent of the plume, as well as the zones of maximum temperatures, what would not be feasible with costly and limited direct measurements.

If information on the initial fluid conductivity is available, ERT results may be interpreted quantitatively in terms of temperature. The temperatures estimated from ERT were relatively close to the ones observed directly during the rise and maximum part of the curve. An overestimation, likely related to 3D effects, was observed for the tail of the breakthrough curve. The error made can be estimated to be between 10 and 20%, which is a fair value for indirect measurements. The precision of the method may be better in more favorable cases, for example in no or low flow conditions. 3D imaging procedure using more than two wells should also improve the reliability of electrical resistivity monitoring results, yielding a better characterization of temperature distribution.

The limit of quantification of temperature changes depends on the noise level observed on the site. ERT requires an error

assessment in order to avoid artifacts in the inverted sections. The higher the noise level, the lower the resolution of ERT to derive temperature changes. In this case, we observed after inversion positive changes of electrical resistivity up to 3% in the saturated zone. Those changes were not physically related to the tracing experiments and enabled us to estimate a limit of quantification for ERT around 1.2 °C for temperature changes.

In contrast with surface ERT, the resolution of crosshole ERT is not depth-dependent but depends mostly on the aspect ratio, the electrode spacing and the distance to the boreholes. In this case, we achieve an aspect ratio of 0.75 with 13 electrodes. A greater distance between boreholes would require a greater electrode spacing or the use of more electrodes. Standard measurement devices generally accept 24–32 electrodes per borehole. Considering an electrode spacing $a = 0.5$ m, we successfully imaged a heterogeneous heat plume with a thickness about $5a$ and a width of about $4a$. The results obtained in this study could be easily extended to other experiment keeping similar parameters. The resolution could even be refined using better aspect ratio or more electrodes. The scale of this experiment could be applied for the control of aquifer thermal energy storage (ATES) located in alluvial plains. For deeper and larger systems, it would require larger distances between electrodes and boreholes or the use of set-up with more than two boreholes.

In this experiment, we only achieve a time resolution of a few hours. Our measuring procedure takes about 45 min. However, it is possible to reduce acquisition delay and acquisition time of each measurement. It would allow to achieve a time resolution of less than 30 min. Avoiding the complete collection of reciprocal at each time step would further divide the time to collect the data by two.

The results presented in this paper suggest that ERT should be considered when designing heat tracing experiments to derive the parameters governing heat flow and transport in the subsurface or geothermal systems. It should also be used to assess the complexity of the concerned reservoirs. It also appears that ERT could be a useful tool to monitor and control geothermal systems once they are in operation. A proper configuration of ERT wells, depending on the installed configuration, should enable to control the temperature distribution in the reservoir. This may be of crucial importance to better describe the thermal affected zone or assess the possible influence of the system on groundwater chemistry or microbiology.

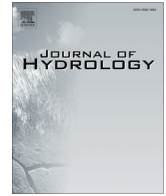
Acknowledgements

We would like to thank the associate editor and two anonymous reviewers for their pertinent comments and suggestions which have helped to improve the manuscript. We also thank the F.R.S. - FNRS (grant no. FC 87116) and the Fondation Roi Baudouin - Prix Ernest Dubois (grant no. 2013-8126501-F002) for their financial support during the PhD of Thomas Hermans.

References

- Allen, A., Milenic, D., 2003. Low-enthalpy geothermal energy resources from groundwater in fluvio-glacial gravels of buried valleys. *Appl. Energy* 74, 9–19.
- Arango-Galván, C., Prol-Ledesma, R.M., Flores-Márquez, E.L., Canet, C., Villanueva Estrada, R.E., 2011. Shallow submarine and subaerial, low-enthalpy hydrothermal manifestations on Punta Banda, Baja California, Mexico: geophysical and geochemical characterization. *Geothermics* 40, 102–111.
- Archie, G.E., 1942. The electrical resistivity log as an aid in determining some reservoir characteristics. *Trans. AIME* 146, 54–62.
- Atekwana, E.A., Sauck, W.A., Werkema, D.D., 2000. Investigations of geoelectrical signatures at a hydrocarbon contaminated site. *J. Appl. Geophys.* 44, 167–180.
- Anderson, M.P., 2005. Heat as a ground water tracer. *Ground Water* 43, 951–968.
- Bergmann, P., Schmidt-Hattenberger, C., Kiessling, D., Rucker, C., Labitzke, T., Hennings, J., Baumann, G., Schütt, H., 2012. Surface-downhole electrical resistivity tomography applied to monitoring of CO₂ storage at Ketzin, Germany. *Geophysics* 77, B253–B267.
- Binley, A., Winship, P., West, L.J., Pokar, M., Middleton, R., 2002. Seasonal variation of moisture content in unsaturated sandstone inferred from borehole radar and resistivity profiles. *J. Hydrol.* 267, 160–172.
- Briellmann, H., Griebler, C., Schmidt, S.I., Michel, R., Lueders, T., 2009. Effects of thermal energy discharge on shallow groundwater ecosystems. *FEMS Microbiol. Ecol.* 68, 273–286.
- Brouyère, S., (Ph.D. thesis) 2001. Etude et modélisation du transport et du piégeage des solutés en milieu souterrain variablement saturé. University of Liege (unpublished).
- Bruno, P.P.G., Paoletti, V., Grimaldi, M., Rapolla, A., 2000. Geophysical exploration for geothermal low enthalpy resources in Lipari Island, Italy. *J. Volcanol. Geotherm. Res.* 98, 173–188.
- Busby, J., Lewis, M., Reeves, H., Lawley, R., 2009. Initial geological considerations before installing ground source heat pump systems. *Q. J. Eng. Geol. Hydrogeol.* 42, 295–306.
- Caterina, D., Beaujean, J., Robert, T., Nguyen, F., 2013. A comparison study of different image appraisal tools for electrical resistivity tomography. *Near Surf. Geophys.* 11 (6), 639–657. <http://dx.doi.org/10.3997/1873-0604.2013022>.
- Dassargues, A., 1997. Modeling baseflow from an alluvial aquifer using hydraulic-conductivity data obtained from a derived relation with apparent electrical resistivity. *Hydrogeol. J.* 5 (3), 97–108.
- de Groot-Hedlin, C., Constable, S., 1990. Occam's inversion to generate smooth, two dimensional models from magnetotelluric data. *Geophysics* 55, 1613–1624.
- de Paly, M., Hecht-Méndez, J., Beck, M., Blum, P., Zell, A., Bayer, P., 2012. optimization of energy extraction for closed shallow geothermal systems using linear programming. *Geothermics* 43, 57–65. <http://dx.doi.org/10.1016/j.geothermics.2012.03.001>.
- Derouane, J., Dassargues, A., 1998. Delineation of groundwater protection zones based on tracer tests and transport modelling in alluvial sediments. *Environ. Geol.* 36 (1–2), 27–36.
- Doetsch, J.A., Coscia, I., Greenhalgh, S., Linde, N., Green, A., Günther, T., 2010. The borehole-fluid effect in electrical resistivity imaging. *Geophysics* 75 (4), F107–F114. <http://dx.doi.org/10.1190/1.3467824>.
- Garg, S.K., Pritchett, J.W., Wannamaker, P.E., Combs, J., 2007. Characterization of geothermal reservoirs with electrical surveys: beowave geothermal field. *Geothermics* 36, 487–517.
- Giambastiani, B.M.S., Colombari, N., Mastrocicco, M., 2012. Limitation of using heat as a groundwater tracer to define aquifer properties: experiment in a large tank model. *Environ. Earth Sci.* <http://dx.doi.org/10.1007/s12665-012-2157-2>, published online December 2012.
- Haehnlein, S., Bayer, P., Blum, P., 2010. International legal status of the use of shallow geothermal energy. *Renew. Sustain. Energy Rev.* <http://dx.doi.org/10.1016/j.rser.2010.07.069>.
- Haffen, S., Geraud, Y., Diraison, M., Dezayes, C., 2013. Determination of fluid-flow zones in a geothermal sandstone reservoir using thermal conductivity and temperature logs. *Geothermics* 46, 32–41.
- Hayley, K., Bentley, L.R., Gharibi, M., Nightingale, M., 2007. Low temperature dependence of electrical resistivity: implications for near surface geophysical monitoring. *Geophys. Res. Lett.* 34, L18402. <http://dx.doi.org/10.1029/2007GL031124>.
- Hermans, T., Caterina, D., Nguyen, F., 2014. Case studies of prior information in electrical resistivity tomography: comparison of different approaches. *Near Surf. Geophys.* <http://dx.doi.org/10.3997/1873-0604.2013070> (in press).
- Hermans, T., Daoudi, M., Vandenbohede, A., Robert, T., Caterina, D., Nguyen, F., 2012a. Comparison of temperature estimates from heat transport model and electrical resistivity tomography during a shallow heat injection and storage experiment. 1st International Workshop on Geoelectrical Monitoring, Vienna. *Berichte Geol. Bundesanstalt* 93, 43–48.
- Hermans, T., Vandenbohede, A., Lebbe, L., Nguyen, F., 2012b. A shallow geothermal experiment in a sandy aquifer monitored using electric resistivity tomography. *Geophysics* 77 (1), B11–B21. <http://dx.doi.org/10.1190/GEO2011-0199.1>.
- Hermans, T., Vandenbohede, A., Lebbe, L., Martin, R., Kemna, A., Beaujean, J., Nguyen, F., 2012c. Imaging artificial salt water infiltration using electrical resistivity tomography constrained by geostatistical data. *J. Hydrol.* 438–439, 168–180. <http://dx.doi.org/10.1016/j.jhydrol.2012.03.021>.
- Irving, J., Singha, K., 2010. Stochastic inversion of tracer test and electrical geophysical data to estimate hydraulic conductivities. *Water Resour. Res.* 46, W11514.
- Jesušek, A., Grandel, S., Dahmke, A., 2013. Impacts of subsurface heat storage on aquifer hydrogeochemistry. *Environ. Earth Sci.* 69 (6), 1999–2012. <http://dx.doi.org/10.1007/s12665-012-2037-9>.
- Karaoulis, M.C., Kim, J.H., Tsourlos, P.I., 2011. 4D active time constrained resistivity inversion. *J. Appl. Geophys.* 73, 25–34. <http://dx.doi.org/10.1016/j.jappgeo.2010.11.002>.
- Karaoulis, M., Tsourlos, P., Kim, J.-H., Revil, A., 2014. 4D time-lapse ERT inversion: introducing combined time and space constraints. *Near Surf. Geophys.* 12, 25–34. <http://dx.doi.org/10.3997/1873-0604.2013004>.
- Kemna, A., (Ph.D. thesis) 2000. Tomographic Inversion of Complex Resistivity: Theory and Application. University of Bochum.
- Kemna, A., Vanderborght, J., Kulesa, B., Vereecken, H., 2002. Imaging and characterization of subsurface solute transport using electrical resistivity tomography (ERT) and equivalent transport models. *J. Hydrol.* 267, 125–146.
- Koestel, J., Kemna, A., Javaux, M., Binley, A., Vereecken, H., 2008. Quantitative imaging of solute transport in an unsaturated and undisturbed soil monolith with 3-D ERT and TDR. *Water Resour. Res.* 44, W12411. <http://dx.doi.org/10.1029/2007WR006755>.
- LaBrecque, D.J., Miletto, M., Daily, W., Ramirez, A., Owen, E., 1996a. The effects of noise on Occam's inversion of resistivity tomography data. *Geophysics* 61, 538–548. <http://dx.doi.org/10.1190/1.1443980>.
- LaBrecque, D.J., Ramirez, A.L., Daily, W.D., Binley, A.M., Schima, S.A., 1996b. ERT monitoring of environmental remediation processes. *Meas. Sci. Technol.* 7, 375–383. <http://dx.doi.org/10.1088/0957-0233/7/3/019>.
- LaBrecque, D.J., Yang, X., 2000. Difference inversion of ERT data: a fast inversion method for 3-D in-situ monitoring. In: *Proc. Symp. Appl. Geophys. Eng. Environ. Problems. Environ. Eng. Geophys. Soc.*, pp. 723–732.
- Leaf, A.T., Hart, D.J., Bahr, J.M., 2012. Active thermal tracer tests for improved hydrostratigraphic characterization. *Ground Water* 50 (5), 726–735.
- Liang, J., Yang, Q., Liu, L., Li, X., 2011. Modeling and performance evaluation of shallow ground water heat pumps in Beijing plain, China. *Energy Buildings* 43, 3131–3138. <http://dx.doi.org/10.106/j.enbuild.2011.08.007>.
- Lo Russo, S., Civita, M.V., 2009. Open-loop groundwater heat pumps development for large buildings: a case study. *Geothermics* 38, 335–345. <http://dx.doi.org/10.1016/j.geothermics.2008.12.009>.
- Mattsson, N., Steinmann, G., Laloui, L., 2008. Advanced compact device for the in situ determination of geothermal characteristics of soils. *Energy Buildings* 40, 1344–1352.
- Miller, C., Routh, P., Brosten, T., McNamara, J., 2008. Application of time-lapse ERT imaging to watershed characterization. *Geophysics* 73 (3), G7–G17.
- Molson, J.W., Frind, E.O., Palmer, C.D., 1992. Thermal energy storage in an unconfined aquifer 2. Model development, validation and application. *Water Resour. Res.* 28, 2857–2867.
- Nguyen, F., Kemna, A., Antonsson, A., Engesgaard, P., Kuras, O., Ogilvy, R., Gisbert, J., Jorretto, S., Pulido-Bosch, A., 2009. Characterization of seawater intrusion using 2D electrical imaging. *Near Surf. Geophys.* 7, 377–390.
- Nguyen, F., Kemna, A., Robert, T., Hermans, T., Daoudi, M., Flores-Orozco, A., 2011. Inversion of multi-temporal geoelectrical data sets: insights from several case studies. In: 1st Workshop on Geoelectrical monitoring, GELMON, Vienna, Austria.
- Nimmer, R.E., Osiensky, J.L., Binley, A.M., Williams, B.C., 2008. Three-dimensional effects causing artifacts in two-dimensional, cross-borehole, electrical imaging. *J. Hydrol.* 359, 59–70. <http://dx.doi.org/10.1016/j.jhydrol.2008.06.022>.
- Palmer, C.D., Blowes, D.W., Frind, E.O., Molson, J.W., 1992. Thermal energy storage in an unconfined aquifer 1. Field injection experiment. *Water Resour. Res.* 28, 2845–2866.
- Pérez Flores, M.A., Gomez Trevino, E., 1997. Dipole-dipole resistivity imaging of the Ahuachapán-Chipilapa geothermal field, El Salvador. *Geothermics* 26, 657–680.
- Perri, M.T., Cassiani, G., Gervasio, I., Deiana, R., Binley, A., 2012. A saline tracer test monitored via both surface and cross-borehole electrical resistivity tomography: comparison of time-lapse results. *J. Appl. Geophys.* 79, 6–16.
- Prevedel, B., Wohlgemuth, L., Legarth, B., Hennings, J., Schütt, H., Schmidt-Hattenberger, C., Norden, B., Förster, A., Hurter, S., 2009. The CO₂SINK boreholes for geological CO₂-storage testing. *Energy Proc.* 1, 2087–2094. <http://dx.doi.org/10.1016/j.egypro.2009.01.272>.
- Ramirez, A., Daily, W., LaBrecque, D., Owen, E., Chesnut, D., 1993. Monitoring an underground steam injection process using electrical resistance tomography. *Water Resour. Res.* 29, 73–87.
- Raymond, J., Therrien, R., Gosselin, L., Lefebvre, R., 2011. A review of thermal response test analysis using pumping test concepts. *Ground Water* 49, 932–945. <http://dx.doi.org/10.1111/j.1745-6584.2010.00791.x>.
- Revil, A., Cathles, L.M., Losh, S., Nunn, J.A., 1998. Electrical conductivity in shaly sands with geophysical applications. *J. Geophys. Res.* 103, 23925–23936.
- Revil, A., Linde, N., 2006. Chemico-electrochemical coupling in microporous media. *J. Colloid Interface Sci.* 302, 682–694.
- Revil, A., Skold, M., Karaoulis, M., Schmutz, M., Hubbard, S.S., Mehlhorn, T.L., Watson, D.B., 2013. Hydrogeophysical investigations of the former S-3 ponds contaminant plumes, Oak Ridge Integrated Field Research Challenge site, Tennessee. *Geophysics* 78 (4), EN29–EN41. <http://dx.doi.org/10.1190/geo2012-0177.1>.
- Robert, T., Caterina, D., Decuster, J., Kaufmann, O., Nguyen, F., 2012. A salt tracer test monitored with surface ERT to detect preferential flow and transport paths in fractured/karstified limestones. *Geophysics* 77, B55–B67.
- Robert, T., Hermans, T., Dumont, G., Nguyen, F., Rwabuhungu, D., 2013. Reliability of ERT-derived temperature: insights from laboratory measurements. *Extended Abstract Tu-2Sa-10*. *Near Surf. Geosci.* 2013, 11–13, September 2013, Bochum, Germany.
- Saar, M.O., 2011. Review: geothermal heat as a tracer of large-scale groundwater flow and as a means to determine permeability fields. *Hydrogeol. J.* 19, 31–52. <http://dx.doi.org/10.1007/s10040-010-0657-2>.

- Sen, P.N., Goode, P.A., 1992. Influence of temperature on electrical conductivity on shaly sands. *Geophysics* 46, 781–795.
- Sherrod, L., Sauck, W., Werkema Jr., D.D., 2012. A low-cost, in-situ resistivity and temperature monitoring system. *Ground Water Monitor. Remediation* 32, 31–39, <http://dx.doi.org/10.1111/j1745-6592.2011.01380.x>.
- Slater, L., Binley, A.M., Daily, W., Johnson, R., 2000. Cross-hole electrical imaging of a controlled saline tracer injection. *J. Appl. Geophys.* 44, 85–102.
- Tikhonov, A.N., Arsenin, V.A., 1977. *Solution of Ill-posed Problems*. Winston & Sons, Washington.
- Vandenbohede, A., Louwyck, A., Lebbe, L., 2009. Conservative solute versus heat transport in porous media during push–pull tests. *Transport Porous Media* 76, 265–287.
- Vandenbohede, A., Hermans, T., Nguyen, F., Lebbe, L., 2011. Shallow heat injection and storage experiment: heat transport simulation and sensitivity analysis. *J. Hydrol.* 409, 262–272.
- Vandenborgh, J., Kemna, A., Hardelauf, H., Vereecken, H., 2005. Potential of electrical resistivity tomography to infer aquifer transport characteristics from tracer studies: a synthetic case study. *Water Resour. Res.* 41, W06013, <http://dx.doi.org/10.1029/2004WR003774>.
- Vanhoudt, D., Desmedt, J., Van Bael, J., Robeyn, N., Hoes, H., 2011. An aquifer thermal storage system in a Belgian hospital: long-term experimental evaluation of energy and cost savings. *Energy Buildings* 43, 3657–3665, <http://dx.doi.org/10.1016/j.enbuild.2011.09.040>.
- Vereecken, H., Binley, A., Cassiani, G., Revil, A., Titov, K., 2006. *Applied Hydrogeophysics*, Nato Science Series IV. Earth and Environmental Sciences, vol. 71. Springer, Dordrecht, Netherlands.
- Warner, D.L., Algan, U., 1984. Thermal impact of residential ground-water heat pumps. *Ground Water* 22, 6–12.
- Zhou, B., Greenhalgh, S.A., 2000. Cross-hole resistivity tomography using different electrode configurations. *Geophys. Prospect.* 48, 887–912.



Research papers

Heat tracer test in an alluvial aquifer: Field experiment and inverse modelling



Maria Klepikova^{a,c,*}, Samuel Wildemeersch^a, Thomas Hermans^d, Pierre Jamin^a, Philippe Orban^a, Frédéric Nguyen^b, Serge Brouyère^a, Alain Dassargues^a

^aUniversity of Liege, ArGenCo, GEO³, Hydrogeology and Environmental Geology Unit, Liège, Belgium

^bUniversity of Liege, ArGenCo, GEO³, Applied Geophysics Unit, Liège, Belgium

^cETH Zurich, Geological Institute, Zurich, Switzerland

^dDepartment of Geological Sciences, Stanford University, United States

ARTICLE INFO

Article history:

Received 23 March 2016

Received in revised form 14 June 2016

Accepted 16 June 2016

Available online 30 June 2016

This manuscript was handled by P. Kitanidis, Editor-in-Chief, with the assistance of Niklas Linde, Associate Editor

Keywords:

Thermal tracer test

Inverse modelling

Pilot points

ABSTRACT

Using heat as an active tracer for aquifer characterization is a topic of increasing interest. In this study, we investigate the potential of using heat tracer tests for characterization of a shallow alluvial aquifer. A thermal tracer test was conducted in the alluvial aquifer of the Meuse River, Belgium. The tracing experiment consisted in simultaneously injecting heated water and a dye tracer in an injection well and monitoring the evolution of groundwater temperature and tracer concentration in the pumping well and in measurement intervals. To get insights in the 3D characteristics of the heat transport mechanisms, temperature data from a large number of observation wells closely spaced along three transects were used.

Temperature breakthrough curves in observation wells are contrasted with what would be expected in an ideal layered aquifer. They reveal strongly unequal lateral and vertical components of the transport mechanisms. The observed complex behavior of the heat plume is explained by the groundwater flow gradient on the site and heterogeneities in the hydraulic conductivity field. Moreover, due to high injection temperatures during the field experiment a temperature-induced fluid density effect on heat transport occurred. By using a flow and heat transport numerical model with variable density coupled with a pilot point approach for inversion of the hydraulic conductivity field, the main preferential flow paths were delineated. The successful application of a field heat tracer test at this site suggests that heat tracer tests is a promising approach to image hydraulic conductivity field. This methodology could be applied in aquifer thermal energy storage (ATES) projects for assessing future efficiency that is strongly linked to the hydraulic conductivity variability in the considered aquifer.

© 2016 Elsevier B.V. All rights reserved.

1. Introduction

Quantification of transport in heterogeneous aquifers is an issue of great importance to ground water contamination prevention as well as geothermal reservoir exploitation and heat storage that still provides many challenges (e.g. Ptak et al., 2004; Jiménez et al., 2015). Recently it was shown that using heat as a groundwater tracer provides complementary information on groundwater flow and transport pathways (Anderson, 2005; Saar, 2011). For example, ambient temperature profiles were extensively used to quantify vertical or horizontal groundwater flow velocities in porous aquifers (e.g. Bredehoeft and Papaopulos, 1965; Bense and Kooi, 2004; Anderson, 2005) and to achieve a better understanding of

the main structures for flow in fractured (Klepikova et al., 2011; Guihéneuf et al., 2014) and karstified aquifers (Chatelier et al., 2011). Thermal perturbation tests conducted in open (Freifeld et al., 2008; Leaf et al., 2012; Liu et al., 2013; Read et al., 2014; Hausner et al., 2015) and in boreholes sealed using continuous, water-inflated, flexible liners (FLUTE) (Pehme et al., 2013; Coleman et al., 2015) were used to provide detailed information on the locations of groundwater inflows from both fractures and porous media as well as corresponding flow rates.

Klepikova et al. (2016) demonstrated the interest of active thermal tracer tests as a complement to solute tracers tests in fractured media to get new insights about fracture geometry and aperture. The main difference between solute and thermal tracers behavior is due to the higher value of thermal diffusivity compared to solute dispersion. In heterogeneous geological media, high thermal diffusivity allows heat to be transported not only through high conductive flowpaths like solutes, but also through zones of low

* Corresponding author at: Institute of Geology, ETH Zurich, Sonneggstrasse 5, 8092 Zürich, Switzerland.

E-mail address: maria.klepikova@erdw.ethz.ch (M. Klepikova).

permeability (Irvine et al., 2015). Cross-borehole heat (Read et al., 2013) and solute (Dorn et al., 2012) tracer tests conducted in the granitic aquifer of Ploemeur (France), revealed that a significant time lag can be observed between a thermal and solute breakthrough. Moreover, these authors observed that breakthrough locations of heat and solute are different, potentially due to channeling and local density effects, thus confirming that these tracers do not provide the same information on transport patterns in heterogeneous media.

Several works were intended to characterize heterogeneities of alluvial aquifers by performing active heat tracer tests. Among them, Vandenbohede et al. (2009, 2011) studied the sensitivity of push-pull solute and heat tracer tests in porous media to a range of transport parameters. They found that longitudinal solute dispersivity and thermal diffusivity could be inferred from coupled solute and thermal push-pull tests. Giambastiani et al. (2013) studied heat transport in alluvial aquifers with small groundwater velocities and found that aquifer parameters can hardly be deduced from temperature observations alone, since heat transport in thermal diffusion dominated systems is relatively insensitive to the longitudinal dispersivity. Ma et al. (2012) made a numerical simulation study of a combined bromide and heat tracer experiment in order to evaluate the utility of bromide and heat tracers for aquifer characterization. They found that for heat transport in an advection-dominated regime (high Peclet numbers) the hydraulic conductivity is the primary calibration parameter. This finding was used to calibrate hydraulic conductivities of a simple layered model by fitting simulated to measured temperatures of a thermal tracer test in a sedimentary aquifer (Wagner et al., 2014).

Despite positive results from field heat tracer tests, several improvements are still needed for a more quantitative analysis of transport processes. Thus, in order to characterize the 3D characteristics of the transport mechanisms in heterogeneous media, Wagner et al. (2014) suggested to use space-filling arrangements of observation wells (e.g. several observation well transects). More recently, Doro et al. (2015) presented the experimental design of a tracer tomography field method using heat a tracer and showed that in order to address the problem of highly damped temperature breakthrough curves, one would need to increase the injection temperature, although precautions must be taken when analyzing those data to account for temperature dependence of fluid properties. Ma et al. (2012) found that vertical intraborehole flows can take place in fully screened monitoring wells and it influences the measured temperature and concentration fields. In order to avoid the effect of vertical intraborehole flows, some modifications are required during the heat tracer test experiment. Possible technical solutions could be to use boreholes with several short screen levels, to install mid-screen packers or to install temperature sensors on the outer wall of the wellbore.

Finally, one of the main objective of heat tracer tests can be to provide input data for an inverse problem for estimating aquifer parameters. Schwede et al. (2014) proposed a geostatistical approach for joint inversion of hydraulic heads and thermal tracer tests data. Based on a synthetic test case, they showed the usefulness of thermal tracer test data for a better estimation of the spatial distribution of hydraulic conductivity. Recently, Somogyvári et al. (2016) used a synthetic example to demonstrate the usability of active thermal tracer tomography to reconstruct cross-borehole hydraulic conductivity profiles. Nevertheless, to reduce the computational effort only the mean arrival time of thermal signals was used. As yet, data from a full transient heat tracer test have never been used for the inversion of the 3D spatial distribution of aquifer properties.

The main objective of the present study is to demonstrate that temperature data can be inverted to provide valuable insights in the 3D characteristics of heterogeneous aquifers. We present a

study of an active heat tracer test in a previously well characterized alluvial aquifer and the use of a subsequent inverse modelling approach for estimation of the hydraulic conductivity field.

2. Thermal tracer test experiment

2.1. Field site

The experimental field site is located in Hermalle-sous-Argenteau (Belgium) and lies in the alluvial plain of the Meuse River. Based on borehole logs, the alluvial deposits can be divided into three main lithological units. The upper layer is 1–1.5 m thick and is composed of loam with clay lenses. The second unit consists of sandy loam with gravels which proportion increases with depth down to 3 m depth. These two layers are located in the unsaturated zone, while the groundwater table is located at approximately 3.2 m depth. From 3 to 10 m below the ground surface, the third layer is mainly composed of gravel and pebbles in a sandy matrix. The quantity of sand decreases with depth, whereas the size of the pebbles increases with depth, so that an increase of hydraulic conductivity (K) with depth is expected. Lateral variability in flow and transport parameters is also expected due to the complex local fluvial sedimentological context. Below the alluvial deposits, low permeability carboniferous shale and sandstone formations are considered as the basement of the alluvial aquifer.

The test site has been subject to numerous hydraulic and geophysical tests, including pumping and tracer tests (Wildemeersch et al., 2014; Dassargues, 1997; Derouane and Dassargues, 1998; Brouyère, 2001), geophysical surveys and temperature measurements, including fiber optic measurements (Hermans et al., 2015a,b). Pumping tests conducted at the site (Brouyère, 2001) showed a mean hydraulic conductivity, K , for the alluvial aquifer ranging from $2 \cdot 10^{-3}$ m/s to $1.2 \cdot 10^{-1}$ m/s. The natural hydraulic gradient at the site is estimated to be around 0.06% directed towards the north-east. Local groundwater fluxes at the site were measured using the Finite Volume Point Dilution Method (FVPDM) (Brouyère et al., 2008), allowing direct measurement of the Darcy fluxes. These measurements indicate that groundwater flow in the lower part of the aquifer is about one order of magnitude higher ($1 \cdot 10^{-3}$ – $8 \cdot 10^{-3}$ m/s) than in the upper part ($1 \cdot 10^{-4}$ – $1 \cdot 10^{-3}$ m/s) (Wildemeersch et al., 2014).

Through the use of solute tracer tests at different scales a longitudinal macrodispersivity coefficient for the test site was found to be ranging between 0.5 and 5 m (Brouyère, 2001) depending on the solute transport trajectory (scale effect), an effective (transport) porosity from 4% to 8% and a total porosity was found to be around 11%. During the experiment described in the present paper, sodium naphthionate, was also used as solute tracer. Wildemeersch et al. (2014) used the recorded naphthionate breakthrough curve to estimate transport parameters by fitting the model with focus on reproducing the first arrival and modal times. These data yielded an effective porosity of 4% and a longitudinal dispersivity of 3 m. Similar values were also found by Batlle-Aguilar et al. (2009) as the result of multi-tracer tests conducted in alluvial sediments of the Meuse, but on a different site (Flémalle). Measurements of the thermal conductivity and the heat capacity of the alluvial aquifer in the vicinity of this experimental site were performed within the ThermoMap project (Bertermann et al., 2013): values of 1.37 and 1.86 W/mK for thermal conductivity and 2.22 and 2.34 MJ/m³ K for volumetric heat capacity have been calculated for respectively two layers from 3 to 6 m depth and a second layer from 6 to 10 m depth.

The experimental site consists of one pumping well PP (0.152 m internal diameter, screened from 3 to 9.5 m depth) and 11 observation wells (0.05 m in diameter) organized as three transverse

control planes across the main groundwater flow direction, at respective distances of 17, 12 and 5 m from the pumping well. An injection well Pz09 (0.05 m in diameter) is situated 20 m upgradient the pumping well PP. Fig. 1a shows the layout of the boreholes. Nine boreholes were screened at two different levels, with a 2 m lower screen segment set at the bottom of the aquifer between 8 and 10 m depth and an upper screen segment placed between 5 and 6 m depth. The use of such nested wells with multiple screens installed at different depths avoids the problem of vertical intraborehole flow. The injection well Pz9 and the outermost wells from the second (central) transverse control plane, Pz13 and Pz17, are fully screened from 3 to 10 m depth. Detailed information on the wells used for the thermal tracer test is shown in Fig. 1b.

2.2. Setup of the tracer test

The tracer experiment was performed under converging groundwater flow conditions towards the pumping well (PP) by pumping at a constant discharge rate of 30 m³/h. The induced drawdown in the well itself was 0.05 m and 0.04 m at Pz19 located 5 m upgradient. During the tracer injection, 3 m³/h of the pumped water was heated using a mobile water heater (Swingtec Aquamobile DH6 boiler) and injected in Pz09. At this rate, the heater allowed us to inject water at a constant temperature of 38 K into a groundwater at an ambient temperature of 13 K. The tracer injection lasted for 24 h and 20 min. For heat tracer monitoring, the 18 screen segments of the 9 wells located in the control planes (Pz10–Pz12, Pz14–Pz16 and Pz18–Pz20) were equipped either with Schlumberger Diver or In-Situ Level Troll automated temperature

and pressure probes which allowed for the monitoring of hydraulic head and temperatures during the whole experiment duration, with a measurement time step of 10 min. Loggers were placed in the middle of each screened zone. The pumping well was also equipped with an In-Situ Level Troll probe to monitor the heat tracer breakthrough. The injection well Pz09, and the two outer wells of the middle control plane, Pz13 and Pz17, were equipped with a fiber optic distributed temperature sensor (DTS) for temperature logging. For more details on the setup of the DTS measurements refer to Hermans et al. (2015b).

As mentioned above, during the experiment, sodium naphtionate was also injected in Pz09. A dosing pump was used to inject the solute tracer with an injection rate of 3.9 L/h and an homogenized concentration of 4000 ppm. Previous experiments on the site (Brouyère, 2001) demonstrated a linear degradation and the absence of sorption for this tracer. Naphtionate concentrations of the fluid discharged from the pumping well PP was monitored by a GGUN-FL30 field fluorimeter with a measurement every 2 min. More technical details about the experiment can be found in Wildemeersch et al. (2014).

3. Flow and heat transport model

3.1. Model setup

In order to understand measured temperature distributions, a three-dimensional groundwater flow and heat transport model was developed using the HydroGeosphere code (HGS) (Therrien et al., 2010). The general equation for saturated subsurface heat transport is given by:

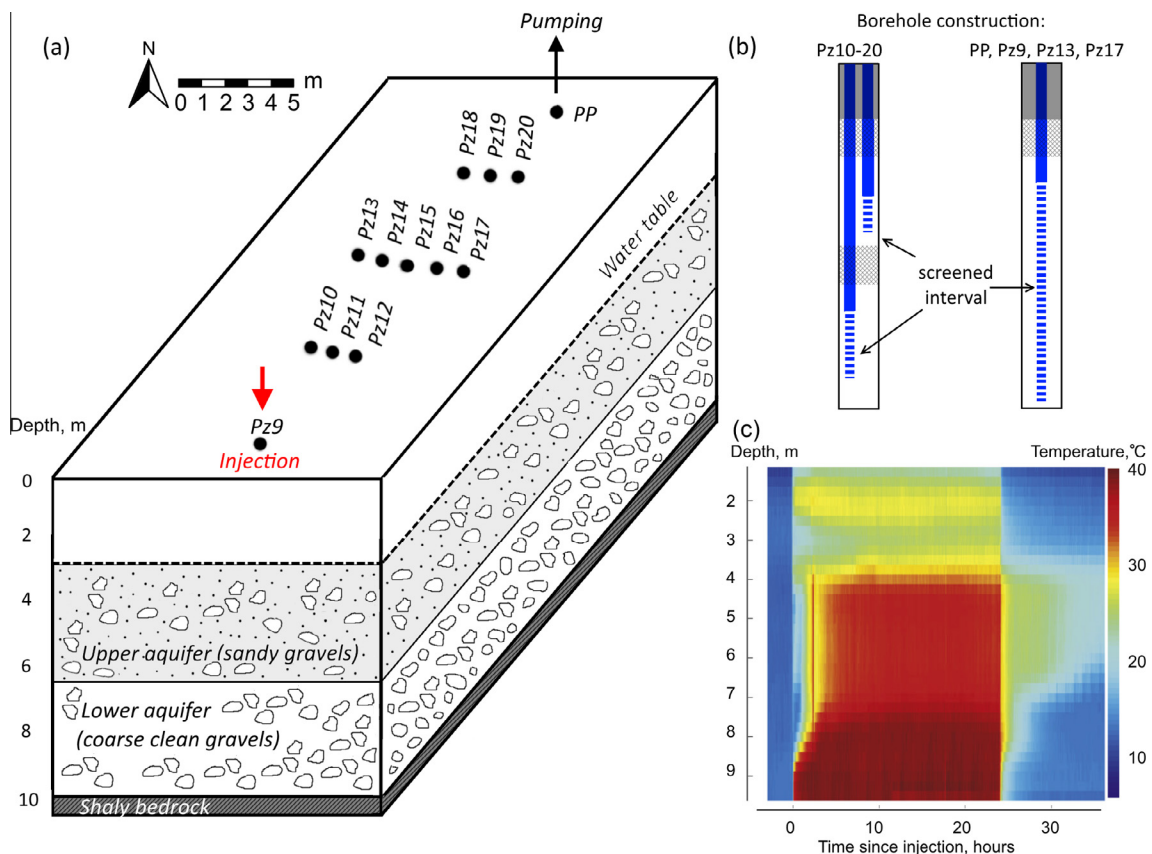


Fig. 1. (a) Layout of the experimental field site and setup of the thermal tracer test. Well Pz9 was used as injection well and Pz10–Pz20 served as observation wells during the test. (b) Wells are either screened in the whole alluvial aquifer, or screened at two different levels (nested wells), with an upper screen segment located within the sandy gravels, and a lower screen segment located within the coarse gravels. (c) Vertical temperature profiles as a function of time monitored by DTS at the injection well Pz09 (from Wildemeersch et al., 2014).

$$\frac{\partial \rho_b c_b T}{\partial t} = -\nabla \cdot [q \rho_w c_w T - (k_b + c_b \rho_b D) \nabla T] \pm Q_T \quad (1)$$

where ρ is the density, c is the heat capacity, T is the temperature of the bulk subsurface, t is the time, q is the Darcy groundwater flux, k is the thermal conductivity term, D is the thermal dispersion term and Q_T is a thermal source/sink. The subscript b denotes a bulk term, whereas w represents the aqueous phase. The water density in the flow equation may be or may not be updated by the changes in temperature depending on the type of simulation models (see next section). The bulk parameters are calculated by a volumetric average approximation; for example

$$\rho_b = (1 - \theta) \rho_s + \theta \rho_w \quad (2)$$

where the subscript s represents the solids and θ is the total porosity of the aquifer.

The total size of the numerical model is 40 m × 60 m × 7 m (Fig. 2a), which is considered large enough to minimize boundary effects near the injection and observation wells. The total area is discretized with 84,280 rectangular elements with an increasing resolution of the numerical mesh towards the well transect. The mesh shown in Fig. 2 is designed so that the distance between the numerical nodes decreases from the model boundary to the well transect by a factor of 100. Various tests were performed to get a mesh-independent result.

The unsaturated part as well as the underlying aquitard of the aquifer are not considered in the model. According to our numerical tests, vertical conductive heat losses into these zones have only a minor influence on the resulting temperature distribution. Based on our knowledge of the site, the aquifer is represented as a layered aquifer with a sandy gravels and a coarse clean gravels levels with an equal thickness of 3.5 m (Wildemeersch et al., 2014). The direction of the ambient natural groundwater flow was assured by imposing fixed heads at vertical boundaries of the model. The values of piezometric heads assigned as Dirichlet boundary conditions were extracted from the regional groundwater flow model (Brouyère, 2001) by interpolation of the calculated piezometric heads from the regional model to the corresponding nodes of the local grid. The resulting interpolation of the hydraulic heads (Fig. 2b) provides the best estimation for the local groundwater flow direction. No-flow boundary conditions are set at horizontal

boundaries. No groundwater recharge from the surface was assumed because no rainfall was recorded before and during the experiment. At the bottom boundary, the effect of vertical leakage to the lower carboniferous shales can be considered as negligible on the groundwater flow in the alluvial aquifer due to the high permeability of the gravels.

The initial groundwater temperature was set to 13.48 °C and the same temperature was assigned at all boundaries. This corresponds to the average temperature measured in borehole screens before the beginning of the experiment. In order to simulate the injection realistically, the injection borehole was explicitly represented in the model and a specified nodal water flux and temperature flux were assigned to a node close to the bottom of the well (Therrien et al., 2010). Because of the change in the steady-state flow field due to tracer injection, a transient flow conditions were considered.

To analyze the ratio between advection and thermal conduction, we employed Peclet number as proposed by Ma et al. (2012)

$$Pe = \frac{c_w q l}{k_b}, \quad (3)$$

where l is a characteristic length (here the minimum distance between observation wells). Heat transport in both parts of the aquifer was found to be highly dominated by advection. Peclet numbers ranging from $Pe = 300$ for the upper part of the aquifer to about $Pe = 14,000$ for the lower part of the aquifer were computed. As indicated by previous studies, in advection-dominated groundwater flow regime, thermal response of the aquifer is indeed less sensitive to thermal properties and strongly controlled by the hydraulic conductivity field (Ma et al., 2012; Wagner et al., 2014). We also verified this finding by conducting preliminary sensitivity analysis (not provided here) including hydraulic conductivity, thermal parameters and porosity (Goderniaux et al., 2015).

As previously highlighted by Anderson (2005), the choice of the thermal dispersivity values needs a particular attention, as conflicting points of view regarding the magnitude of the thermal dispersivity exist in the literature. Thermal dispersion has been often neglected in heat transport simulation problems (e.g. Vandenbohede et al., 2009; Rau et al., 2012). In particular, laboratory experiments of Rau et al. (2012) showed that for homogenous

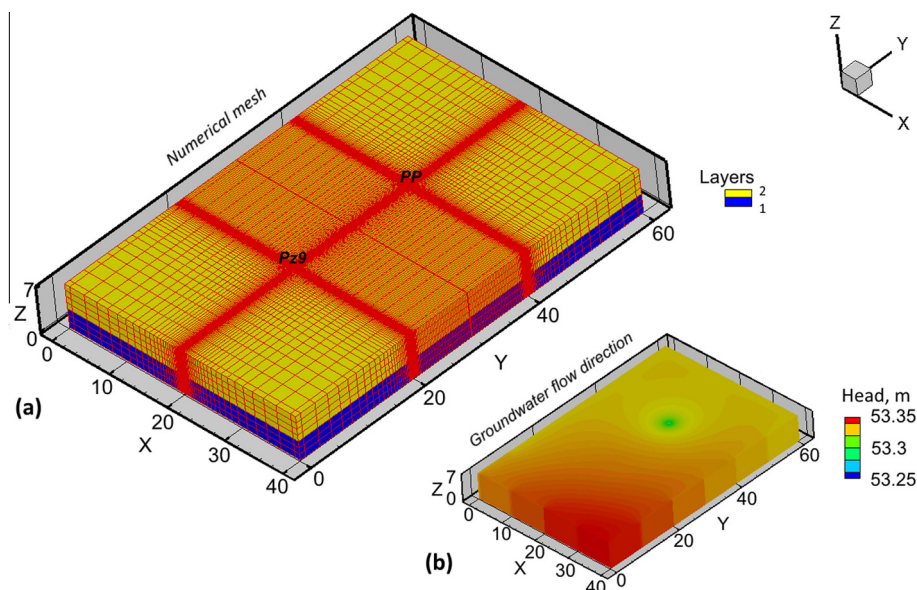


Fig. 2. Three-dimensional sketch of the model domain: numerical mesh (a) and hydraulic head distribution within the model domain resulting from natural hydraulic gradient enhanced by the gradients induced by the pumping during the experiment (b).

media, in which the thermal dispersion depends only on the magnitude of groundwater flow, thermal dispersivity is not important. Nevertheless, a recent analytical study of [Molina-Giraldo et al. \(2011\)](#) demonstrated that for advection-dominated groundwater flow conditions, typical in medium sand to gravel aquifers, thermal dispersion can have a non-negligible effect on the temperature plume distribution and the development of the temperature profiles. Moreover, they have concluded that for scale of 10 m and larger, thermal dispersion should be assumed to be comparable to solute dispersion. Consequently, dispersivity and effective porosity values were set according to values measured by the previous field tests (involving solute tracer tests). The transversal dispersivity is set to one tenth of the longitudinal one. Thermal properties (thermal conductivity and heat capacity) of the aquifer were set according to the measurements that were made in the vicinity of the experimental site within the ThermoMap project ([Bertermann et al., 2013](#)). All transport and thermal parameters used in the numerical model are summarized in [Table 1](#).

3.2. Density effect

In order to increase the computational efficiency, most of works modelling the heat transport in porous media do not take into account the density and viscosity effects. [Ma and Zheng \(2010\)](#) studied the conditions under which the density and viscosity effects on heat transport modelling can be neglected. Their results showed

Table 1
Initial hydraulic and thermal parameter applied for the numerical simulation.

Parameters	Aquifer part	
	Lower part	Upper part
Hydraulic conductivity, m/s	$7 \cdot 10^{-2}$	$2 \cdot 10^{-2}$
Effective porosity	0.08	0.04
Thermal conductivity, W/mK	1.86	1.37
Volumetric heat capacity, MJ/m ³ K	2.34	2.22
Bulk density, kg/m ³	1500	1800
Longitudinal dispersivity, m	3	3
Transverse dispersivity, m	0.3	0.3

that model discrepancy caused by viscosity is negligible when the temperature difference across the model domain is less than 30 K. Nevertheless, they also found that fluid density cannot be assumed constant when the maximum temperature difference across the model domain exceeds 15 K. The temperature anomaly we created reaches 25 K during the injection period and thus according to the above mentioned study the density effects should play a role in our case (at least during the injection period and in the immediate vicinity of the injection well), while viscosity effects should not influence the results. The water density changes and density dependent groundwater flow and transport were calculated in the HGS simulations as a function of the temperature ([Graf and Therrien, 2005](#)). Our preliminary modelling results also confirmed that neglecting density effects would yield misleading results.

As it will be shown further, the experiment results were actually influenced by the density effect in the vicinity of the injection borehole. Nevertheless, due to overwhelming heat transfer from the porous matrix, the temperature difference ΔT created by the injection across the flow domain decreases to 15 K (a threshold below which density effects on heat transport modelling can be neglected) within several hours after injection ([Fig. 4](#)). We used this observation by adopting a reasonable compromise between accuracy and computational efficiency. In the model, we simulate coupled density-dependent groundwater flow and heat transport during the first 24 h and afterward density effects were assumed to be negligible. By using the developed numerical model of heat and flow, we then verified that this simplification causes only very minor changes in the calculated breakthrough curves and temperature distributions. The results of this simulation are discussed later ([Section 4.2.2](#) and [Fig. 10](#)).

3.3. Inverse model description

For the calibration of the model, we first used a zonation approach and we calibrated hydraulic conductivities for the two horizontal layers shown in [Fig. 2](#). Furthermore, we applied the pilot point method implemented in the model-independent Parameter ESTimation and uncertainty analysis tool (PEST) ([Doherty, 2003](#); [Zhou et al., 2014](#)) in the HGS modelling environment ([Moock](#)

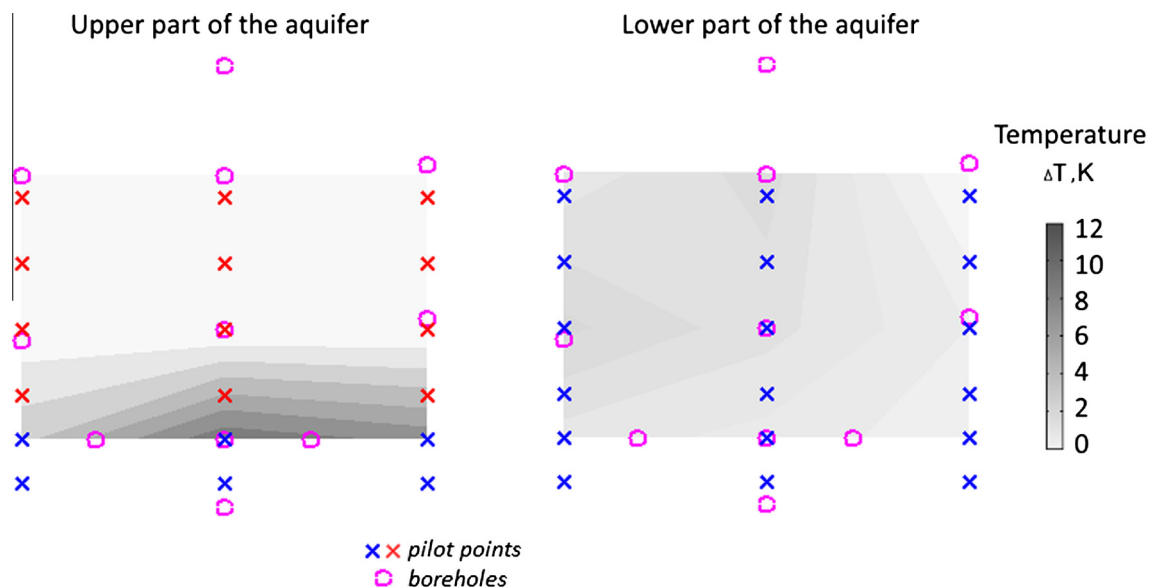


Fig. 3. Model domain with locations of 11 wells (pink circles) and 36 (18 in each part of the aquifer) uniformly distributed pilot points (x-symbols). The calibration of the K -distribution was performed in two steps: (1) assignment of K values to pilot point shown by blue symbols from the earlier part of the transient temperature responses considering density effect and (2) assignment of K values to pilot point shown by red symbols from the later part of the transient temperature responses without considering density effect. (For interpretation of the references to color in this figure legend, the reader is referred to the web version of this article.)

et al., 2015). Pilot points introduce a great flexibility to calibrate heterogeneous models compared to classical zonation approaches (Zhou et al., 2014; Sanchez-León et al., 2015). The principle of this approach is to estimate hydraulic property values at a set of discrete locations, denoted as pilot points, distributed in the model domain. The parameter values at the pilot points are estimated

by the Levenberg-Marquardt method. Then ordinary kriging based on the exponential semivariogram model is used to interpolate parameter values from the pilot points to the model grid.

During the calibration process, PEST assigns hydraulic conductivity values to pilot points in order to minimize the objective function defined as the weighted sum of squared differences between

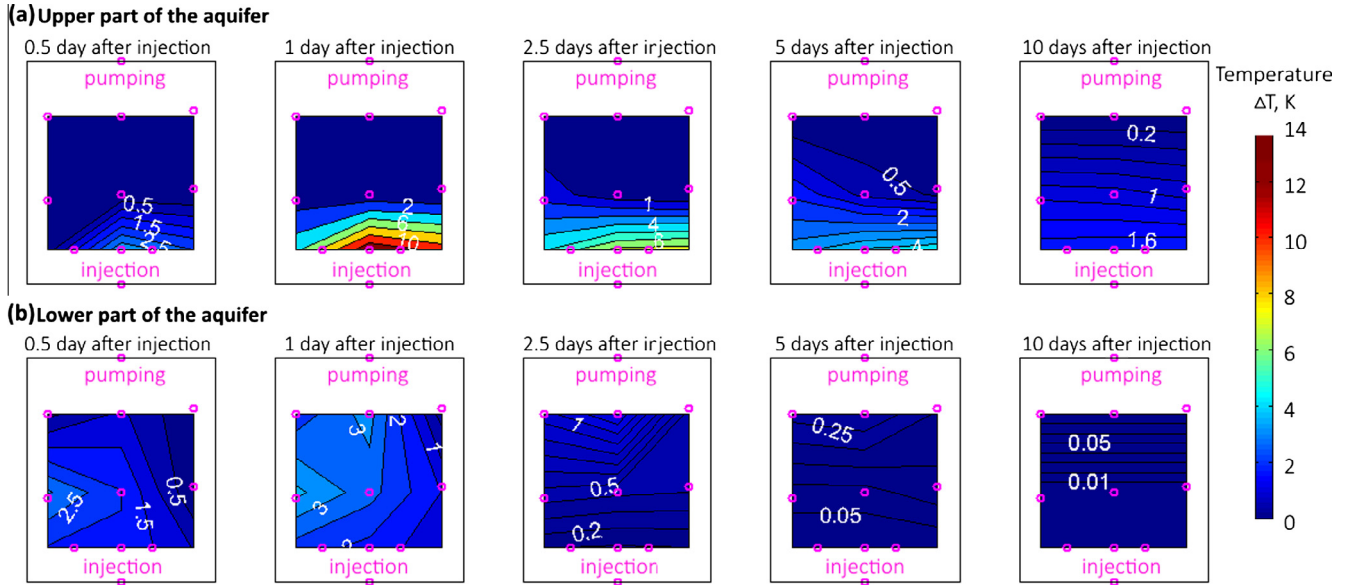


Fig. 4. Heat plume movement in the upper (a) and in the lower (b) parts of the aquifer at different times (0.5, 1, 2.5, 5 and 10 days) after the hot water injection.

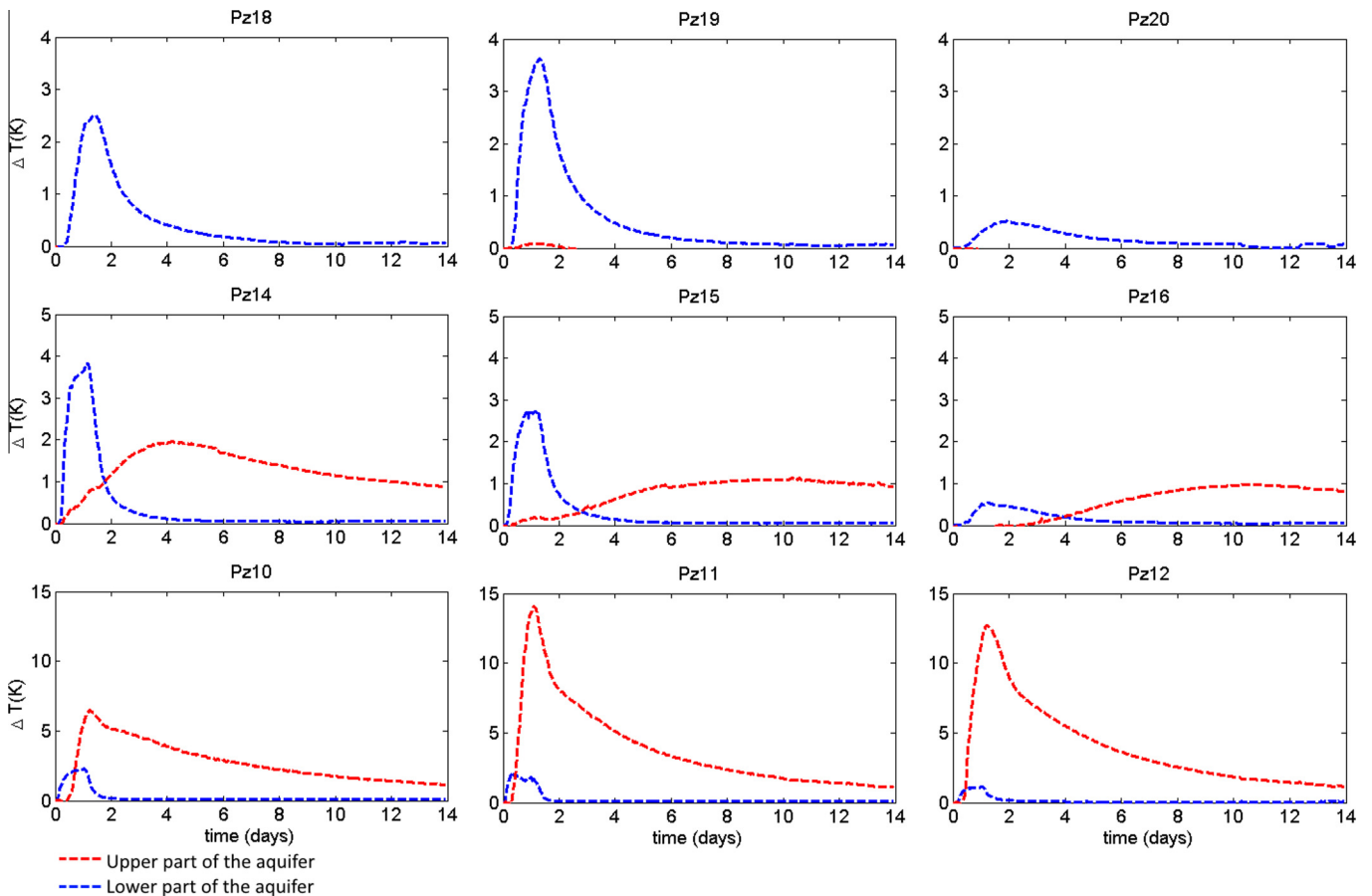


Fig. 5. Observed temperature breakthrough curves in the upper (red) and in the lower (blue) parts of the aquifer. (For interpretation of the references to color in this figure legend, the reader is referred to the web version of this article.)

the observed and modelled values (Doherty, 2003). This procedure is applied here minimizing the objective function for temperature data. Thus, transient temperature data served here as the

calibration targets for the groundwater flow and heat transport model. Note, that borehole hydraulic heads data were not used for the model calibration.

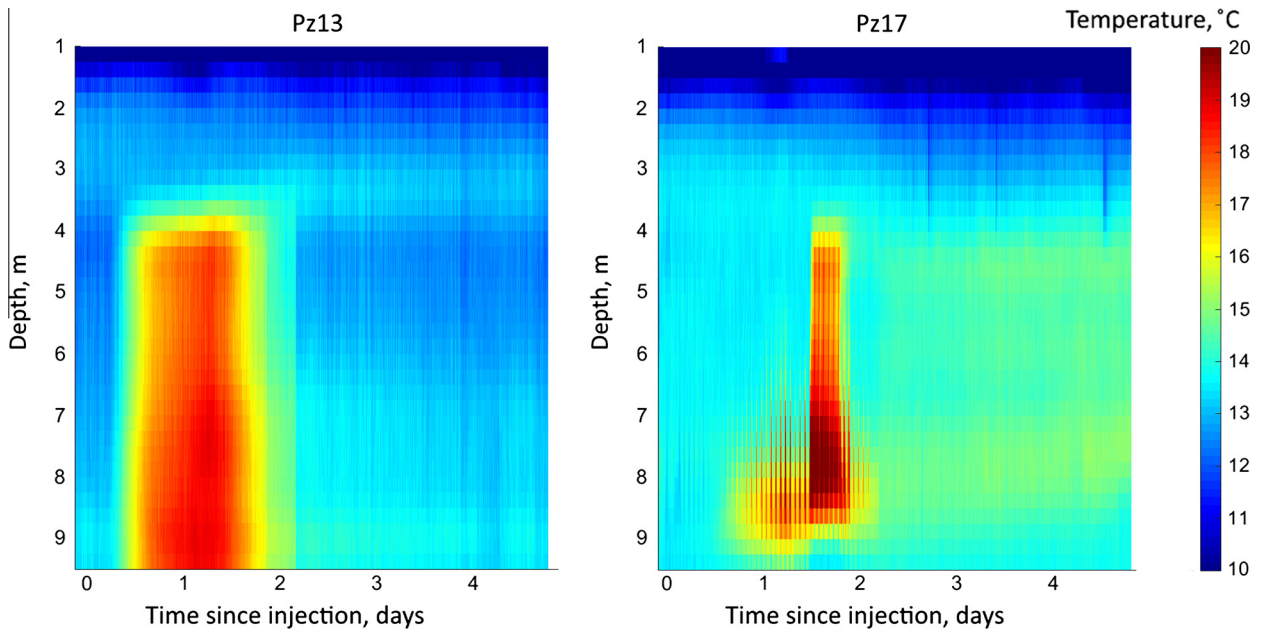


Fig. 6. Vertical temperature profiles monitored by DTS in Pz13 and Pz17 well. Intraborehole groundwater flow in these two fully screened wells manifests through the vertical smoothing of temperature signals. Consequently, these two temperature profiles are not taken into account in the subsequent analysis.

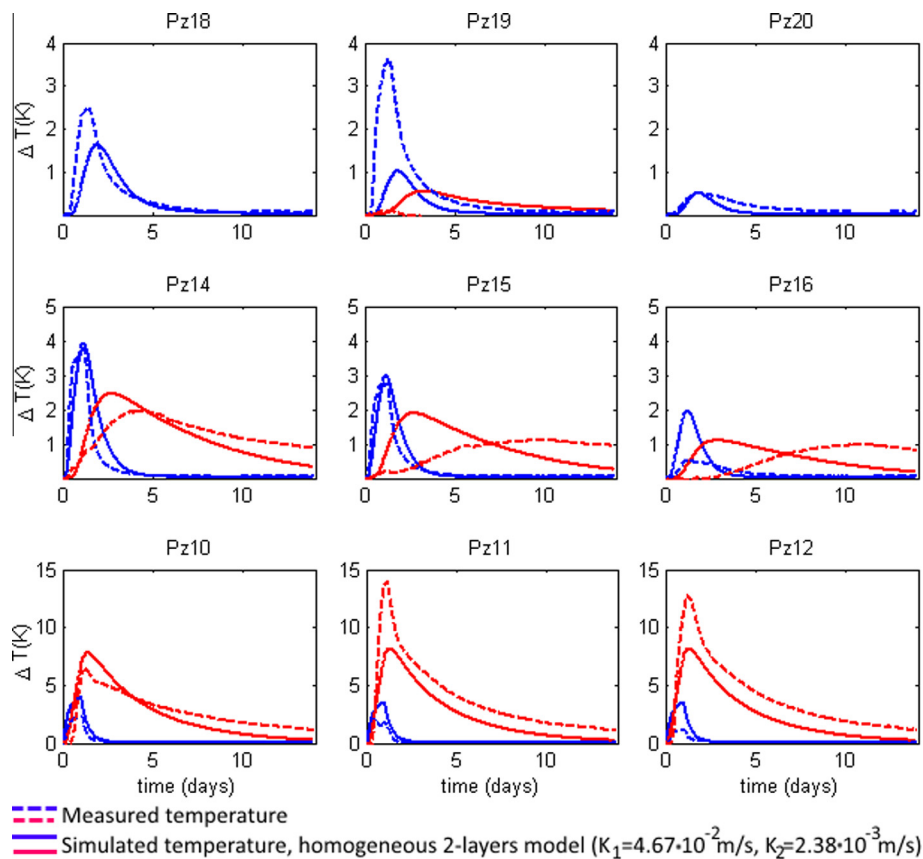


Fig. 7. Comparison of observed (dashed lines) and simulated temperature breakthrough (bold lines) curves in the upper (red) and in the lower (blue) parts of the aquifer. Simulated temperature development was calculated using a two-layered homogeneous numerical heat-transport model. (For interpretation of the references to color in this figure legend, the reader is referred to the web version of this article.)

As suggested by Doherty and Hunt (2010), pilot points were placed at measurements locations and between observation boreholes along the direction of the groundwater gradient. The total number of 18 pilot points were therefore placed in each layer of the model domain. The uniform distribution of pilot points in the model domain is shown in Fig. 3. The heterogeneity of the hydraulic conductivity field in the vertical direction was represented through consideration of two layers (36 pilot points were considered in total). Although the model boundaries were extended beyond the site in order to minimize the effect of boundary conditions, only the hydraulic conductivity in the vicinity of points where the temperature data were available was calibrated. Our numerical tests showed that an increase of number of pilot points will not necessarily improve structure identification as additional

pilot points are less sensitivity to model outcomes. We thus argue that the proposed parametrization is sufficient to capture the main structures, while placement of additional pilot points would substantially increase inversion time.

The calibration of the K -distribution was performed in two steps: the model first optimized K values to pilot points located in the area reached by the thermal plume during the first 24 h. As discussed above, we explicitly modelled density effects during this period. The values for the remaining pilot points (shown by red symbols in Fig. 3) were kept constant through this step. These values were calibrated in a second step using the later part of the transient temperature responses without considering density effect. The initial values and values assigned to zones extended beyond the site were taken from the results of the zonation model.

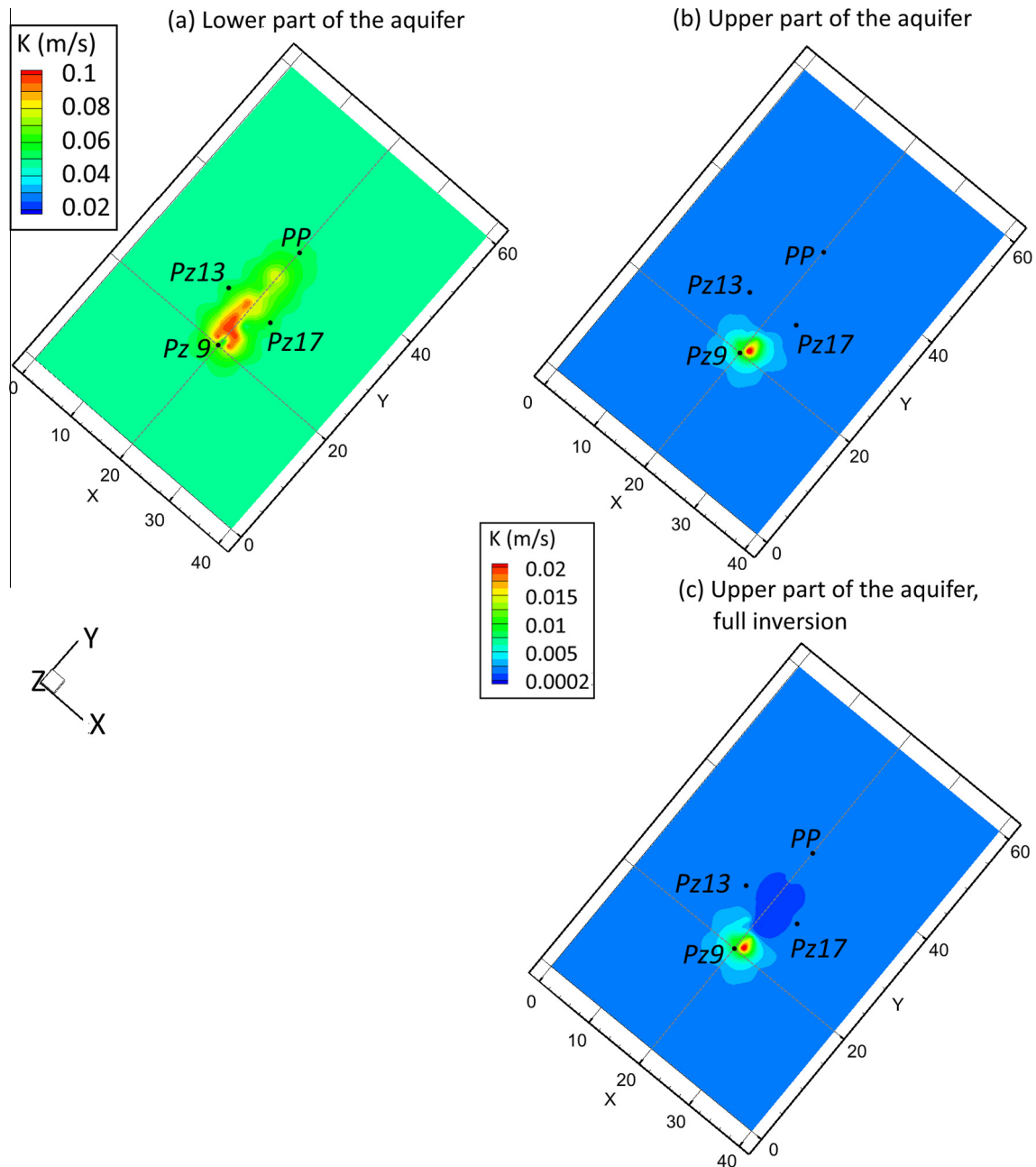


Fig. 8. Two-dimensional K (m/s) tomogram for the lower (a) and upper ((b) first step of the calibration procedure and (c) second step of the calibration procedure) parts of the aquifer obtained from the inversion of transient temperature responses.

4. Results and discussion

4.1. Experimental results

The evolution of the temperature in the injection borehole collected by the DTS is shown in Fig. 1c (Wildemeersch et al., 2014). During the injection period a maximum injection temperature of 38 °C was reached at the lower part of the borehole and 34 °C was observed at the upper part. At the end of the injection, the temperature decreased and the rate of temperature decrease was higher in the lower part of the well. This temperature stratification is related to generally higher values of hydraulic conductivity in the lower part of the aquifer (consisting mainly of coarser gravels) resulting in a fast flushing of the heat out of the injection well.

The trajectory of the measured heat plume was interpolated from point measurements in boreholes and presented in Fig. 4 for the upper (A) and in the lower (B) part of the aquifer. As shown in Fig. 4, the heat plume generally followed the direction of the groundwater flow and deviations from this direction reflect local lateral heterogeneities of the hydraulic conductivity at the site. Moreover, as expected from previous studies, transport is faster in the lower part of the aquifer. The maximum temperature was observed in the upper screen segments of the boreholes from the first control plane one day after injection. As the hot water was injected near the bottom of Pz9, this indicates heat and possible

groundwater upflow resulting from the density effect in the vicinity of the injection well. Furthermore, the signal in the upper part of the aquifer is attenuated quickly due to thermal diffusion.

More detailed insights into the heat transport can be provided by considering variations in the arrival times and peaks of thermal tracer breakthrough curves shown in Fig. 5. The comparison between temperature breakthrough curves in the lower (blue curves) and the upper (red curves) parts of the aquifer confirms that heat transfer is faster in the lower part of the aquifer: breakthrough peaks recorded in the lower part of the aquifer arrives almost at the same time in all boreholes (1.04 days in Pz10 versus 1.85 days in Pz20) and their amplitudes vary over narrow range between 0.5 and 4 K. Small increase of peak amplitudes in the lower part of the aquifer from the first to the second transverse plane is due to the slight difference in depths at which temperature transducers were placed (1 m deeper in Pz10–Pz12 wells). The breakthrough curves in the upper part of the aquifer are much more affected by diffusive transport with high peak attenuation (15 K in Pz11 versus 0.1 K in Pz19) and also by longer tailings. Lateral spreading of the heat plume presented at all depths is also explained by the direction of natural groundwater flow at the site (Fig. 2b) and by the heterogeneity of the alluvial deposit.

The observed complex heat pattern was also confirmed by time-lapse electrical resistivity tomography (ERT) data collected during the experiment. An ERT section was set up across the main

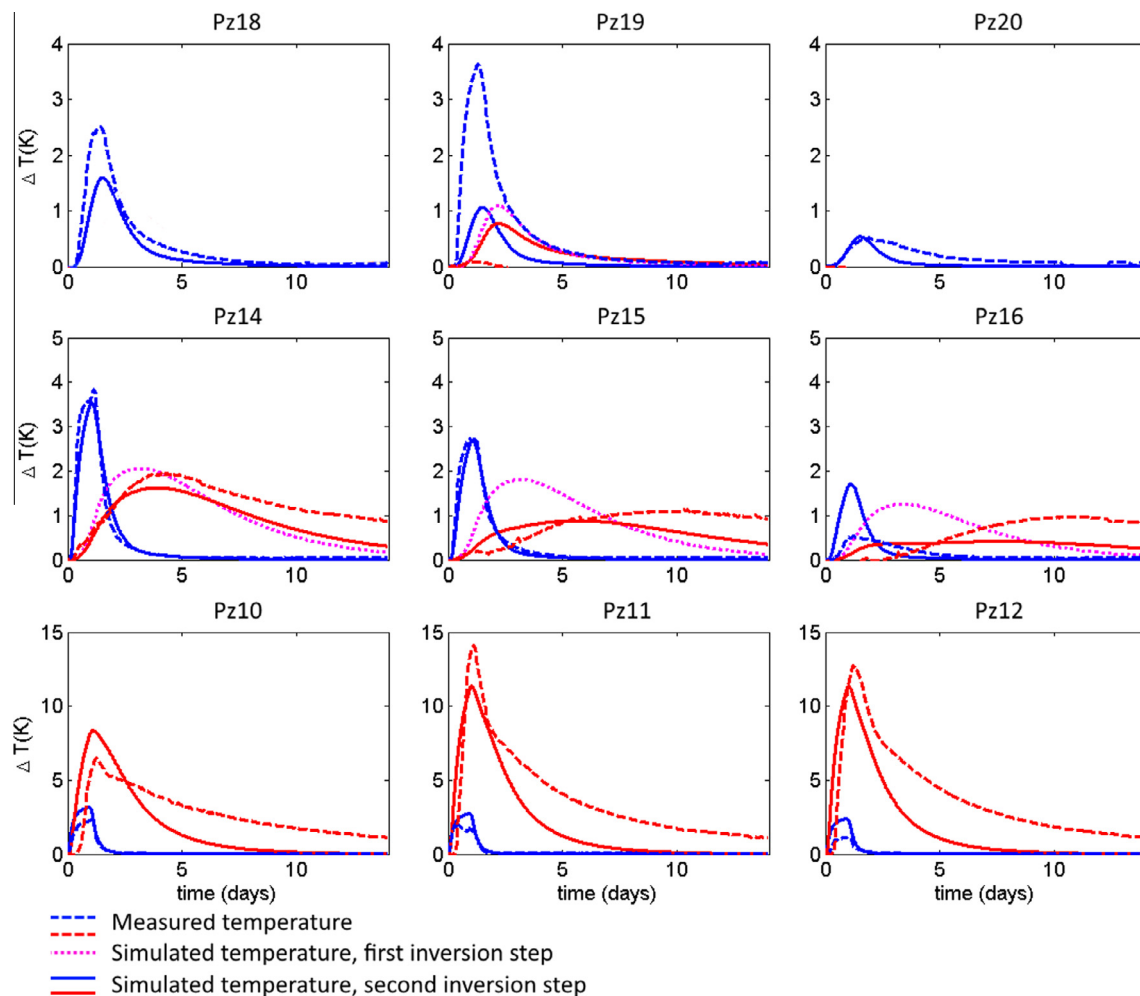


Fig. 9. Comparison of observed (dashed lines) and simulated temperature breakthrough (bold lines) curves in the upper (red) and in the lower (blue) parts of the aquifer. Pink dashed line shows the thermal breakthrough curves simulated with a hydraulic conductivity field obtained after the first step of the inversion (Fig. 8b). (For interpretation of the references to color in this figure legend, the reader is referred to the web version of this article.)

flow direction between Pz13 et Pz17 wells to cross the heat plume. The results of ERT were transformed into temperature using calibrated petrophysical relationships and the comparison of ERT results with direct measurements show a very good agreement with the maximum error of 10–20% made on temperature (Hermans et al., 2015b). However, the vertical temperature profile collected in Pz13 well is almost constant and not in accordance with other data. This can be explained by the fact that intrawell mixing can be present in this fully screened well (Ma et al., 2012). This effect is also visible in Pz17 but to a lesser extent. These two temperature profiles are presented in Fig. 6 and are consequently not taken into account in the subsequent analysis.

4.2. Calibration of the numerical model

4.2.1. Zonation model

The hydraulic conductivity values of a zonation model with two layers were calibrated using PEST. For the more conductive lower aquifer layer, a value of $4.67 \cdot 10^{-2}$ m/s was derived and in the upper aquifer part a value of $2.38 \cdot 10^{-3}$ m/s was optimized. These results are in a good agreement with the Darcy flux measurements conducted previously in each screen segment of every borehole at the site (Wildemeersch et al., 2014). The comparison between measured data (bold lines) and simulated temperature breakthrough (dashed line) curves is presented in Fig. 7. Partly a good agreement was achieved between the simulated and observed temperatures in the lower aquifer layer (blue curves). However, significant disparities exist between the simulated and measured temperatures in the upper layer (red curves). For the zonation model with this parameter set, the minimum root mean square error (RMSE) used to quantify the goodness-of-fit between all simulated and measured temperature breakthrough equals to 1 K. Thus, even we reached some similarities, we consider that the temperature signal was not matched well enough and that a more complex heterogeneity should be introduced into the model.

4.2.2. Pilot points model

The model domain was then parametrized through pilot points, meaning that hydraulic conductivity values were assigned to the considered pilot points rather than directly to the grid of the numerical model. Outside the site, hydraulic conductivity values were not calibrated and we assumed that hydraulic conductivity is homogeneous and was set to values derived from the calibration of the 2-layered model described above ($4.67 \cdot 10^{-2}$ m/s and $2.38 \cdot 10^{-3}$ m/s for the lower and upper layers respectively). Applying this pilot point method, the calibrated hydraulic conductivity field for both layers was inverted to obtain values mapped in Fig. 8.

Experimental results show that the injected heat pulse has passed lower screen segments of all observation boreholes one day after injection (Fig. 4b). We thus calibrated hydraulic conductivity of the lower layer of the aquifer by the inversion of only early time data (24 h). The resulting tomogram for the lower part of the aquifer (Fig. 8a) clearly shows a fast flow pathway to the left from the Y axis of the model domain. This feature explains lateral spreading of the heat plume as well as its high velocity of propagation.

Heat transport in the upper part of the aquifer is much slower and thus all transient temperature data were used in the calibration process. As discussed earlier, the values for pilot points distributed in the upper layer were assigned in two steps. The result of the first step, where only early time data were used is shown in Fig. 8b. Calibrated hydraulic conductivity field reveals a higher conductivity zone located in between the injection borehole and Pz11–Pz12 wells, explaining higher temperatures measured in these observation wells. The second tomogram where the values

of the remaining pilot points (red points in Fig. 3) were obtained through inversion of late time data is presented in Fig. 8c. Resulting inverted hydraulic conductivity distribution shows a region with a lower hydraulic conductivity value located in the east-central portion of the field site. This zone of lower conductivity induces slower and weaker temperature signals in Pz15 and Pz16 wells.

The resulting modelled breakthrough curves are presented in Fig. 9 (blue curves correspond to the lower part of the aquifer and red curves correspond to the upper part of the aquifer) in comparison with measured temperatures (dashed lines). Pink curves shown in Fig. 9 for the second and third control planes result from the first step of the calibration procedure, while red curves correspond to the best overall fit to the full data set. Comparison of red and pink curves shows improvements in the fit (RMSE decreased from 0.85 K to 0.7 K) taking into account the full 14-days data set instead of considering only the first 24 h. The overall match between the observed and simulated values was remarkably improved with respect to the simple two layers model (RMSE decreased from 1 K to 0.7 K). Significant improvements in the data fit could be seen in the lower part of Pz10, Pz11, Pz14 and Pz15 wells and in the upper part of Pz11, Pz12, Pz15 and Pz16 wells (compare red and blue curves in Figs. 7 and 9). Some discrepancies still exist and could be related to vertical hydraulic heterogeneities within aquifer layers. Another plausible reason could be small-scale local heterogeneities around observation boreholes possibly created during drilling operations. Finally, no immobile/mobile

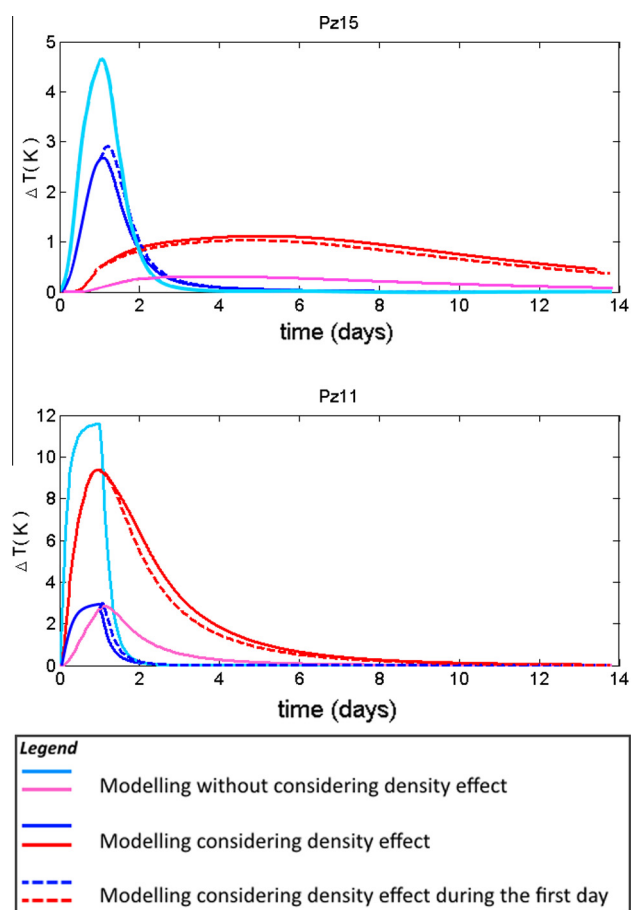


Fig. 10. Comparison of simulated temperature breakthrough curves in the upper (red and pink) and in the lower (blue) parts of the aquifer with and without considering the density effect in two selected wells. (For interpretation of the references to color in this figure legend, the reader is referred to the web version of this article.)

water regions were considered in our study although it is likely to happen in this aquifer (Brouyère, 2001).

The overall values obtained for hydraulic conductivity are consistent with previous pumping test studies and with results from the FVPDM technique, that showed a spread of the measured Darcy fluxes at the site of about two orders of magnitude (Brouyère et al., 2008; Wildemeersch et al., 2014). We also verified that the calibrated K -values induce only minor effects on the calculated piezometric map (i.e. computed by the groundwater flow model) and resulting hydraulic heads in wells are in close agreement with heads measured in boreholes during the experiment.

Finally, we used the obtained K distribution in order to show clearly the density effect caused by injection of hot water. To do so, the simulated temperatures presented in Fig. 9 were compared to temperatures simulated using a model considering a constant water density, and to temperatures simulated using a model considering density effect for the entire simulation. Fig. 10 shows the comparison of simulated temperature breakthrough curves for two boreholes Pz11 and Pz15. The density effect has a strong impact on temperature variations: in the first control plane up to 10 K difference is observed between temperature peaks from the model without (blue and pink lines for lower and upper screen segments, respectively) and with consideration of density effects (dark blue and red lines for lower and upper screen segments, respectively). This vertical distribution of heat due to injection of hot water influences then temperature distribution in all boreholes. As expected, density effect plays a significant role only during the first day, so neglecting the effect at late times causes only very minor changes in the calculated breakthrough curves (dashed blue and red lines versus bold blue and red lines, respectively).

5. Conclusions

A coupled solute and heat tracer test experiment was designed and conducted in saturated heterogeneous alluvial sediments at the Hermalle-sous-Argenteau site near Liege (Belgium). In our previous study (Wildemeersch et al., 2014), temperature and concentration measurements in the pumping well were used in order to assess specific heat capacity, effective porosity and longitudinal dispersivity values for the experimental site. In the present study, detailed temperature measurements in other observation wells were explicitly analyzed. The space-filling arrangement (e.g. three observation well transects) as well as nested configuration of monitoring wells allowed detailed assessments of the three-dimensional spreading of the injected heat plume. Thermal breakthrough curves collected during this experiment showed large vertical and lateral thermal plume spreading.

By inversion of temperature breakthrough curves measured in observation boreholes, valuable insights in the 3D characteristics of the heat transport mechanisms were obtained. The observed complex behavior of the heat plume was explained by high lateral and vertical heterogeneity of the hydraulic conductivity field combined to the groundwater flow gradient on the site. Additionally, a clear temperature-induced water density effect was detected. Initial calibration of the developed numerical model to the measured temperature breakthrough curves was based on a simple zonation approach. Those first results demonstrated that more flexible parametrization of the spatial variability of hydraulic properties was needed to be considered. Then by using the pilot-point based inversion approach, the main preferential paths were characterized as providing a reasonably good fit to all observed thermal breakthrough curves.

Due to high injection temperatures during the field experiment a temperature-induced water density effect occurred in the vicinity of the injection well and at least during the injection period.

This may be clearly seen from the vertical distributions of temperatures in the aquifer (higher temperatures are observed in the upper part of the aquifer close to the injection well). This density effect affects many processes of groundwater flow and transport. The interpretation of temperature data becomes more complicated with the accompanying intensive computational demands especially for inverting the parameter field. Nevertheless, lower injection temperature would lead to highly damped temperature signals within a short distance from the injection well and, thus, would not allow characterization of the upper part of the aquifer.

Finally, this study considers heat transport processes playing a predominant role in heat storage projects, open shallow and low temperature geothermal projects. Our results indicate that the actual efficiency of these projects will be strongly affected by the heterogeneity of the K -field. Heat tracer tests, combined with detailed inversion procedures could be a useful approach for constraining groundwater flow and heat transport models used for assessing low temperature geothermal systems as well as of many similar projected geothermal systems efficiency in urban zones.

Acknowledgments

M. Klepikova gratefully acknowledges the financial support from the University of Liège and the EU through the Marie Curie BeIPD-COFUND postdoctoral fellowship program (2013–2014).

References

- Anderson, Mary P., 2005. Heat as a ground water tracer. *Ground Water* 43 (6), 951–968. <http://dx.doi.org/10.1111/j.1745-6584.2005.00052.x>, ISSN 1745-6584RL.
- Batlle-Aguilar, Jordi, Brouyère, Serge, Dassargues, Alain, Morasch, Barbara, Hunkeler, Daniel, Höhener, Patrick, Diels, Ludo, Vanbroekhoven, Karolien, Seuntjens, Piet, Halen, Henri, 2009. Benzene dispersion and natural attenuation in an alluvial aquifer with strong interactions with surface water. *J. Hydrol.* 369 (34), 305–317. <http://dx.doi.org/10.1016/j.jhydrol.2009.02.014> <<http://www.sciencedirect.com/science/article/pii/S0022169409001061>>, ISSN 0022-1694 (Transfer of pollutants in soils, sediments and water systems: From small to large scale (AquaTerra)).
- Bense, V.F., Kooi, H., 2004. Temporal and spatial variations of shallow subsurface temperature as a record of lateral variations in groundwater flow. *J. Geophys. Res.: Solid Earth* 109 (B4). <http://dx.doi.org/10.1029/2003JB002782>, n/a–n/a. ISSN 2156-2202 B04103.
- Bertermann, D., Rohn, J., Bialas, C., 2013. Thermomap Area Mapping of Superficial Geothermic Resources by Soil and Groundwater Data. <<http://www.thermomap-project.eu/wp-content/uploads/2012/04/Poster-ThermoMap-English-2012.pdf>>.
- Bredehoeft, J.D., Papaopulos, I.S., 1965. Rates of vertical groundwater movement estimated from the earth's thermal profile. *Water Resour. Res.* 1 (2), 325–328. <http://dx.doi.org/10.1029/WR001i002p00325>, ISSN 1944-7973.
- Brouyère, S., 2001. Etude et modélisation du transport et du piégeage des solutés en milieu souterrain variablement saturé (study and modelling of transport and retardation of solutes in variably saturated media) (French. Ph.D. Thesis). University of Liège, Faculty of Applied Sciences.
- Brouyère, Serge, Batlle-Aguilar, Jordi, Goderniaux, Pascal, Dassargues, Alain, 2008. A new tracer technique for monitoring groundwater fluxes: the finite volume point dilution method. *J. Contam. Hydrol.* 95 (34), 121–140. <http://dx.doi.org/10.1016/j.jconhyd.2007.09.001>, ISSN 0169-7722. <<http://www.sciencedirect.com/science/article/pii/S0169772207001064>>.
- Chatelier, Marion, Ruelleu, Sébastien, Bour, Olivier, Porel, Gilles, Delay, Frederick, 2011. Combined fluid temperature and flow logging for the characterization of hydraulic structure in a fractured karst aquifer. *J. Hydrol.* 400 (34), 377–386. <http://dx.doi.org/10.1016/j.jhydrol.2011.01.051>, ISSN 0022-1694 <<http://www.sciencedirect.com/science/article/pii/S0022169411000850>>.
- Coleman, Thomas I., Parker, Beth L., Maldaner, Carlos H., Mondanos, Michael J., 2015. Groundwater flow characterization in a fractured bedrock aquifer using active DTS tests in sealed boreholes. *J. Hydrol.* 528, 449–462. <http://dx.doi.org/10.1016/j.jhydrol.2015.06.061>, ISSN 0022-1694 <<http://www.sciencedirect.com/science/article/pii/S0022169415004746>>.
- Dassargues, A., 1997. Modeling baseflow from an alluvial aquifer using hydraulic-conductivity data obtained from a derived relation with apparent electrical resistivity. *Hydrogeol. J.* 5 (3), 97–108. <http://dx.doi.org/10.1007/s100400050125>, ISSN 1431-2174.
- Derouane, J., Dassargues, A., 1998. Delineation of groundwater protection zones based on tracer tests and transport modeling in alluvial sediments. *Environ. Geol.* 36 (1–2), 27–36. <http://dx.doi.org/10.1007/s002540050317>, ISSN 0943-0105.

- Doherty, John, 2003. Ground water model calibration using pilot points and regularization. *Ground Water* 41 (2), 170–177. <http://dx.doi.org/10.1111/j.1745-6584.2003.tb02580.x>, ISSN 1745-6584.
- Doherty, John E., Hunt, Randall J., 2010. Approaches to Highly Parameterized Inversion: A Guide to using PEST for Groundwater-model Calibration: U.S. Geological Survey Scientific Investigations Report 2010–5169, p. 59.
- Dorn, Caroline, Linde, Niklas, Le Borgne, Tanguy, Bour, Olivier, Klepikova, Maria, 2012. Inferring transport characteristics in a fractured rock aquifer by combining single-hole GPR reflection monitoring and tracer test data. *Water Resour. Res.* 48.
- Doro, Kennedy O., Cirpka, Olaf A., Leven, Carsten, 2015. Tracer tomography: design concepts and field experiments using heat as a tracer. *Groundwater* 53 (S1), 139–148. <http://dx.doi.org/10.1111/gwat.12299>, ISSN 1745-6584.
- Freifeld, B.M., Finsterle, S., Onstott, T.C., Toole, P., Pratt, L.M., 2008. Ground surface temperature reconstructions: using in situ estimates for thermal conductivity acquired with a fiber-optic distributed thermal perturbation sensor. *Geophys. Res. Lett.* 35 (14). <http://dx.doi.org/10.1029/2008GL034762>, n/a–n/a. ISSN 1944-8007.
- Giambastiani, B.M.S., Colombani, N., Mastrocicco, M., 2013. Limitation of using heat as a groundwater tracer to define aquifer properties: experiment in a large tank model. *Environ. Earth Sci.* 70 (2), 719–728. <http://dx.doi.org/10.1007/s12665-012-2157-2>, ISSN 1866-6280.
- Goderniaux, Pascal, Brouyère, Serge, Wildemeersch, Samuel, Therrien, René, Dassargues, Alain, 2015. Uncertainty of climate change impact on groundwater reserves application to a chalk aquifer. *J. Hydrol.* 528, 108–121. <http://dx.doi.org/10.1016/j.jhydrol.2015.06.018>, ISSN 0022-1694. <<http://www.sciencedirect.com/science/article/pii/S002216941500431X>>.
- Graf, Thomas, Therrien, René, 2005. Variable-density groundwater flow and solute transport in porous media containing nonuniform discrete fractures. *Adv. Water Resour.* 28 (12), 1351–1367. <http://dx.doi.org/10.1016/j.advwatres.2005.04.011>, ISSN 0309-1708. <<http://www.sciencedirect.com/science/article/pii/S0309170805001041>>.
- Guihéneuf, N., Boisson, A., Bour, O., Dewandel, B., Perrin, J., Dausse, A., Viossanges, M., Chandra, S., Ahmed, S., Maréchal, J.C., 2014. Groundwater flows in weathered crystalline rocks: impact of piezometric variations and depth-dependent fracture connectivity. *J. Hydrol.* 511, 320–334. <http://dx.doi.org/10.1016/j.jhydrol.2014.01.061>, ISSN 0022-1694. <<http://www.sciencedirect.com/science/article/pii/S0022169414000833>>.
- Hausner, Mark B., Kryder, Levi, Klenke, John, Reinke, Richard, Tyler, Scott W., 2015. Interpreting variations in groundwater flows from repeated distributed thermal perturbation tests. *Groundwater*. <http://dx.doi.org/10.1111/gwat.12393>, n/a–n/a. ISSN 1745-6584.
- Hermans, Thomas, Nguyen, Frédéric, Caers, Jef, 2015a. Uncertainty in training image-based inversion of hydraulic head data constrained to ERT data: workflow and case study. *Water Resour. Res.* 51 (7), 5332–5352. <http://dx.doi.org/10.1002/2014WR016460>, ISSN 1944-7973.
- Hermans, Thomas, Wildemeersch, Samuel, Jamin, Pierre, Orban, Philippe, Brouyère, Serge, Dassargues, Alain, Nguyen, Frédéric, 2015b. Quantitative temperature monitoring of a heat tracing experiment using cross-borehole [ERT]. *Geothermics* 53 (0), 14–26. <http://dx.doi.org/10.1016/j.geothermics.2014.03.013>, ISSN 0375-6505. <<http://www.sciencedirect.com/science/article/pii/S0375650514000376>>.
- Irvine, Dylan J., Simmons, Craig T., Werner, Adrian D., Graf, Thomas, 2015. Heat and solute tracers: how do they compare in heterogeneous aquifers? *Groundwater* 53 (S1), 10–20. <http://dx.doi.org/10.1111/gwat.12146>, ISSN 1745-6584.
- Jiménez, S., Brauchler, R., Hu, R., Hu, L., Schmidt, S., Ptak, T., Bayer, P., 2015. Prediction of solute transport in a heterogeneous aquifer utilizing hydraulic conductivity and specific storage tomograms. *Water Resour. Res.* 51 (7), 5504–5520.
- Klepikova, Maria V., Le Borgne, Tanguy, Bour, Olivier, Davy, Philippe, 2011. A methodology for using borehole temperature-depth profiles under ambient, single and cross-borehole pumping conditions to estimate fracture hydraulic properties. *J. Hydrol.* 407 (14), 145–152. <http://dx.doi.org/10.1016/j.jhydrol.2011.07.018>, ISSN 0022-1694. <<http://www.sciencedirect.com/science/article/pii/S0022169411004604>>.
- Klepikova, M.V., Le Borgne, T., Bour, O., Dentz, M., Hochreutener, R., Lavenant, N., 2016. Heat as a tracer for understanding transport processes in fractured media: theory and field assessment from multi-scale thermal push-pull tracer tests. *Water Resour. Res.* <http://dx.doi.org/10.1002/2016WR018789>, accepted for publication.
- Leaf, Andrew T., Hart, David J., Bahr, Jean M., 2012. Active thermal tracer tests for improved hydrostratigraphic characterization. *Ground Water* 50 (5), 726–735. <http://dx.doi.org/10.1111/j.1745-6584.2012.00913.x>, ISSN 1745-6584.
- Liu, G., Knobbe, S., Butler, J.J., 2013. Resolving centimeter-scale flows in aquifers and their hydrostratigraphic controls. *Geophys. Res. Lett.* 40 (6), 1098–1103. <http://dx.doi.org/10.1002/grl.50282>, ISSN 1944-8007.
- Ma, Rui, Zheng, Chunmiao, 2010. Effects of density and viscosity in modeling heat as a groundwater tracer. *Ground Water* 48 (3), 380–389. <http://dx.doi.org/10.1111/j.1745-6584.2009.00660.x>, ISSN 1745-6584.
- Ma, Rui, Zheng, Chunmiao, Zachara, John M., Tonkin, Matthew, 2012. Utility of bromide and heat tracers for aquifer characterization affected by highly transient flow conditions. *Water Resour. Res.* 48 (8). <http://dx.doi.org/10.1029/2011WR011281>, n/a–n/a. ISSN 1944-7973 W08523.
- Moeck, Christian, Hunkeler, Daniel, Brunner, Philip, 2015. Tutorials as a flexible alternative to GUIs: an example for advanced model calibration using pilot points. *Environ. Model. Softw.* 66, 78–86. <http://dx.doi.org/10.1016/j.envsoft.2014.12.018>. <<http://www.sciencedirect.com/science/article/pii/S1364815214003752>>.
- Molina-Giraldo, Nelson, Bayer, Peter, Blum, Philipp, 2011. Evaluating the influence of thermal dispersion on temperature plumes from geothermal systems using analytical solutions. *Int. J. Therm. Sci.* 50 (7), 1223–1231. <http://dx.doi.org/10.1016/j.ijthermalsci.2011.02.004>, ISSN 1290-0729 <<http://www.sciencedirect.com/science/article/pii/S129007291100038X>>.
- Pehme, P.E., Parker, B.L., Cherry, J.A., Molson, J.W., Greenhouse, J.P., 2013. Enhanced detection of hydraulically active fractures by temperature profiling in lined heated bedrock boreholes. *J. Hydrol.* 484, 1–15. <http://dx.doi.org/10.1016/j.jhydrol.2012.12.048>, ISSN 0022-1694. <<http://www.sciencedirect.com/science/article/pii/S002216941300019X>>.
- Ptak, T., Piepenbrink, M., Martac, E., 2004. Tracer tests for the investigation of heterogeneous porous media and stochastic modelling of flow and transport—a review of some recent developments. *J. Hydrol.* 294, 122–163. <http://dx.doi.org/10.1016/j.jhydrol.2004.01.020>.
- Rau, Gabriel C., Andersen, Martin S., Ian Acworth, R., 2012. Experimental investigation of the thermal dispersivity term and its significance in the heat transport equation for flow in sediments. *Water Resour. Res.* 48 (3). <http://dx.doi.org/10.1029/2011WR011038>, n/a–n/a. ISSN 1944-7973 W03511.
- Read, T., Bour, O., Selker, J.S., Bense, V.F., Le Borgne, T., Hochreutener, R., Lavenant, N., 2014. Active-distributed temperature sensing to continuously quantify vertical flow in boreholes. *Water Resour. Res.* 50 (5), 3706–3713. <http://dx.doi.org/10.1002/2014WR015273>, ISSN 1944-7973.
- Read, Tom, Bour, Olivier, Bense, V., Le Borgne, Tanguy, Goderniaux, Pascal, Klepikova, M.V., Hochreutener, Rebecca, Lavenant, Nicolas, Boscherio, Vincent, 2013. Characterizing groundwater flow and heat transport in fractured rock using fiber-optic distributed temperature sensing. *Geophys. Res. Lett.* 40 (10), 2055–2059.
- Saar, Martin O., 2011. Review: geothermal heat as a tracer of large-scale groundwater flow and as a means to determine permeability fields. *Hydrogeol. J.* 19 (1), 31–52. <http://dx.doi.org/10.1007/s10040-010-0657-2>, ISSN 1431-2174.
- Sanchez-León, E., Leven, C., Haslauer, C.P., Cirpka, O.A., 2015. Combining 3d hydraulic tomography with tracer tests for improved transport characterization. *Groundwater*. <http://dx.doi.org/10.1111/gwat.12381>, n/a–n/a. ISSN 1745-6584.
- Schwede, Ronnie L., Li, Wei, Leven, Carsten, Cirpka, Olaf A., 2014. Three-dimensional geostatistical inversion of synthetic tomographic pumping and heat-tracer tests in a nested-cell setup. *Adv. Water Resour.* 63 (0), 77–90. <http://dx.doi.org/10.1016/j.advwatres.2013.11.004>, ISSN 0309-1708. <<http://www.sciencedirect.com/science/article/pii/S0309170813002248>>.
- Somogyvári, M., Bayer, P., Brauchler, R., 2016. Travel time based thermal tracer tomography. *Hydrol. Earth Syst. Sci. Discuss.*, 1–43 <http://dx.doi.org/10.5194/hess-2015-509>. <<http://www.hydrol-earth-syst-sci-discuss.net/hess-2015-509/>>.
- Therrien, R., McLaren, R.G., Sudicky, E.A., Panday, S.M., 2010. *Hydrogeosphere: A Three-dimensional Numerical Model Describing Fully-integrated Subsurface and Surface Flow and Solute Transport*. Groundwater Simulations Group, University of Waterloo, Waterloo, ON.
- Vandenbohede, A., Louwyck, A., Lebbe, L., 2009. Conservative solute versus heat transport in porous media during push-pull tests. *Transp. Porous Media* 76 (2), 265–287. <http://dx.doi.org/10.1007/s11242-008-9246-4>, ISSN 0169-3913.
- Vandenbohede, Alexander, Hermans, Thomas, Nguyen, Frédéric, Lebbe, Luc, 2011. Shallow heat injection and storage experiment: heat transport simulation and sensitivity analysis. *J. Hydrol.* 409 (12), 262–272. <http://dx.doi.org/10.1016/j.jhydrol.2011.08.024>, ISSN 0022-1694. <<http://www.sciencedirect.com/science/article/pii/S0022169411005701>>.
- Wagner, Valentin, Li, Tao, Bayer, Peter, Leven, Carsten, Dietrich, Peter, Blum, Philipp, 2014. Thermal tracer testing in a sedimentary aquifer: field experiment (Lauswiesen, Germany) and numerical simulation. *Hydrogeol. J.* 22 (1), 175–187. <http://dx.doi.org/10.1007/s10040-013-1059-z>, ISSN 1431-2174.
- Wildemeersch, S., Jamin, P., Orban, P., Hermans, T., Klepikova, M., Nguyen, F., Brouyère, S., Dassargues, A., 2014. Coupling heat and chemical tracer experiments for estimating heat transfer parameters in shallow alluvial aquifers. *J. Contam. Hydrol.* 169 (0), 90–99. <http://dx.doi.org/10.1016/j.jconhyd.2014.08.001>, ISSN 0169-7722. <<http://www.sciencedirect.com/science/article/pii/S0169772214001247>>.
- Zhou, Haiyan, Jaime Gómez-Hernández, J., Li, Liangping, 2014. Inverse methods in hydrogeology: evolution and recent trends. *Adv. Water Resour.* 63, 22–37. <http://dx.doi.org/10.1016/j.advwatres.2013.10.014>, ISSN 0309-1708. <<http://www.sciencedirect.com/science/article/pii/S0309170813002017>>.

5. INFO

WEDNESDAY 7/3

Timing

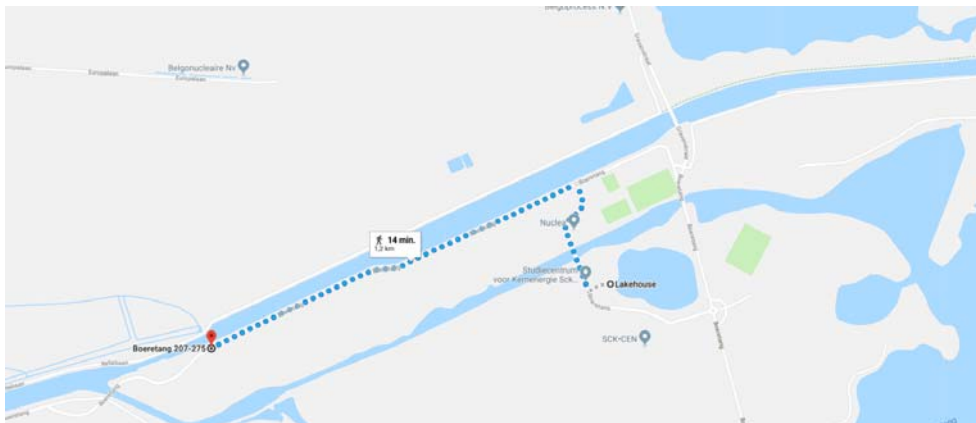
- Registration and lunch starts at 12:00
- The workshop will begin at 13:00

Venue and transportation

VITO, building TAP
Boeretang 282
2400 Mol

For the fellows of INSPIRATION: please take the 9:37 train (Brussel central station) with arrival at 11:02 in Mol

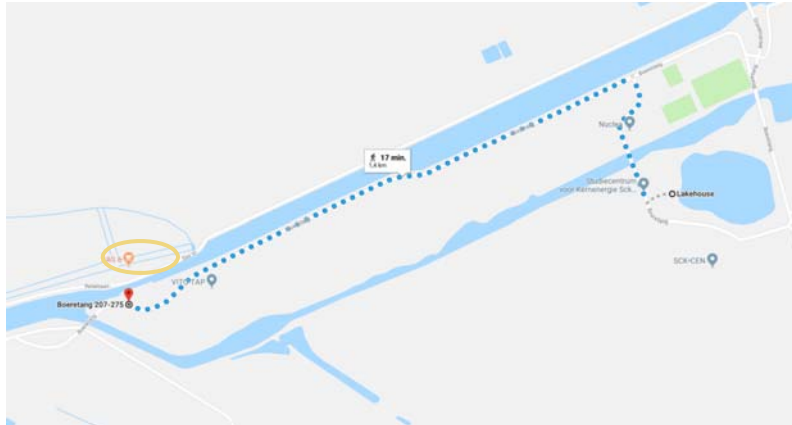
- Make sure you buy your tickets beforehand: [link](#) to public transportation website
- A taxi will be waiting to drop you off at the Lake house, so you can first check-in and afterwards you can walk to the venue



If you are an external participant, you are welcome to join the taxi at 11:00. However, if you are unable to catch this train, we are happy to pick you up at any other moment. Please let us know your itinerary and we will make sure a car is waiting at the train station.

Evening program (at own expenses)

Dinner is reserved at walking distance of Hotel Lake House
Location: Sas 6: [link](#)



THURSDAY 8/3

Timing

- Registration and assembly at 8:15 at VITO, Building TAP
- The bus will leave at 8:30
- Lunch will be provided on site
- Wrap up 15:30 (bus trip of +- 1,5 hours)

Venue and transportation

Field visit to Hermalle-sous-Argenteau

- Make sure you bring appropriate shoes and clothes (weather forecast: 8°C and rain)

Evening program (at own expenses)

Dinner is reserved at Mol

Location: De Onthaasting [link](#)

A taxi will pick you up at 19:00 at lake house.

Gisela will call the taxi for the ride back.

FRIDAY 9/3

Timing

- Registration starts at 09:00
- The workshop ends at 12.30

Lunch

Sandwiches have been foreseen.

Transportation to Mol station

Participants will be transported to the station based on the requested needs.